Density Model for Humpback Whale (*Megaptera novaeangliae*) for the U.S. East Coast: Supplementary Report

Model Version 11.1

Duke University Marine Geospatial Ecology Laboratory*

2023-05-27

Citation

When citing our methodology or results generally, please cite Roberts et al. (2016, 2023). The complete references appear at the end of this document. We are preparing a new article for a peer-reviewed journal that will eventually replace those. Until that is published, those are the best general citations.

When citing this model specifically, please use this reference:

Roberts JJ, Yack TM, Cañadas A, Fujioka E, Halpin PN, Barco SG, Boisseau O, Chavez-Rosales S, Cole TVN, Cotter MP, Cummings EW, Davis GE, DiGiovanni Jr. RA, Garrison LP, Gowan TA, Jackson KA, Kenney RD, Khan CB, Lockhart GG, Lomac-MacNair KS, McAlarney RJ, McLellan WA, Mullin KD, Nowacek DP, O'Brien O, Pabst DA, Palka DL, Quintana-Rizzo E, Redfern JV, Rickard ME, White M, Whitt AD, Zoidis AM (2022) Density Model for Humpback Whale (*Megaptera novaeangliae*) for the U.S. East Coast, Version 11.1, 2023-05-27, and Supplementary Report. Marine Geospatial Ecology Laboratory, Duke University, Durham, North Carolina.

Copyright and License

This document and the accompanying results are © 2023 by the Duke University Marine Geospatial Ecology Laboratory and are licensed under a Creative Commons Attribution 4.0 International License.

Model Version History

Version	Date	Description
1	2013-05-03	Initial version.
2	2013-05-08	Figures regenerated with improved label placement.

*For questions or to offer feedback please contact Jason Roberts (jason.roberts@duke.edu) and Tina Yack (tina.yack@duke.edu)

(continued)

Version	Date	Description
3	2014-03-01	Switched from four seasonal models to two. Reformulated density model using a Horvitz-Thompson estimator. Eliminated GAM for group size (consequence of above). Added group size as a candidate covariate in detection functions (benefit of above). Added survey ID as a candidate covariate in NOAA NARWSS detection functions. Took more care in selecting right-truncation distances. Fitted models with contemporaneous predictors, for comparison to climatological. Switched SST and SST fronts predictors from NOAA Pathfinder to GHRSST CMC0.2deg L4. Changed SST fronts algorithm to use Canny operator instead of Cayula-Cornillon. Switched winds predictors from SCOW to CCMP (SCOW only gives climatol. estimates.) Added DistToEddy predictors, based on Chelton et al. (2011) eddy database. Added cumulative VGPM predictors, summing productivity for 45, 90, and 180 days. Added North Atlantic Oscillation (NAO) predictor; included 3 and 6 month lags. Transformed predictors more carefully, to better minimize leverage of outliers. Implemented hybrid hierarchical-forward / exhaustive model selection procedure. Model selection procedure better avoids concurvity between predictors. Allowed GAMs to select between multiple formulations of dynamic predictors. Adjusted land mask to eliminate additional estuaries and hard-to-predict cells.
4	2014-05-14	Added discussion of acoustic monitoring studies to text. Eliminated accidentally-included off-effort sighting at Cape Lookout (2006-04-20 14:14:00). Refitted summer model.
5	2014-05-20	Fixed bug in temporal variability plots. Density models unchanged.
6	2014-09-02	Added surveys: NJ-DEP, Virginia Aquarium, NARWSS 2013, UNCW 2013. Extended study area up Scotian Shelf. Added SEAPODYM predictors. Switched to mgcv estimation of Tweedie p parameter (family=tw()).
7	2014-10-15	Added Palka (2006) survey-specific g(0) estimates. Removed distance to eddy predictors and wind speed predictor from all models; they were not ecologically justified. Fixed missing pixels in several climatological predictors, which led to not all segments being utilized. Eliminated Cape Cod Bay subregion.
8	2014-11-11	Reconfigured detection hierarchy and adjusted NARWSS detection functions based on additional information from Tim Cole. Removed CumVGPM180 predictor. Updated documentation.
9	2014-12-03	Fixed bug that applied the wrong detection function to segments NE_narwss_1999_widgeon_hapo dataset. Refitted models. Updated documentation.
9.1	2015-03-05	Updated the documentation. No changes to the model.
9.2	2015-05-14	Updated calculation of CVs. Switched density rasters to logarithmic breaks. No changes to the model.
9.3	2015-09-26	Updated the documentation. No changes to the model.
9.4	2016-04-21	Switched calculation of monthly 5% and 95% confidence interval rasters to the method used to produce the year-round rasters. (We intended this to happen in version 9.2 but I did not implement it properly.) Updated the monthly CV rasters to have value 0 where we assumed the species was absent, consistent with the year-round CV raster. No changes to the other (non-zero) CV values, the mean abundance rasters, or the model itself. Model files released as supplementary information to Roberts et al. (2016).
10	2017-06-01	Began update to Roberts et al. (2015) model. Introduced new surveys from AMAPPS, NARWSS, UNCW, VAMSC, and the SEUS NARW teams. Updated modeling methodology. Refitted detection functions and spatial models from scratch using new and reprocessed covariates. Model released as part of a scheduled update to the U.S. Navy Marine Species Density Database (NMSDD).

(continued)

Version	Date	Description
11	2022-06-20	This model is a major update over the prior version, with substantial additional data, improved statistical methods, and an increased spatial resolution. It was released as part of the final delivery of the U.S. Navy Marine Species Density Database (NMSDD) for the Atlantic Fleet Testing and Training (AFTT) Phase IV Environmental Impact Statement. Several new collaborators joined and contributed survey data: New York State Department of Environmental Conservation, TetraTech, HDR, and Marine Conservation Research. We incorporated additional surveys from all continuing and new collaborators through the end of 2020. (Because some environmental covariates were only available through 2019, certain models only extend through 2019.) We increased the spatial resolution to 5 km and, at NOAA's request, we extended the model further inshore from New York through Maine. We reformulated and refitted all detection functions and spatial models. We updated all enviromental covariates to newer products, when available, and added several covariates to the set of candidates. For models that incorporated dynamic covariates, we estimated model uncertainty using a new method that accounts for both model parameter error and temporal variability.
11.1	2023-05-27	Completed the supplementary report documenting the details of this model. The model itself was not changed.

1 Survey Data

Although a large portion of the humpback population feeding in northeast waters of the U.S. Atlantic in summer migrates to Caribbean breeding grounds in winter (Kennedy et al. 2014), numerous sightings have been reported across the eastern U.S. throughout winter, including over 100 during systematic surveys of Florida and Georgia by teams monitoring the North Atlantic right whale (NARW) calving grounds over the past two decades. Consistent surveying of these areas reached an important milestone in 2003, when in the northeast the NOAA NEFSC NARWSS aerial program began monitoring the Gulf of Maine with the de Havilland Twin Otter aircraft still used today, and in the southeast the NARW Early Warning System teams began for the first time to monitor the NARW calving grounds using the same survey protocol for all teams. Given the apparent importance of these areas to humpbacks, and the recent knowledge that the humpback population has been growing over this period (Robbins and Pace 2018), we built our model from surveys starting at that time (Table 1, Figure 1). Specifically, we built a summer (April-November) seasonal model from surveys conducted from 2003-2020, and a winter (December-March) model from surveys from the winter of 2001/02 through 2019/20, in order to include surveys of the mid-Atlantic and Carolinas conducted by NOAA SEFSC and UNCW during January-March of 2002. For surveys monitoring the NARW calving grounds, we restricted the model to transects with sea states of Beaufort 3 or less, following Gowan and Ortega-Ortiz (2014). Elsewhere, we accepted up to Beaufort 4 or 5, depending on the survey program and data availability. We also excluded transects with poor weather or visibility for surveys that reported those conditions.

Table 1: Survey effort and observations considered for this model. Effort is tallied as the cumulative length of on-effort transects. Observations are the number of groups and individuals encountered while on effort. Off effort observations and those lacking an estimate of group size or distance to the group were excluded.

			Effort	Observations		
Institution	Program	Period	1000s km	Groups	Individuals	Mean Group Size
Aerial Surveys						
FWRI	SEUS NARW EWS	2003-2020	668	56	56	1.0
HDR	Navy Norfolk Canyon	2018-2019	11	9	22	2.4
NEAq	CNM	2017-2020	2	2	2	1.0
NEAq	MMS-WEA	2017-2020	37	51	116	2.3
NEAq	NLPSC	2011-2015	43	59	124	2.1
NEAq	SEUS NARW EWS	2003-2010	227	8	8	1.0
NEFSC	AMAPPS	2010-2019	89	148	195	1.3
NEFSC	NARWSS	2003-2020	484	3,288	6,675	2.0
NEFSC	Pre-AMAPPS	2004-2008	34	93	126	1.4
NJDEP	NJEBS	2008-2009	11	3	5	1.7
NYS-DEC/TT	NYBWM	2017-2020	77	57	159	2.8
SEFSC	AMAPPS	2010-2020	114	15	20	1.3
SEFSC	MATS	2002-2005	21	4	4	1.0
UNCW	MidA Bottlenose	2002-2002	17	3	4	1.3
UNCW	Navy Cape Hatteras	2011-2017	34	6	9	1.5
UNCW	Navy Jacksonville	2009-2017	92	2	2	1.0
UNCW	Navy Norfolk Canyon	2015-2017	14	3	4	1.3
UNCW	Navy Onslow Bay	2007-2011	49	1	2	2.0
UNCW	SEUS NARW EWS	2005-2008	114	10	16	1.6
VAMSC	MD DNR WEA	2013-2015	16	2	2	1.0
VAMSC	Navy VACAPES	2016-2017	19	7	8	1.1
VAMSC	VA CZM WEA	2012-2015	21	12	20	1.7
WLT/SSA/CMARI	SEUS NARW EWS	2003-2020	652	45	50	1.1
		Total	**2,847**	**3,884**	**7,629**	**2.0**
Shipboard Surveys						
MCR	SOTW Visual	2012-2019	9	20	33	1.6
NEFSC	AMAPPS	2011-2016	16	124	178	1.4
NEFSC	Pre-AMAPPS	2004-2007	6	162	274	1.7
NJDEP	NJEBS	2008-2009	14	7	9	1.3
SEFSC	AMAPPS	2011-2016	17	1	1	1.0
SEFSC	Pre-AMAPPS	2002-2006	20	0	0	
		Total	**81**	**314**	**495**	**1.6**

Table 1: Survey effort and observations considered for this model. Effort is tallied as the cumulative length of on-effort transects. Observations are the number of groups and individuals encountered while on effort. Off effort observations and those lacking an estimate of group size or distance to the group were excluded. *(continued)*

			Effort	Observations		
Institution	Program	Period	1000s km	Groups	Individuals	Mean Group Size
		Grand Total	**2,928**	**4,198**	**8,124**	**1.9**

Table 2: Institutions that contributed surveys used in this model.

Institution	Full Name
FWRI	FWC Fish and Wildlife Research Institute
HDR	HDR, Inc.
MCR	Marine Conservation Research
NEAq	New England Aquarium
NEFSC	NOAA Northeast Fisheries Science Center
NJDEP	New Jersey Department of Environmental Protection
NYS-DEC/TT	New York State Department of Environmental Conservation and Tetra Tech, Inc.
SEFSC	NOAA Southeast Fisheries Science Center
UNCW	University of North Carolina Wilmington
VAMSC	Virginia Aquarium & Marine Science Center
WLT/SSA/CMARI	Wildlife Trust, Sea to Shore Alliance, and Clearwater Marine Aquarium Research Institute

Table 3: Descriptions and references for survey programs used in this model.

Program	Description	References
AMAPPS	Atlantic Marine Assessment Program for Protected Species	Palka et al. (2017), Palka et al. (2021)
CNM	Northeast Canyons Marine National Monument Aerial Surveys	Redfern et al. (2021)
MATS	Mid-Atlantic Tursiops Surveys	
MD DNR WEA	Aerial Surveys of the Maryland Wind Energy Area	Barco et al. (2015)
MidA Bottlenose	Mid-Atlantic Onshore/Offshore Bottlenose Dolphin Surveys	Torres et al. (2005)
MMS-WEA	Marine Mammal Surveys of the MA and RI Wind Energy Areas	Quintana-Rizzo et al. (2021), O'Brien et al. (2022)
NARWSS	North Atlantic Right Whale Sighting Surveys	Cole et al. (2007)
Navy Cape Hatteras	Aerial Surveys of the Navy's Cape Hatteras Study Area	McLellan et al. (2018)
Navy Jacksonville	Aerial Surveys of the Navy's Jacksonville Study Area	Foley et al. (2019)
Navy Norfolk Canyon	Aerial Surveys of the Navy's Norfolk Canyon Study Area	Cotter (2019), McAlarney et al. (2018)
Navy Onslow Bay	Aerial Surveys of the Navy's Onslow Bay Study Area	Read et al. (2014)
Navy VACAPES	Aerial Survey Baseline Monitoring in the Continental Shelf Region of the VACAPES OPAREA	Mallette et al. (2017)
NJEBS	New Jersey Ecological Baseline Study	Geo-Marine, Inc. (2010), Whitt et al. (2015)
NLPSC	Northeast Large Pelagic Survey Collaborative Aerial Surveys	Leiter et al. (2017), Stone et al. (2017)
NYBWM	New York Bight Whale Monitoring Surveys	Zoidis et al. (2021)

Table 3: Descriptions and references for survey programs used in this model. *(continued)*

Program	Description	References
Pre-AMAPPS	Pre-AMAPPS Marine Mammal Abundance Surveys	Mullin and Fulling (2003), Garrison et al. (2010), Palka (2006)
SEUS NARW EWS	Southeast U.S. Right Whale Early Warning System Surveys	Gowan and Ortega-Ortiz (2014)
SOTW Visual	R/V Song of the Whale Visual Surveys	Ryan et al. (2013)
VA CZM WEA	Virginia CZM Wind Energy Area Surveys	Mallette et al. (2014), Mallette et al. (2015)

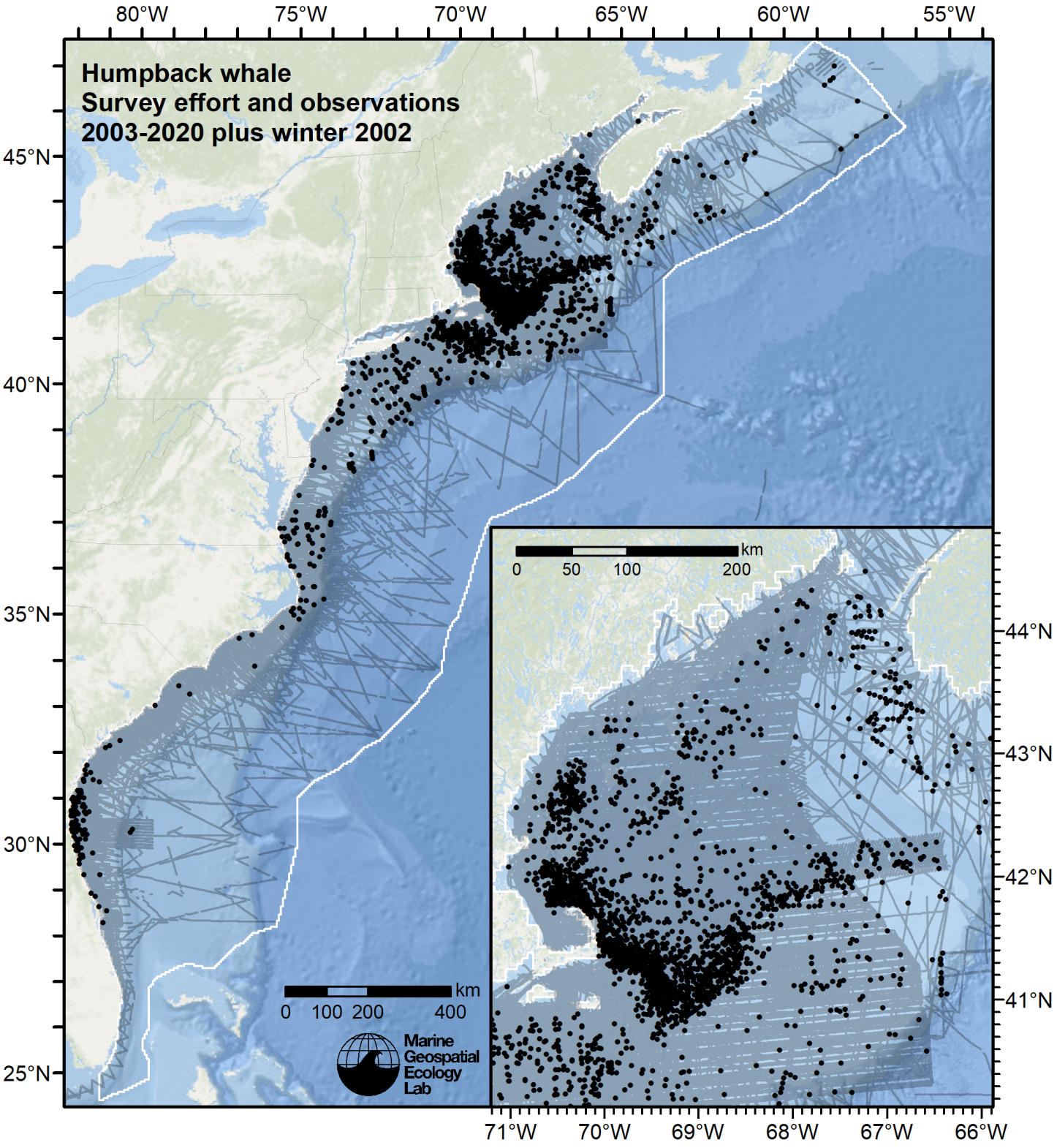

Figure 1: Survey effort and humpback whale observations available for density modeling, after detection functions were applied, and excluded segments and truncated observations were removed.

2 Detection Functions

2.1 With a Taxonomic Covariate

We fitted the detection functions in this section to pools of species with similar detectability characteristics and used the taxonomic identification as a covariate (ScientificName) to account for differences between them. We consulted the literature and observer teams to determine appropriate poolings. We usually employed this approach to boost the counts of observations in the detection functions, which increased the chance that other covariates such as Beaufort sea state could be used to account for differences in observing conditions. When defining the taxonomic covariate, we sometimes had too few observations of species to allocate each of them their own level of the covariate and had to group them together, again consulting the literature and observers for advice on species similarity. Also, when species were observed frequently enough to be allocated their own levels but statistical tests indicated no significant difference between the levels, we usually grouped them together into a single level.

2.1.1 Aerial Surveys

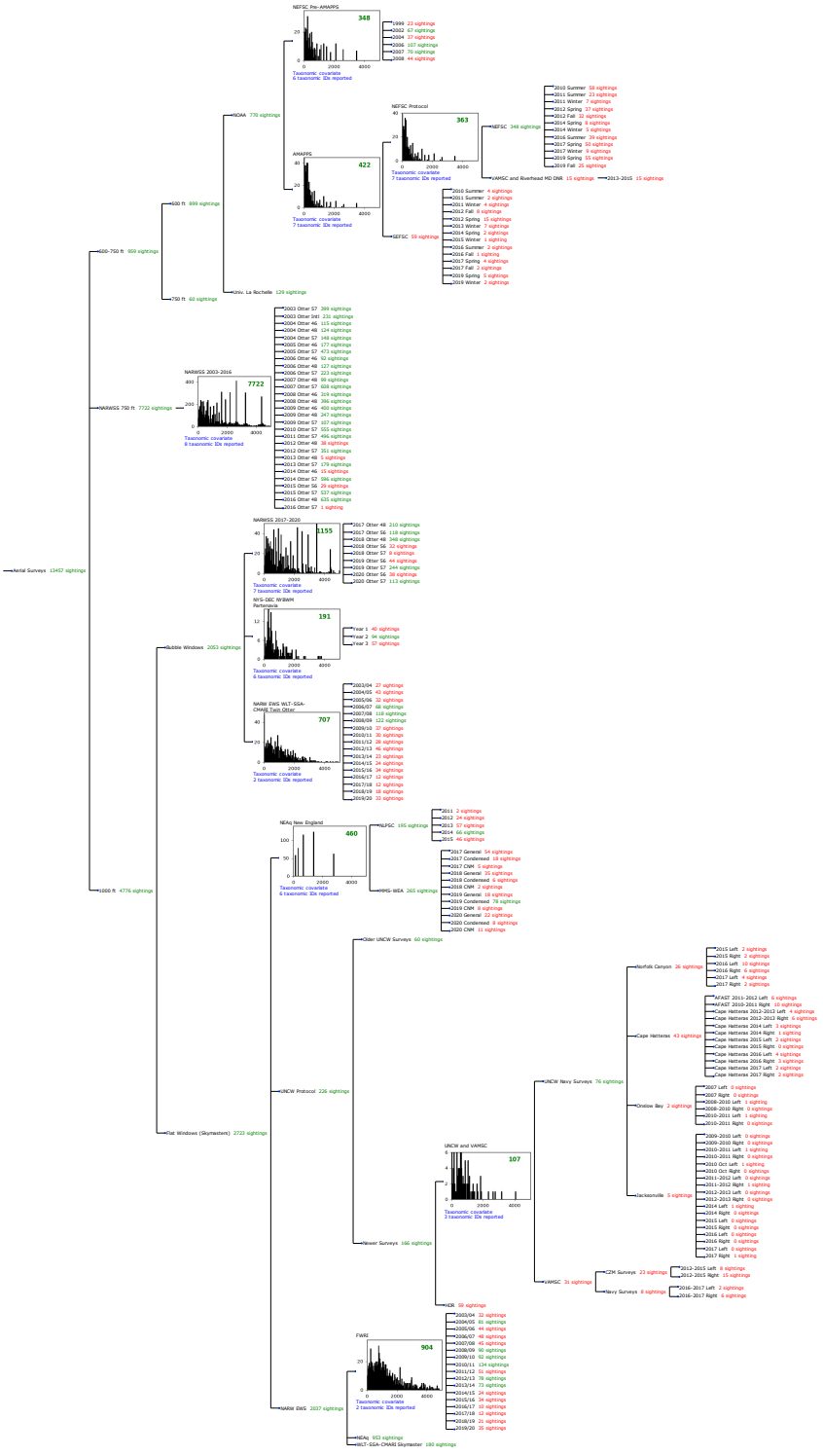

Figure 2: Detection hierarchy for aerial surveys, showing how they were pooled during detectability modeling, for detection functions that pooled multiple taxa and used used a taxonomic covariate to account for differences between them. Each histogram represents a detection function and summarizes the perpendicular distances of observations that were pooled to fit it, prior to truncation. Observation counts, also prior to truncation, are shown in green when they met the recommendation of Buckland et al. (2001) that detection functions utilize at least 60 sightings, and red otherwise. For rare taxa, it was not always possible to meet this recommendation, yielding higher statistical uncertainty. During the spatial modeling stage of the analysis, effective strip widths were computed for each survey using the closest detection function above it in the hierarchy (i.e. moving from right to left in the figure). Surveys that do not have a detection function above them in this figure were either addressed by a detection function presented in a different section of this report, or were omitted from the analysis.

2.1.1.1 NEFSC Pre-AMAPPS

After right-truncating observations greater than 1500 m, we fitted the detection function to the 312 observations that remained (Table 4). The selected detection function (Figure 3) used a hazard rate key function with Beaufort (Figure 4) and OriginalScientificName (Figure 5) as covariates.

Table 4: Observations used to fit the NEFSC Pre-AMAPPS detection function.

ScientificName	n
Balaenoptera borealis	7
Balaenoptera borealis/physalus	29
Balaenoptera physalus	117
Eubalaena glacialis	29
Megaptera novaeangliae	113
Physeter macrocephalus	17
Total	**312**

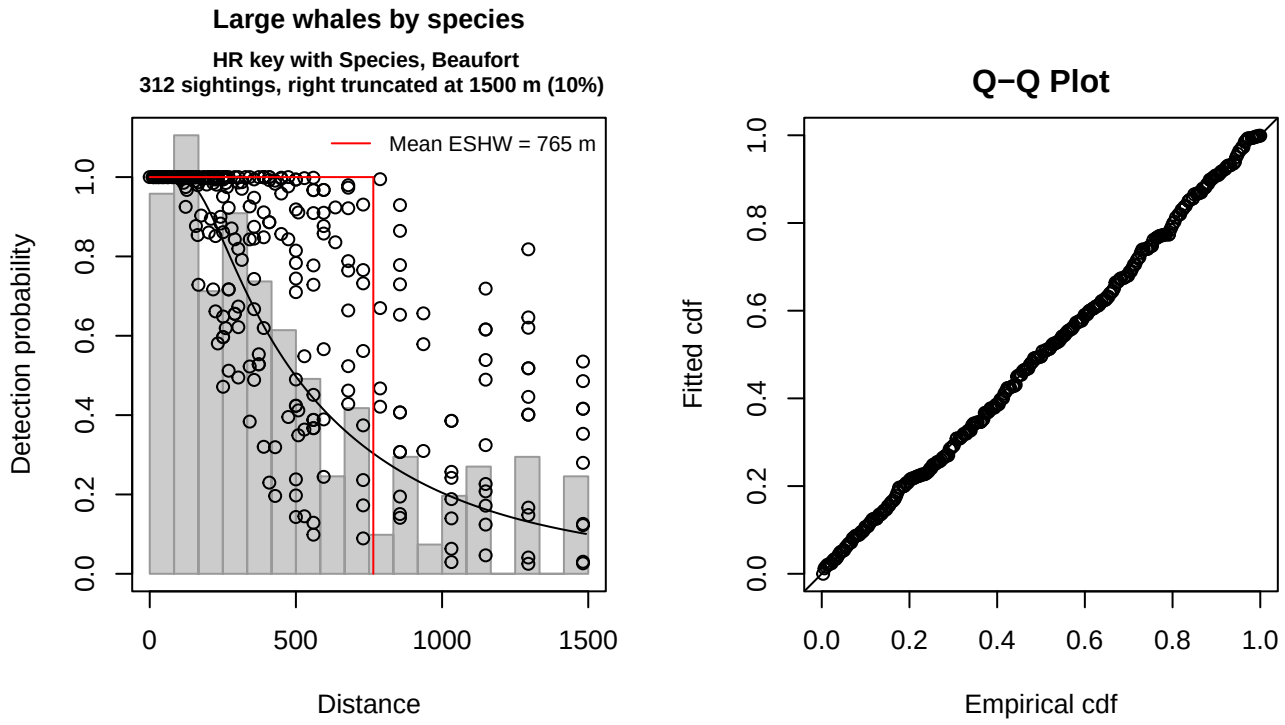

Figure 3: NEFSC Pre-AMAPPS detection function and Q-Q plot showing its goodness of fit.

Statistical output for this detection function:

```
Summary for ds object
Number of observations :  312
Distance range         :  0  -  1500
AIC                    :  4374.841

Detection function:
 Hazard-rate key function

Detection function parameters
Scale coefficient(s):
                                  estimate         se
(Intercept)                     5.0768091 0.24837645
```

```
OriginalScientificNameHumpback, Right  0.9199384 0.16439351
OriginalScientificNameUnid. fin or sei 0.4943579 0.25189646
Beaufort                               0.3122214 0.08477314

Shape coefficient(s):
             estimate        se
(Intercept) 0.8162868 0.1272435

                       Estimate          SE         CV
Average p             0.4257901  0.03176212 0.07459573
N in covered region 732.7553573 64.19166079 0.08760313

Distance sampling Cramer-von Mises test (unweighted)
Test statistic = 0.028690  p = 0.980269
```

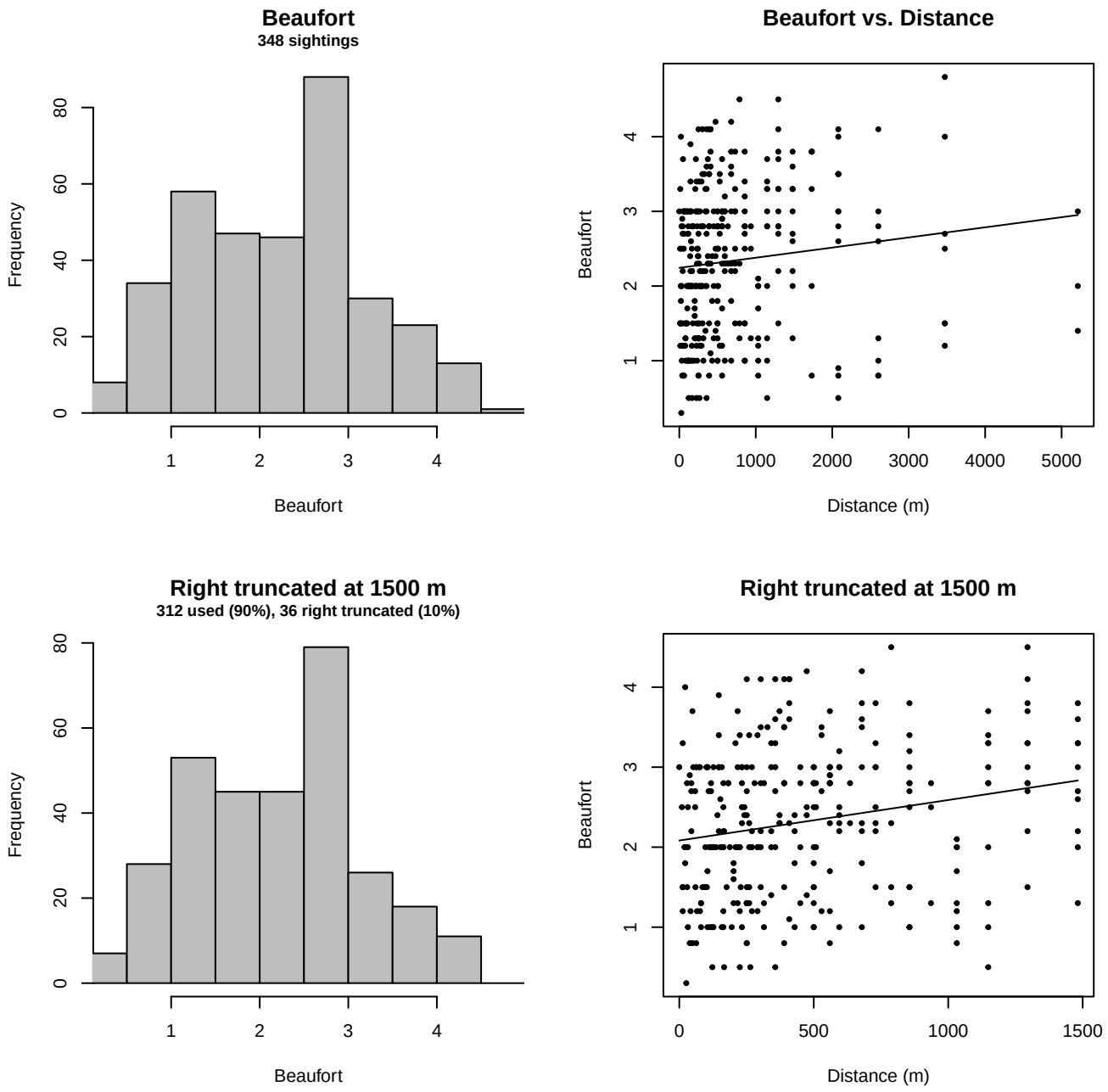

Figure 4: Distribution of the Beaufort covariate before (top row) and after (bottom row) observations were truncated to fit the NEFSC Pre-AMAPPS detection function.

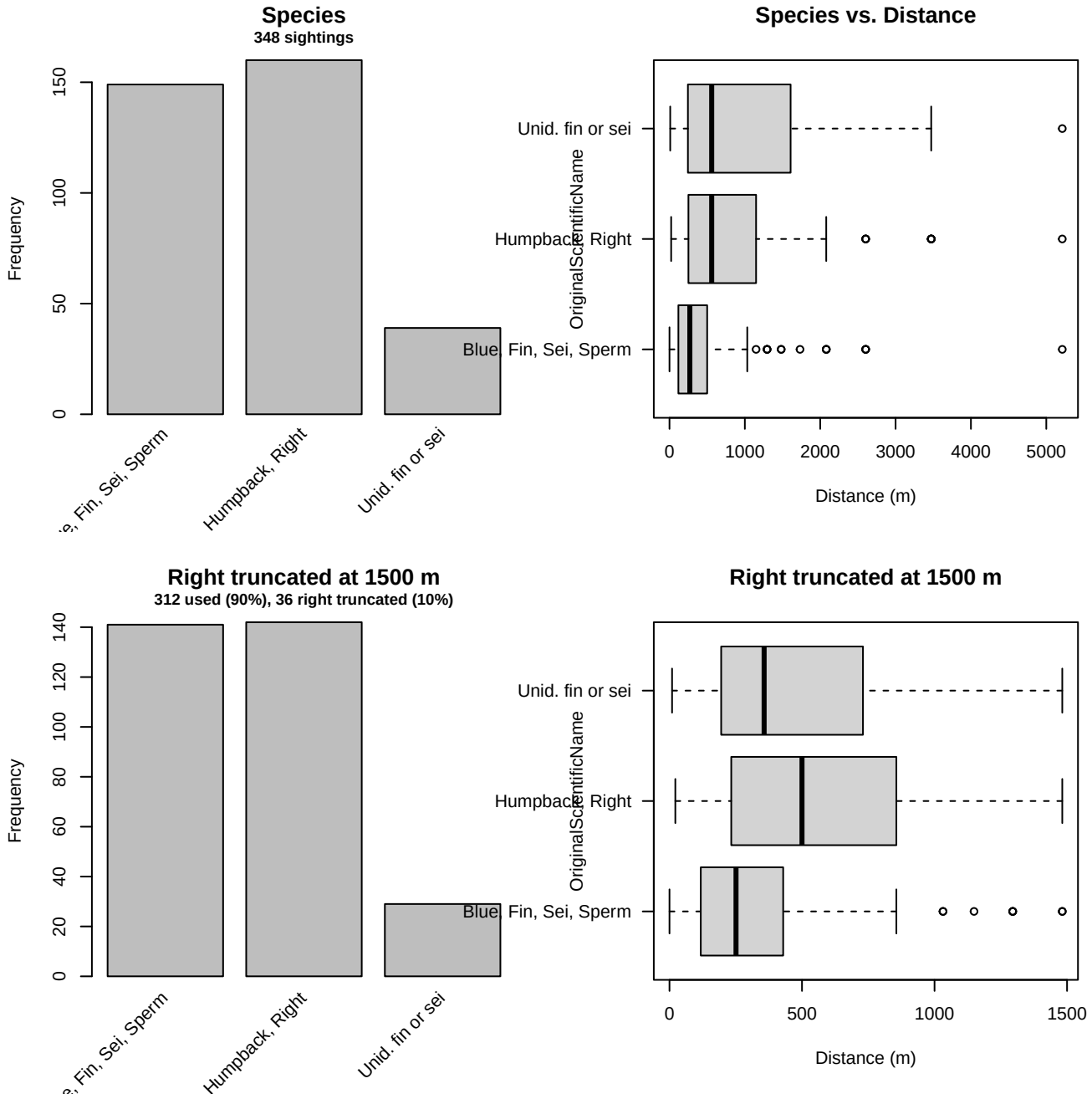

Figure 5: Distribution of the OriginalScientificName covariate before (top row) and after (bottom row) observations were truncated to fit the NEFSC Pre-AMAPPS detection function.

2.1.1.2 NEFSC AMAPPS Protocol

After right-truncating observations greater than 1500 m, we fitted the detection function to the 342 observations that remained (Table 5). The selected detection function (Figure 6) used a hazard rate key function with Beaufort (Figure 7), OriginalScientificName (Figure 8) and Season (Figure 9) as covariates.

Table 5: Observations used to fit the NEFSC AMAPPS Protocol detection function.

ScientificName	n
Balaenoptera borealis	14
Balaenoptera borealis/physalus	26
Balaenoptera musculus	1
Balaenoptera physalus	116
Eubalaena glacialis	23
Megaptera novaeangliae	150
Physeter macrocephalus	12
Total	**342**

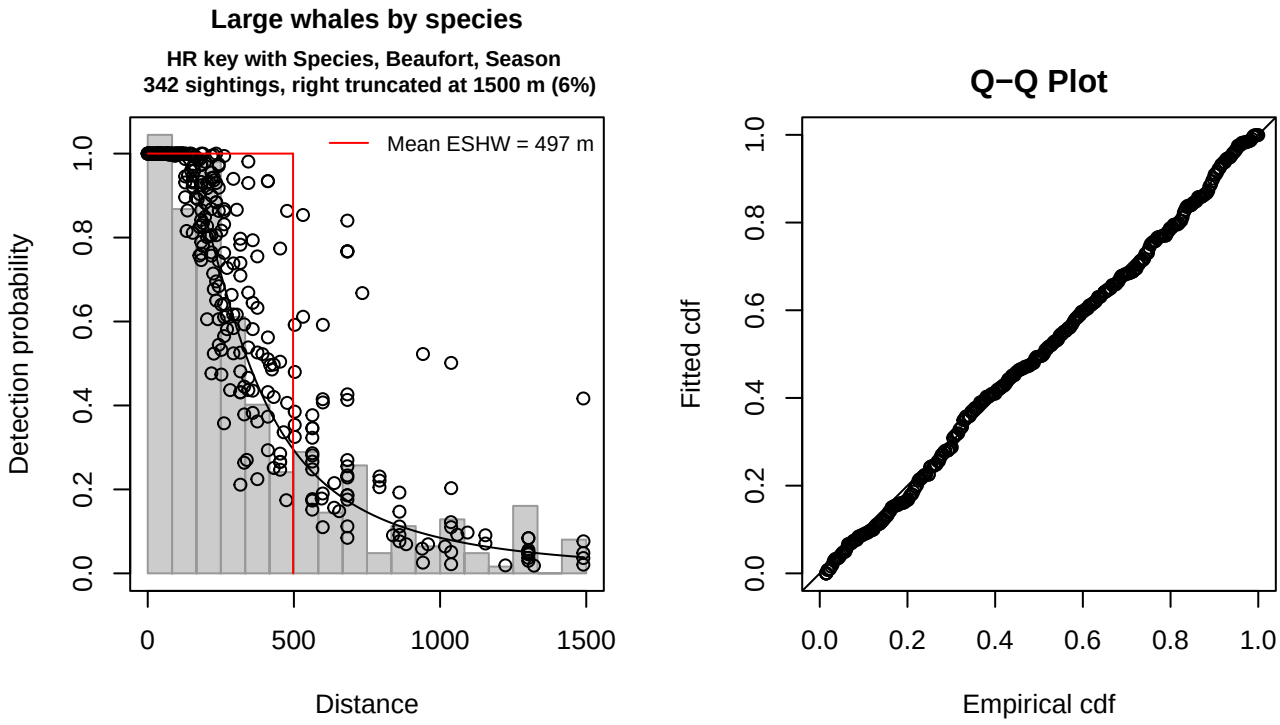

Figure 6: NEFSC AMAPPS Protocol detection function and Q-Q plot showing its goodness of fit.

Statistical output for this detection function:

```
Summary for ds object
Number of observations :  342
Distance range         :  0  -  1500
AIC                    :  4666.929

Detection function:
 Hazard-rate key function

Detection function parameters
Scale coefficient(s):
                                      estimate         se
(Intercept)                          5.1473984 0.28568102
OriginalScientificNameHumpback, Right   0.3396040 0.14675903
OriginalScientificNameUnid. fin or sei  1.0647525 0.34041574
Beaufort                             0.2004836 0.08188346
SeasonSummer, Fall, Winter          -0.2694922 0.15571712
```

```
Shape coefficient(s):
            estimate         se
(Intercept) 0.748414 0.08996968

                          Estimate          SE         CV
Average p                0.3053758  0.02225385 0.07287364
N in covered region 1119.9314103 96.45660426 0.08612724

Distance sampling Cramer-von Mises test (unweighted)
Test statistic = 0.064193  p = 0.787617
```

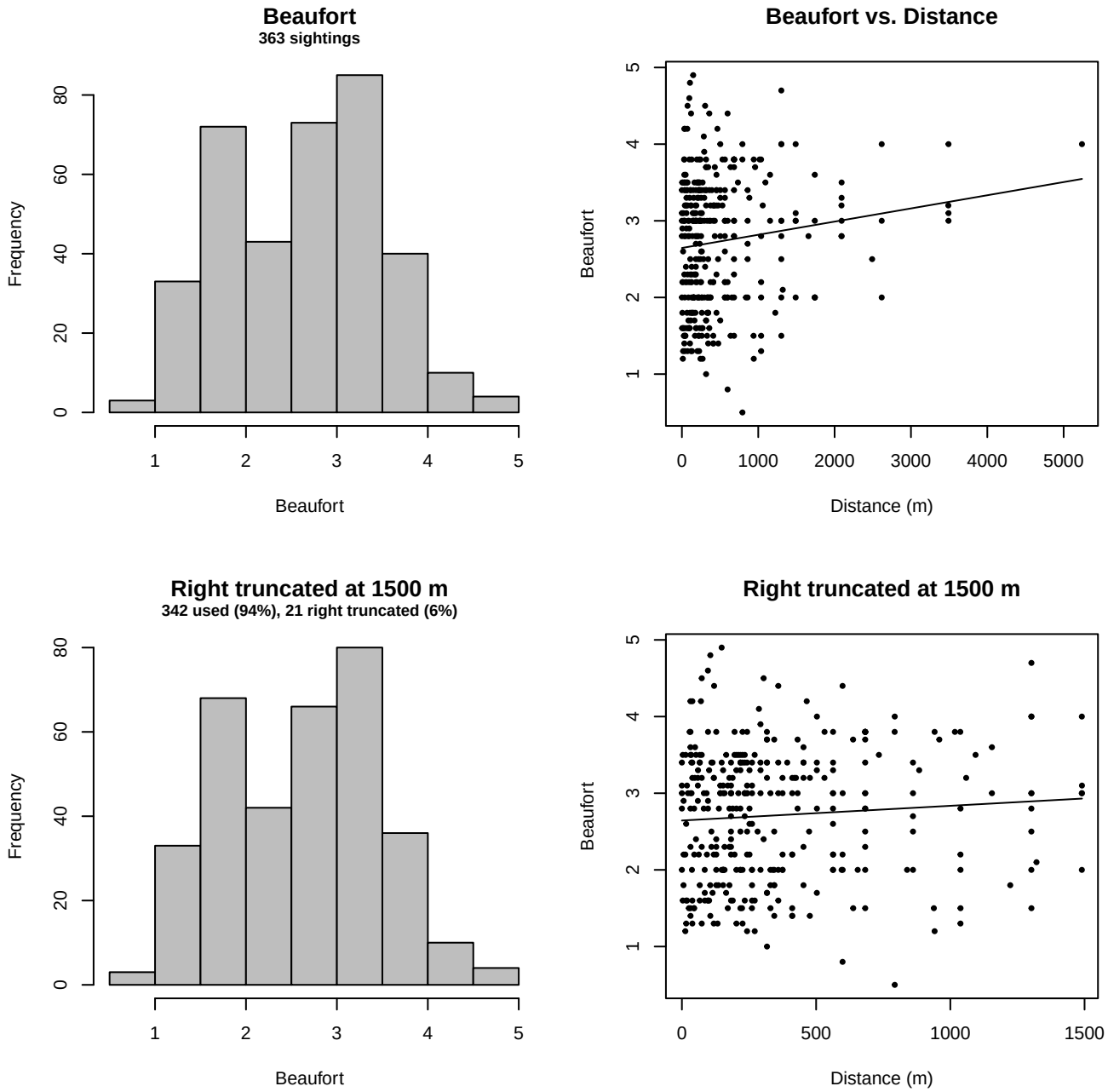

Figure 7: Distribution of the Beaufort covariate before (top row) and after (bottom row) observations were truncated to fit the NEFSC AMAPPS Protocol detection function.

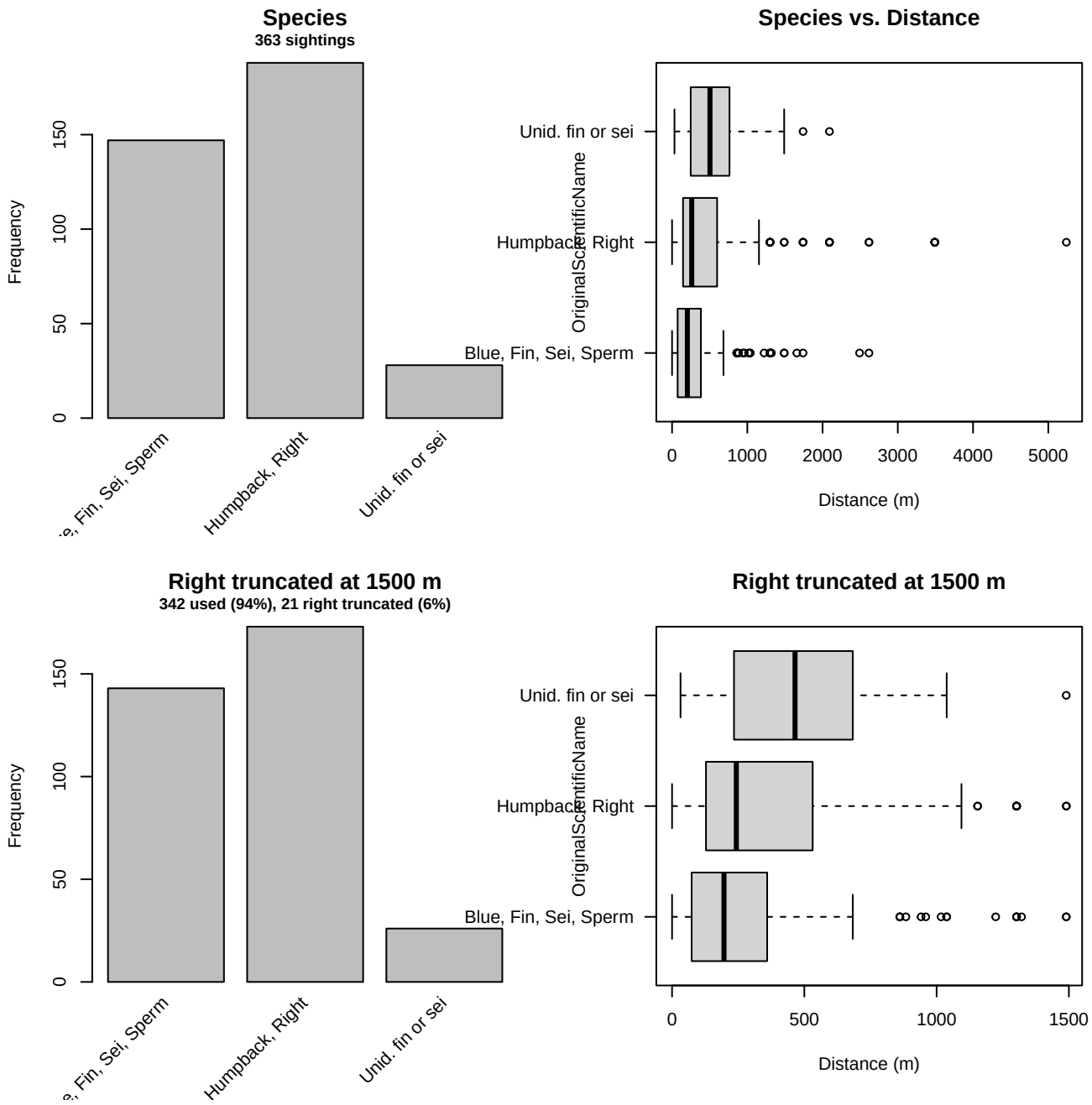

Figure 8: Distribution of the OriginalScientificName covariate before (top row) and after (bottom row) observations were truncated to fit the NEFSC AMAPPS Protocol detection function.

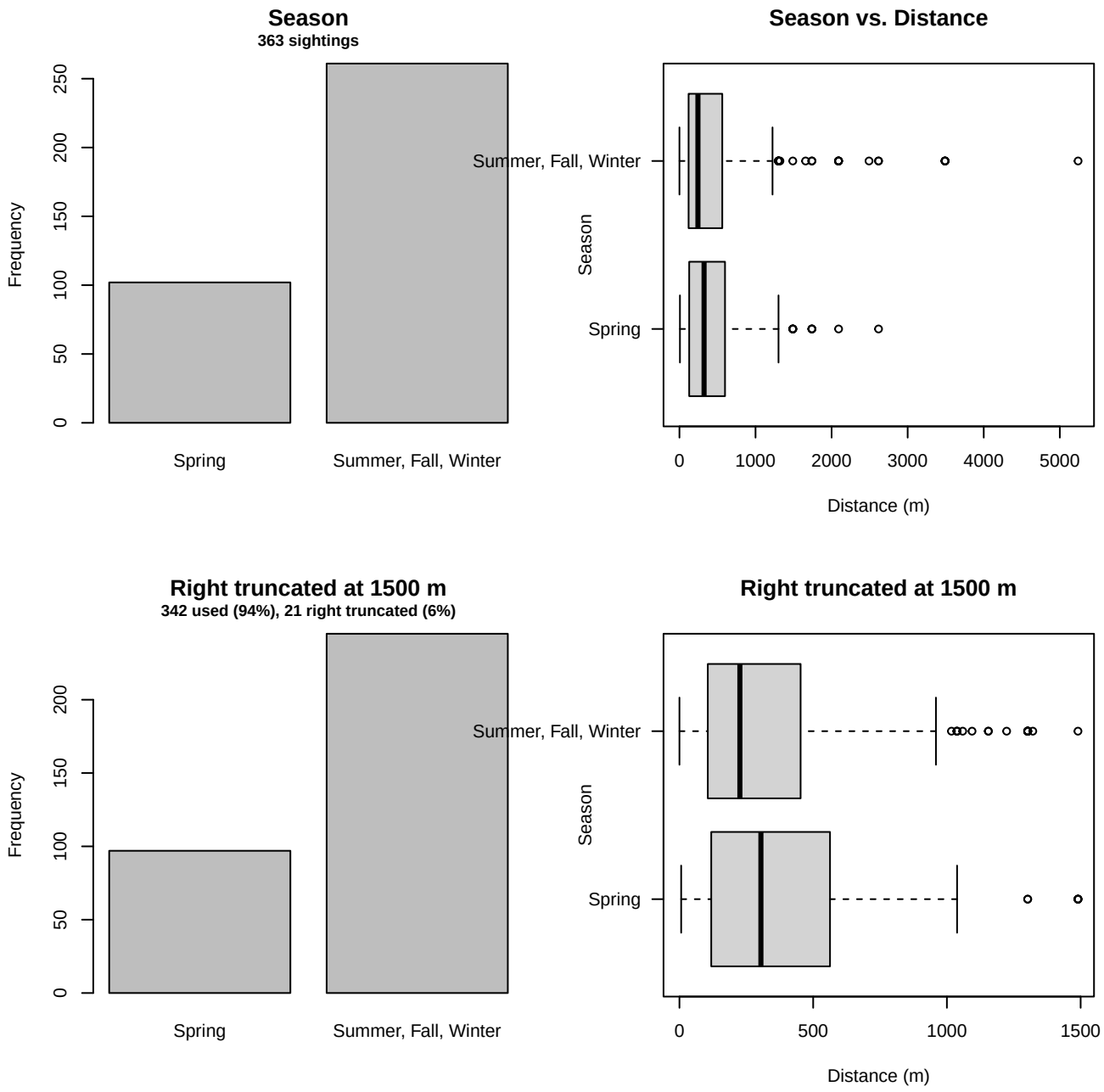

Figure 9: Distribution of the Season covariate before (top row) and after (bottom row) observations were truncated to fit the NEFSC AMAPPS Protocol detection function.

2.1.1.3 AMAPPS

After right-truncating observations greater than 600 m, we fitted the detection function to the 341 observations that remained (Table 6). The selected detection function (Figure 10) used a hazard rate key function with OriginalScientificName (Figure 11) as a covariate.

Table 6: Observations used to fit the AMAPPS detection function.

ScientificName	n
Balaenoptera borealis	11
Balaenoptera borealis/physalus	16
Balaenoptera musculus	1
Balaenoptera physalus	132
Eubalaena glacialis	26
Megaptera novaeangliae	137
Physeter macrocephalus	18
Total	**341**

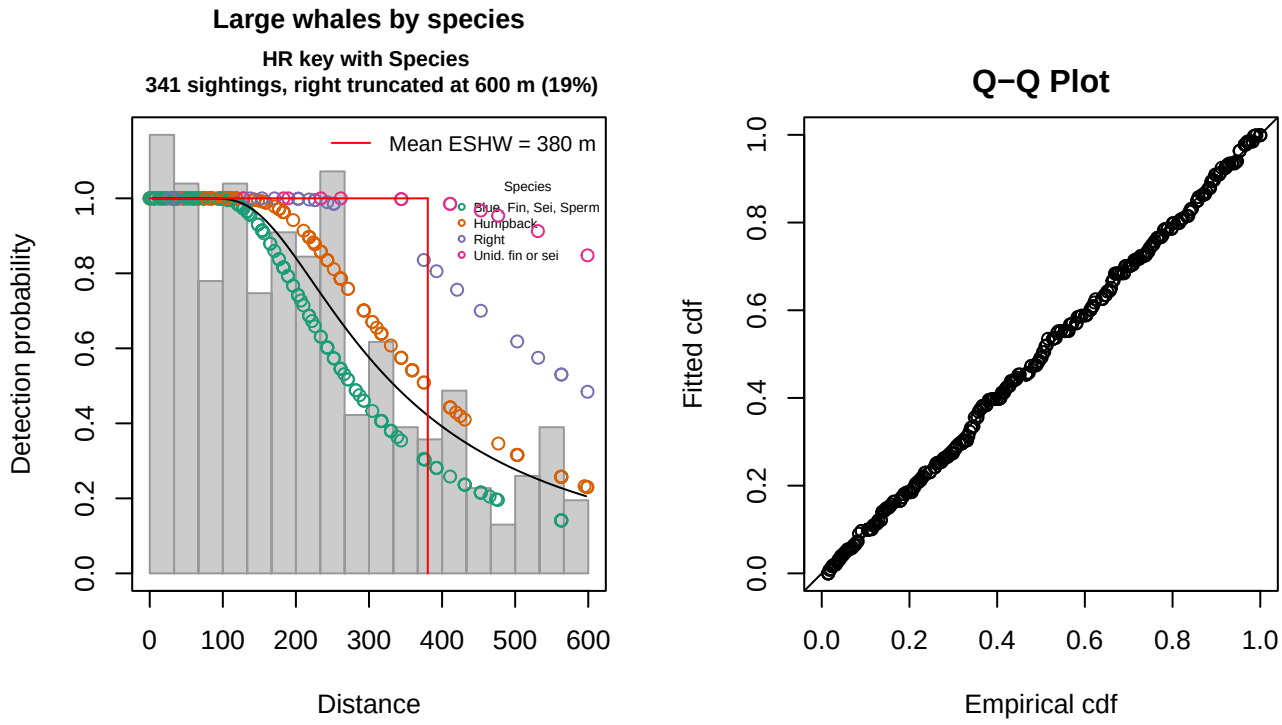

Figure 10: AMAPPS detection function and Q-Q plot showing its goodness of fit.

Statistical output for this detection function:

```
Summary for ds object
Number of observations :  341
Distance range         :  0  -  600
AIC                    :  4279.869

Detection function:
 Hazard-rate key function

Detection function parameters
Scale coefficient(s):
                                    estimate        se
(Intercept)                        5.4543823 0.1418158
OriginalScientificNameHumpback     0.3133386 0.1690242
OriginalScientificNameRight        0.7482762 0.3681078
OriginalScientificNameUnid. fin or sei 1.2365031 1.2174894

Shape coefficient(s):
```

```
             estimate        se
(Intercept) 0.7615805 0.1934441

                      Estimate          SE         CV
Average p             0.615325  0.03870801 0.06290662
N in covered region 554.178703 39.73247609 0.07169614

Distance sampling Cramer-von Mises test (unweighted)
Test statistic = 0.031782  p = 0.969954
```

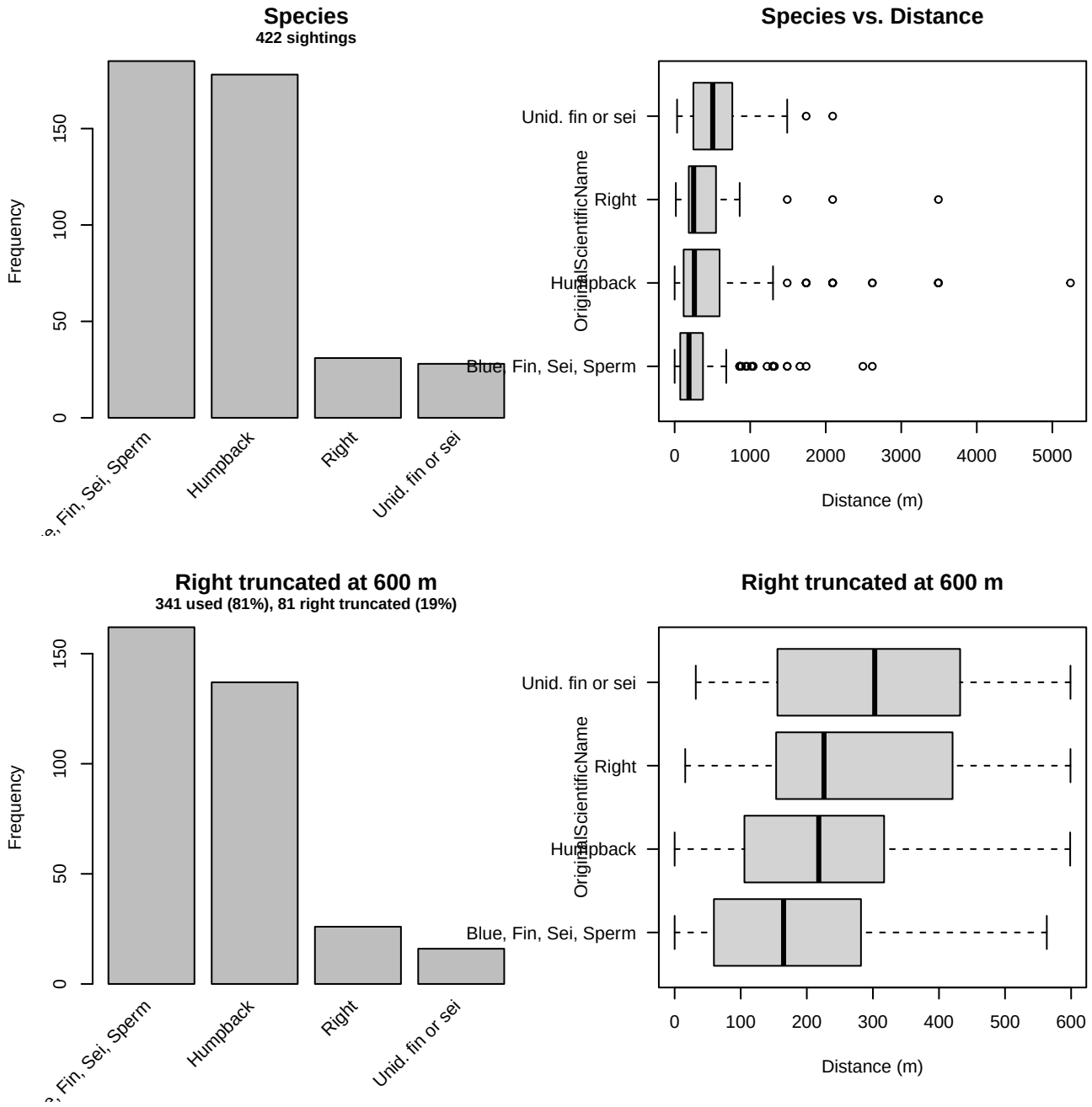

Figure 11: Distribution of the OriginalScientificName covariate before (top row) and after (bottom row) observations were truncated to fit the AMAPPS detection function.

2.1.1.4 NARWSS 2003-2016

After right-truncating observations greater than 5236 m, we fitted the detection function to the 7315 observations that remained (Table 7). The selected detection function (Figure 12) used a hazard rate key function with Beaufort (Figure 13), Glare (Figure 14), OriginalScientificName (Figure 15) and Visibility (Figure 16) as covariates.

Table 7: Observations used to fit the NARWSS 2003-2016 detection function.

ScientificName	n
Balaena mysticetus	1
Balaenoptera borealis	849
Balaenoptera borealis/physalus	550
Balaenoptera musculus	8
Balaenoptera physalus	1605
Eubalaena glacialis	1340
Megaptera novaeangliae	2890
Physeter macrocephalus	72
Total	**7315**

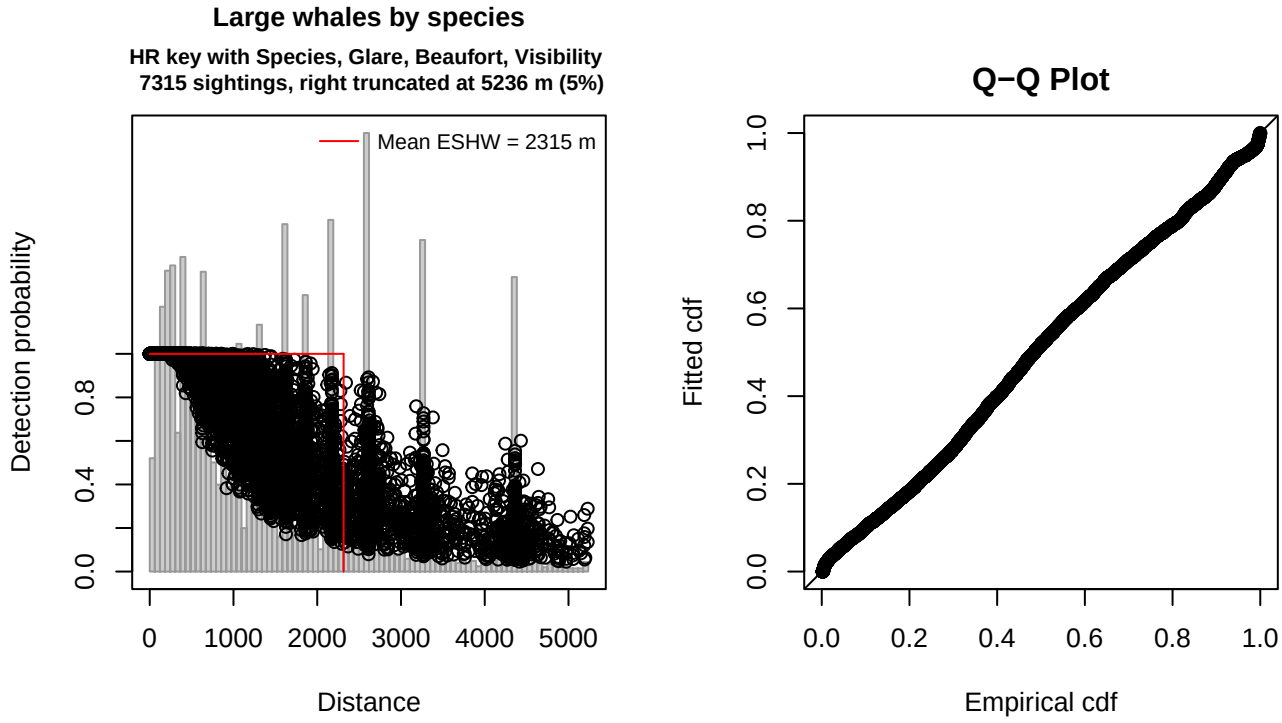

Figure 12: NARWSS 2003-2016 detection function and Q-Q plot showing its goodness of fit.

Statistical output for this detection function:

```
Summary for ds object
Number of observations :  7315
Distance range         :  0  -  5236
AIC                    :  121443.8

Detection function:
 Hazard-rate key function

Detection function parameters
Scale coefficient(s):
```

```
                                        estimate          se
(Intercept)                           6.441965720 0.099786764
OriginalScientificNameHumpback         0.514291401 0.053837700
OriginalScientificNameRight, Bowhead   0.246897383 0.063136414
OriginalScientificNameSei, Bryde's    -0.161553308 0.069396712
OriginalScientificNameSperm            0.319075357 0.224385467
OriginalScientificNameUnid. fin or sei 0.829751791 0.098643556
GlareSevere                            0.362397475 0.058132933
Beaufort                               0.093367857 0.021887375
Visibility                             0.007771288 0.002225131

Shape coefficient(s):
             estimate         se
(Intercept) 0.4992226 0.03060822

                         Estimate           SE         CV
Average p           4.138072e-01 7.450829e-03 0.01800555
N in covered region 1.767731e+04 3.571549e+02 0.02020414

Distance sampling Cramer-von Mises test (unweighted)
Test statistic = 1.329669  p = 0.000424
```

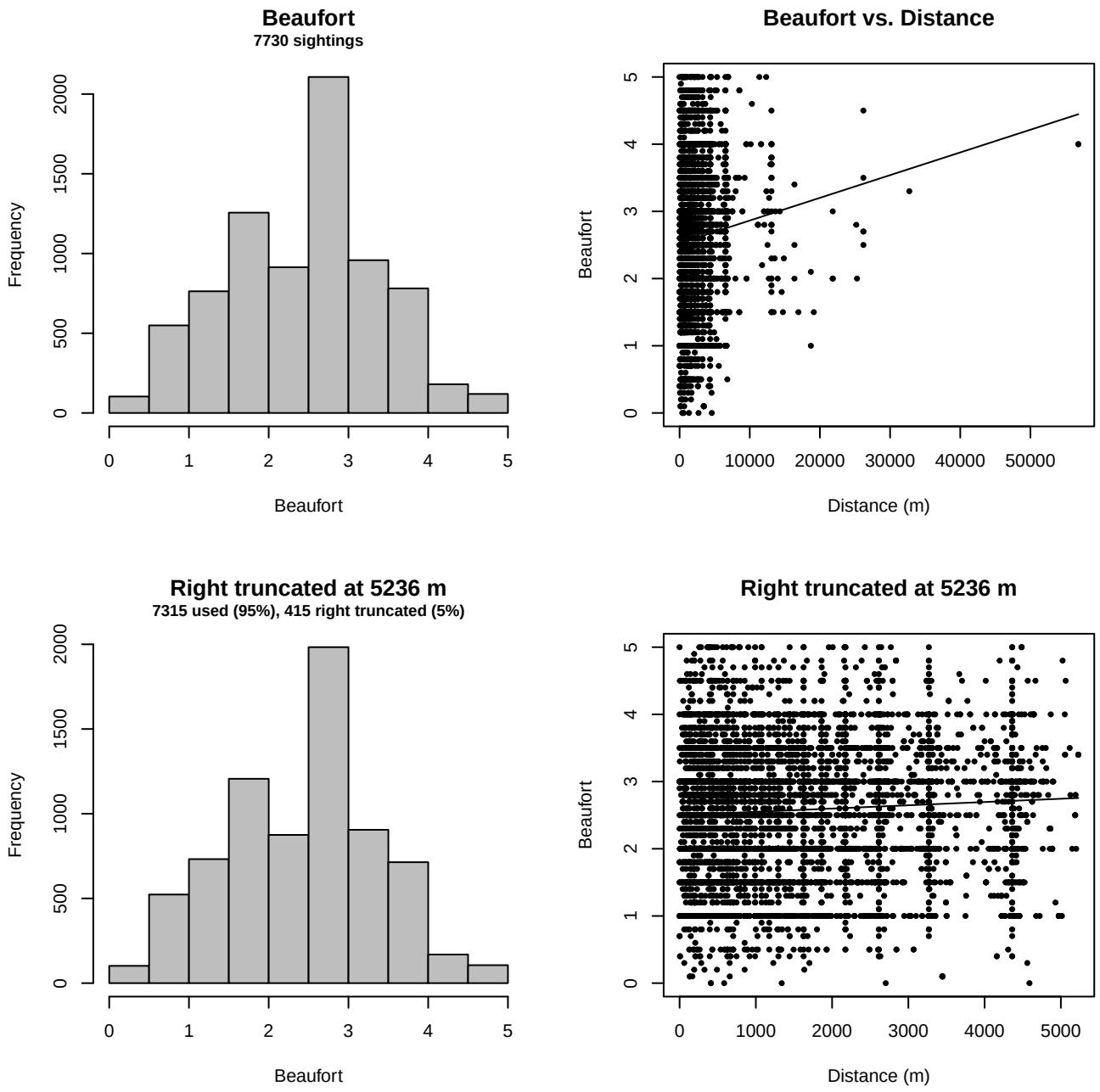

Figure 13: Distribution of the Beaufort covariate before (top row) and after (bottom row) observations were truncated to fit the NARWSS 2003-2016 detection function.

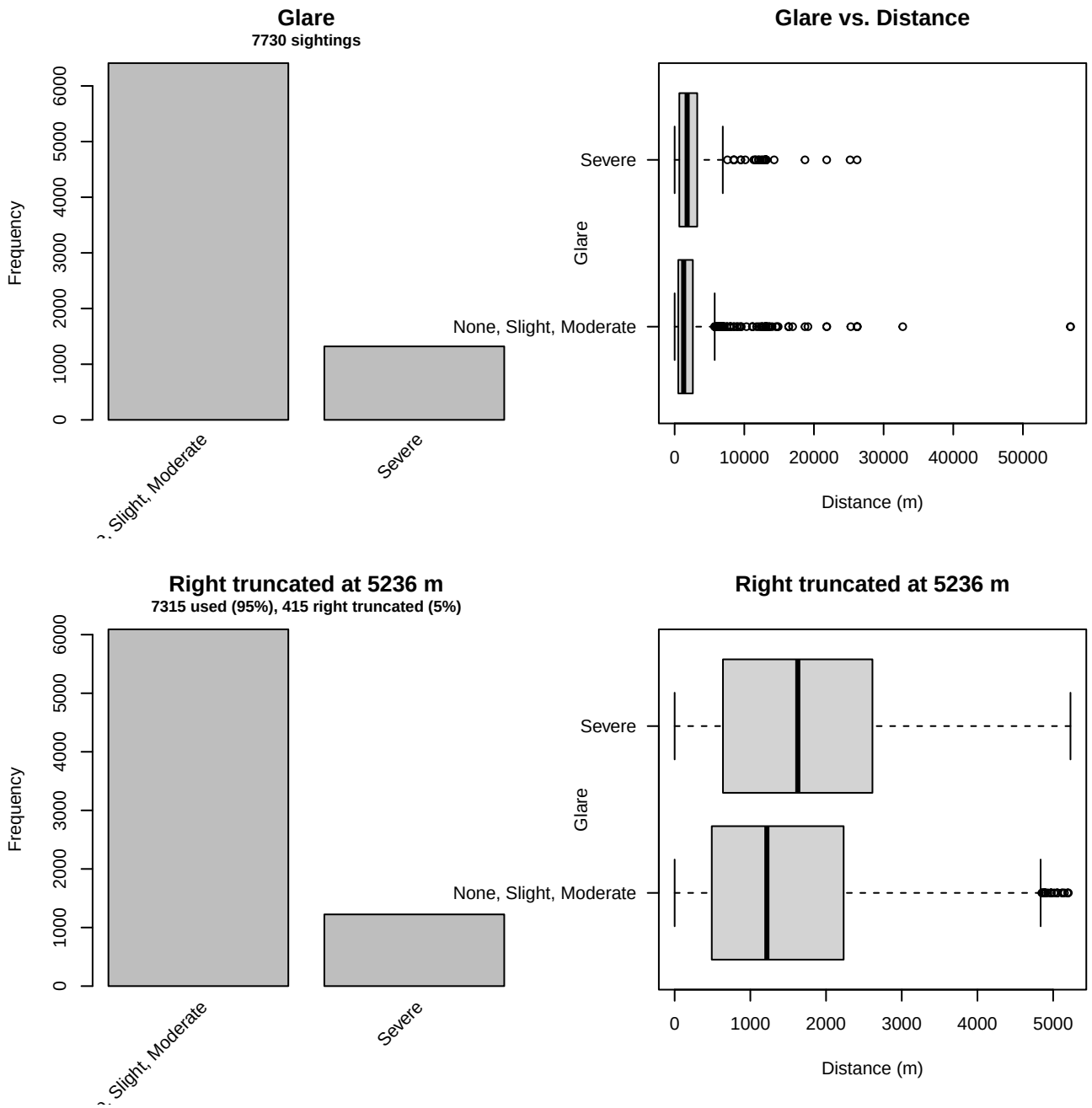

Figure 14: Distribution of the Glare covariate before (top row) and after (bottom row) observations were truncated to fit the NARWSS 2003-2016 detection function.

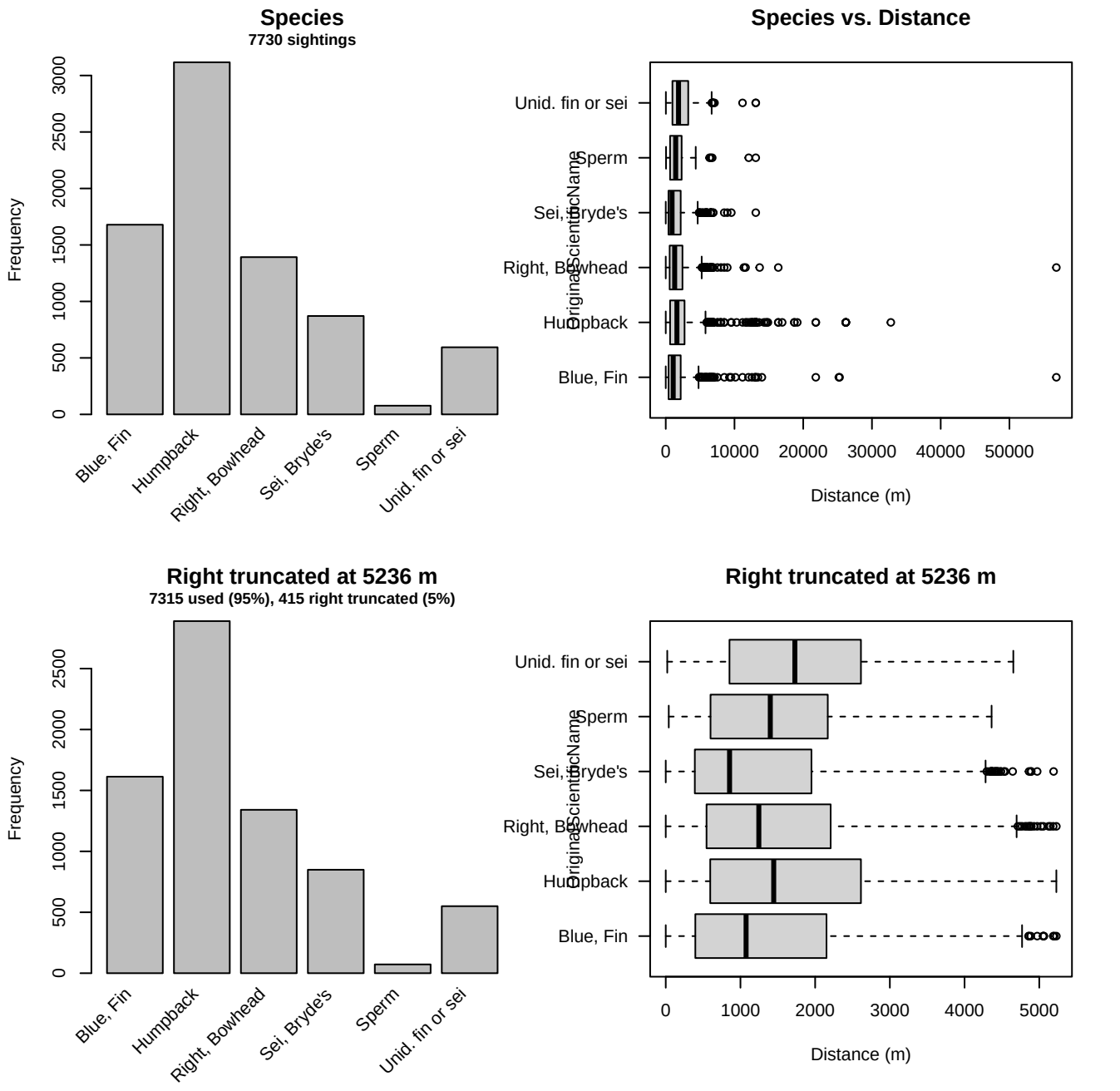

Figure 15: Distribution of the OriginalScientificName covariate before (top row) and after (bottom row) observations were truncated to fit the NARWSS 2003-2016 detection function.

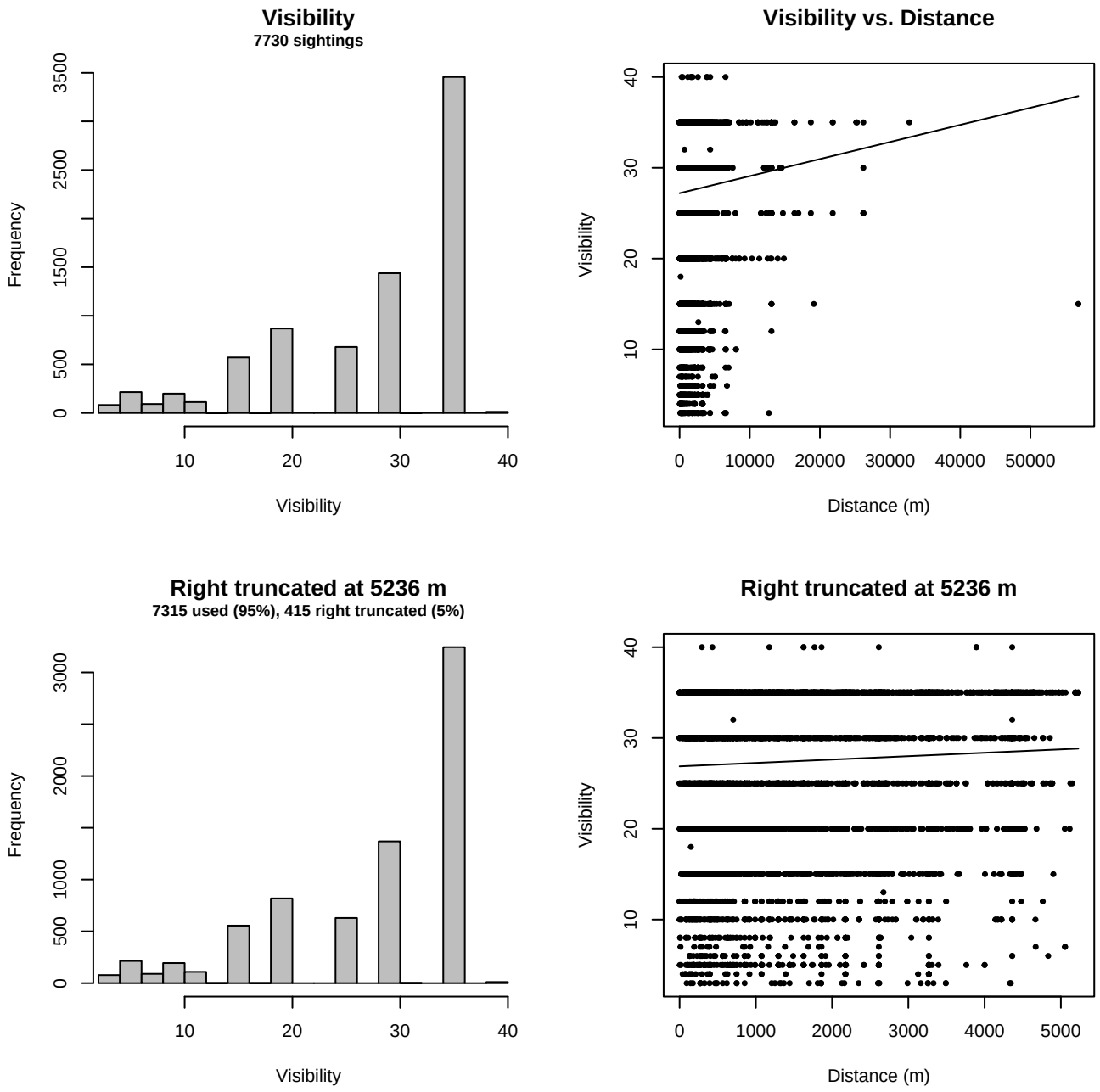

Figure 16: Distribution of the Visibility covariate before (top row) and after (bottom row) observations were truncated to fit the NARWSS 2003-2016 detection function.

2.1.1.5 NARWSS 2017-2020

After right-truncating observations greater than 5236 m, we fitted the detection function to the 1088 observations that remained (Table 8). The selected detection function (Figure 17) used a hazard rate key function with OriginalScientificName (Figure 18) and QualityCode (Figure 19) as covariates.

Table 8: Observations used to fit the NARWSS 2017-2020 detection function.

ScientificName	n
Balaena mysticetus	2
Balaenoptera borealis	163
Balaenoptera borealis/physalus	39
Balaenoptera physalus	242
Eubalaena glacialis	233
Megaptera novaeangliae	402
Physeter macrocephalus	7
Total	**1088**

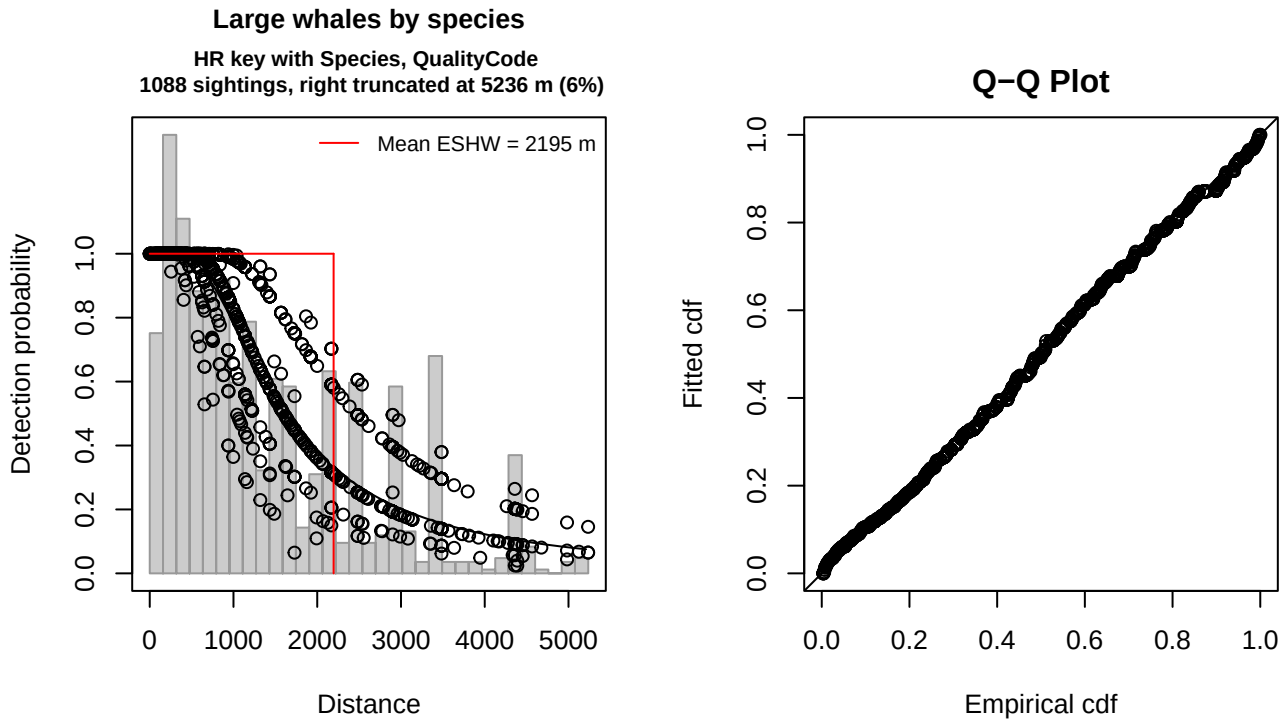

Figure 17: NARWSS 2017-2020 detection function and Q-Q plot showing its goodness of fit.

Statistical output for this detection function:

```
Summary for ds object
Number of observations :  1088
Distance range         :  0  -  5236
AIC                    :  17913.86

Detection function:
 Hazard-rate key function

Detection function parameters
Scale coefficient(s):
                                    estimate         se
(Intercept)                        7.1921029 0.08301497
OriginalScientificNameHumpback     0.4314943 0.09757578
OriginalScientificNameSei, Bryde's -0.2566332 0.12547460
OriginalScientificNameUnid. fin or sei  0.5879315 0.27089226
QualityCodeGood                   -0.4330452 0.11641444
QualityCodeModerate               -0.8540468 0.46513807
```

```
Shape coefficient(s):
             estimate         se
(Intercept) 0.6773699 0.07059228

                          Estimate           SE         CV
Average p                0.3933208   0.01632601 0.04150813
N in covered region 2766.1897508 132.78849331 0.04800412

Distance sampling Cramer-von Mises test (unweighted)
Test statistic = 0.142983  p = 0.411684
```

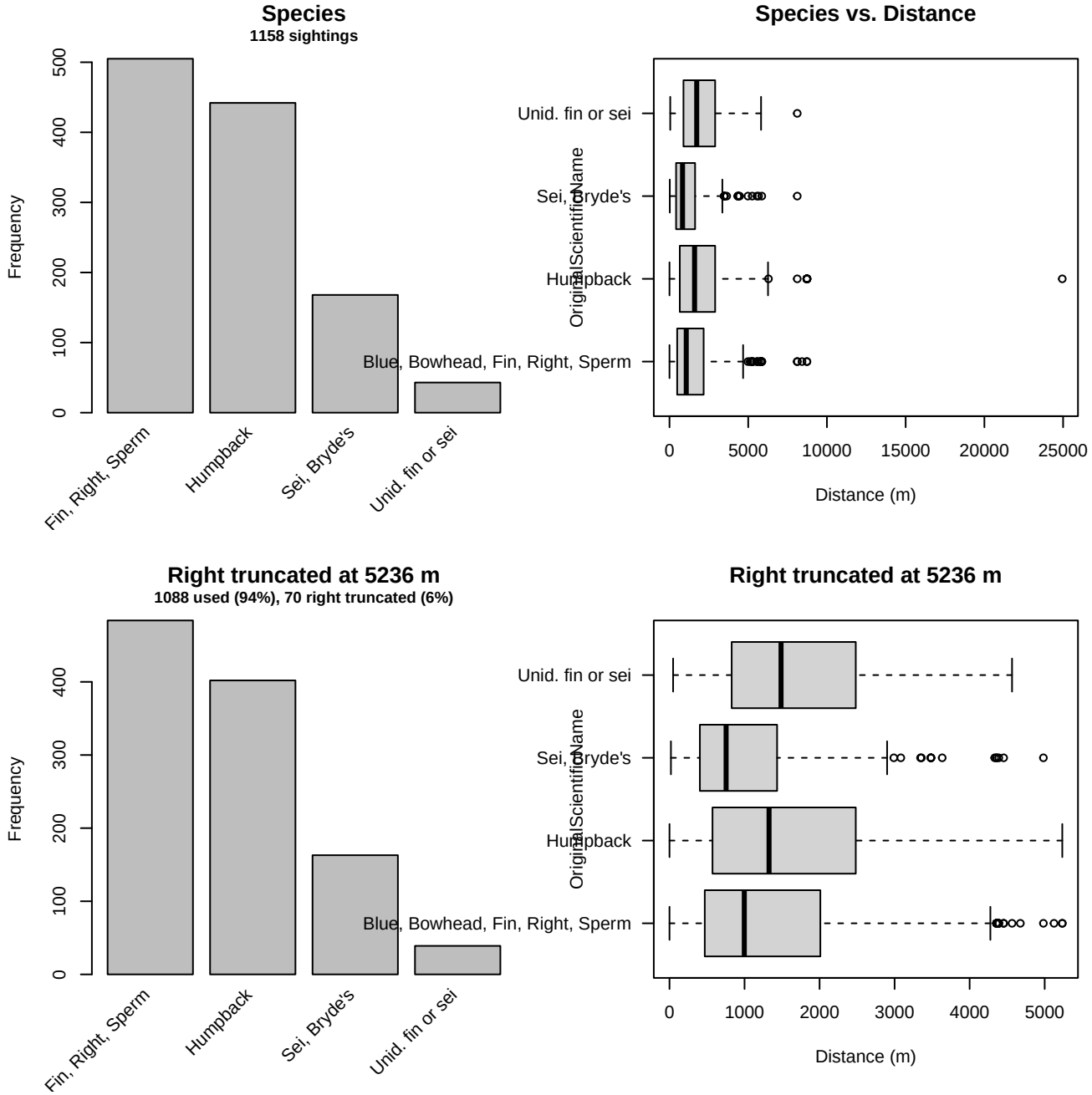

Figure 18: Distribution of the OriginalScientificName covariate before (top row) and after (bottom row) observations were truncated to fit the NARWSS 2017-2020 detection function.

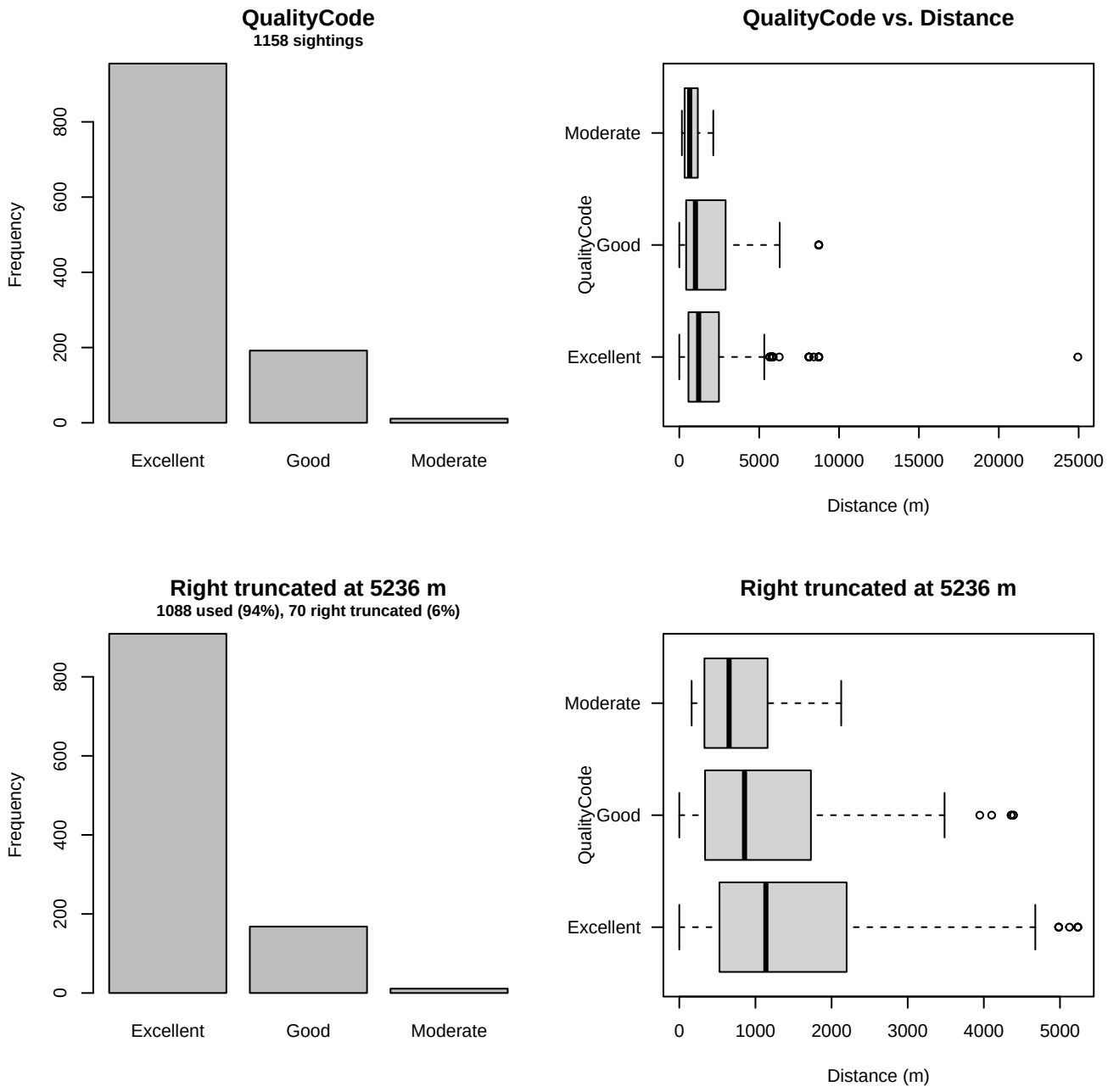

Figure 19: Distribution of the QualityCode covariate before (top row) and after (bottom row) observations were truncated to fit the NARWSS 2017-2020 detection function.

2.1.1.6 NYS-DEC NYBWM Partenavia

After right-truncating observations greater than 2100 m and left-truncating observations less than 125 m (Figure 21), we fitted the detection function to the 172 observations that remained (Table 9). The selected detection function (Figure 20) used a hazard rate key function with OriginalScientificName (Figure 22), Season (Figure 23) and SurveyID (Figure 24) as covariates.

Table 9: Observations used to fit the NYS-DEC NYBWM Partenavia detection function.

ScientificName	n
Balaenoptera borealis	2
Balaenoptera musculus	2
Balaenoptera physalus	82
Eubalaena glacialis	12
Megaptera novaeangliae	57
Physeter macrocephalus	17
Total	**172**

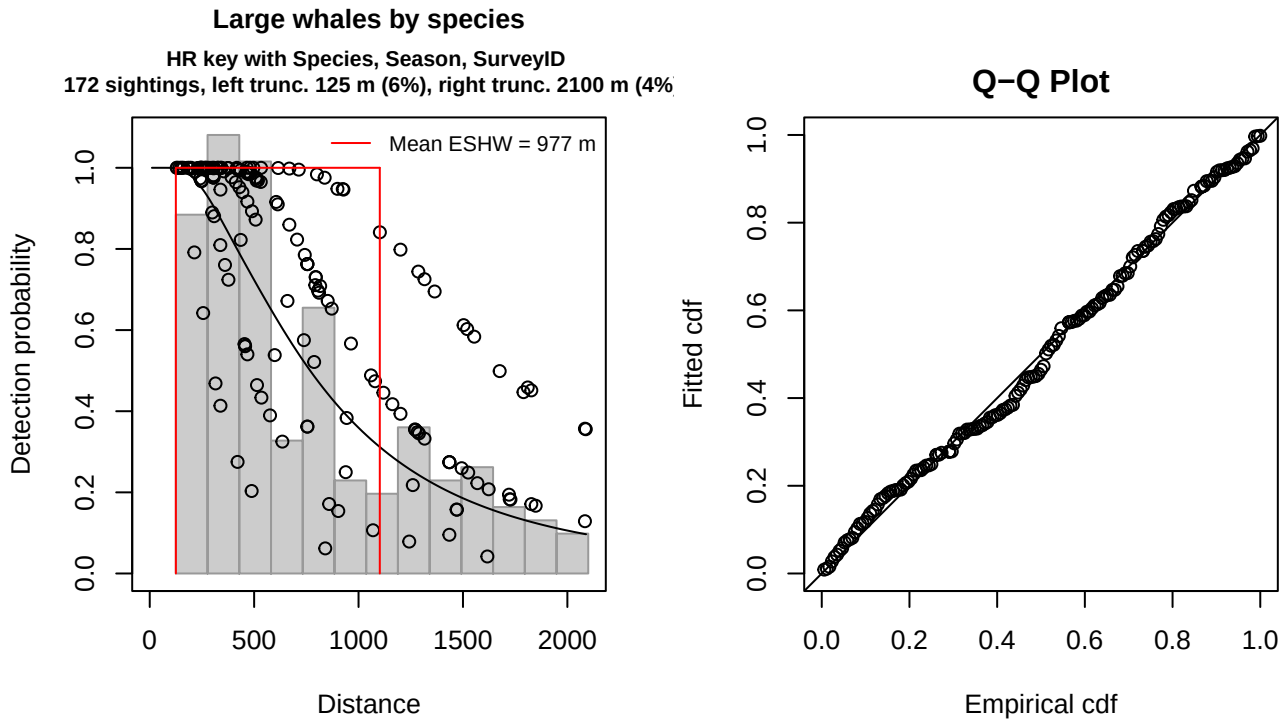

Figure 20: NYS-DEC NYBWM Partenavia detection function and Q-Q plot showing its goodness of fit.

Statistical output for this detection function:

```
Summary for ds object
Number of observations :  172
Distance range         :  125  -  2100
AIC                    :  2521.205

Detection function:
 Hazard-rate key function

Detection function parameters
Scale coefficient(s):
                                    estimate        se
(Intercept)                        5.5563867 0.3693793
OriginalScientificNameHumpback, Right 0.4977955 0.2125828
SeasonSpring                       0.7279337 0.2896812
SeasonSummer                       0.7542217 0.2477951
SurveyIDYears 2-3                  0.4837030 0.2648931

Shape coefficient(s):
```

```
             estimate       se
(Intercept) 0.8485132 0.197714

                        Estimate          SE        CV
Average p               0.4075964  0.06072428 0.1489814
N in covered region 421.9860458 68.23264910 0.1616941

Distance sampling Cramer-von Mises test (unweighted)
Test statistic = 0.068137  p = 0.763045
```

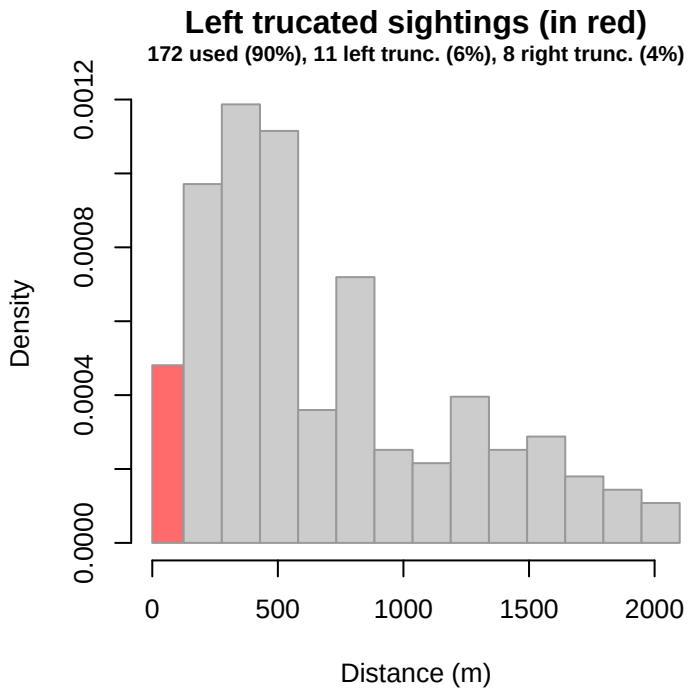

Figure 21: Density histogram of observations used to fit the NYS-DEC NYBWM Partenavia detection function, with the left-most bar showing observations at distances less than 125 m, which were left-truncated and excluded from the analysis [Buckland et al. (2001)]. (This bar may be very short if there were very few left-truncated sightings, or very narrow if the left truncation distance was very small; in either case it may not appear red.)

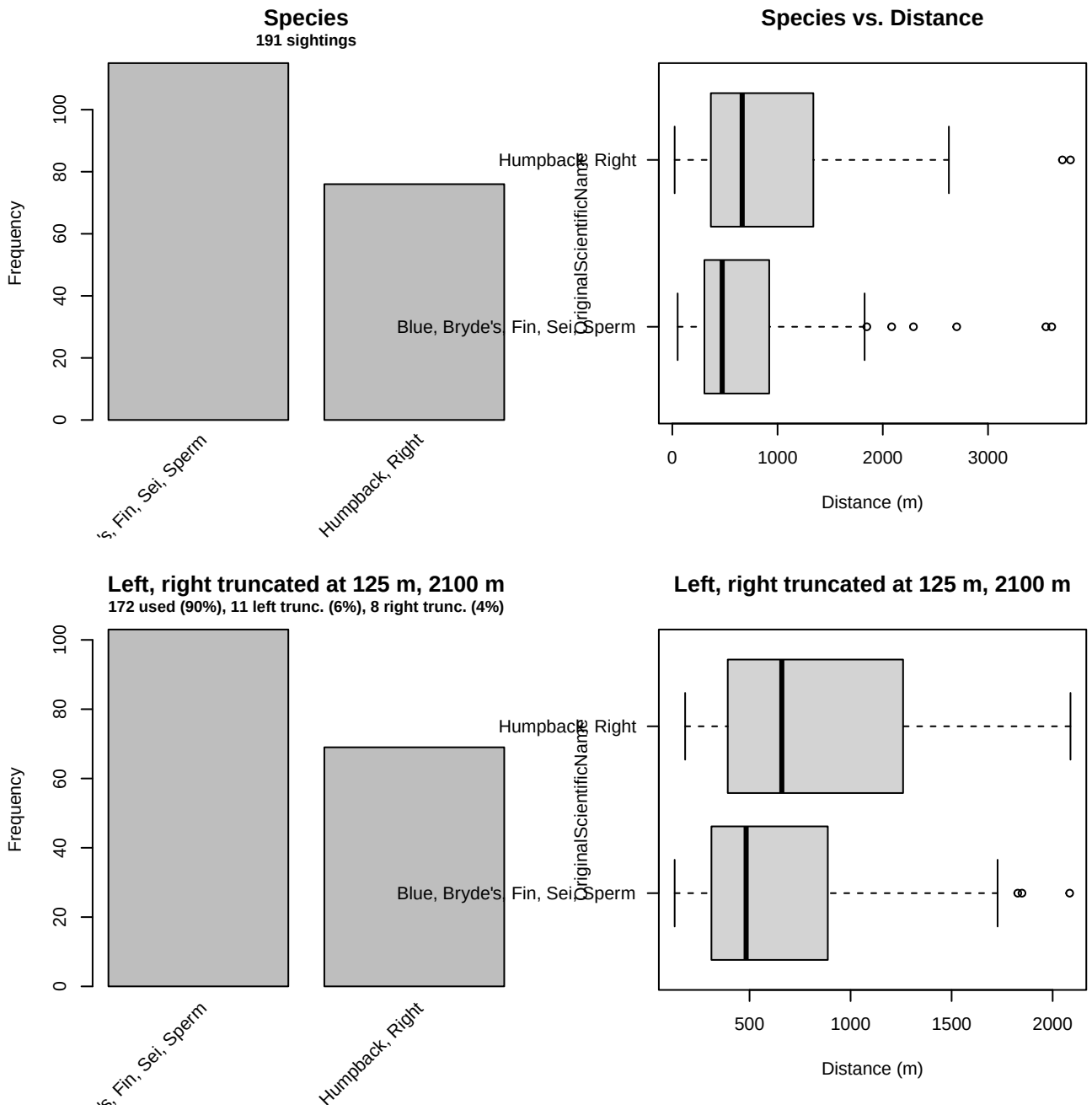

Figure 22: Distribution of the OriginalScientificName covariate before (top row) and after (bottom row) observations were truncated to fit the NYS-DEC NYBWM Partenavia detection function.

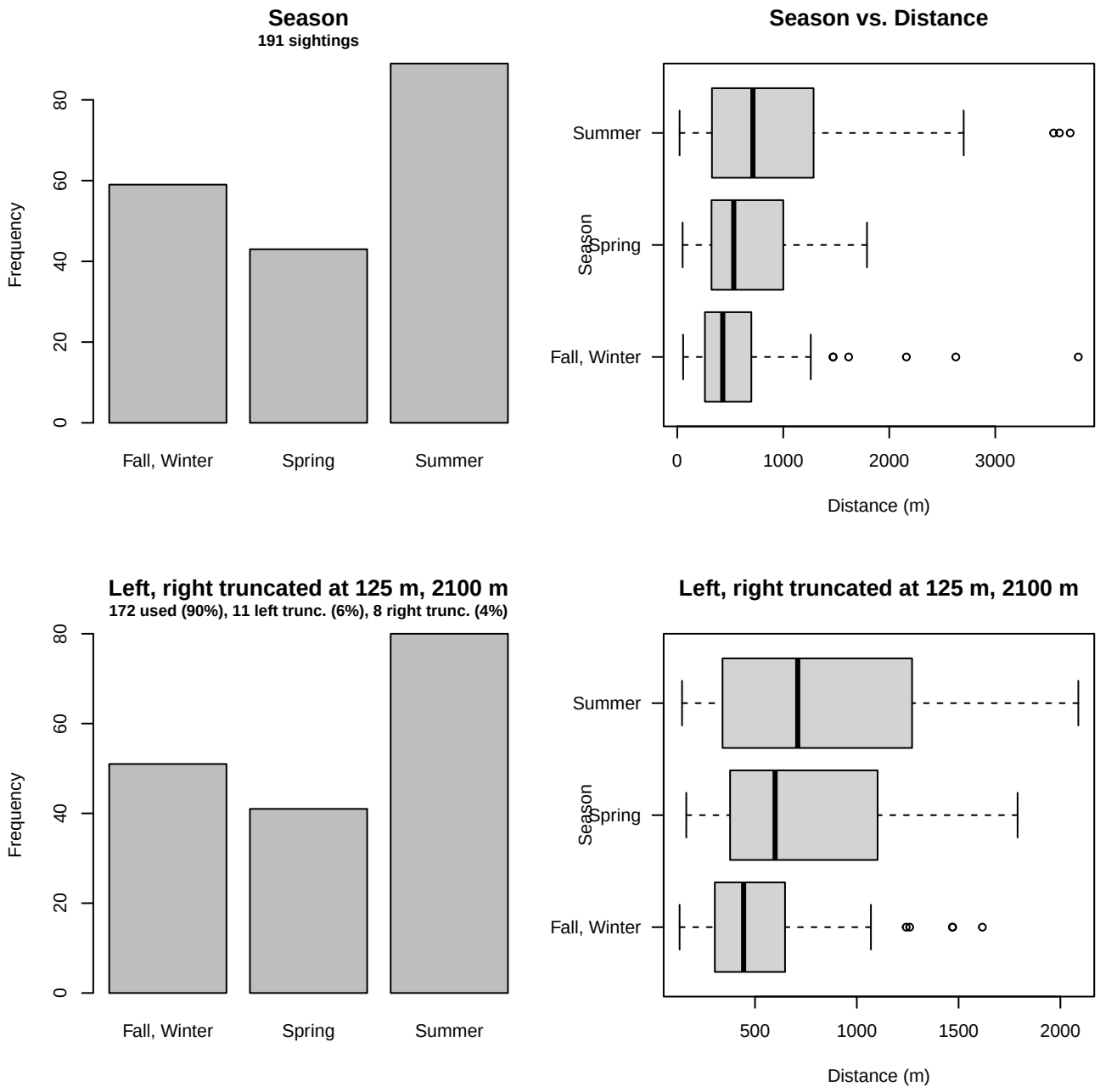

Figure 23: Distribution of the Season covariate before (top row) and after (bottom row) observations were truncated to fit the NYS-DEC NYBWM Partenavia detection function.

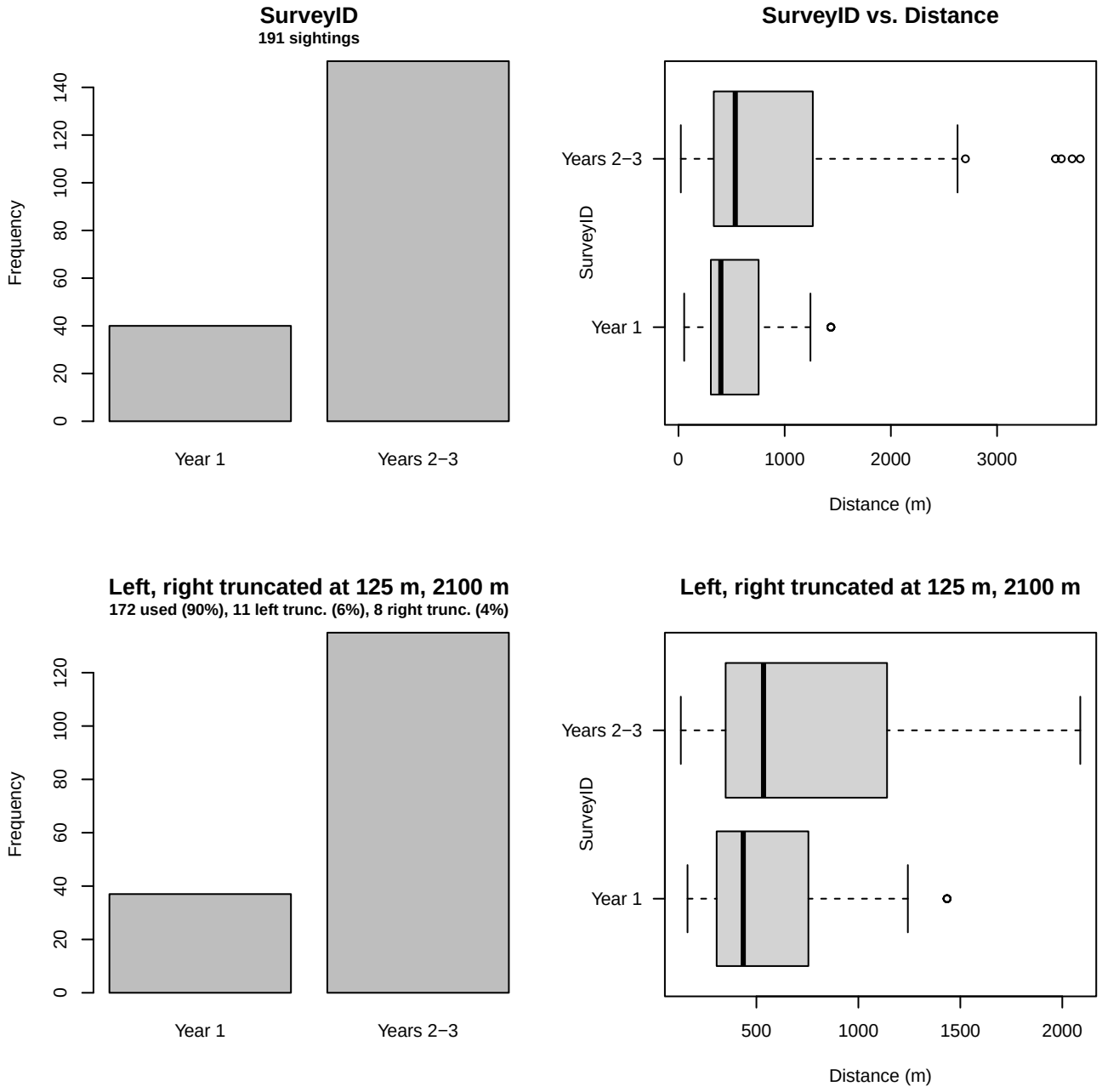

Figure 24: Distribution of the SurveyID covariate before (top row) and after (bottom row) observations were truncated to fit the NYS-DEC NYBWM Partenavia detection function.

2.1.1.7 NARW EWS WLT-SSA-CMARI Twin Otter

After right-truncating observations greater than 3500 m, we fitted the detection function to the 690 observations that remained (Table 10). The selected detection function (Figure 25) used a hazard rate key function with Beaufort (Figure 26), Clouds (Figure 27) and OriginalScientificName (Figure 28) as covariates.

Table 10: Observations used to fit the NARW EWS WLT-SSA-CMARI Twin Otter detection function.

ScientificName	n
Eubalaena glacialis	650
Megaptera novaeangliae	40
Total	**690**

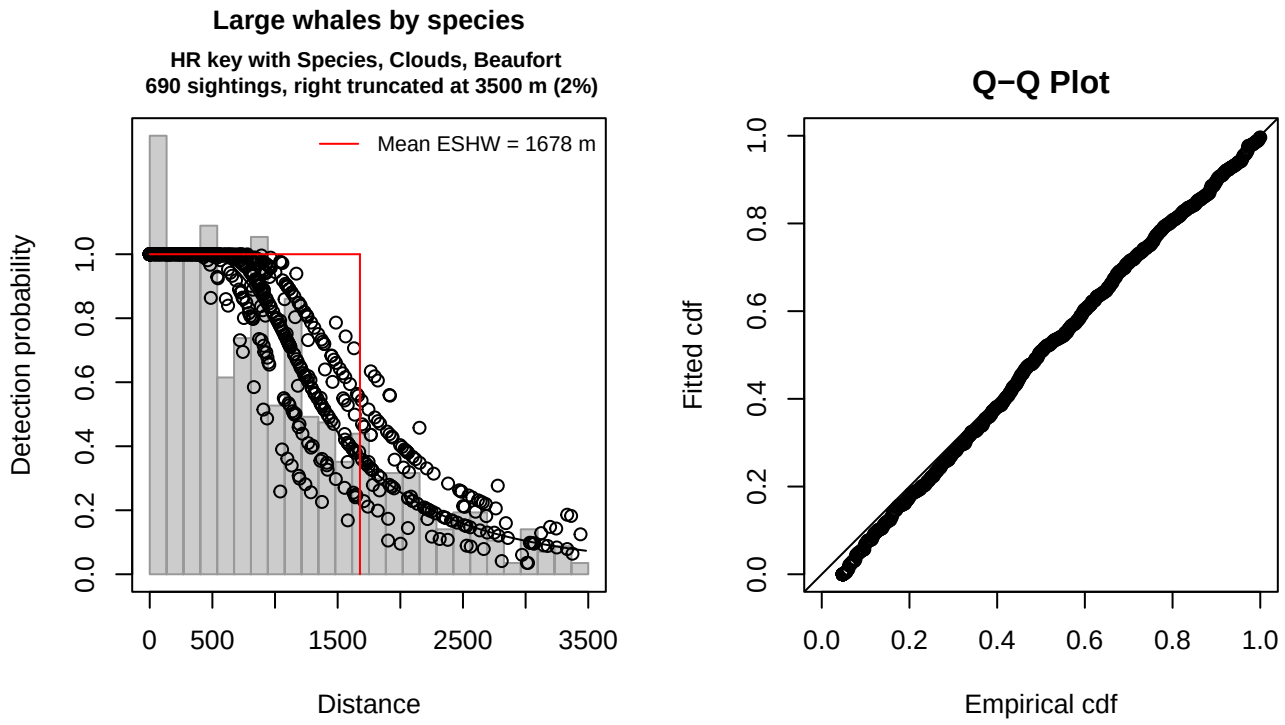

Figure 25: NARW EWS WLT-SSA-CMARI Twin Otter detection function and Q-Q plot showing its goodness of fit.

Statistical output for this detection function:

```
Summary for ds object
Number of observations :  690
Distance range         :  0  -  3500
AIC                    :  10853.45

Detection function:
 Hazard-rate key function

Detection function parameters
Scale coefficient(s):
                                              estimate        se
(Intercept)                                  6.6800193 0.1481932
OriginalScientificNameMegaptera novaeangliae -0.2149176 0.1720359
CloudsClear, Scattered                        0.2060768 0.1208231
CloudsOvercast                                0.3486646 0.1606490
Beaufort2                                     0.2229601 0.1188583
Beaufort3                                     0.4490960 0.1359044

Shape coefficient(s):
             estimate         se
(Intercept) 0.9140986 0.09579769

                       Estimate         SE         CV
Average p              0.466199  0.0192781 0.04135166
N in covered region 1480.054585 74.0421940 0.05002666

Distance sampling Cramer-von Mises test (unweighted)
Test statistic = 0.238997  p = 0.203109
```

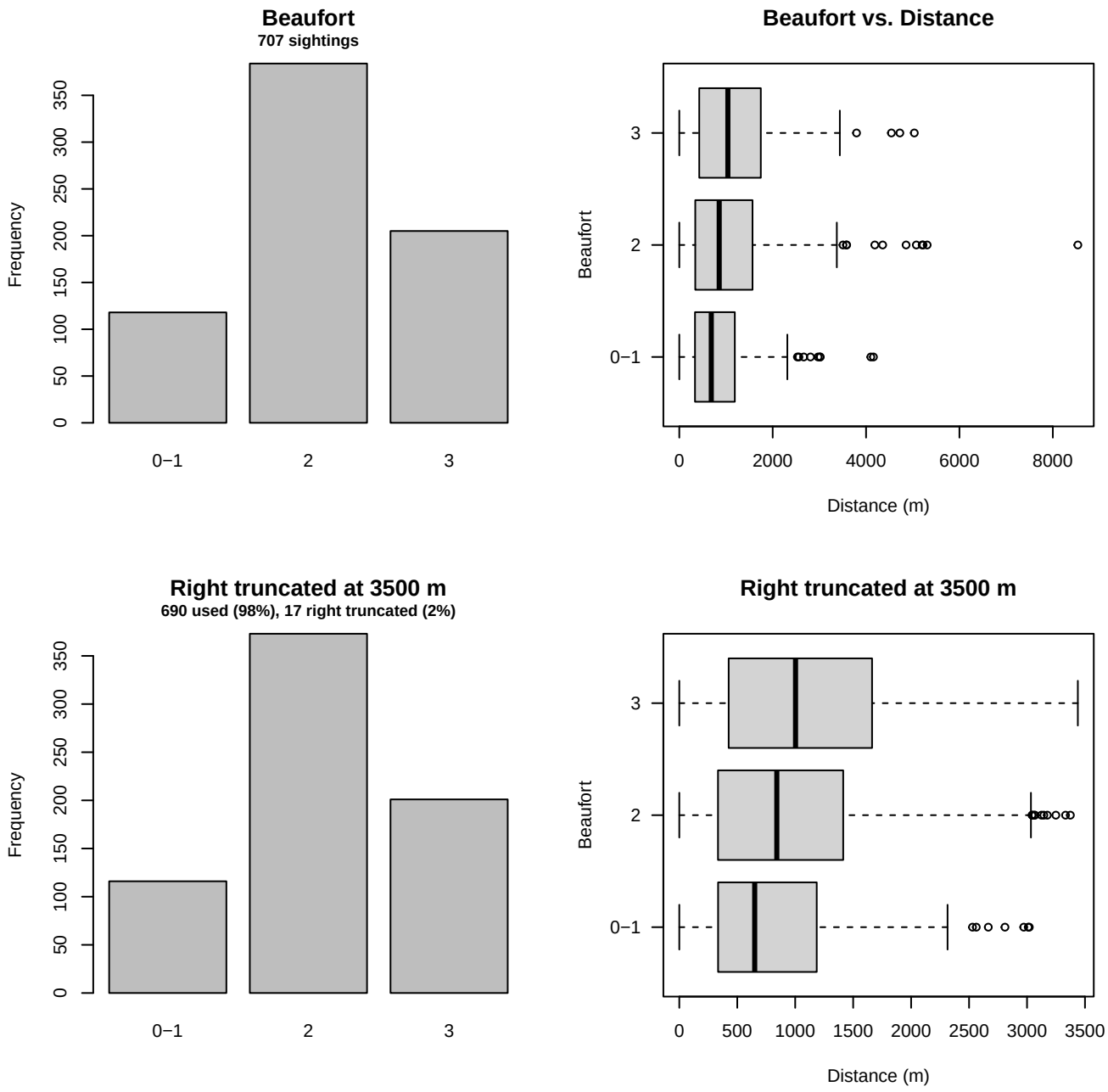

Figure 26: Distribution of the Beaufort covariate before (top row) and after (bottom row) observations were truncated to fit the NARW EWS WLT-SSA-CMARI Twin Otter detection function.

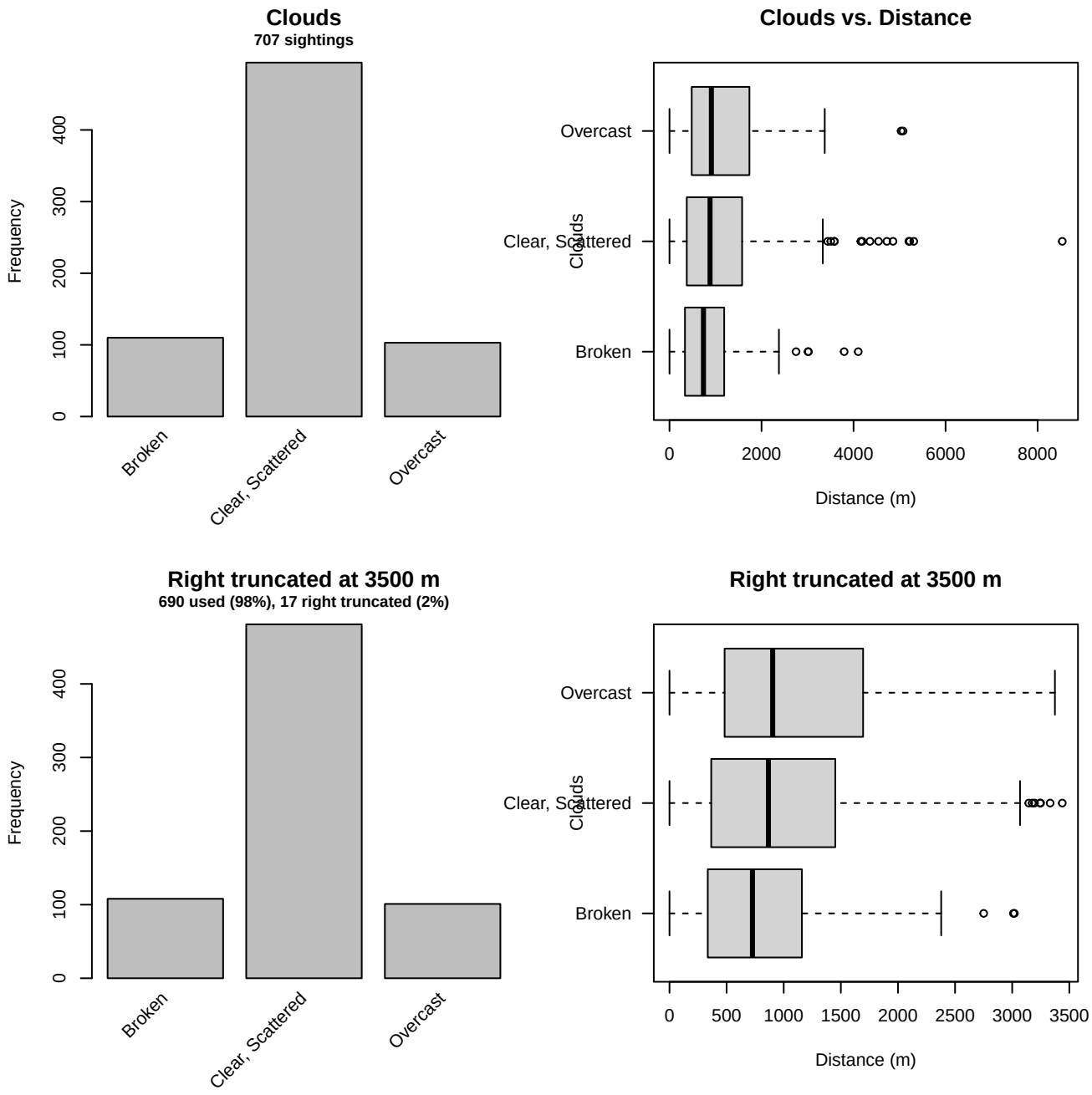

Figure 27: Distribution of the Clouds covariate before (top row) and after (bottom row) observations were truncated to fit the NARW EWS WLT-SSA-CMARI Twin Otter detection function.

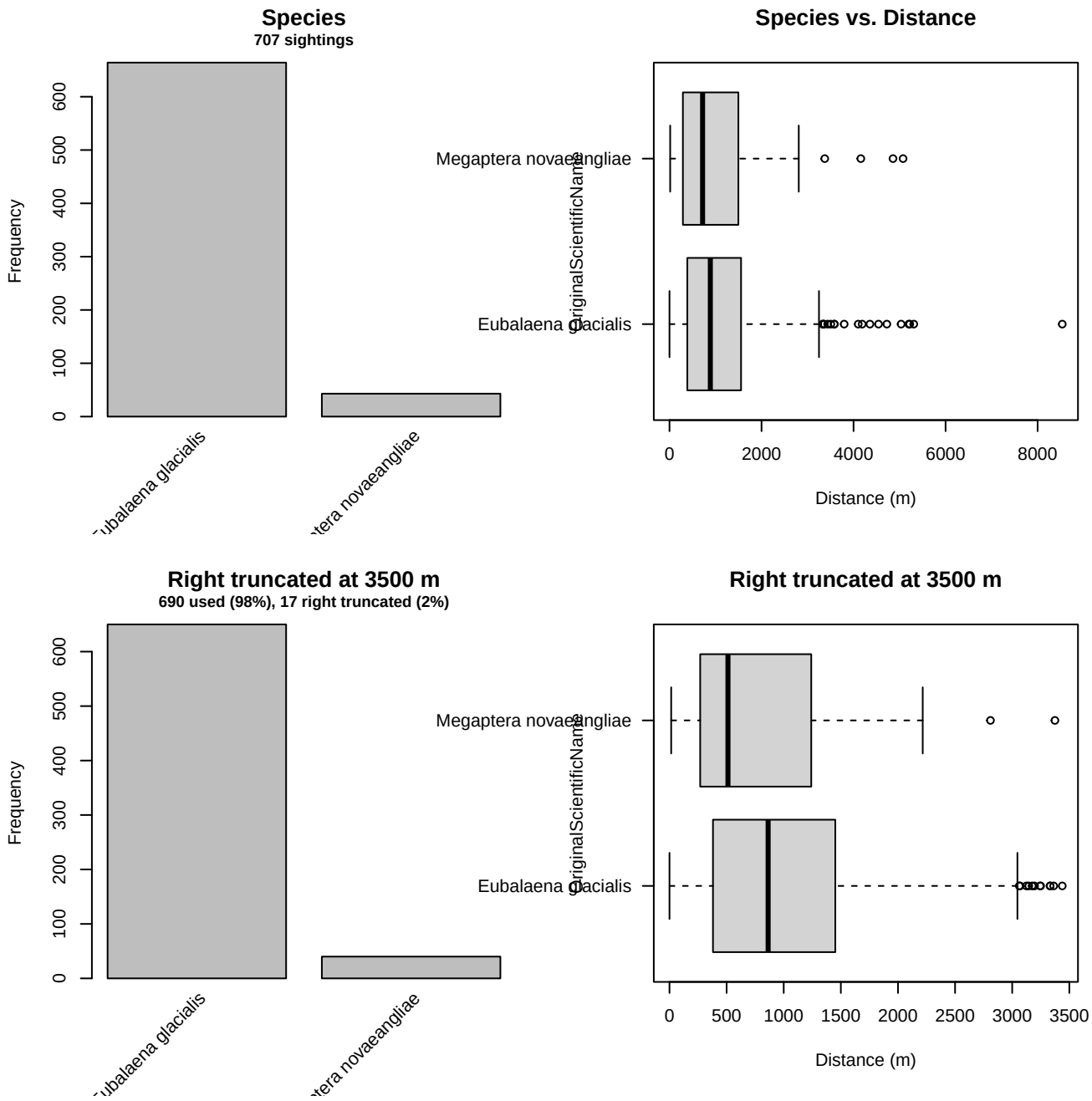

Figure 28: Distribution of the OriginalScientificName covariate before (top row) and after (bottom row) observations were truncated to fit the NARW EWS WLT-SSA-CMARI Twin Otter detection function.

2.1.1.8 NEAq New England

After right-truncating observations greater than 3704 m and left-truncating observations less than 71 m (Figure 30), we fitted the detection function to the 441 observations that remained (Table 11). The selected detection function (Figure 29) used a half normal key function with Beaufort (Figure 31), Glare (Figure 32) and OriginalScientificName (Figure 33) as covariates.

Table 11: Observations used to fit the NEAq New England detection function.

ScientificName	n
Balaenoptera borealis	44
Balaenoptera musculus	2
Balaenoptera physalus	128
Eubalaena glacialis	146
Megaptera novaeangliae	112
Physeter macrocephalus	9
Total	**441**

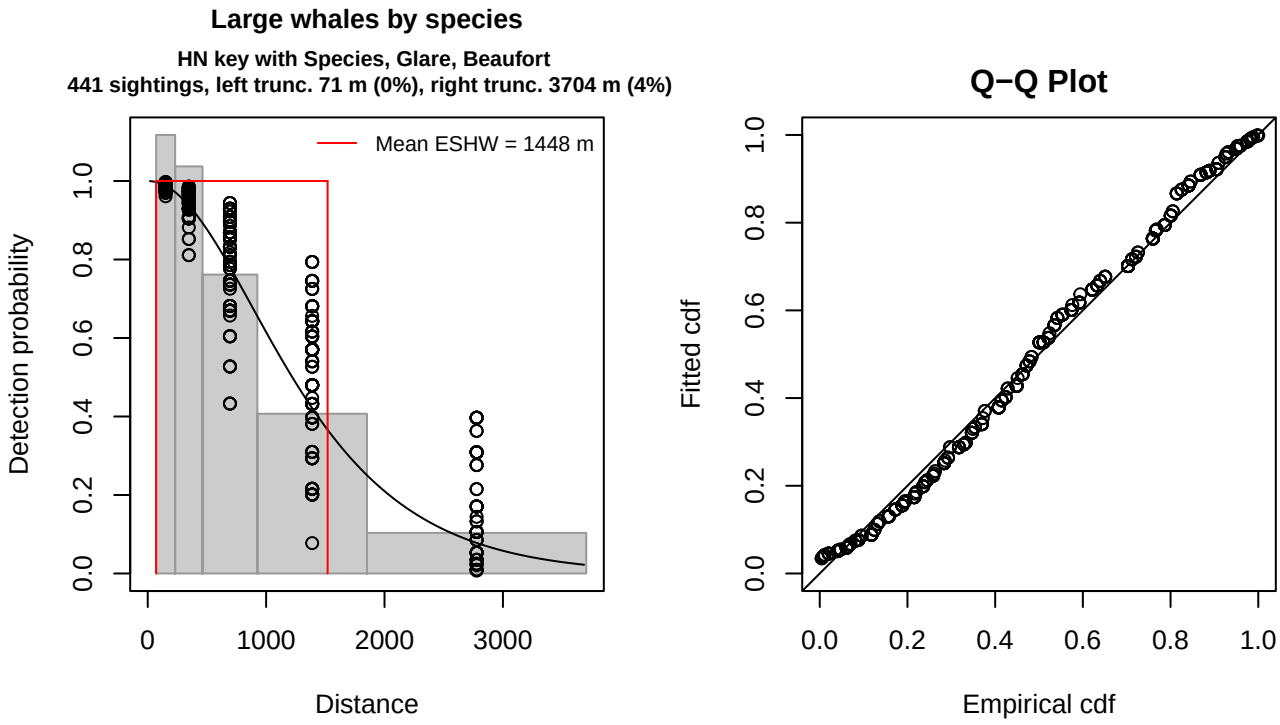

Figure 29: NEAq New England detection function and Q-Q plot showing its goodness of fit.

Statistical output for this detection function:

```
Summary for ds object
Number of observations :  441
Distance range         :  71  -  3704
AIC                    :  1351.833

Detection function:
 Half-normal key function

Detection function parameters
Scale coefficient(s):
                                estimate         se
(Intercept)                    6.4199373 0.11956192
OriginalScientificNameHumpback  0.1198260 0.10455078
OriginalScientificNameRight    -0.1344891 0.09839291
GlareSevere                     0.3449677 0.16999750
GlareSlight, Moderate           0.3904627 0.09774396
Beaufort2                       0.3680223 0.09867329
Beaufort3-4                     0.6919932 0.12929768
```

```
                          Estimate          SE         CV
Average p                0.3618698  0.01608762 0.04445694
N in covered region 1218.6704246 72.16746829 0.05921820

Distance sampling Cramer-von Mises test (unweighted)
Test statistic = 0.341945  p = 0.103421
```

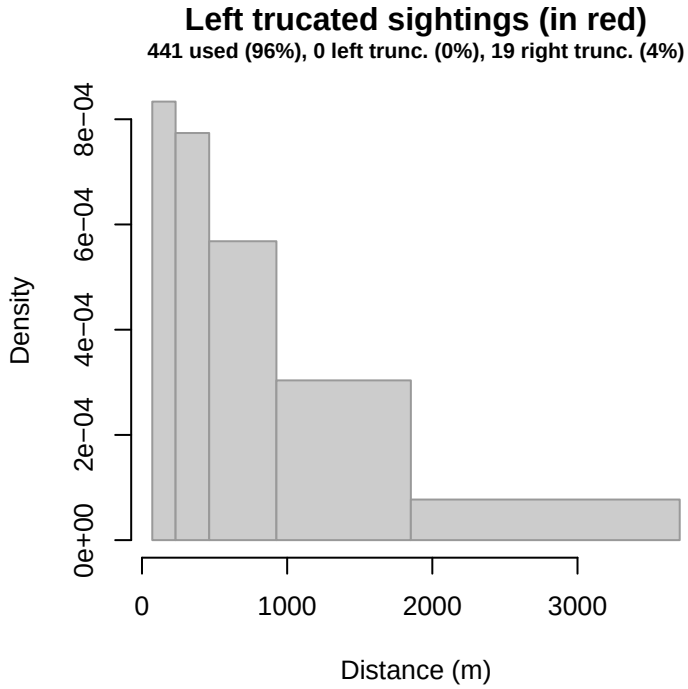

Figure 30: Density histogram of observations used to fit the NEAq New England detection function, with the left-most bar showing observations at distances less than 71 m, which were left-truncated and excluded from the analysis [Buckland et al. (2001)]. (This bar may be very short if there were very few left-truncated sightings, or very narrow if the left truncation distance was very small; in either case it may not appear red.)

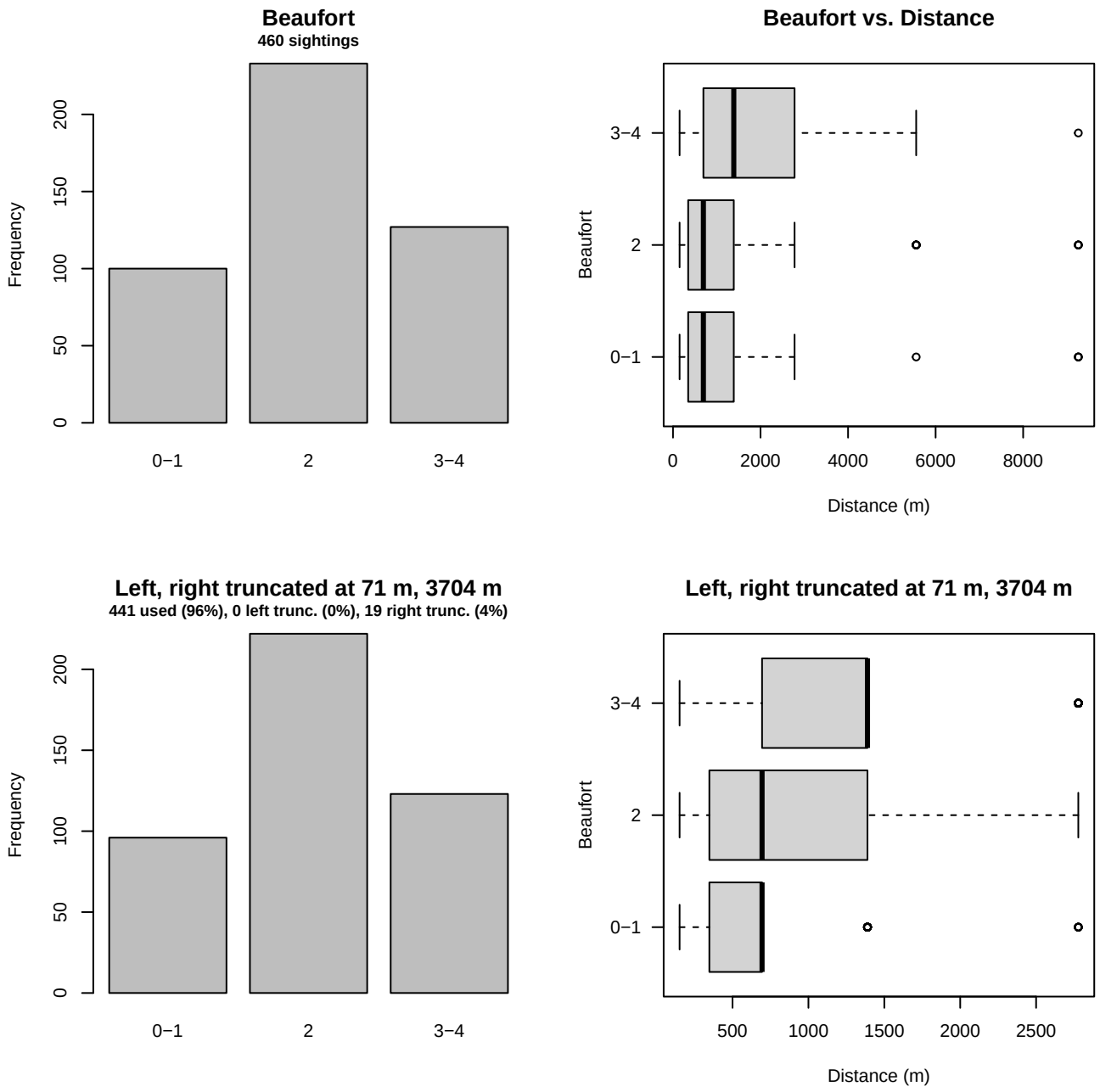

Figure 31: Distribution of the Beaufort covariate before (top row) and after (bottom row) observations were truncated to fit the NEAq New England detection function.

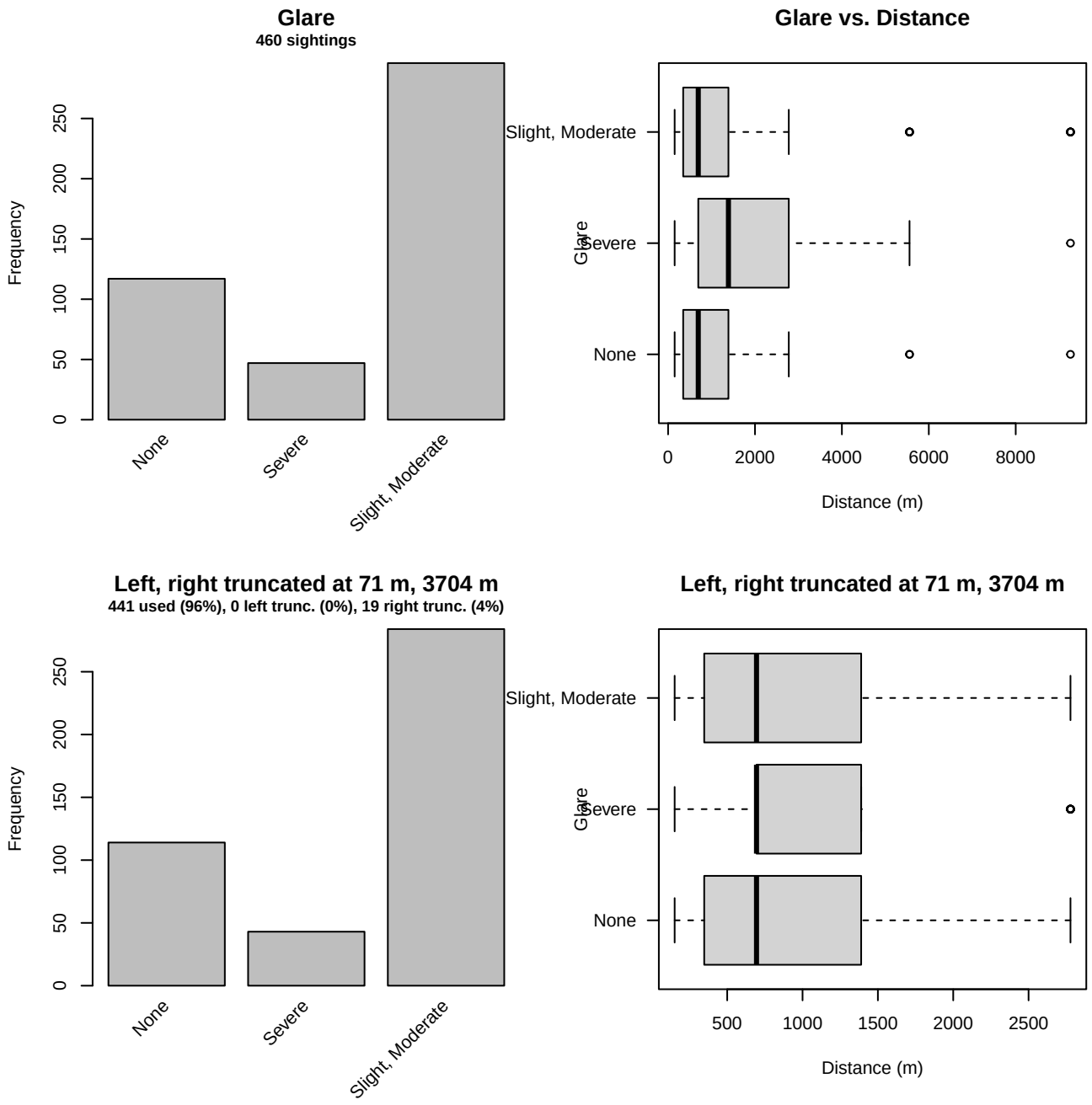

Figure 32: Distribution of the Glare covariate before (top row) and after (bottom row) observations were truncated to fit the NEAq New England detection function.

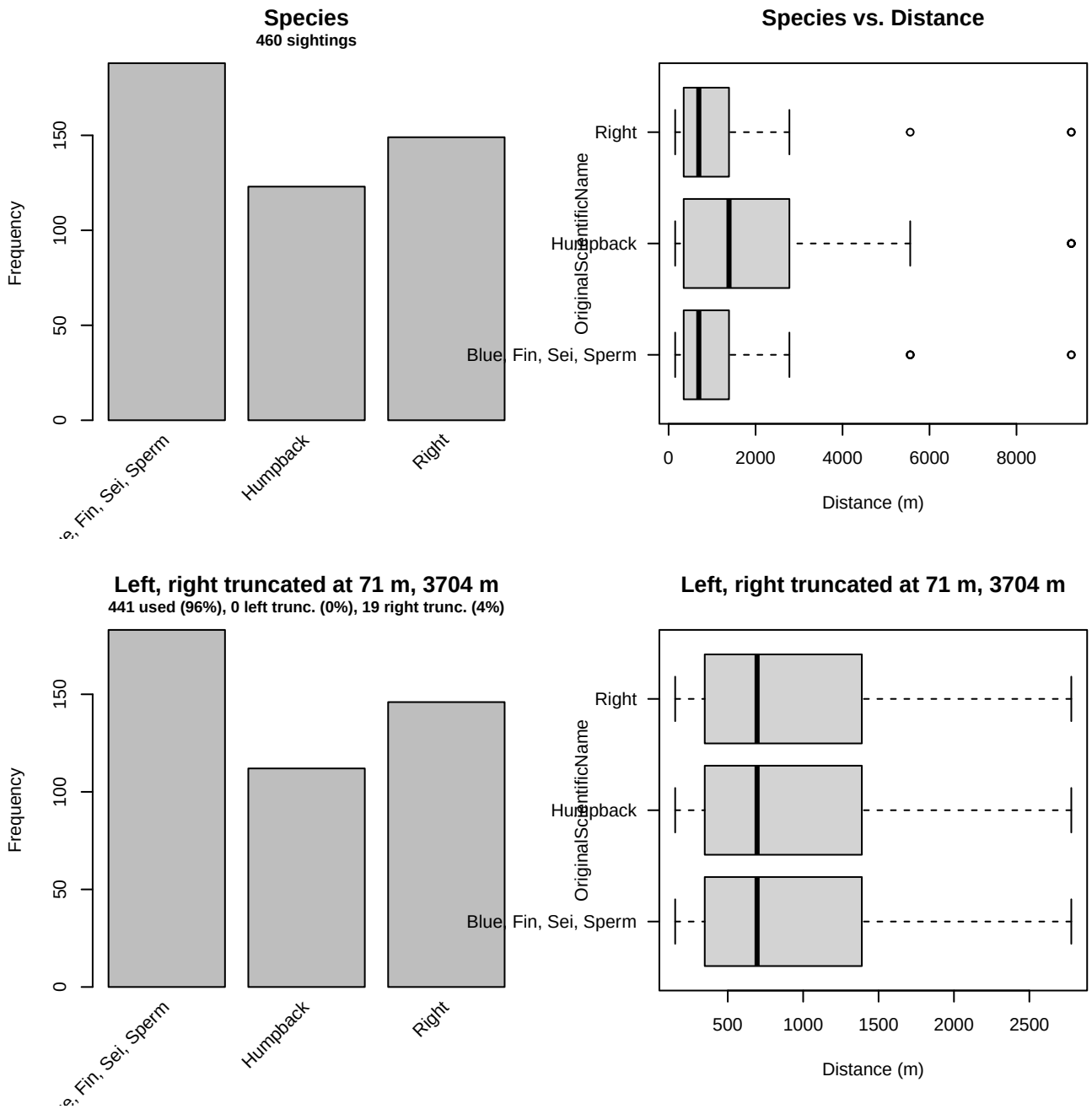

Figure 33: Distribution of the OriginalScientificName covariate before (top row) and after (bottom row) observations were truncated to fit the NEAq New England detection function.

2.1.1.9 UNCW and VAMSC

After right-truncating observations greater than 2000 m, we fitted the detection function to the 100 observations that remained (Table 12). The selected detection function (Figure 34) used a hazard rate key function with OriginalScientificName (Figure 35) as a covariate.

Table 12: Observations used to fit the UNCW and VAMSC detection function.

ScientificName	n
Balaenoptera physalus	27
Megaptera novaeangliae	31
Physeter macrocephalus	42
Total	**100**

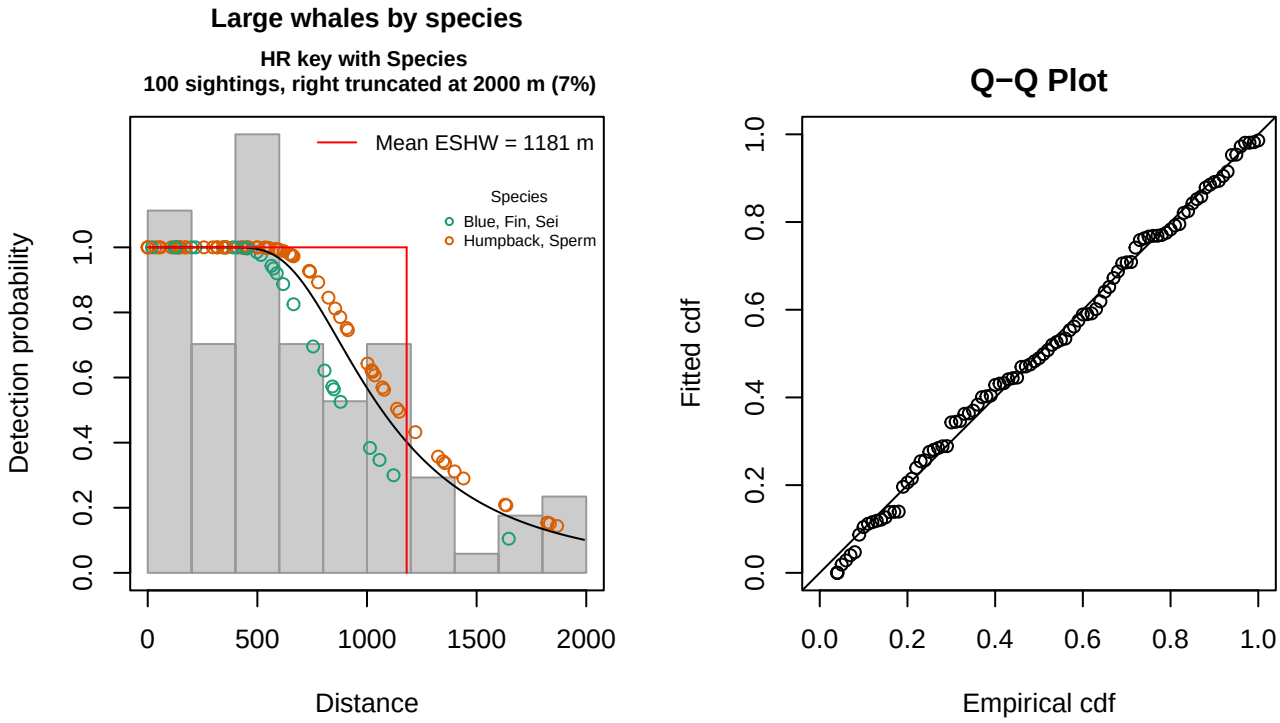

Figure 34: UNCW and VAMSC detection function and Q-Q plot showing its goodness of fit.

Statistical output for this detection function:

```
Summary for ds object
Number of observations :  100
Distance range         :  0  -  2000
AIC                    :  1484.772

Detection function:
 Hazard-rate key function

Detection function parameters
Scale coefficient(s):
                                      estimate        se
(Intercept)                          6.6826489 0.2197841
OriginalScientificNameHumpback, Sperm 0.2371163 0.2278764

Shape coefficient(s):
            estimate        se
(Intercept)  1.11195 0.3071042

                      Estimate          SE        CV
Average p             0.5857436  0.05399642 0.0921844
N in covered region 170.7231622 19.23003142 0.1126387
```

```
Distance sampling Cramer-von Mises test (unweighted)
Test statistic = 0.036117  p = 0.952042
```

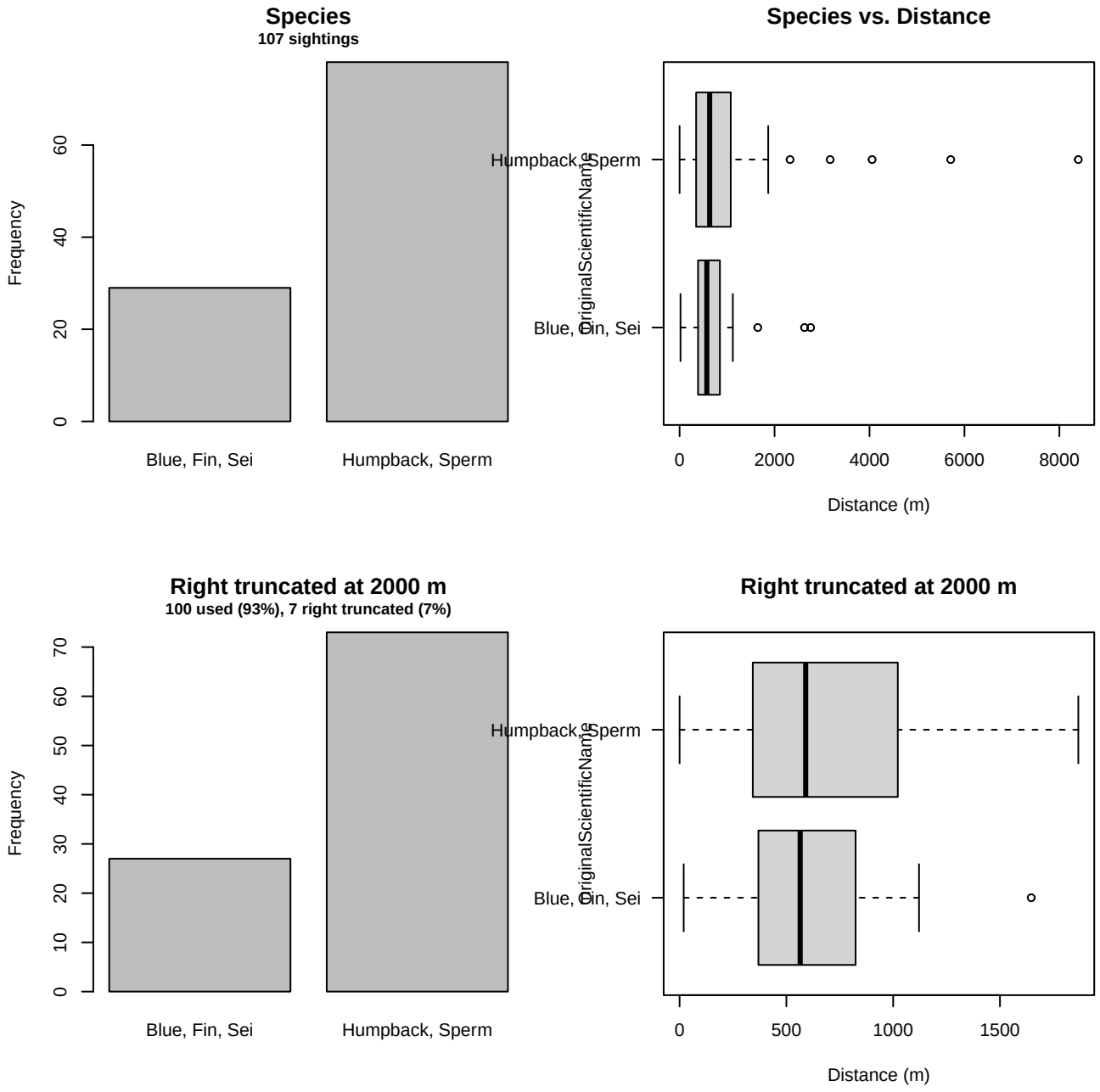

Figure 35: Distribution of the OriginalScientificName covariate before (top row) and after (bottom row) observations were truncated to fit the UNCW and VAMSC detection function.

2.1.1.10 NARW EWS FWRI

After right-truncating observations greater than 4800 m and left-truncating observations less than 71 m (Figure 37), we fitted the detection function to the 862 observations that remained (Table 13). The selected detection function (Figure 36) used a hazard rate key function with Beaufort (Figure 38), OriginalScientificName (Figure 39) and WeatherCode (Figure 40) as covariates.

Table 13: Observations used to fit the NARW EWS FWRI detection function.

ScientificName	n
Eubalaena glacialis	806
Megaptera novaeangliae	56
Total	**862**

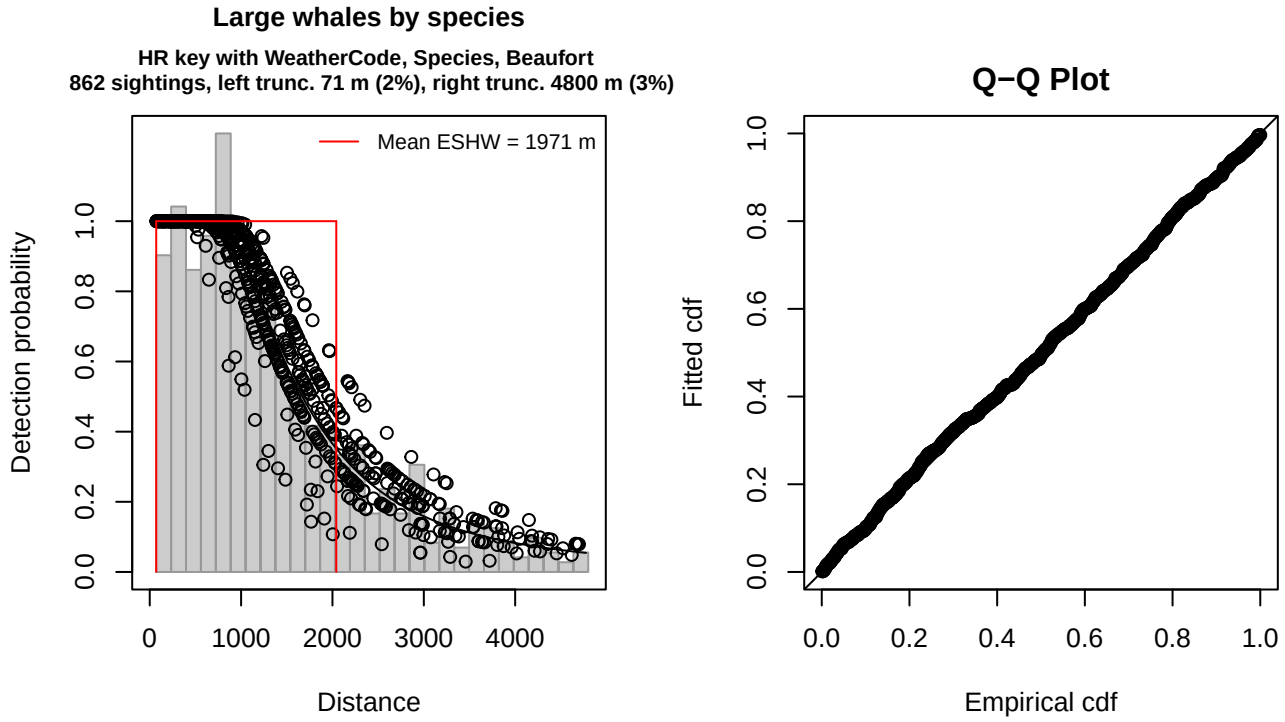

Figure 36: NARW EWS FWRI detection function and Q-Q plot showing its goodness of fit.

Statistical output for this detection function:

```
Summary for ds object
Number of observations :  862
Distance range         :  71  -  4800
AIC                    :  13956.52

Detection function:
 Hazard-rate key function

Detection function parameters
Scale coefficient(s):
                                             estimate         se
(Intercept)                                 7.5817454 0.11269195
WeatherCodeGray, Haze                      -0.2221167 0.08054058
OriginalScientificNameMegaptera novaeangliae -0.3927522 0.14233839
Beaufort2                                  -0.1490882 0.10720238
Beaufort3                                  -0.2543602 0.12482242

Shape coefficient(s):
             estimate         se
(Intercept) 0.8930518 0.07586393

                        Estimate          SE         CV
```

```
Average p              0.4067837   0.01646644 0.04047961
N in covered region 2119.0622892 102.47010867 0.04835635

Distance sampling Cramer-von Mises test (unweighted)
Test statistic = 0.071442  p = 0.742745
```

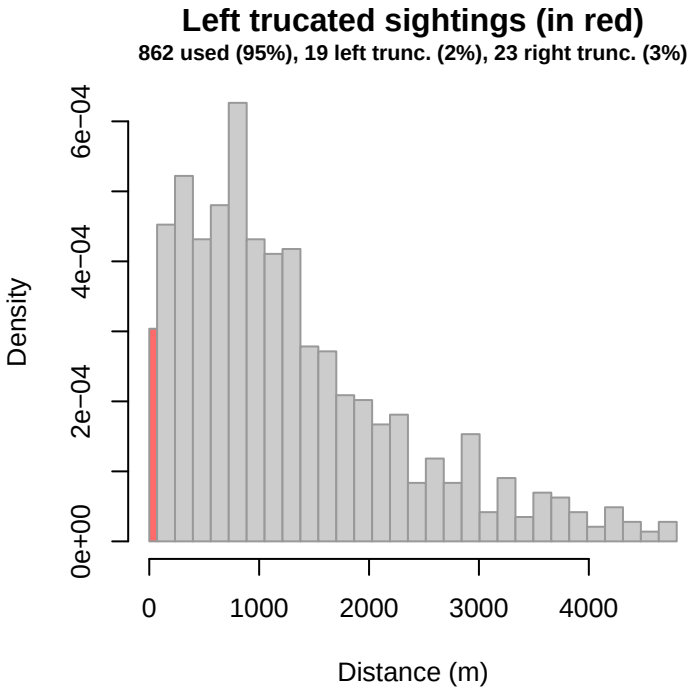

Figure 37: Density histogram of observations used to fit the NARW EWS FWRI detection function, with the left-most bar showing observations at distances less than 71 m, which were left-truncated and excluded from the analysis [Buckland et al. (2001)]. (This bar may be very short if there were very few left-truncated sightings, or very narrow if the left truncation distance was very small; in either case it may not appear red.)

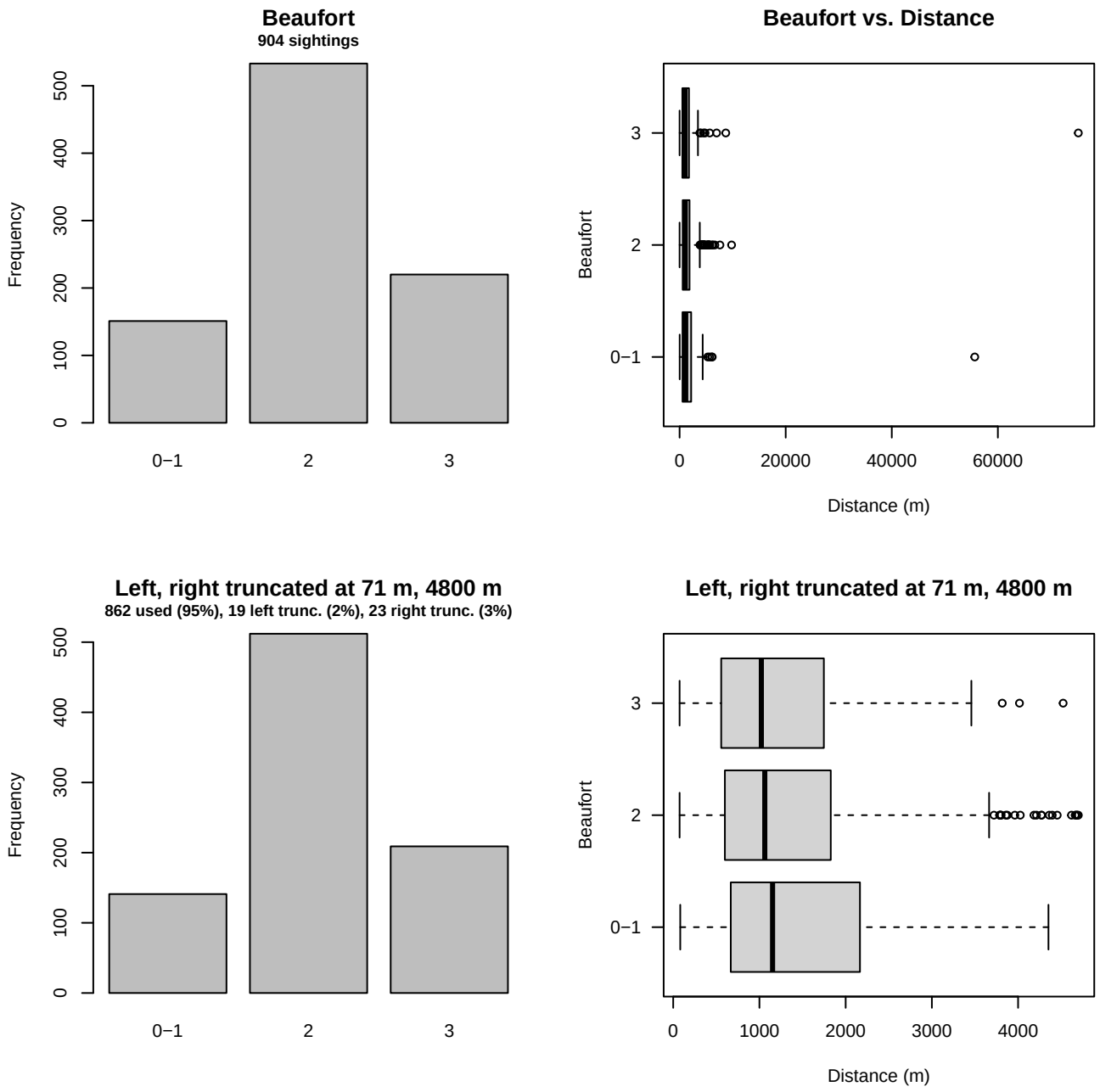

Figure 38: Distribution of the Beaufort covariate before (top row) and after (bottom row) observations were truncated to fit the NARW EWS FWRI detection function.

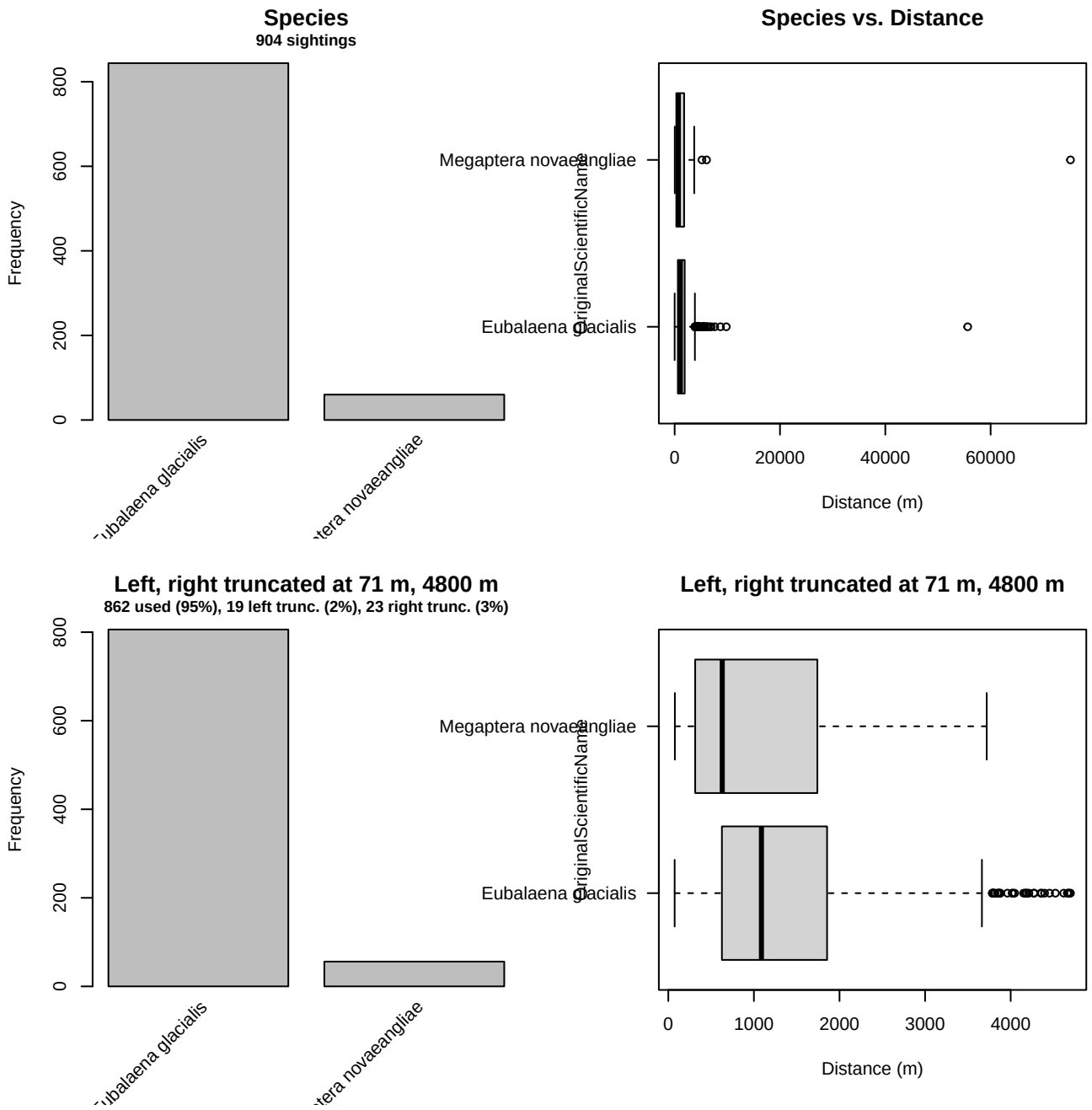

Figure 39: Distribution of the OriginalScientificName covariate before (top row) and after (bottom row) observations were truncated to fit the NARW EWS FWRI detection function.

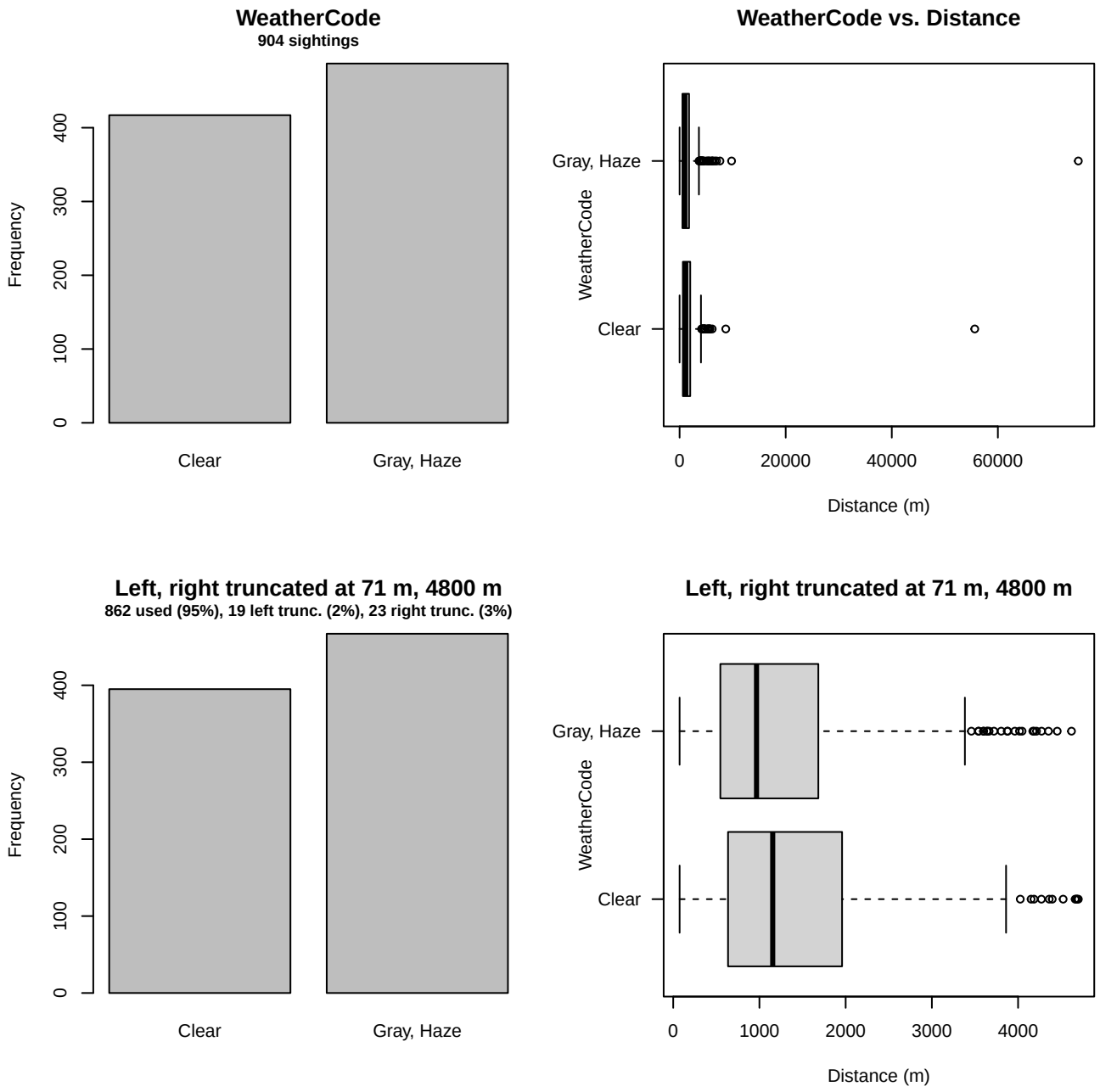

Figure 40: Distribution of the WeatherCode covariate before (top row) and after (bottom row) observations were truncated to fit the NARW EWS FWRI detection function.

2.1.2 Shipboard Surveys

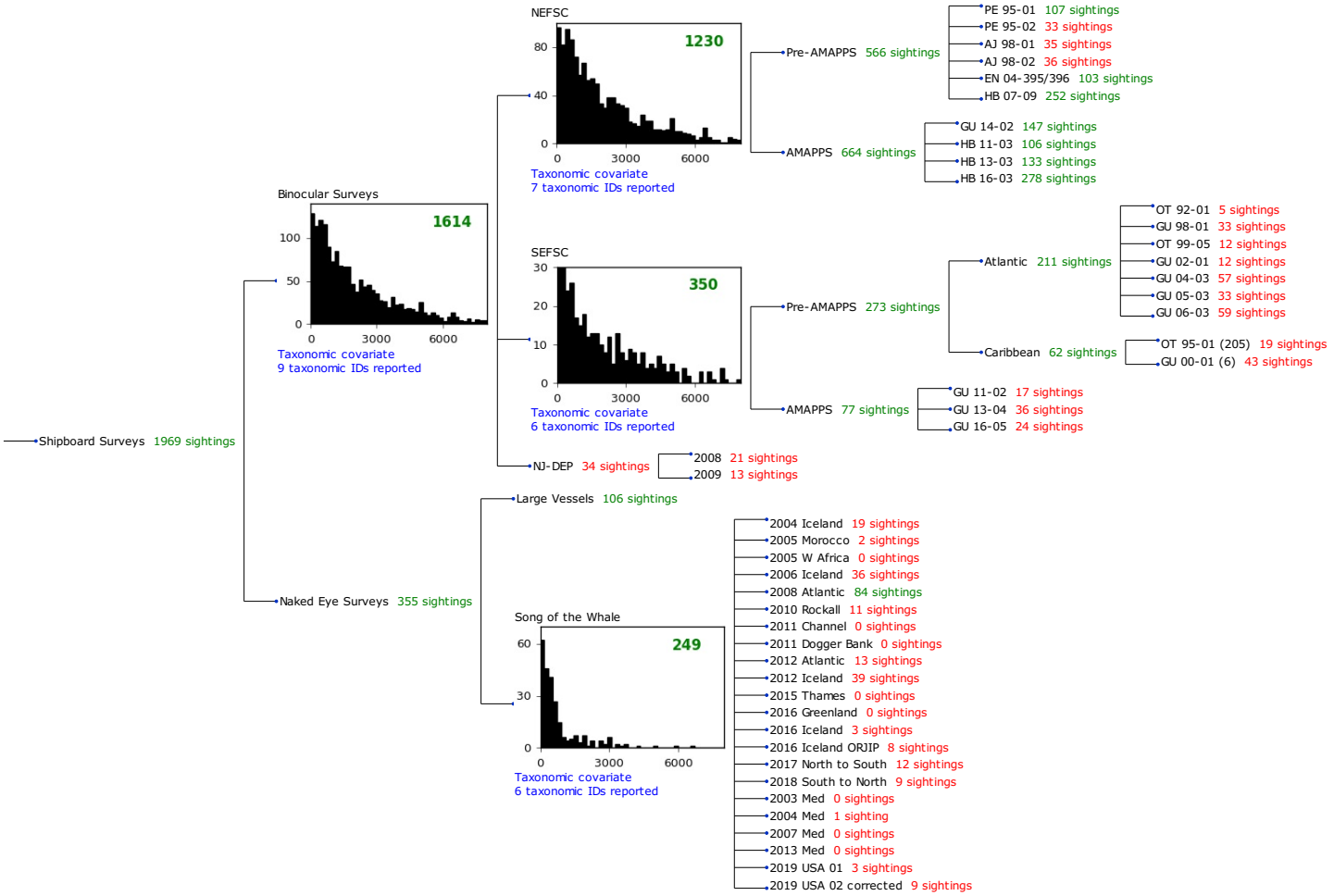

Figure 41: Detection hierarchy for shipboard surveys, showing how they were pooled during detectability modeling, for detection functions that pooled multiple taxa and used used a taxonomic covariate to account for differences between them. Each histogram represents a detection function and summarizes the perpendicular distances of observations that were pooled to fit it, prior to truncation. Observation counts, also prior to truncation, are shown in green when they met the recommendation of Buckland et al. (2001) that detection functions utilize at least 60 sightings, and red otherwise. For rare taxa, it was not always possible to meet this recommendation, yielding higher statistical uncertainty. During the spatial modeling stage of the analysis, effective strip widths were computed for each survey using the closest detection function above it in the hierarchy (i.e. moving from right to left in the figure). Surveys that do not have a detection function above them in this figure were either addressed by a detection function presented in a different section of this report, or were omitted from the analysis.

2.1.2.1 NEFSC

After right-truncating observations greater than 7000 m, we fitted the detection function to the 1201 observations that remained (Table 14). The selected detection function (Figure 42) used a hazard rate key function with OriginalScientificName (Figure 43) and Program (Figure 44) as covariates.

Table 14: Observations used to fit the NEFSC detection function.

ScientificName	n
Balaenoptera borealis	24
Balaenoptera borealis/physalus	88
Balaenoptera musculus	7
Balaenoptera physalus	280
Eubalaena glacialis	53
Megaptera novaeangliae	289
Physeter macrocephalus	460
Total	**1201**

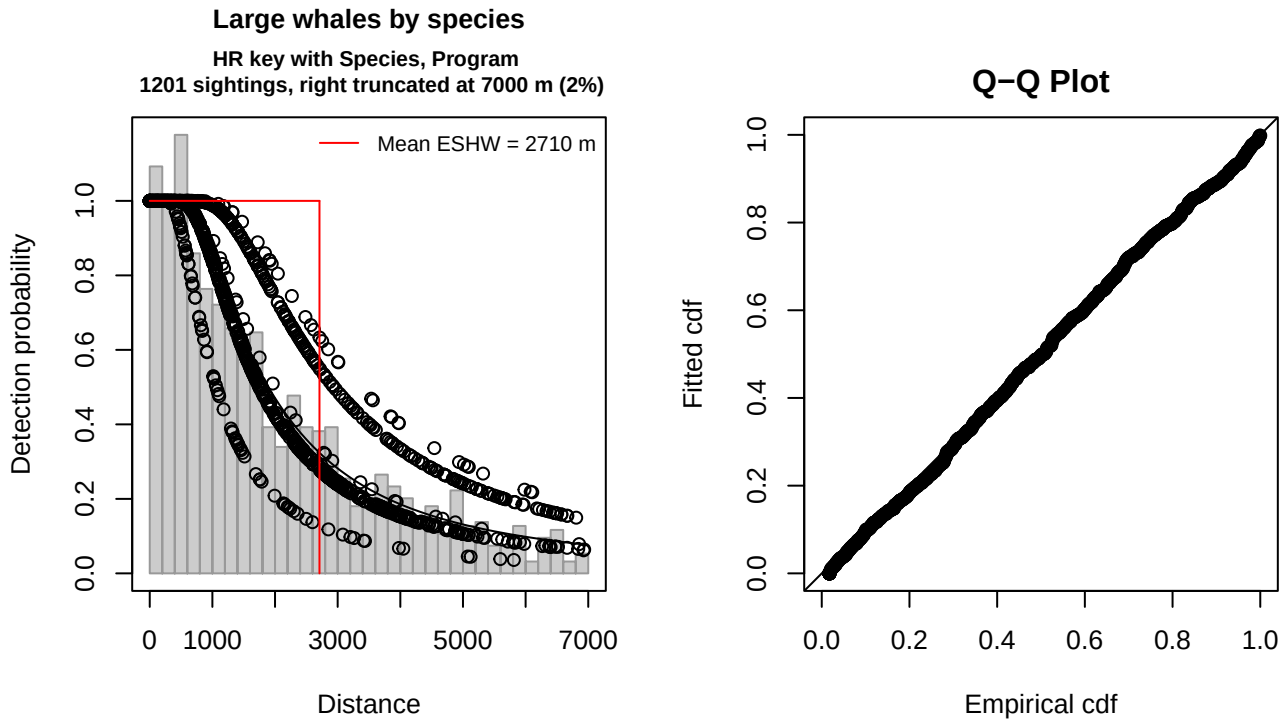

Figure 42: NEFSC detection function and Q-Q plot showing its goodness of fit.

Statistical output for this detection function:

```
Summary for ds object
Number of observations :  1201
Distance range         :  0  -  7000
AIC                    :  20458.33

Detection function:
 Hazard-rate key function

Detection function parameters
Scale coefficient(s):
                                      estimate        se
(Intercept)                          7.2780926 0.1052538
OriginalScientificNameHumpback, Sperm  0.4967174 0.1052988
OriginalScientificNameUnid. fin or sei  0.6284650 0.1945392
ProgramMarine Mammal Abundance Surveys -0.5195829 0.0968891

Shape coefficient(s):
```

```
             estimate        se
(Intercept) 0.5494314 0.0661582

                         Estimate           SE         CV
Average p                0.3639429   0.01592018 0.04374363
N in covered region 3299.9683075 163.75203637 0.04962231

Distance sampling Cramer-von Mises test (unweighted)
Test statistic = 0.126712  p = 0.469029
```

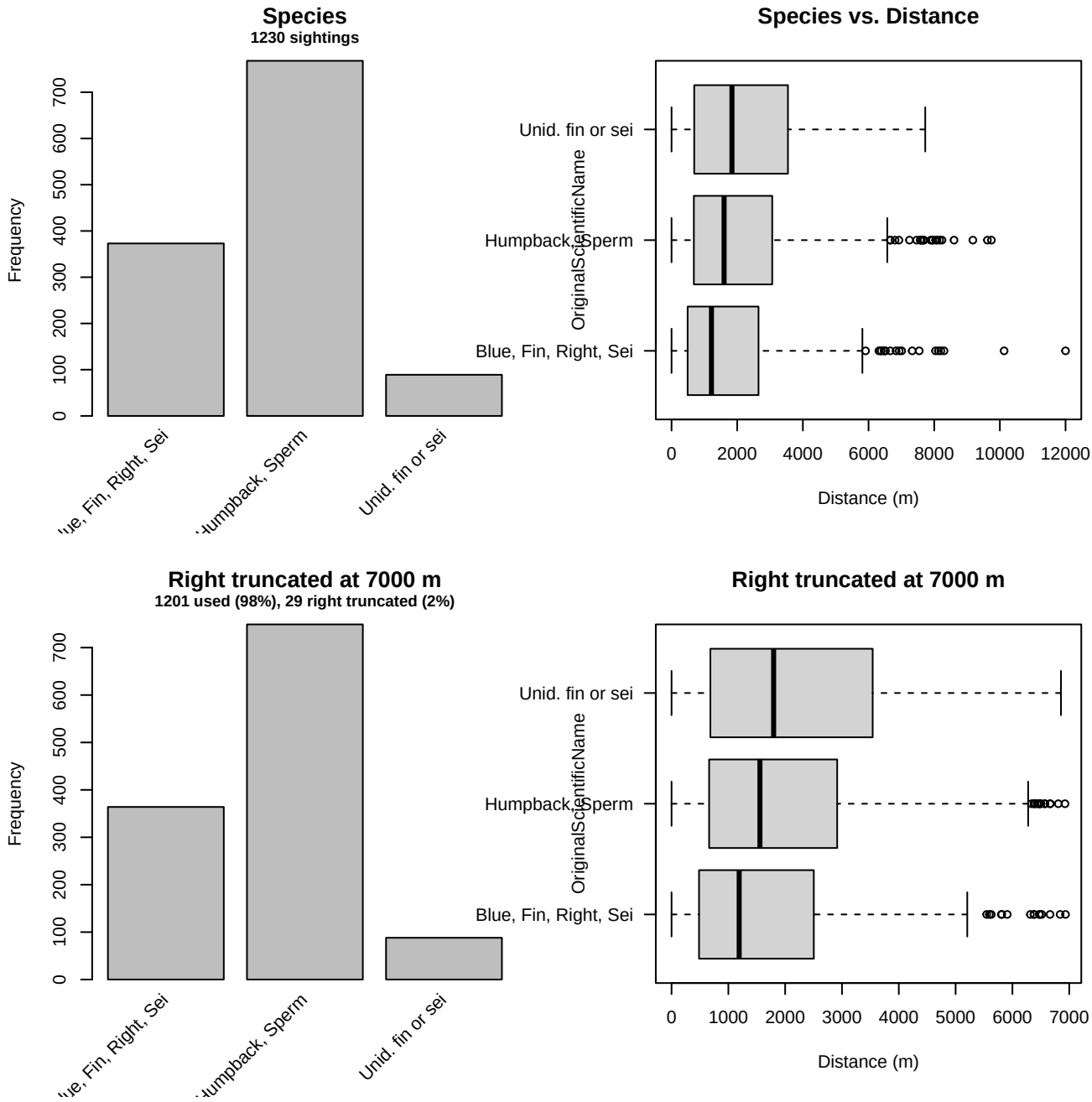

Figure 43: Distribution of the OriginalScientificName covariate before (top row) and after (bottom row) observations were truncated to fit the NEFSC detection function.

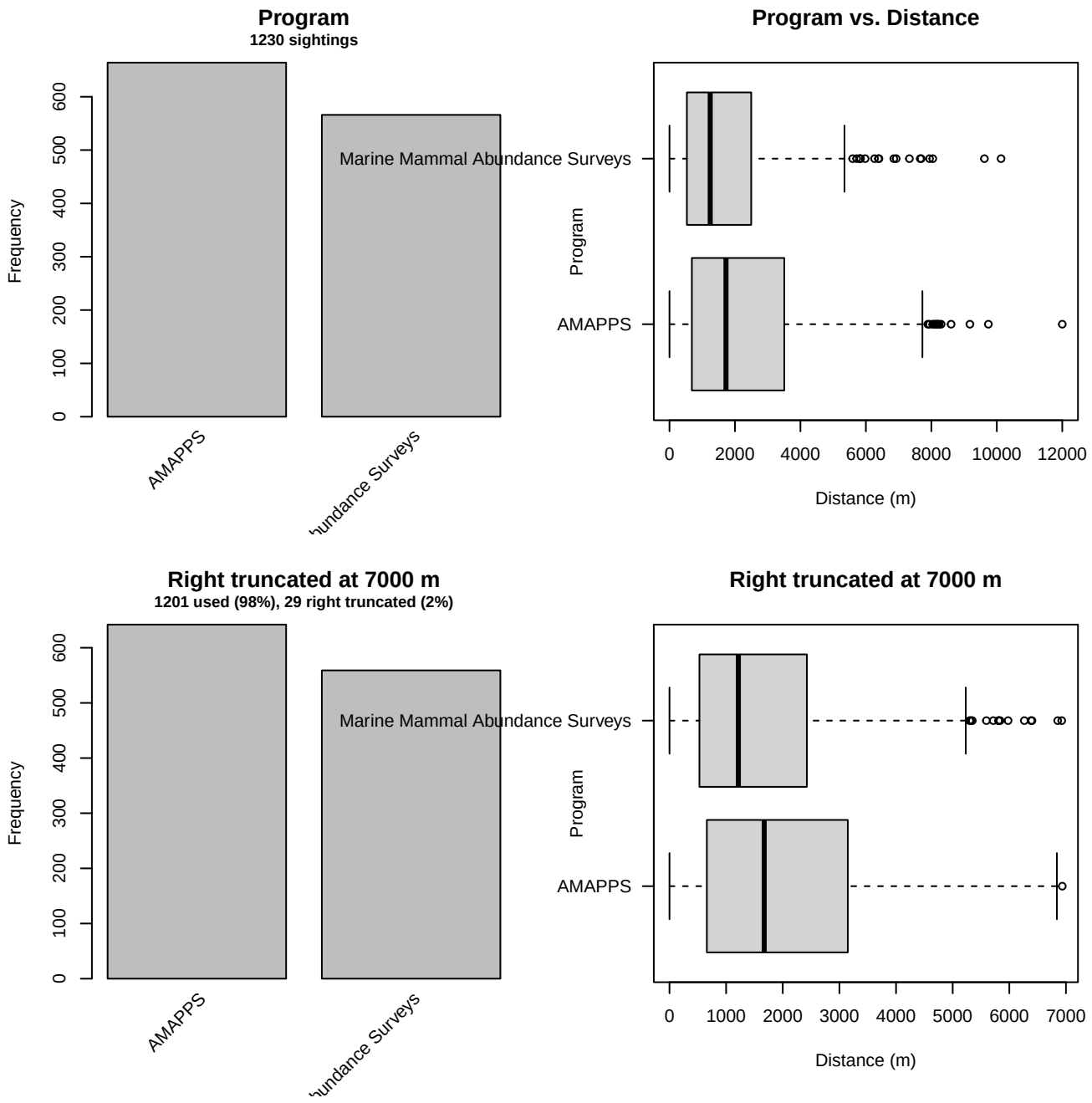

Figure 44: Distribution of the Program covariate before (top row) and after (bottom row) observations were truncated to fit the NEFSC detection function.

2.1.2.2 SEFSC

After right-truncating observations greater than 6000 m, we fitted the detection function to the 332 observations that remained (Table 15). The selected detection function (Figure 45) used a hazard rate key function with Beaufort (Figure 46), OriginalScientificName (Figure 47) and Program (Figure 48) as covariates.

Table 15: Observations used to fit the SEFSC detection function.

ScientificName	n
Balaenoptera borealis/edeni	3
Balaenoptera edeni	10
Balaenoptera physalus	17
Eubalaena glacialis	2
Megaptera novaeangliae	32
Physeter macrocephalus	268
Total	**332**

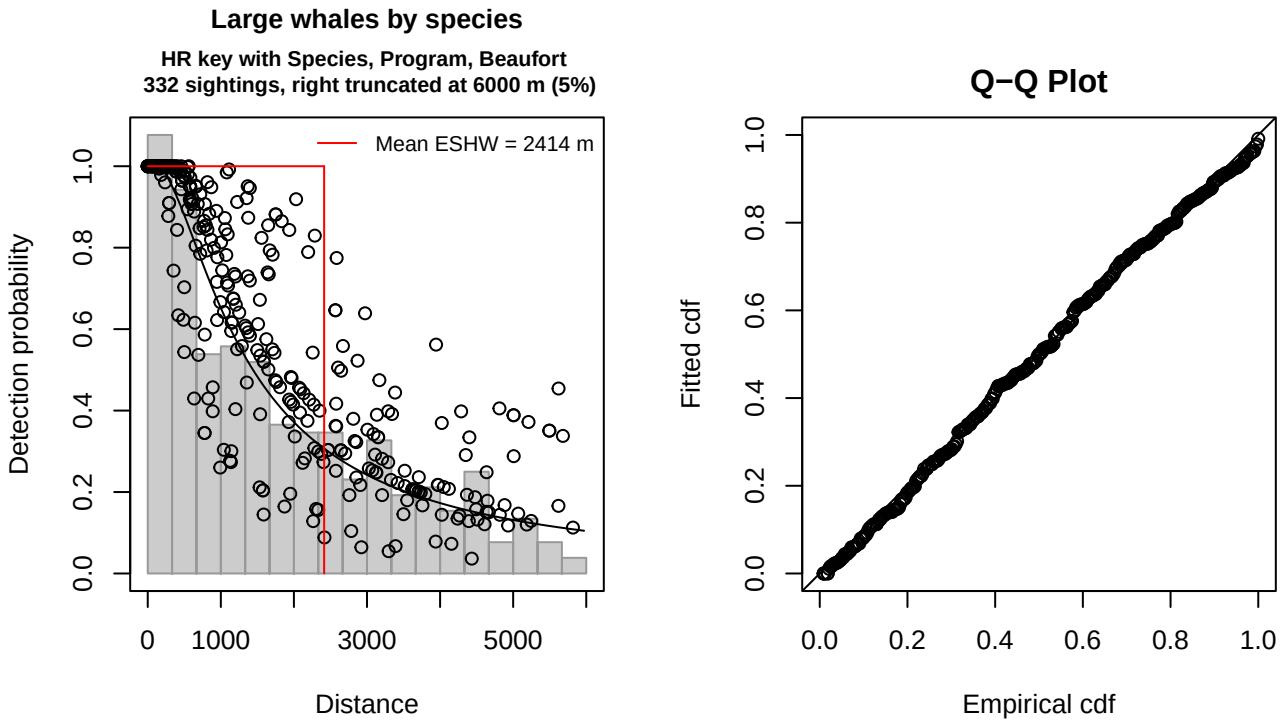

Figure 45: SEFSC detection function and Q-Q plot showing its goodness of fit.

Statistical output for this detection function:

```
Summary for ds object
Number of observations :  332
Distance range         :  0  -  6000
AIC                    :  5604.674

Detection function:
 Hazard-rate key function

Detection function parameters
Scale coefficient(s):
                              estimate        se
(Intercept)                  7.4794246 0.4929618
OriginalScientificNameSperm  0.7957413 0.3448895
ProgramAtlantic Pre-AMAPPS  -0.7295682 0.3154763
ProgramCaribbean            -0.7773443 0.4064337
Beaufort                    -0.1322436 0.1039800

Shape coefficient(s):
```

```
             estimate        se
(Intercept) 0.3345999 0.1370809

                        Estimate           SE        CV
Average p              0.3546416   0.03786854 0.1067797
N in covered region 936.1563072 108.72789053 0.1161429

Distance sampling Cramer-von Mises test (unweighted)
Test statistic = 0.055285  p = 0.843624
```

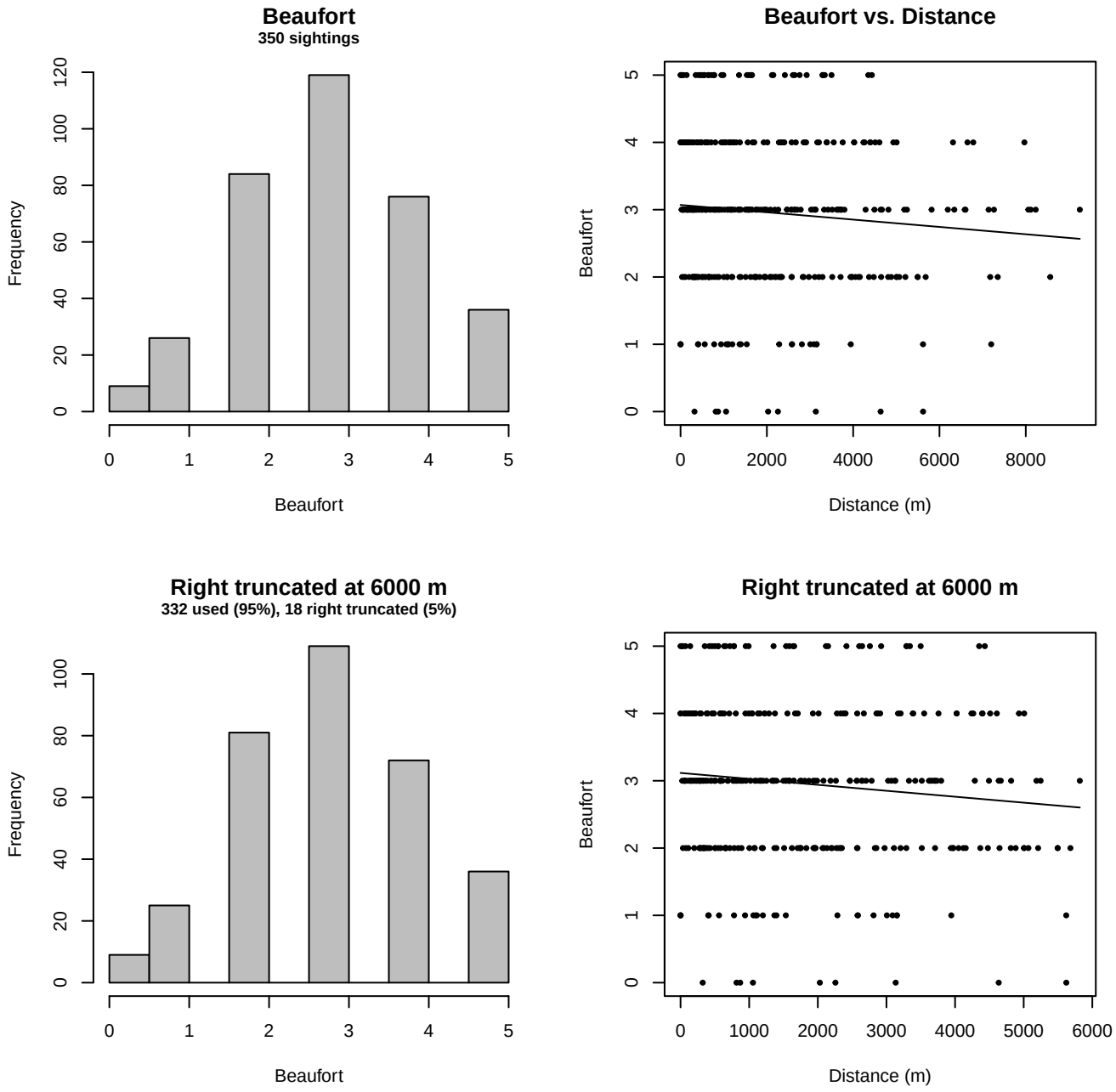

Figure 46: Distribution of the Beaufort covariate before (top row) and after (bottom row) observations were truncated to fit the SEFSC detection function.

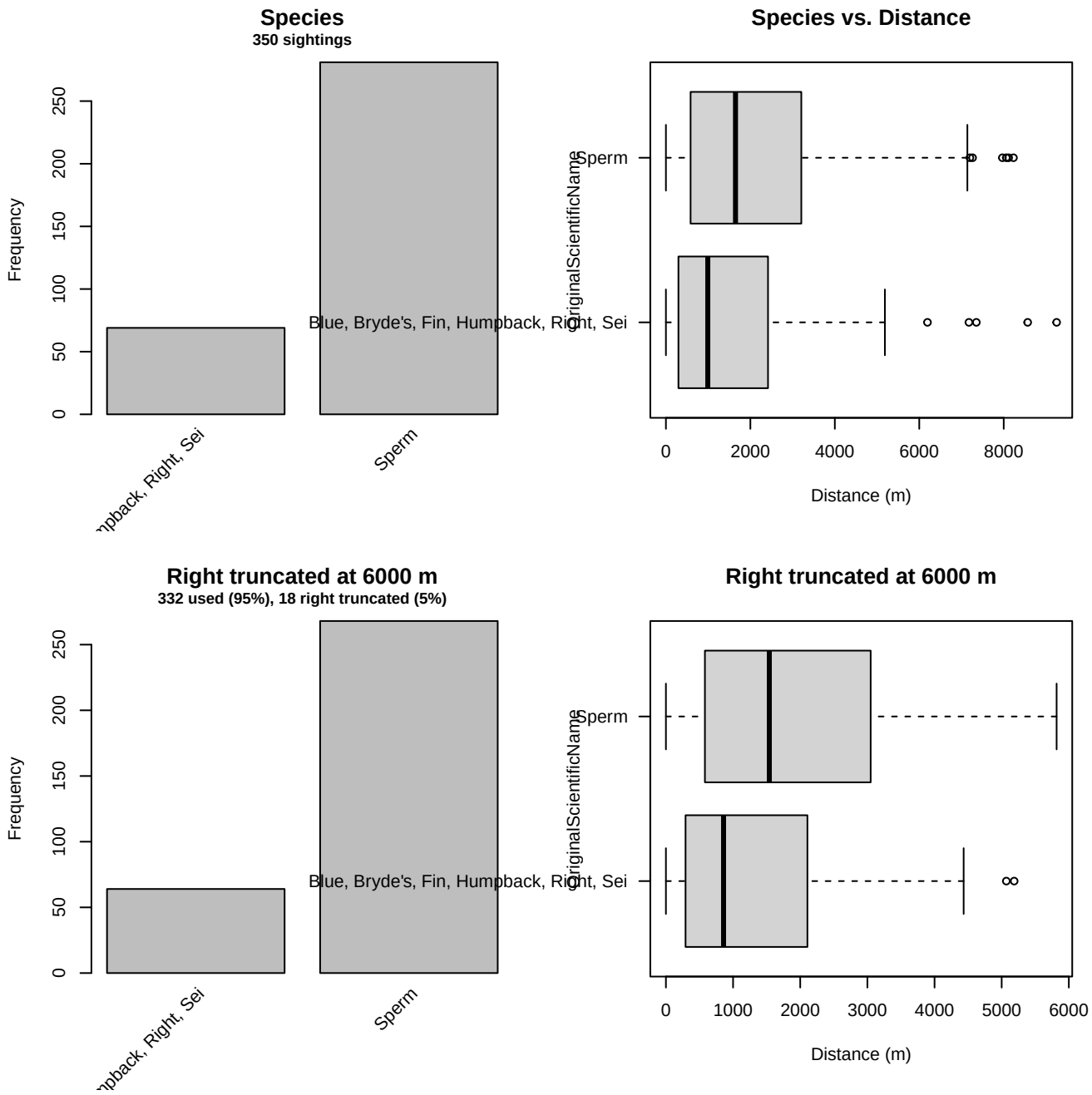

Figure 47: Distribution of the OriginalScientificName covariate before (top row) and after (bottom row) observations were truncated to fit the SEFSC detection function.

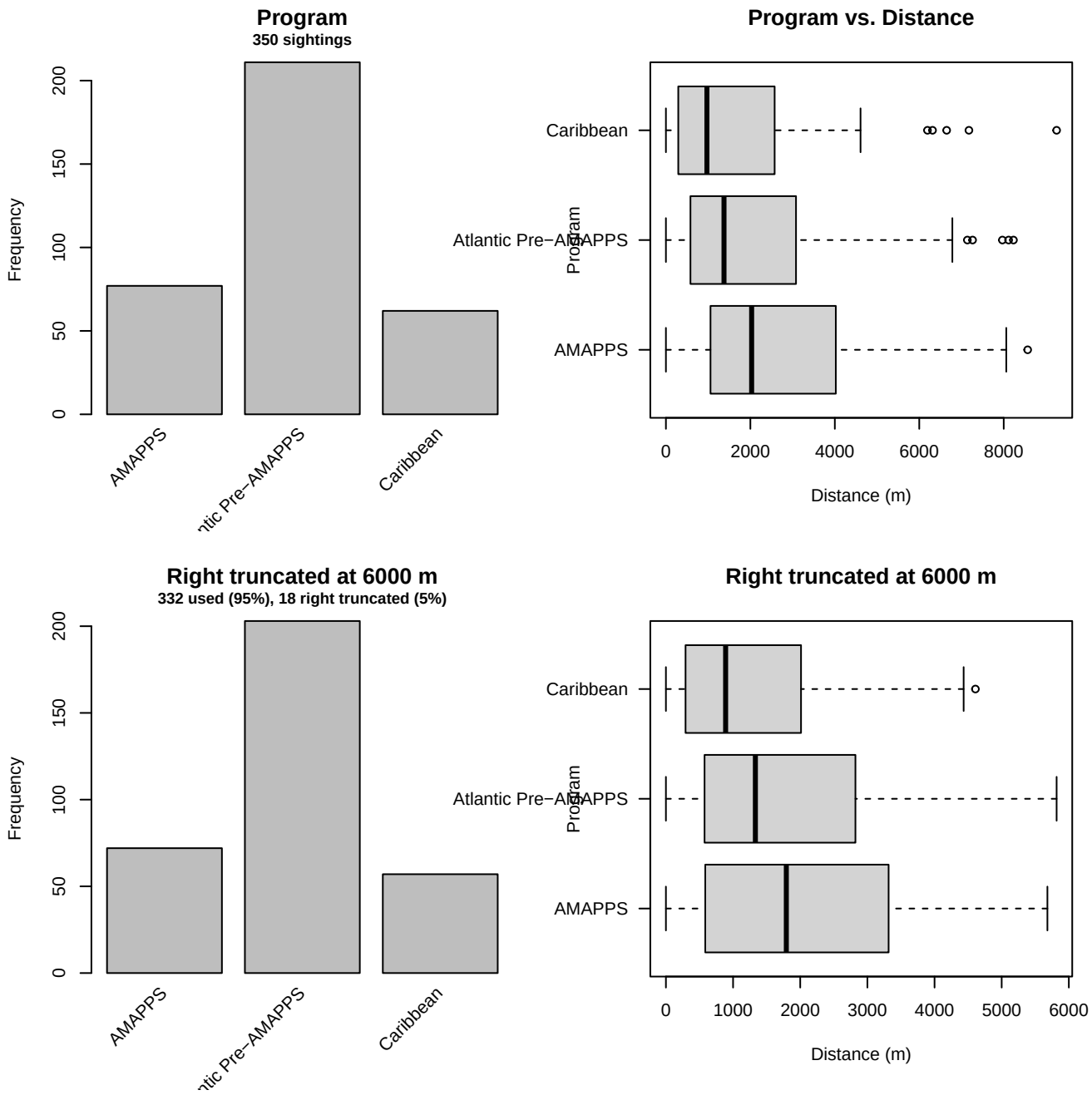

Figure 48: Distribution of the Program covariate before (top row) and after (bottom row) observations were truncated to fit the SEFSC detection function.

2.1.2.3 Binocular Surveys

After right-truncating observations greater than 5000 m, we fitted the detection function to the 1471 observations that remained (Table 16). The selected detection function (Figure 49) used a hazard rate key function with OriginalScientificName (Figure 50) and Program (Figure 51) as covariates.

Table 16: Observations used to fit the Binocular Surveys detection function.

ScientificName	n
Balaenoptera borealis	22
Balaenoptera borealis/edeni	3
Balaenoptera borealis/physalus	79
Balaenoptera edeni	8
Balaenoptera musculus	6
Balaenoptera physalus	308
Eubalaena glacialis	55
Megaptera novaeangliae	307
Physeter macrocephalus	683
Total	**1471**

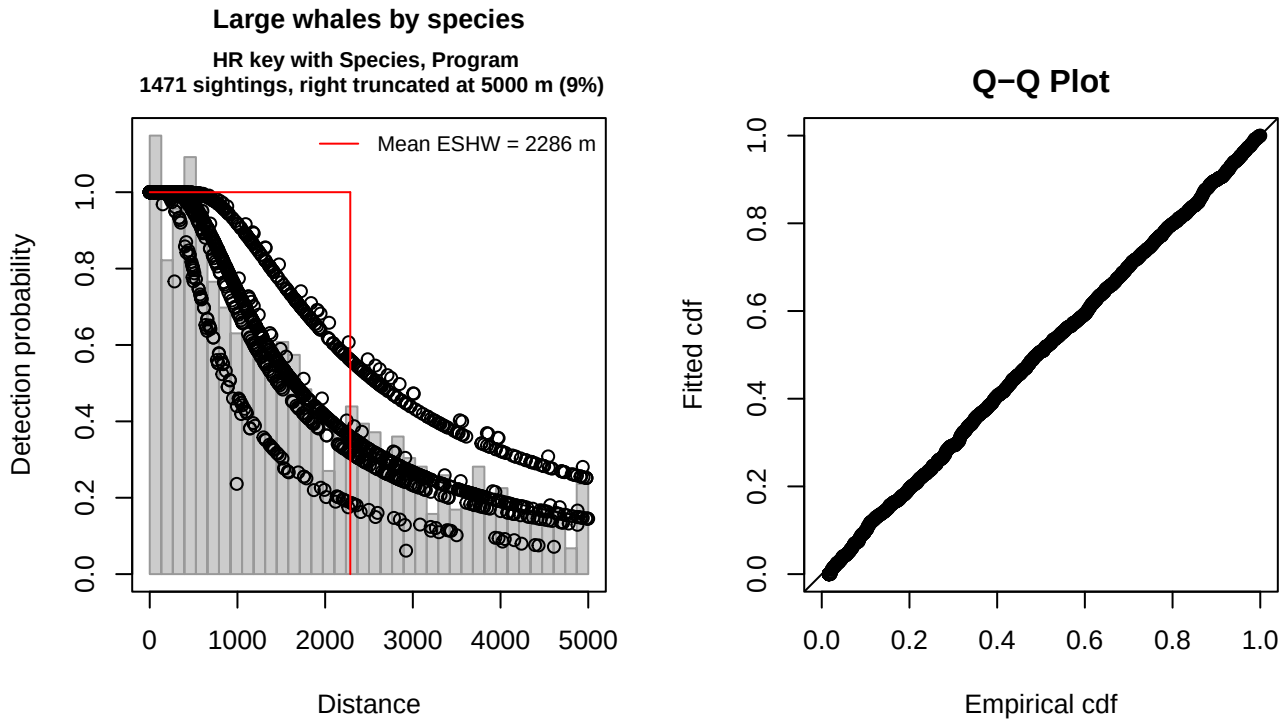

Figure 49: Binocular Surveys detection function and Q-Q plot showing its goodness of fit.

Statistical output for this detection function:

```
Summary for ds object
Number of observations :  1471
Distance range         :  0  -  5000
AIC                    :  24498.15

Detection function:
 Hazard-rate key function

Detection function parameters
Scale coefficient(s):
                                              estimate        se
(Intercept)                                  7.0154074 0.1387774
OriginalScientificNameHumpback, Sperm        0.5736762 0.1427682
OriginalScientificNameUnid. Bryde's, fin, or sei  0.6607853 0.2833819
ProgramAtlantic Pre-AMAPPS                  -0.4551133 0.1309943
```

```
ProgramCaribbean                                -1.0944245 0.3017296

Shape coefficient(s):
             estimate        se
(Intercept) 0.2925203 0.0742023

                          Estimate           SE         CV
Average p                0.4357633   0.02101424 0.04822398
N in covered region 3375.6858719 176.17568539 0.05218960

Distance sampling Cramer-von Mises test (unweighted)
Test statistic = 0.043159  p = 0.916226
```

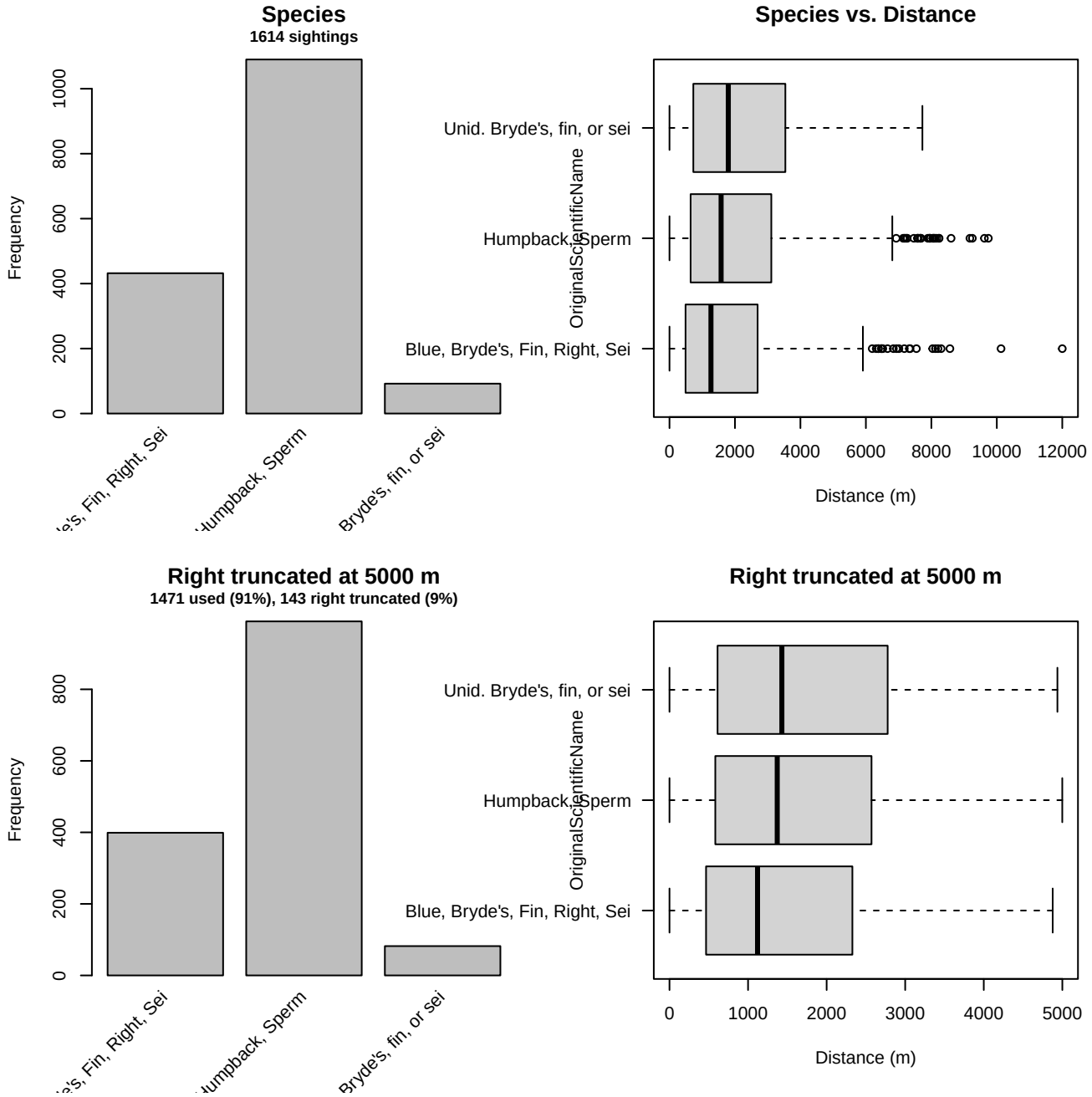

Figure 50: Distribution of the OriginalScientificName covariate before (top row) and after (bottom row) observations were truncated to fit the Binocular Surveys detection function.

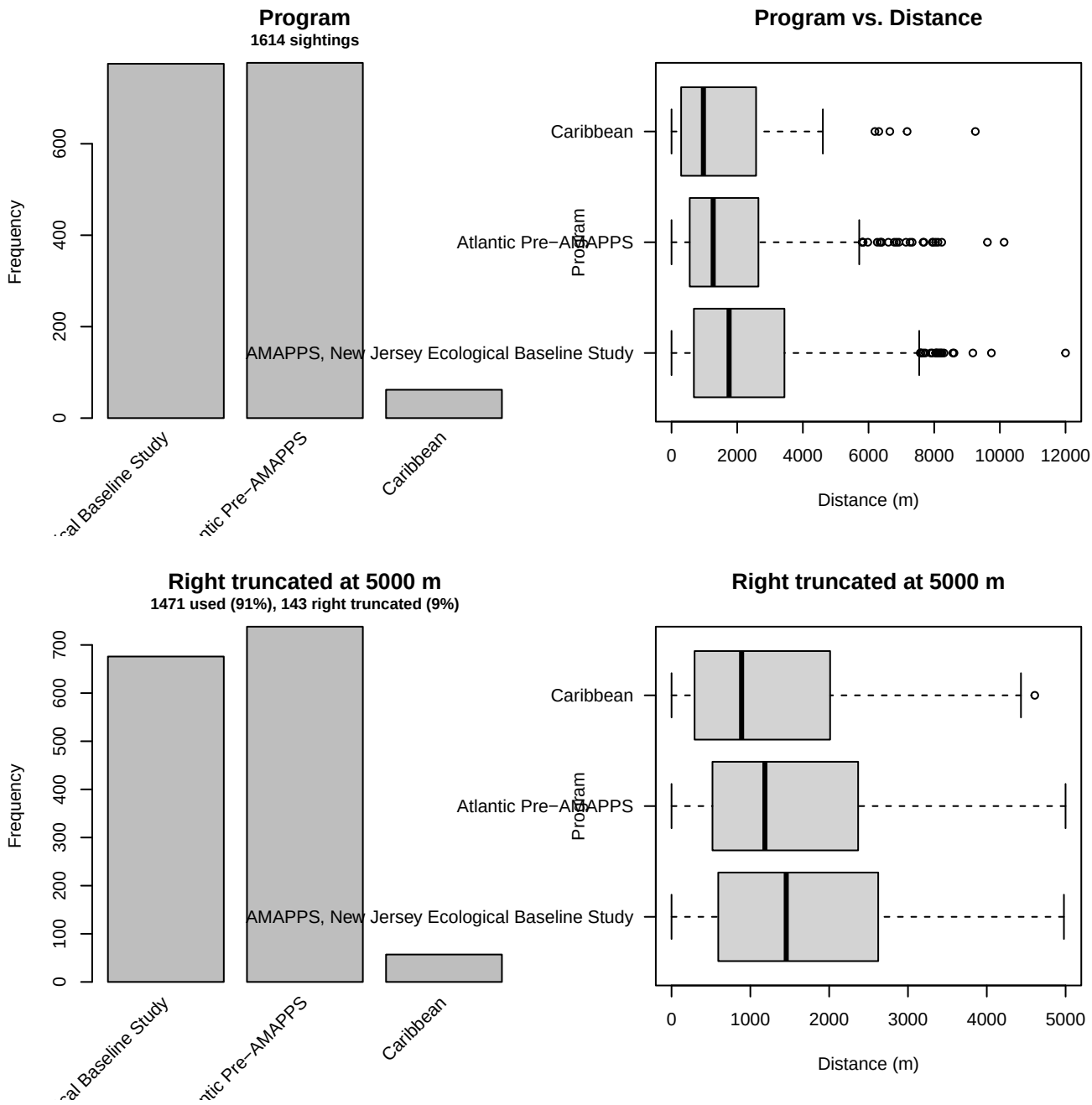

Figure 51: Distribution of the Program covariate before (top row) and after (bottom row) observations were truncated to fit the Binocular Surveys detection function.

2.1.2.4 Song of the Whale

After right-truncating observations greater than 3000 m, we fitted the detection function to the 239 observations that remained (Table 17). The selected detection function (Figure 52) used a hazard rate key function with Glare (Figure 53), OriginalScientificName (Figure 54) and WeatherCode (Figure 55) as covariates.

Table 17: Observations used to fit the Song of the Whale detection function.

ScientificName	n
Balaenoptera borealis	13
Balaenoptera edeni	7
Balaenoptera musculus	8
Balaenoptera physalus	27
Megaptera novaeangliae	69
Physeter macrocephalus	115
Total	**239**

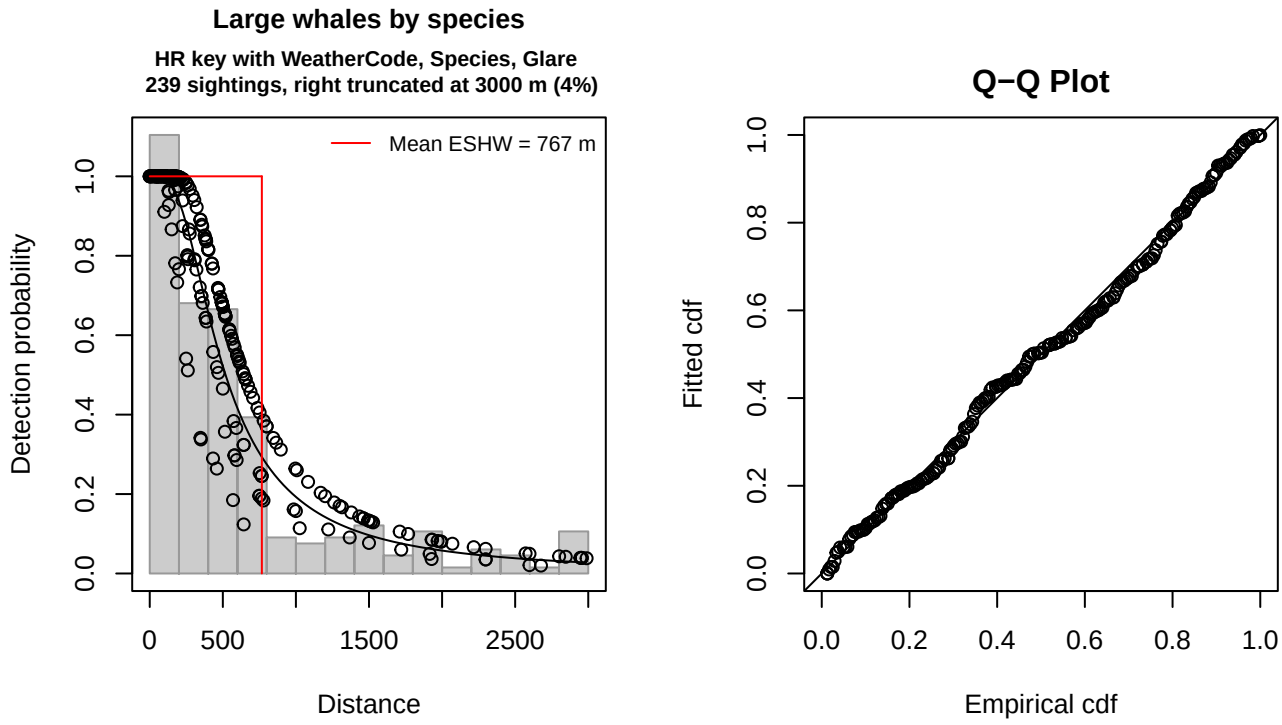

Figure 52: Song of the Whale detection function and Q-Q plot showing its goodness of fit.

Statistical output for this detection function:

```
Summary for ds object
Number of observations :  239
Distance range         :  0  -  3000
AIC                    :  3547.931

Detection function:
 Hazard-rate key function

Detection function parameters
Scale coefficient(s):
                                     estimate        se
(Intercept)                         5.9647631 0.2274130
WeatherCodeHaze                    -0.8889445 0.5747918
OriginalScientificNameHumpback, Sperm  0.3084029 0.2238350
GlareSevere                        -0.4670165 0.2579856

Shape coefficient(s):
             estimate         se
```

```
(Intercept) 0.6276528 0.09675212

                        Estimate           SE       CV
Average p               0.2409962   0.02414927 0.100206
N in covered region 991.7170380 114.27753421 0.115232

Distance sampling Cramer-von Mises test (unweighted)
Test statistic = 0.073160  p = 0.732317
```

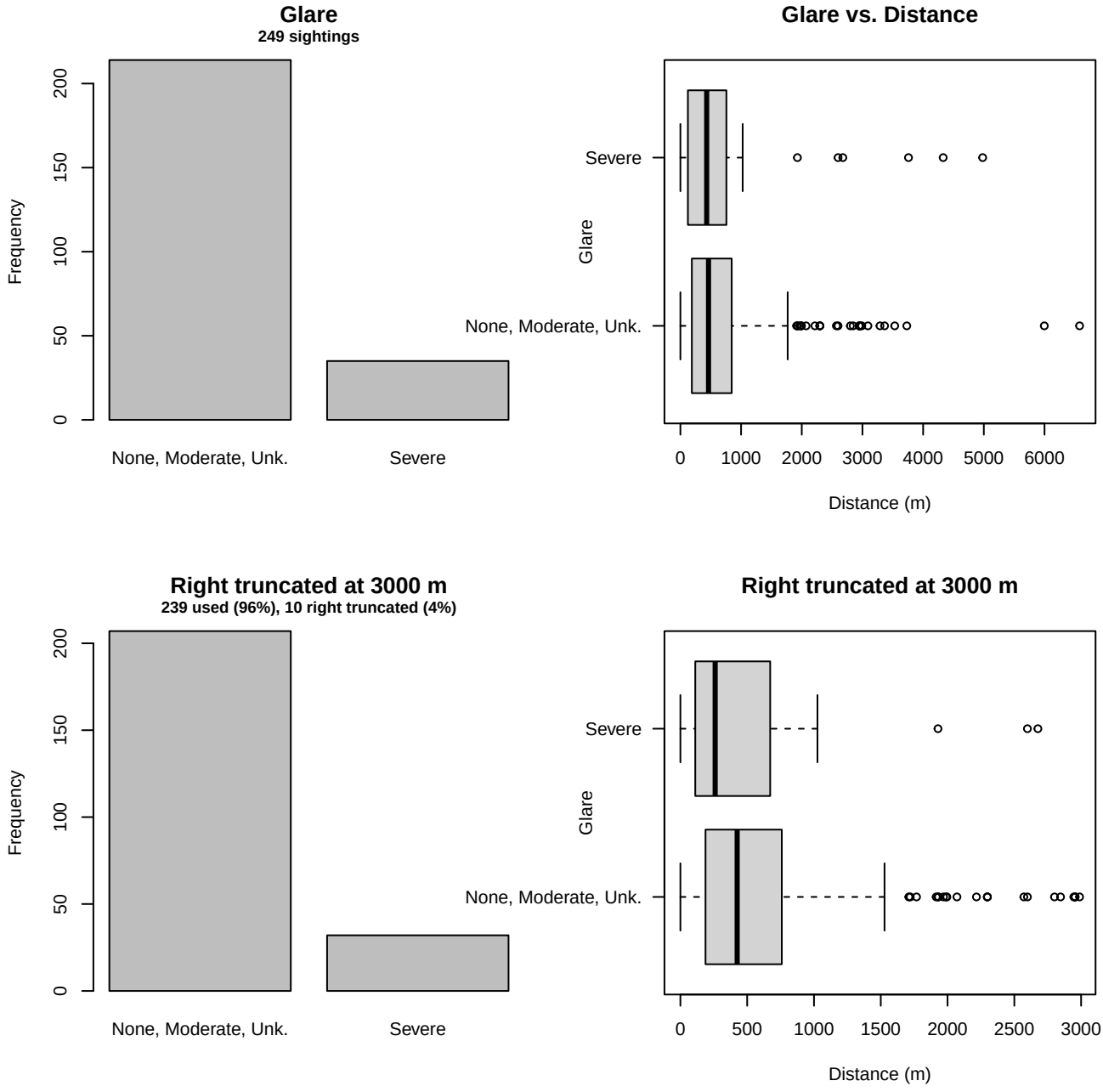

Figure 53: Distribution of the Glare covariate before (top row) and after (bottom row) observations were truncated to fit the Song of the Whale detection function.

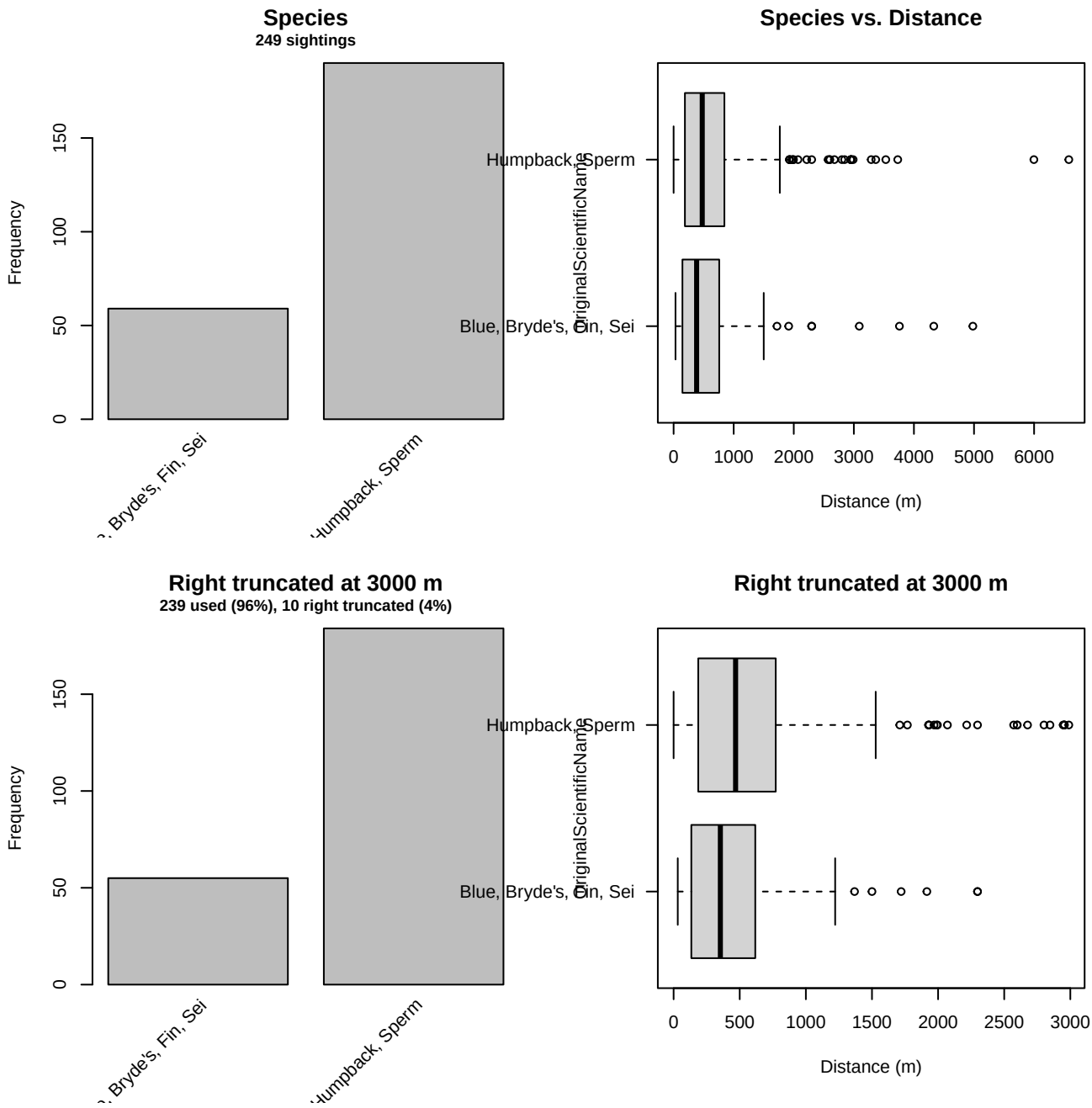

Figure 54: Distribution of the OriginalScientificName covariate before (top row) and after (bottom row) observations were truncated to fit the Song of the Whale detection function.

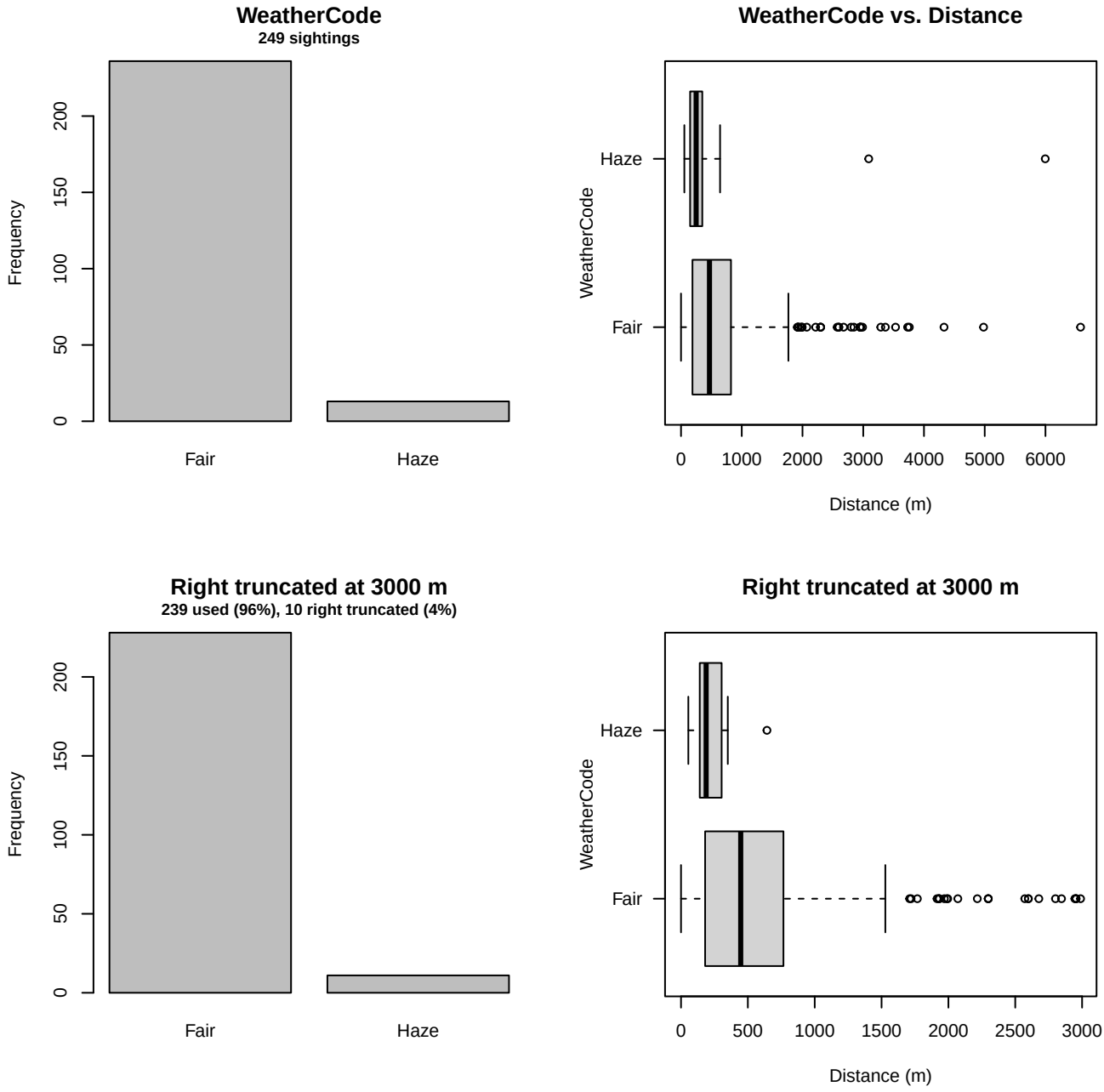

Figure 55: Distribution of the WeatherCode covariate before (top row) and after (bottom row) observations were truncated to fit the Song of the Whale detection function.

2.2 Without a Taxonomic Covariate

We fitted the detection functions in this section to pools of species with similar detectability characteristics but could not use a taxonomic identification as a covariate to account for differences between them. We usually took this approach after trying the taxonomic covariate and finding it had insufficient statistical power to be retained. We also resorted to it when the focal taxon being modeled had too few observations to be allocated its own taxonomic covariate level and was too poorly known for us to confidently determine which other taxa we could group it with.

2.2.1 Aerial Surveys

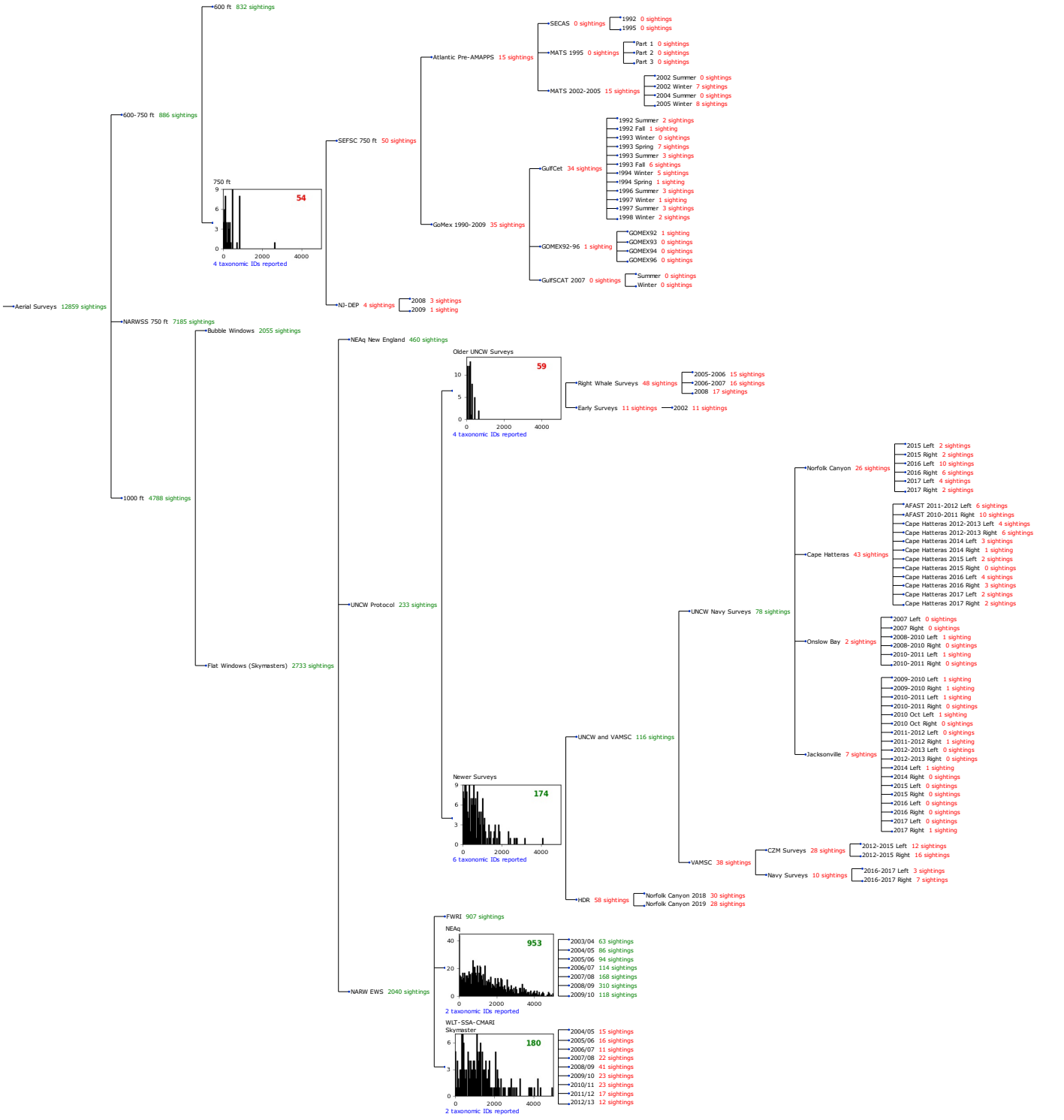

Figure 56: Detection hierarchy for aerial surveys, showing how they were pooled during detectability modeling, for detection functions that pooled multiple taxa but could not use a taxonomic covariate to account for differences between them. Each histogram represents a detection function and summarizes the perpendicular distances of observations that were pooled to fit it, prior to truncation. Observation counts, also prior to truncation, are shown in green when they met the recommendation of Buckland et al. (2001) that detection functions utilize at least 60 sightings, and red otherwise. For rare taxa, it was not always possible to meet this recommendation, yielding higher statistical uncertainty. During the spatial modeling stage of the analysis, effective strip widths were computed for each survey using the closest detection function above it in the hierarchy (i.e. moving from right to left in the figure). Surveys that do not have a detection function above them in this figure were either addressed by a detection function presented in a different section of this report, or were omitted from the analysis.

2.2.1.1 750 ft

After right-truncating observations greater than 1297 m, we fitted the detection function to the 53 observations that remained (Table 18). The selected detection function (Figure 57) used a hazard rate key function with no covariates.

Table 18: Observations used to fit the 750 ft detection function.

ScientificName	n
Balaenoptera physalus	8
Eubalaena glacialis	5
Megaptera novaeangliae	7
Physeter macrocephalus	33
Total	**53**

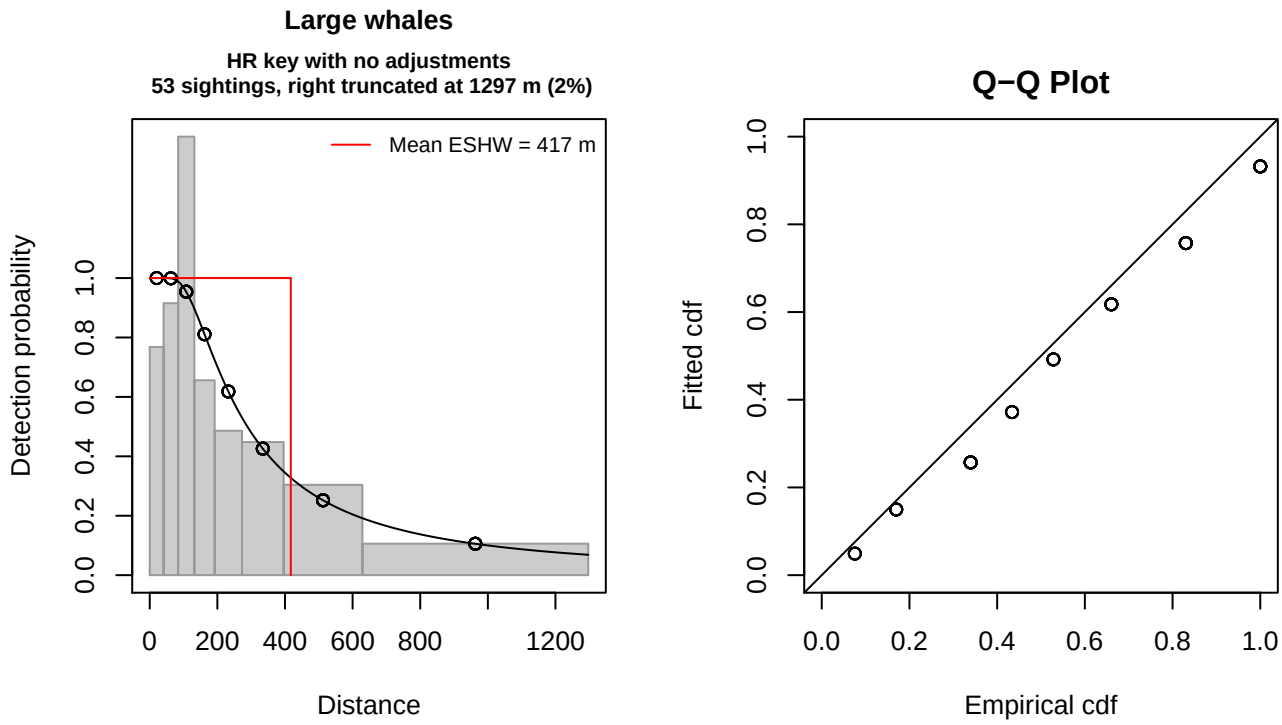

Figure 57: 750 ft detection function and Q-Q plot showing its goodness of fit.

Statistical output for this detection function:

```
Summary for ds object
Number of observations :  53
Distance range         :  0  -  1297
AIC                    :  222.2921

Detection function:
 Hazard-rate key function

Detection function parameters
Scale coefficient(s):
            estimate       se
(Intercept) 5.423929 0.4460729

Shape coefficient(s):
             estimate       se
```

```
(Intercept) 0.4163623 0.3128171

                      Estimate          SE        CV
Average p             0.321688  0.07665669 0.2382951
N in covered region 164.755912 43.46025892 0.2637857

Distance sampling Cramer-von Mises test (unweighted)
Test statistic = 0.101698  p = 0.576612
```

2.2.1.2 Older UNCW Surveys

After right-truncating observations greater than 838 m, we fitted the detection function to the 59 observations that remained (Table 19). The selected detection function (Figure 58) used a hazard rate key function with Beaufort (Figure 59) as a covariate.

Table 19: Observations used to fit the Older UNCW Surveys detection function.

ScientificName	n
Balaenoptera physalus	13
Eubalaena glacialis	24
Megaptera novaeangliae	13
Physeter macrocephalus	9
Total	**59**

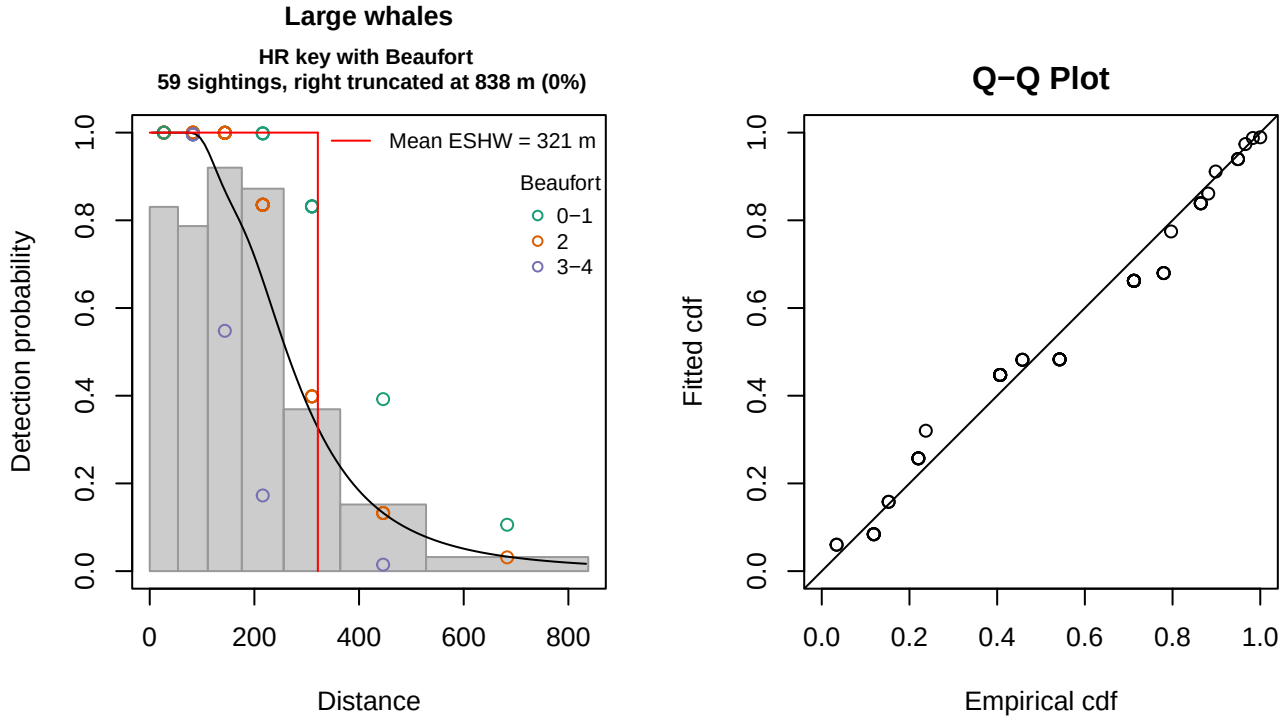

Figure 58: Older UNCW Surveys detection function and Q-Q plot showing its goodness of fit.

Statistical output for this detection function:

```
Summary for ds object
Number of observations :  59
Distance range         :  0  -  838
AIC                    :  218.1082
```

```
Detection function:
 Hazard-rate key function

Detection function parameters
Scale coefficient(s):
              estimate        se
(Intercept)  5.9013957 0.2950158
Beaufort2   -0.3578033 0.3134356
Beaufort3-4 -1.0008354 0.3877033

Shape coefficient(s):
            estimate        se
(Intercept) 1.254247 0.2627137

                       Estimate          SE        CV
Average p              0.3508662  0.04814793 0.1372259
N in covered region 168.1552636 29.31126242 0.1743107

Distance sampling Cramer-von Mises test (unweighted)
Test statistic = 0.291522  p = 0.142842
```

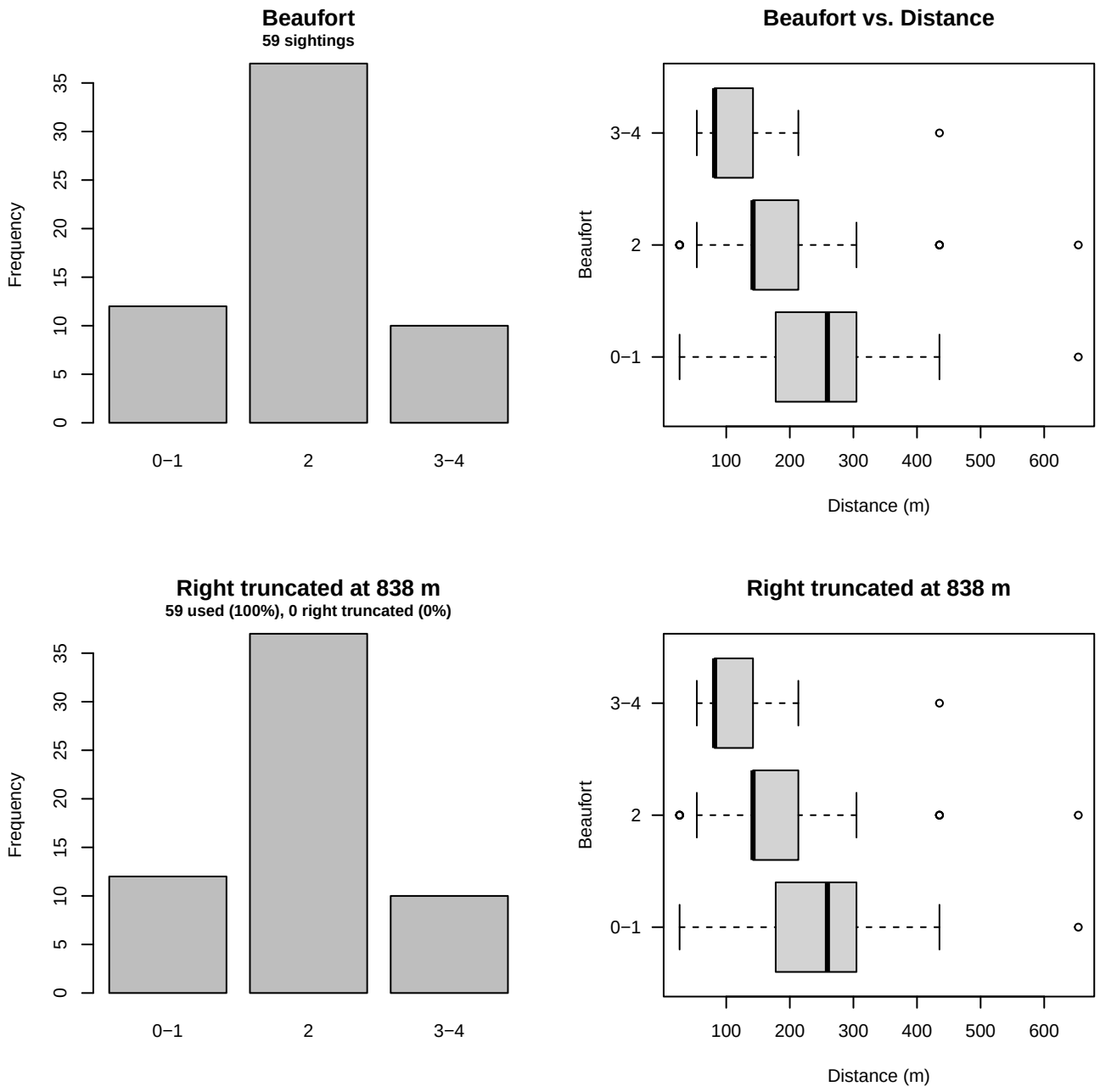

Figure 59: Distribution of the Beaufort covariate before (top row) and after (bottom row) observations were truncated to fit the Older UNCW Surveys detection function.

2.2.1.3 Newer Surveys

After right-truncating observations greater than 2000 m, we fitted the detection function to the 164 observations that remained (Table 20). The selected detection function (Figure 60) used a half normal key function with Beaufort (Figure 61) as a covariate.

Table 20: Observations used to fit the Newer Surveys detection function.

ScientificName	n
Balaenoptera borealis	3
Balaenoptera musculus	1
Balaenoptera physalus	48
Eubalaena glacialis	11
Megaptera novaeangliae	40
Physeter macrocephalus	61
Total	**164**

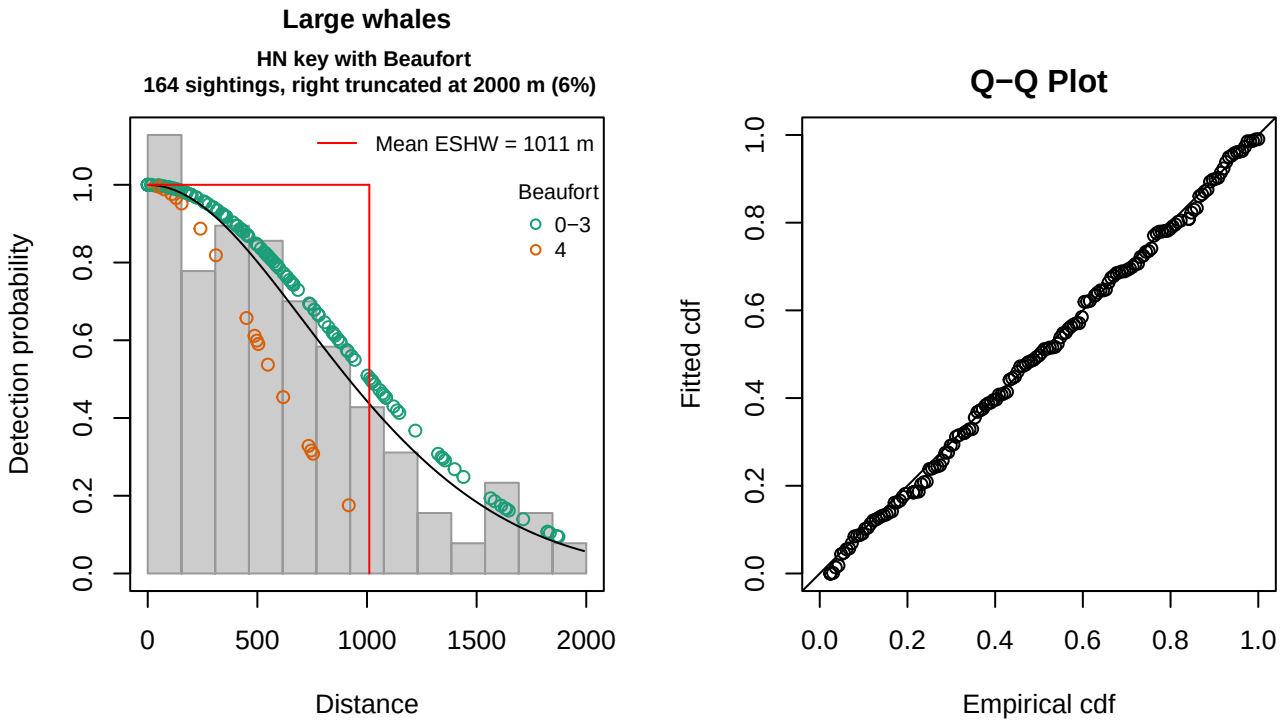

Figure 60: Newer Surveys detection function and Q-Q plot showing its goodness of fit.

Statistical output for this detection function:

```
Summary for ds object
Number of observations :  164
Distance range         :  0  -  2000
AIC                    :  2414.311

Detection function:
 Half-normal key function

Detection function parameters
Scale coefficient(s):
              estimate         se
(Intercept)  6.7601346 0.07305226
Beaufort4   -0.5625984 0.24677736

                       Estimate          SE         CV
Average p             0.4908118  0.03341248 0.06807595
N in covered region 334.1403290 29.56205574 0.08847198
```

```
Distance sampling Cramer-von Mises test (unweighted)
Test statistic = 0.025201  p = 0.989164
```

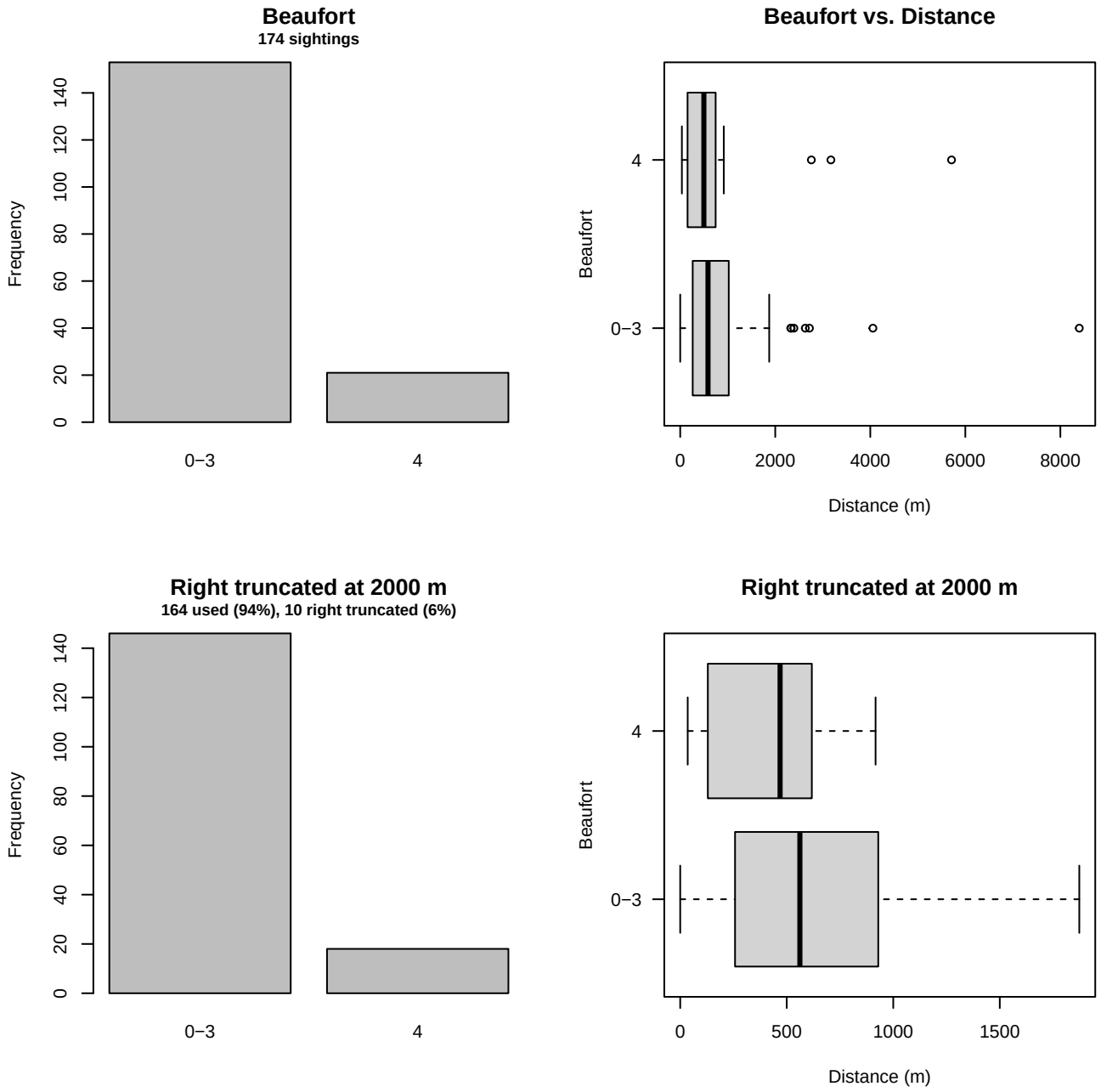

Figure 61: Distribution of the Beaufort covariate before (top row) and after (bottom row) observations were truncated to fit the Newer Surveys detection function.

2.2.1.4 NARW EWS NEAq

After right-truncating observations greater than 6000 m, we fitted the detection function to the 934 observations that remained (Table 21). The selected detection function (Figure 62) used a hazard rate key function with Beaufort (Figure 63) and Clouds (Figure 64) as covariates.

Table 21: Observations used to fit the NARW EWS NEAq detection function.

ScientificName	n
Eubalaena glacialis	926
Megaptera novaeangliae	8
Total	**934**

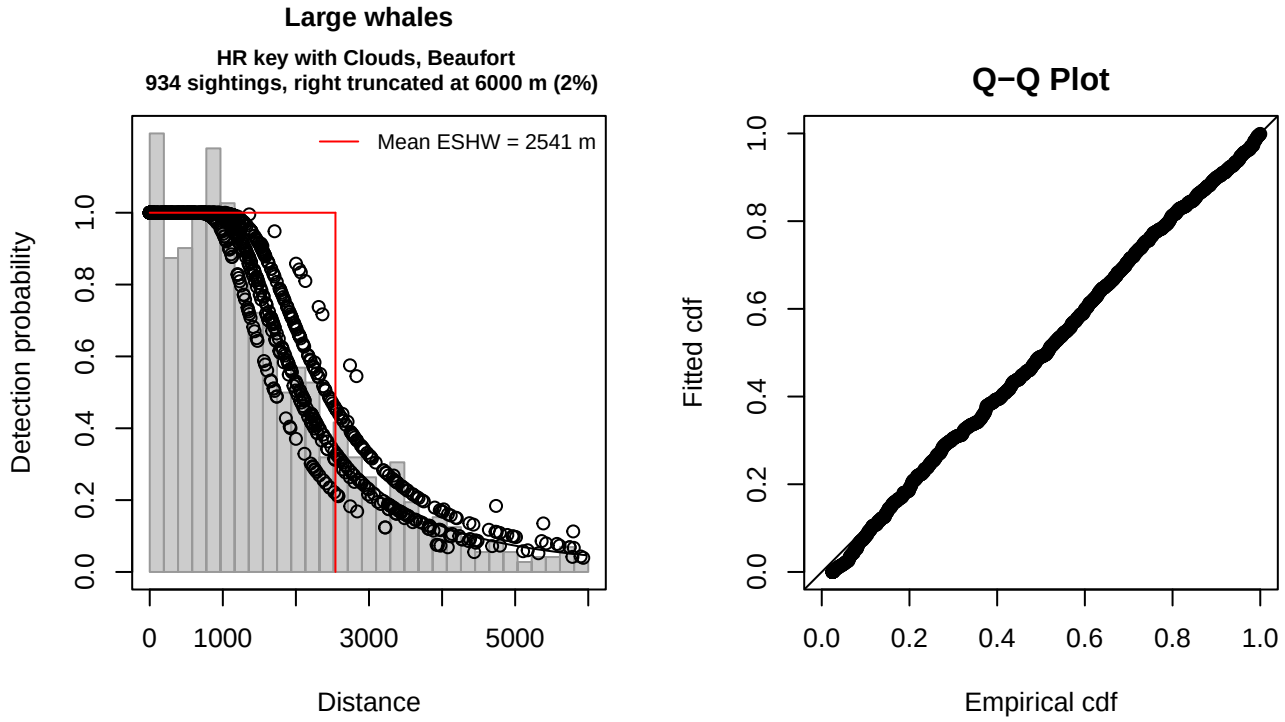

Figure 62: NARW EWS NEAq detection function and Q-Q plot showing its goodness of fit.

Statistical output for this detection function:

```
Summary for ds object
Number of observations :  934
Distance range         :  0  -  6000
AIC                    :  15524.75

Detection function:
 Hazard-rate key function

Detection function parameters
Scale coefficient(s):
                          estimate         se
(Intercept)             7.6701972 0.17405326
CloudsClear, Scattered  0.1864541 0.07305143
Beaufort2              -0.2057395 0.17022085
Beaufort3              -0.3624490 0.17179925

Shape coefficient(s):
             estimate         se
(Intercept) 0.9658338 0.07647527

                         Estimate          SE         CV
Average p               0.4179295  0.01432625 0.03427910
```

```
N in covered region 2234.8268471 94.92666572 0.04247607

Distance sampling Cramer-von Mises test (unweighted)
Test statistic = 0.110435  p = 0.536101
```

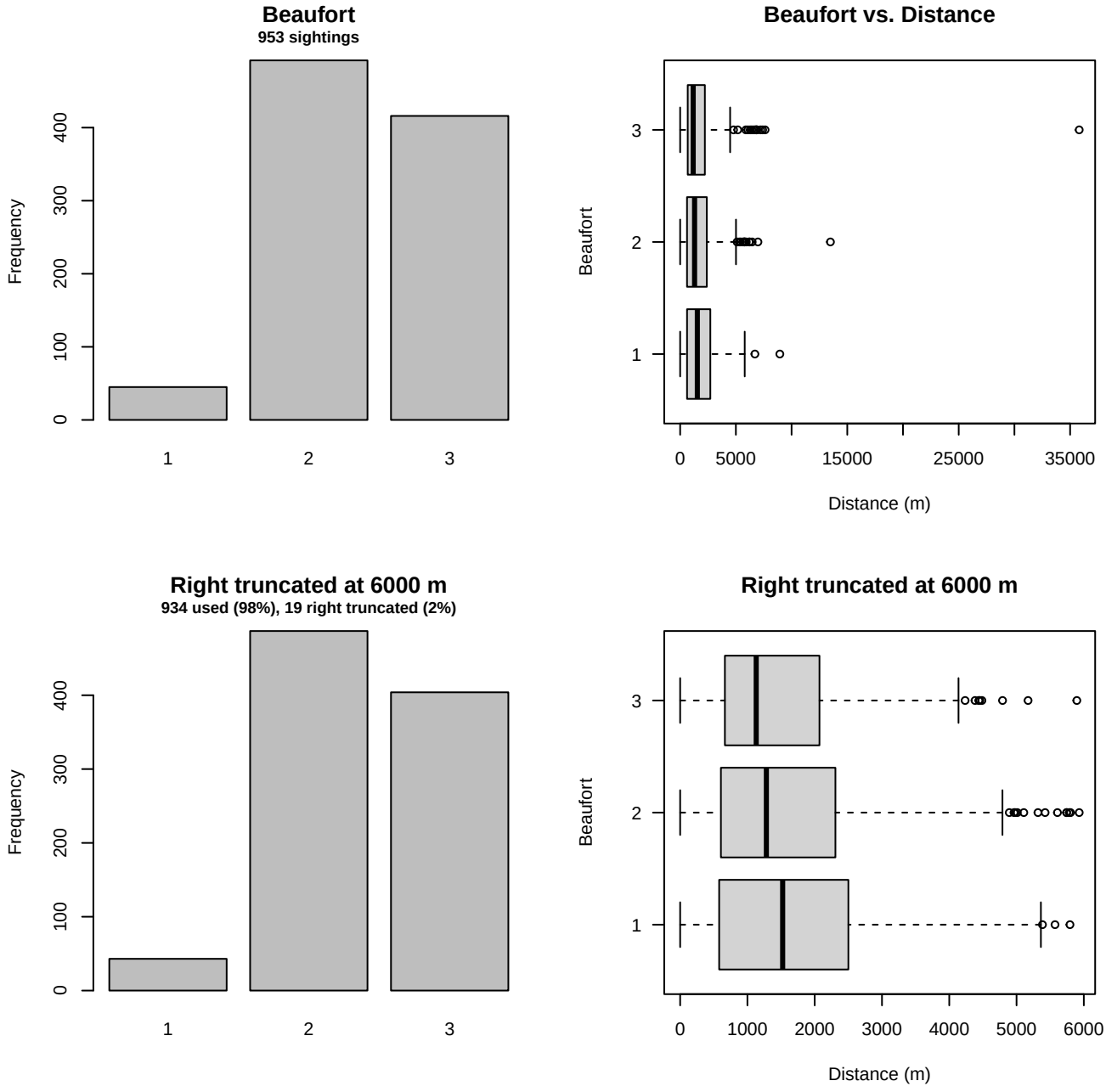

Figure 63: Distribution of the Beaufort covariate before (top row) and after (bottom row) observations were truncated to fit the NARW EWS NEAq detection function.

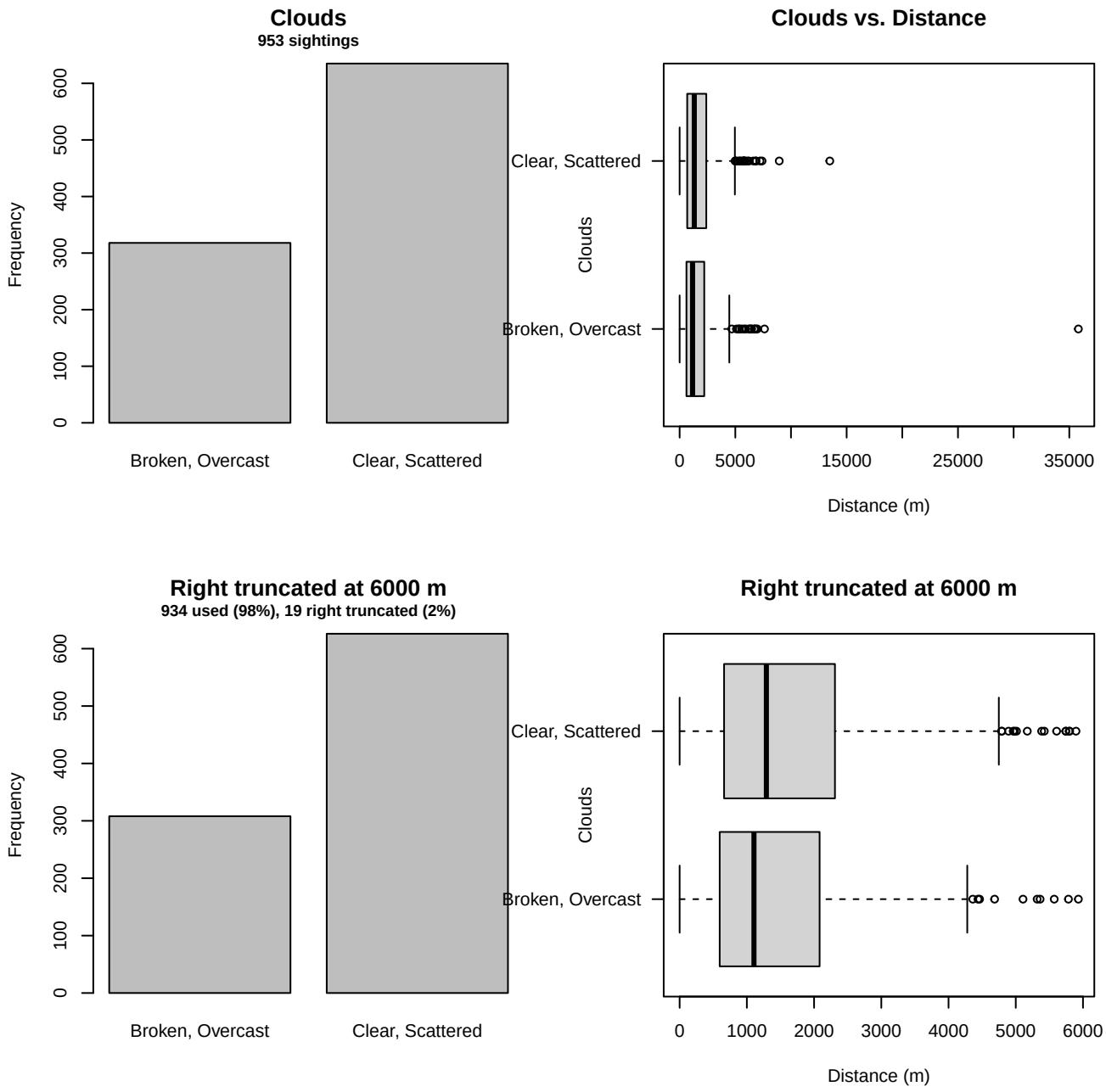

Figure 64: Distribution of the Clouds covariate before (top row) and after (bottom row) observations were truncated to fit the NARW EWS NEAq detection function.

2.2.1.5 NARW EWS WLT-SSA-CMARI Skymaster

After right-truncating observations greater than 5000 m, we fitted the detection function to the 178 observations that remained (Table 22). The selected detection function (Figure 65) used a hazard rate key function with Beaufort (Figure 66) and Glare (Figure 67) as covariates.

Table 22: Observations used to fit the NARW EWS WLT-SSA-CMARI Skymaster detection function.

ScientificName	n
Eubalaena glacialis	173
Megaptera novaeangliae	5
Total	**178**

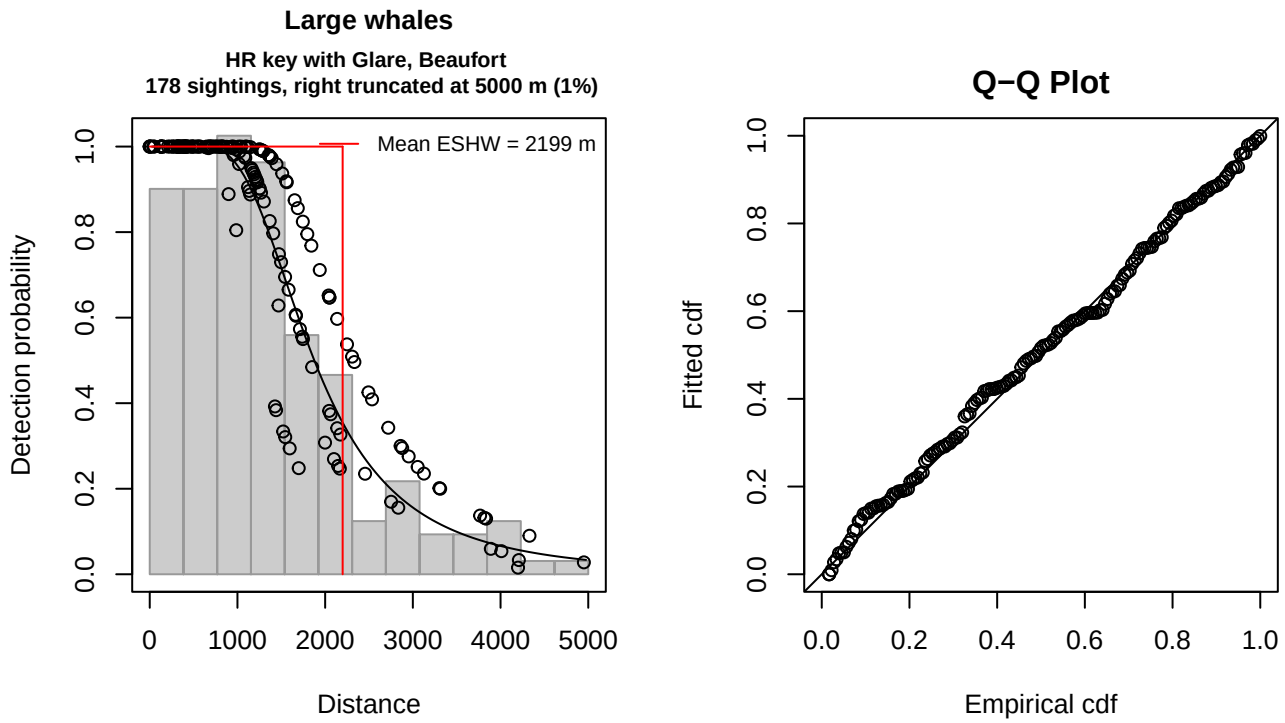

Figure 65: NARW EWS WLT-SSA-CMARI Skymaster detection function and Q-Q plot showing its goodness of fit.

Statistical output for this detection function:

```
Summary for ds object
Number of observations :  178
Distance range         :  0  -  5000
AIC                    :  2886.593

Detection function:
 Hazard-rate key function

Detection function parameters
Scale coefficient(s):
                          estimate        se
(Intercept)              7.6375650 0.1162523
GlareNone, Slight, unk. -0.2420370 0.1356639
Beaufort3               -0.3488458 0.1522188

Shape coefficient(s):
            estimate        se
(Intercept) 1.165805 0.1559101

                       Estimate          SE         CV
Average p             0.4254368  0.02984966 0.07016239
N in covered region 418.3935421 37.96073795 0.09072974

Distance sampling Cramer-von Mises test (unweighted)
Test statistic = 0.067115  p = 0.769384
```

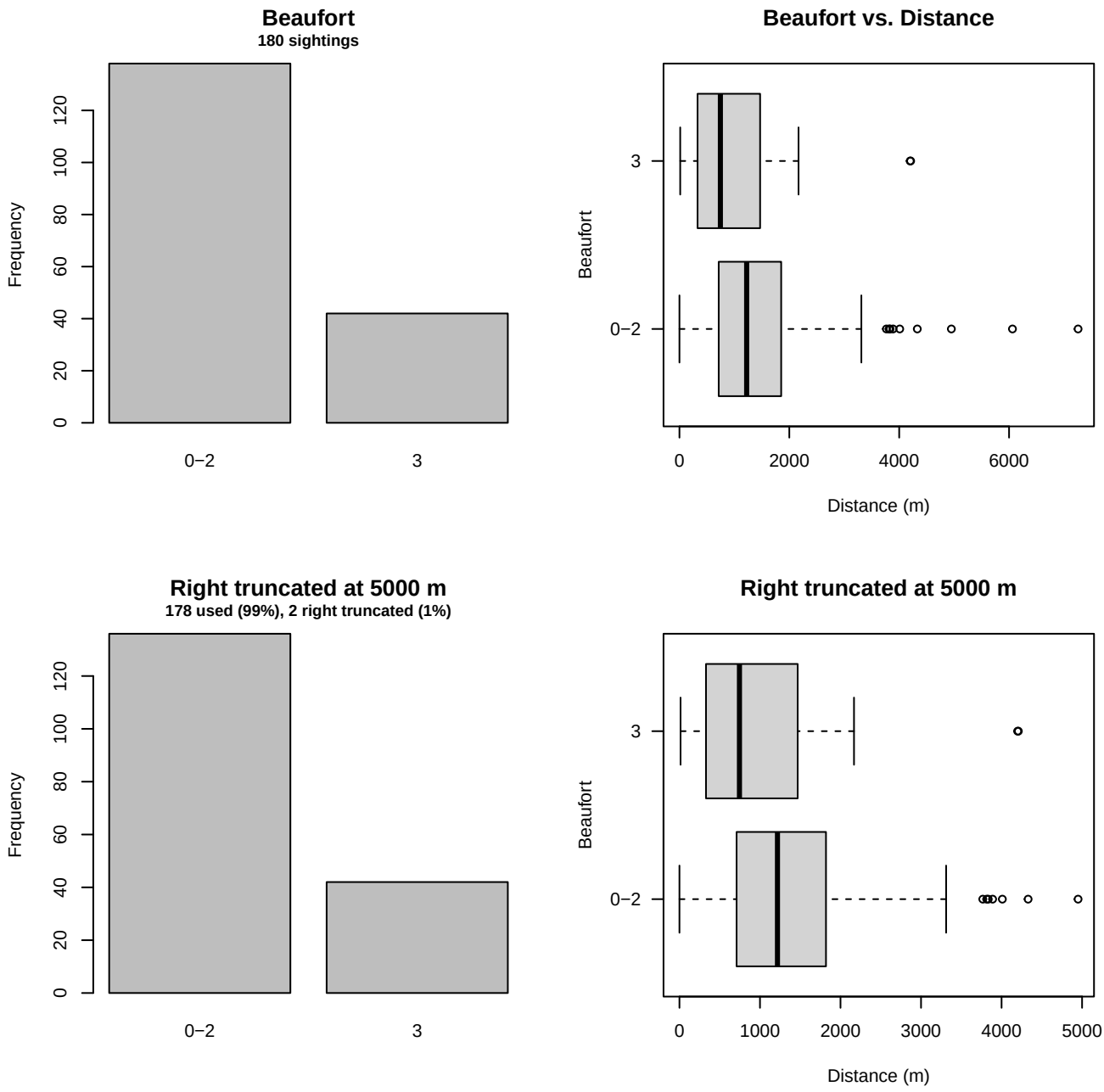

Figure 66: Distribution of the Beaufort covariate before (top row) and after (bottom row) observations were truncated to fit the NARW EWS WLT-SSA-CMARI Skymaster detection function.

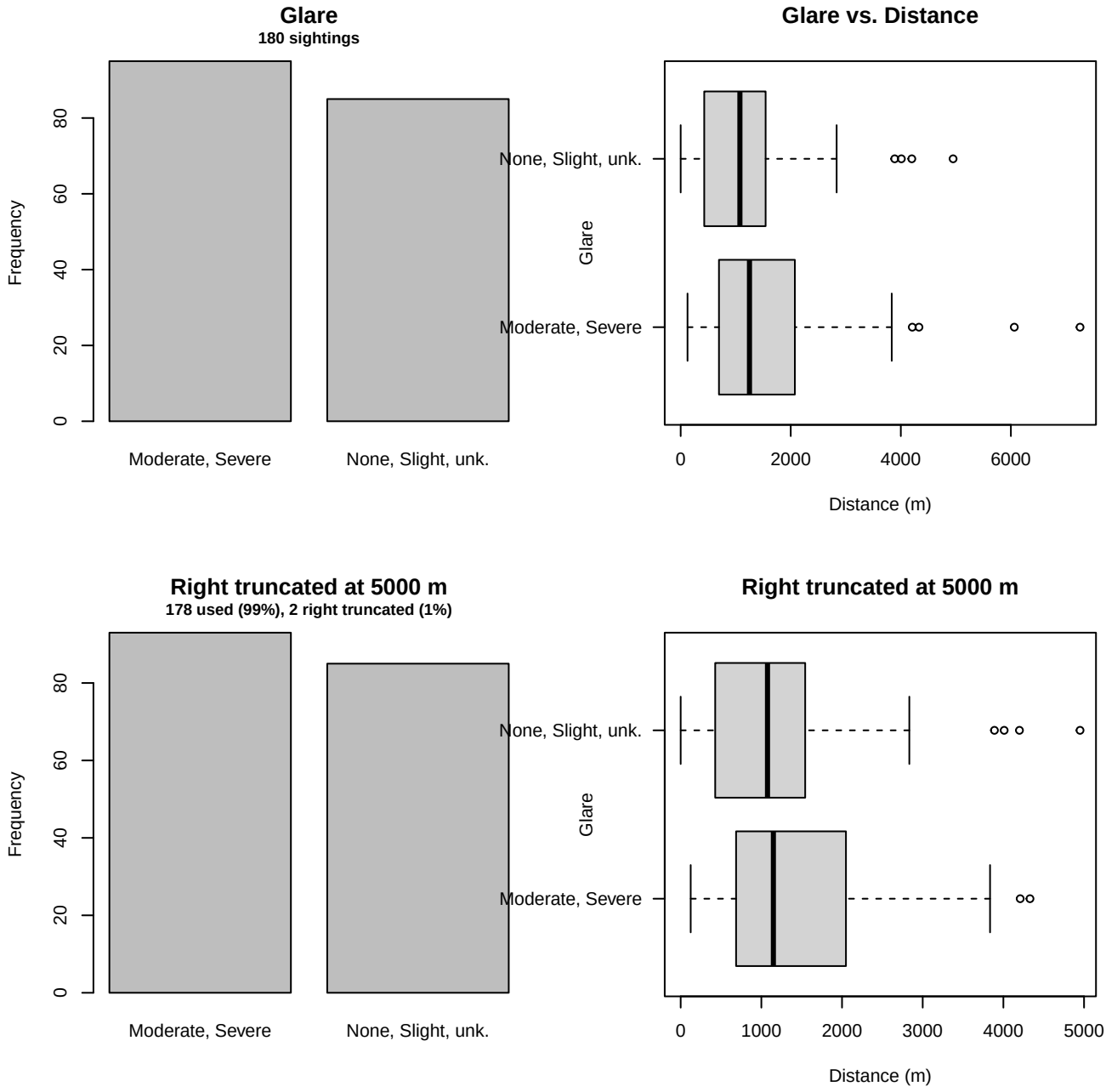

Figure 67: Distribution of the Glare covariate before (top row) and after (bottom row) observations were truncated to fit the NARW EWS WLT-SSA-CMARI Skymaster detection function.

3 Bias Corrections

Density surface modeling methodology uses *distance sampling* (Buckland et al. 2001) to model the probability that an observer on a line transect survey will detect an animal given the perpendicular distance to it from the transect line. Distance sampling assumes that detection probability is 1 when perpendicular distance is 0. When this assumption is not met, detection probability is biased high, leading to an underestimation of density and abundance. This is known as the $g_0 < 1$ problem, where g_0 refers to the detection probability at distance 0. Modelers often try to address this problem by estimating g_0 empirically and dividing it into estimated density or abundance, thereby correcting those estimates to account for the animals that were presumed missed.

Two important sources of bias for visual surveys are known as *availability bias*, in which an animal was present on the transect line but impossible to detect, e.g. because it was under water, and *perception bias*, in which an animal was present and available but not noticed, e.g. because of its small size or cryptic coloration or behavior (Marsh and Sinclair 1989). Modelers often

estimate the influence of these two sources of bias on detection probability independently, yielding two estimates of g_0, hereafter referred to as g_{0A} and g_{0P}, and multiply them together to obtain a final, combined estimate: $g_0 = g_{0A}.g_{0P}$.

Our overall approach was to perform this correction on a per-observation basis, to have the flexibility to account for many factors such as platform type, surveyor institution, group size, group composition (e.g. singleton, mother-calf pair, or surface active group), and geographic location (e.g. feeding grounds vs. calving grounds). The level of complexity of the corrections varied by species according to the amount of information available, with North Atlantic right whale having the most elaborate corrections, derived from a substantial set of publications documenting its behavior, and various lesser known odontocetes having corrections based only on platform type (aerial or shipboard), derived from comparatively sparse information. Here we document the corrections used for humpback whale.

3.1 Aerial Surveys

Palka et al. (2021) developed perception bias corrections using two team, mark recapture distance sampling (MRDS) methodology (Burt et al. 2014) for aerial surveys conducted in 2010-2017 by NOAA NEFSC and SEFSC during the AMAPPS program. These were the only extant perception bias estimates developed from aerial surveys used in our analysis, aside from estimates developed earlier by Palka and colleagues (Palka 2006; Palka et al. 2017). Those earlier efforts utilized older methods and less data than their 2021 analysis, so we applied the Palka et al. (2021) estimates to all aerial survey programs (Table 23).

We applied Palka's estimate for NEFSC to all programs other than SEFSC on the basis that those programs employed a similar visual scanning protocol that allowed observers to scan from the trackline up to the horizon, while SEFSC's protocol generally limited scanning only up to 50° from the trackline, resulting in a smaller effective strip width. UNCW's earlier surveys were an exception, for which detection distances were much closer to SEFSC's for most species, so we applied Palka's SEFSC estimate.

We caution that it is possible that perception bias was different on the other aerial programs, as they often used different aircraft, flew at different altitudes, and were staffed by different personnel. Of particular concern are that many programs flew Cessna 337 Skymasters, which had flat windows, while NOAA flew de Havilland Twin Otters, which had bubble windows, which likely afforded a better view of the transect line and therefore might have required less of a correction than the Skymasters. Correcting the other programs using NOAA's estimate as we have done is likely to yield less bias than leaving them uncorrected, but we urge all programs to undertake their own efforts to estimate perception bias, as resources allow.

We estimated availability bias corrections using the Laake et al. (1997) estimator and dive intervals reported by Palka et al. (2017) (Table 24). To estimate time in view, needed by the Laake estimator, we used results reported by Robertson et al. (2015), rescaled linearly for each survey program according to its target altitude and speed. We caution that Robertson's analysis was done for a de Havilland Twin Otter, which may have a different field of view than that of the other aircraft used here, which mainly comprised Cessna 337 Skymasters with flat windows but also a Partenavia P-68 with bubble windows (on the NYS-DEC/TT surveys). However, we note that McLellan et al. (2018) conducted a sensitivity analysis on the influence of the length of the "window of opportunity" to view beaked whales from a Cessna Skymaster on their final density estimates and found that they varied by only a few thousandths of an animal per kilometer when the window of opportunity more than doubled. Still, we urge additional program-specific research into estimation of availability bias.

To address the influence of group size on availability bias, we applied the group availability estimator of McLellan et al. (2018) on a per-observation basis. Following Palka et al. (2021), who also used that method, we assumed that individuals in the group dived asynchronously. The resulting g_{0A} corrections ranged from about 0.5 to 1 (Figure 68). We caution that the assumption of asynchronous diving can lead to an underestimation of density and abundance if diving is actually synchronous; see McLellan et al. (2018) for an exploration of this effect and Section 6 for further discussion.

Table 23: Perception bias corrections for humpback whale applied to aerial surveys.

Surveys	Group Size	g_{0P}	g_{0P} Source
SEFSC, UNCW 2002-2008	< 3	0.86	Palka et al. (2021): SEFSC
All others	< 3	0.67	Palka et al. (2021): NEFSC
All	≥ 3	1.00	Assumed

Table 24: Surface and dive intervals for humpback whale used to estimate availability bias corrections.

Surface Interval (s)	Dive Interval (s)	Source
144.6	175.6	Palka et al. (2017)

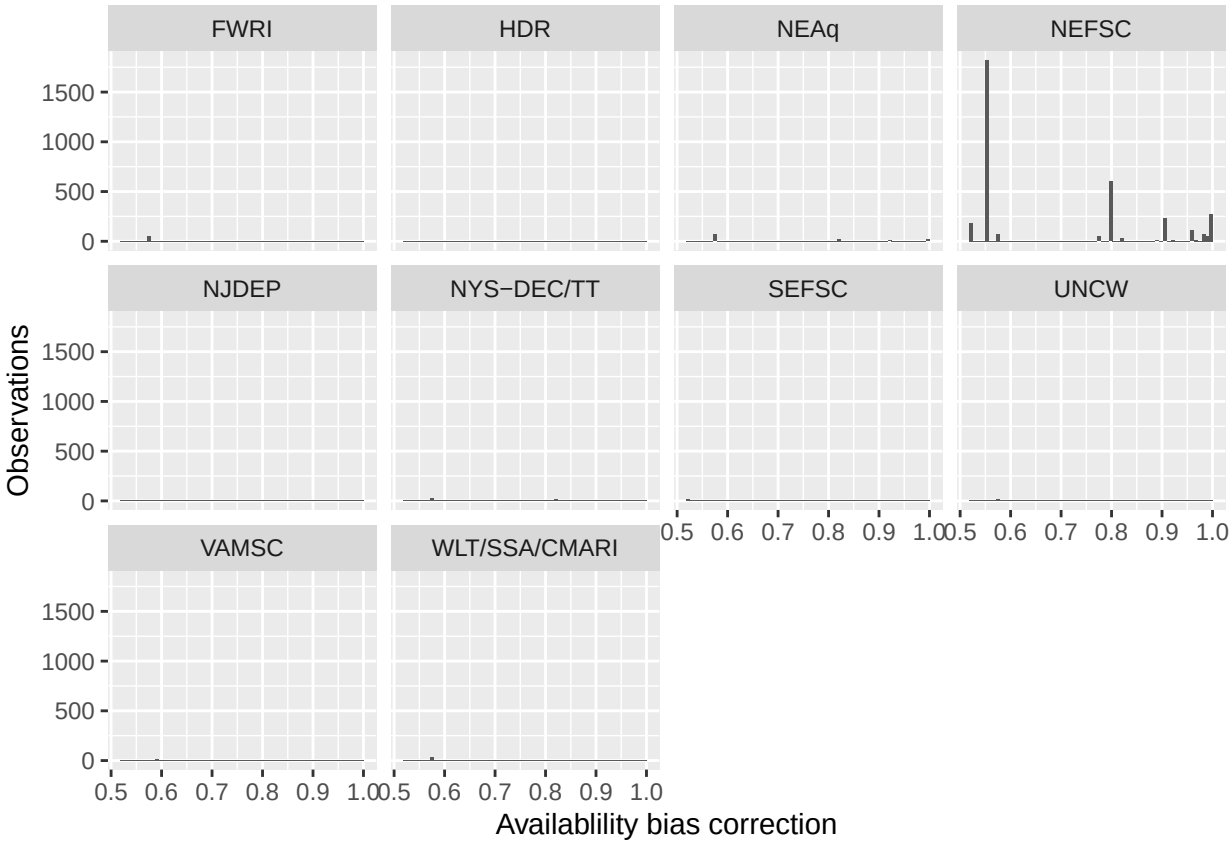

Figure 68: Availability bias corrections for humpback whale for aerial surveys, by institution.

3.2 Shipboard Surveys

Most of the shipboard surveys in our analysis used high-power (25x150), pedestal-mounted binoculars. Similar to aerial surveys, Palka et al. (2021) developed perception bias corrections using two team, MRDS methodology (Burt et al. 2014) for high-power binocular surveys conducted in 2010-2017 by NOAA NEFSC and SEFSC during the AMAPPS program. These were the only extant perception bias estimates developed from high-power binocular surveys used in our analysis, aside from estimates developed earlier by Palka and colleagues (Palka 2006; Palka et al. 2017). Those earlier efforts utilized older methods and less data than their 2021 analysis, so we applied the Palka et al. (2021) estimates to all shipboard surveys that searched with high-power binoculars (Table 25).

Table 25: Perception and availability bias corrections for humpback whale applied to shipboard surveys.

Surveys	Searching Method	Group Size	g_{0P}	g_{0P} Source	g_{0A}	g_{0A} Source
NEFSC, NJDEP	Binoculars	Any	0.39	Palka et al. (2021): NEFSC	1	Assumed
SEFSC	Binoculars	Any	0.57	Palka et al. (2021): SEFSC	1	Assumed
NEFSC (AJ 99-02)	Naked eye	Any	0.38	Palka et al. (2006)	1	Assumed
MCR	Naked eye	Any	0.69	Cañadas et al. (2021)	1	Assumed

A few surveys used naked eyes rather than high-power binoculars. For the one NEFSC naked eye survey (AJ 99-02) used in our analysis, we used the estimate developed for this survey by Palka (2006). For the surveys conducted by MCR on R/V Song of the Whale, for which a program-specific estimate was not available, we used the estimate from Cañadas et al. (2021).

Given that the dive interval of this species (Table 24) was short relative to the amount of time a given patch of water remained in view to shipboard observers, we assumed that no availability bias correction was needed ($g_{0A} = 1$), following Palka et al. (2021), except for the MCR surveys, for which Cañadas et al. (2021) prepared an estimate that was slightly lower ($g_{0A} = 0.99$).

4 Density Model

North Atlantic humpback whales undergo an annual migration in which they migrate to high latitudes in summer to feed and return to low latitudes in winter to breed (Smith et al. 1999). In our study area, humpbacks feed in the Gulf of Maine during summer and breed in the West Indies in the winter (Winn et al. 1975; Stone et al. 1987; Mattila et al. 1989, 1994; Mattila and Clapham 1989; Katona and Beard 1990). Passive acoustic monitoring (Davis et al. 2020) and visual surveys used in this model showed humpbacks present in the Gulf of Maine throughout the year, although most appeared to depart during the fall and return during spring, with a relatively small number remaining to overwinter. NOAA considers the population inhabiting the Gulf of Maine to be distinct stock but notes some uncertainty about how far north the stock might extend, e.g. over the Scotian Shelf (Clapham et al. 2003; Robbins 2007; Hayes et al. 2020).

Acoustics and visual surveys reported humpbacks present southwest of Cape Cod and down the mid-Atlantic shelf throughout the year but particularly winter and spring. The mid-Atlantic may represent a supplementary feeding ground (Swingle et al. 1993; Wiley et al. 1995; Aschettino et al. 2020; Lomac-MacNair et al. 2022) but photographic matching suggests not all of the whales overwintering here are from the Gulf of Maine stock (Barco 2002; Brown et al. 2022). In any case, our approach was to model the density of humpbacks across our study area, irrespective of which stock they might belong to.

Similar to our previous humpback models (Roberts et al. 2016; Roberts et al. 2017), we split the year into two seasons, summer (April-November) and winter (December-March), on the basis that species-habitat relationships are likely to be different in feeding and breeding seasons for this highly migratory species. As before, we designated April the first month of summer because Robbins (2007) (her Table 3.2) reported that the earliest sighting dates of female and male migrants arriving at the Gulf of Maine feeding grounds were 20 March and 19 April, respectively, and because the surveys available for our analysis showed distinctly more sightings in April than in March, while February and March were similar to each other, as were April and May. We designated December as the first month of winter because Robbins (2007) (her Table 3.3) reported that the last sighting dates of female and male migrants in the Gulf of Maine were 19 and 9 December, respectively. However, we caution that the seasonal timing of humpback migrations may be shifting in response to climate change (Ramp et al. 2015; Pendleton et al. 2022), which may require these seasonal definitions to be reexamined in the future.

In Long Island Sound, where no sightings had been reported by surveys in our model or been archived in the OBIS-SEAMAP repository (Halpin et al. 2009), we assumed the species was absent during these months.

4.1 Winter

In winter months (December-March), we lacked substantial survey effort north of the Gulf of Maine, so we excluded the Scotian Shelf and upper Bay of Fundy from the spatiing dates of female and male migrants in the Gulf of Maine were 19 and 9 December, respectively. However, we caution that the seasonal timing of humpback migrations may be shifting in response to climate change (Ramp et al. 2015; Pendleton et al. 2022), which may require these seasonal definitions to be reexamined in the future. We initially modeled this entire region with a single spatial model, but encountered a problem related to the sightings in Florida and Georgia. This small region contained more than double the survey effort of the entire rest of the east coast, contributed by the survey teams targeting right whales on their calving grounds. The inclusion of these data in the model appeared to cause aberrant extrapolations of density across warm waters of the Blake Plateau, where virtually no survey data were available and the model was largely extrapolating. Although two sightings were reported by UNCW along the western side of the Plateau, those sightings required nine years of monthly surveys to accumulate, suggesting such occurrences are rare. Furthermore, acoustic monitoring of the Blake Plateau indicated humpbacks rarely occur here (Weiss et al. 2020; Davis et al. 2020; Kowarski et al. 2022). To fix this problem, we split the area of intense right whale surveys, labelled the Florida-Georgia NARW EWS Area, into a separate model. This eliminated the aberrant predictions.

4.1.1 South of Nova Scotia

The surveys incorporated into the main winter model (i.e. waters other than the Florida-Georgia NARW EWS Area) reported 276 sightings (Figure 69), scattered across the continental shelf from the Gulf of Maine to Florida. The highest concentrations occurred in the Gulf of Maine, but effort was also high in this region, so the concentration of sightings did not necessarily imply a concentration of density.

When ranked by REML score (Wood 2011) or AIC, models with climatological covariates outranked those with contemporaneous covariates. We selected as our final choice the climatological-covariate model that had the best REML score. This model explained 1.3% less deviance than the best-scoring contemporaneous-covariate model, but that model had a worse REML score and exhibited evidence of being overfitted, with predictions showing notable "bands" of density along the continental shelf across several depth ranges, so we stuck with the top climatological-covariate model.

This model retained two static covariates and three dynamic covariates (Table 26). The functional relationship fitted for depth (Figure 72) was hump-shaped and indicated a positive influence for depths of about 20-300 m (1.3-2.5 in $\log_{10}$ scale), a wide range that spanned the entire continental shelf except the shallowest waters. The relationship for distance to the 125 m isobath was a hump that peaked about 10 km on the deep side of the isobath, likely reflecting an affinity of the species for the steep edges of banks in the Gulf of Maine (Hazen et al. 2009) and of the continental shelf down the mid-Atlantic.

Turning to dynamic covariates, the relationship for sea surface salinity indicated a clear preference for the fresher waters found north of Cape Hatteras, while the relationship for sea surface temperature showed a hump that peaked at about 9 °C and flattened to a relatively straight line slightly below zero, suggesting a preference for colder northern waters but not a strong avoidance of warmer southern waters. The relationship with primary productivity, as estimated by the Carbon, Absorption, and Fluorescence Euphotic-resolving (CAFE) model (Silsbe et al. 2016), indicated a preference for more productive waters, which likely acted to boost nearshore densities betwen Cape Hatteras and the higher productivity than in other areas during these months.

4.1.1.1 Final Model

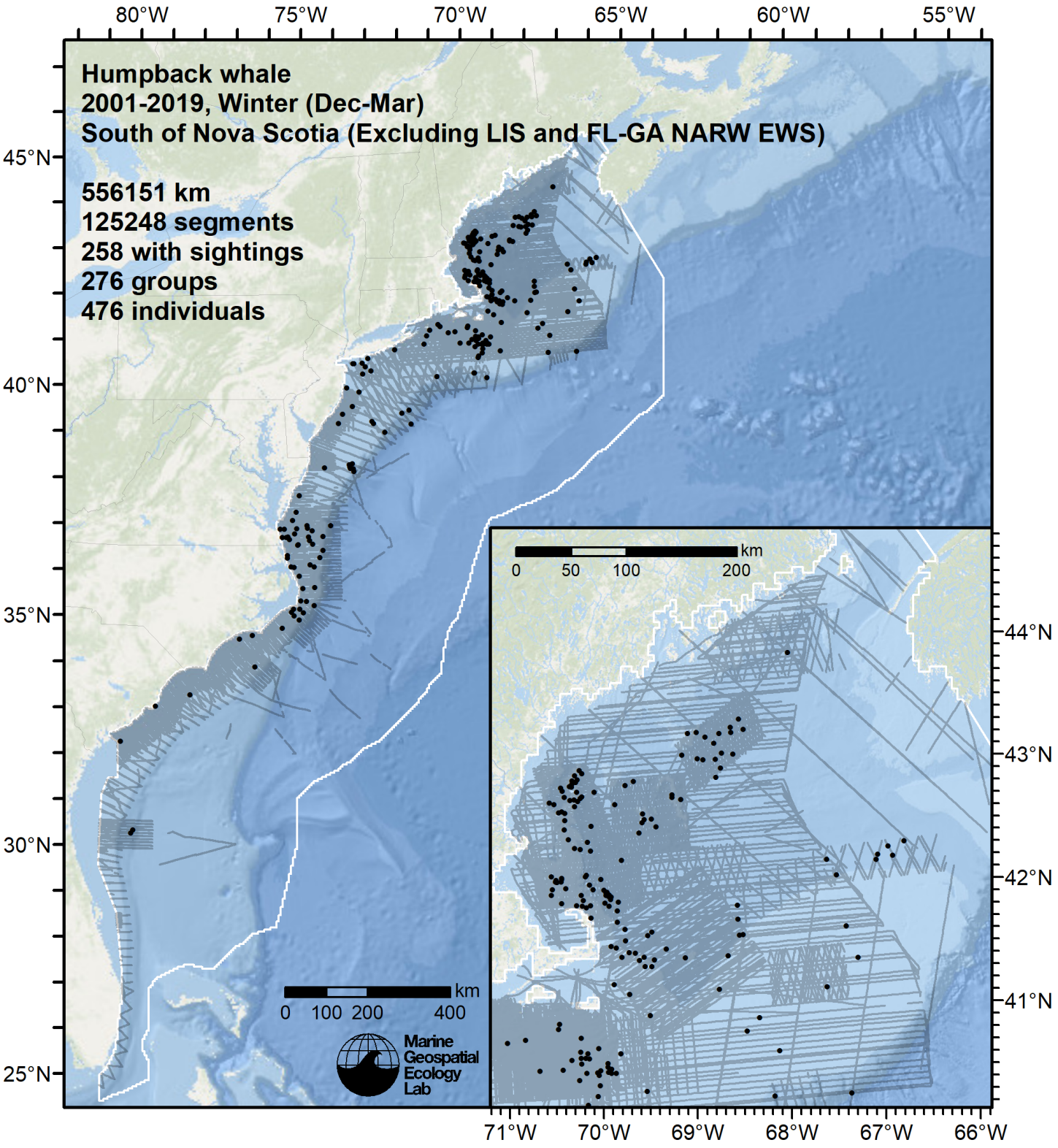

Figure 69: Survey segments used to fit the model for the region South of Nova Scotia (Excluding LIS and FL-GA NARW EWS) for Winter. Black points indicate segments with observations.

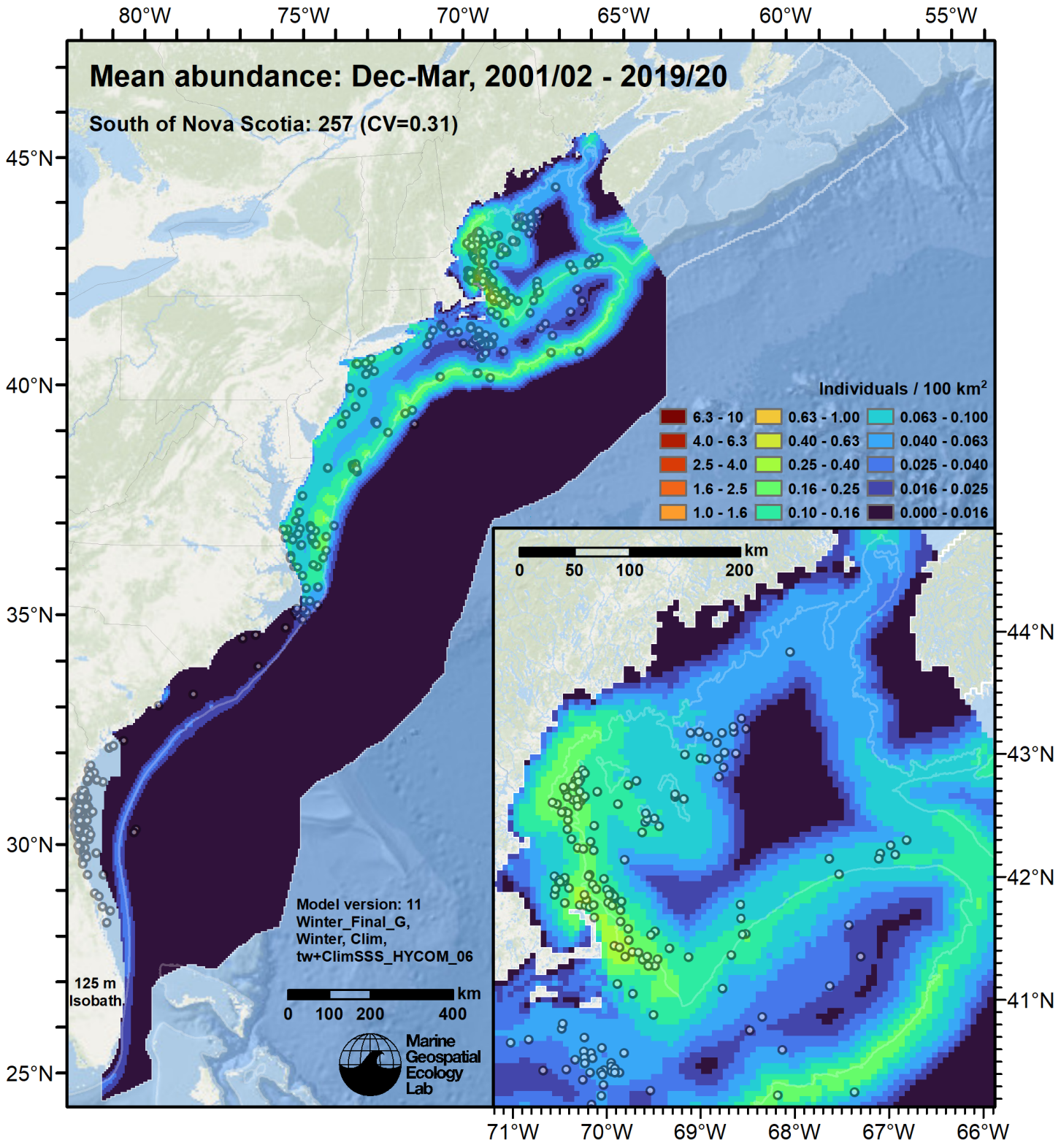

Figure 70: Humpback whale mean density for the indicated period, as predicted by the model for the region South of Nova Scotia (Excluding LIS and FL-GA NARW EWS) for Winter. Open circles indicate segments with observations. Mean total abundance and its coefficient of variation (CV) are given in the subtitle. Variance was estimated with the analytic approach given by Miller et al. (2022), Appendix S1, and accounts both for uncertainty in model parameter estimates and for seasonal variability in dynamic covariates but not interannual variability in them, as these covariates were monthly climatological averages.

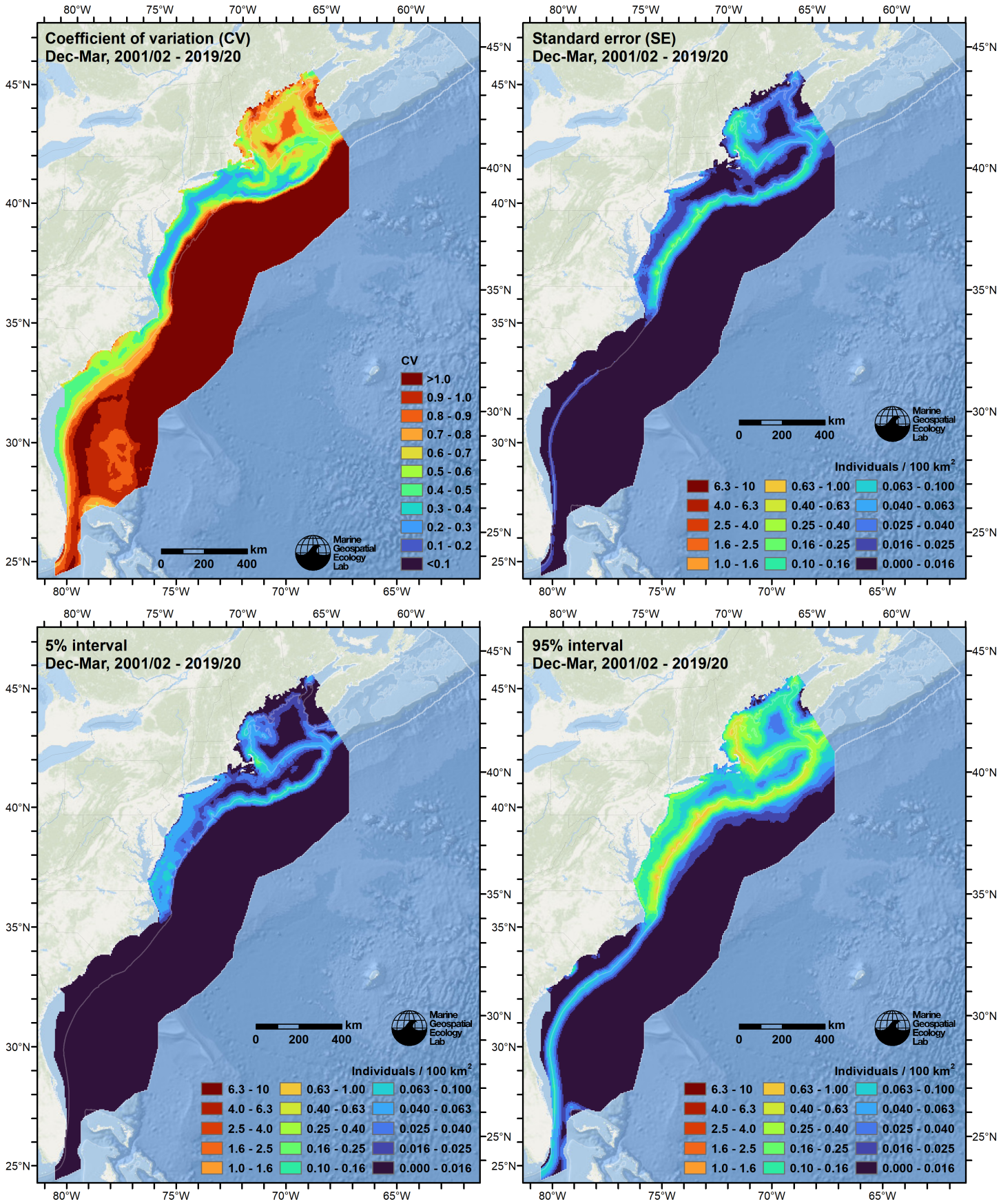

Figure 71: Uncertainty statistics for the humpback whale mean density surface (Figure 70) predicted by the model for the region South of Nova Scotia (Excluding LIS and FL-GA NARW EWS) for Winter. Variance was estimated with the analytic approach given by Miller et al. (2022), Appendix S1, and accounts both for uncertainty in model parameter estimates and for seasonal variability in dynamic covariates but not interannual variability in them, as these covariates were monthly climatological averages.

Statistical output for this model:

```
Family: Tweedie(p=1.123)
Link function: log

Formula:
IndividualsCorrected ~ offset(log(SegmentArea)) + s(pmax(-50,
    pmin(I(DistTo125m/1000), 50)), bs = "ts") + s(log10(pmax(5,
    pmin(Depth, 2000))), bs = "ts") + s(pmax(3, pmin(ClimSST_CMC,
    26)), bs = "ts") + s(pmax(31, pmin(ClimSSS_HYCOM, 36.5)),
    bs = "ts") + s(pmax(250, pmin(ClimPP_CAFE, 850)), bs = "ts")

Parametric coefficients:
            Estimate Std. Error t value Pr(>|t|)
(Intercept) -22.7176     0.1481  -153.4   <2e-16 ***
---
Signif. codes:  0 '***' 0.001 '**' 0.01 '*' 0.05 '.' 0.1 ' ' 1

Approximate significance of smooth terms:
                                          edf Ref.df     F  p-value
s(pmax(-50, pmin(I(DistTo125m/1000), 50))) 3.966      9 8.668  < 2e-16 ***
s(log10(pmax(5, pmin(Depth, 2000))))       2.796      9 1.242  0.00263 **
s(pmax(3, pmin(ClimSST_CMC, 26)))          3.998      9 3.724  < 2e-16 ***
s(pmax(31, pmin(ClimSSS_HYCOM, 36.5)))     1.090      9 2.179 2.62e-06 ***
s(pmax(250, pmin(ClimPP_CAFE, 850)))       2.918      9 7.384  < 2e-16 ***
---
Signif. codes:  0 '***' 0.001 '**' 0.01 '*' 0.05 '.' 0.1 ' ' 1

R-sq.(adj) =  0.00916   Deviance explained = 17.7%
-REML =   2058  Scale est. = 5.753     n = 125248

Method: REML   Optimizer: outer newton
full convergence after 14 iterations.
Gradient range [-0.0004981109,0.0005094342]
(score 2058.007 & scale 5.752955).
Hessian positive definite, eigenvalue range [0.4285423,2650.637].
Model rank =  46 / 46

Basis dimension (k) checking results. Low p-value (k-index<1) may
indicate that k is too low, especially if edf is close to k'.

                                           k'  edf k-index p-value
s(pmax(-50, pmin(I(DistTo125m/1000), 50))) 9.00 3.97    0.88   0.050 *
s(log10(pmax(5, pmin(Depth, 2000))))       9.00 2.80    0.87   0.040 *
s(pmax(3, pmin(ClimSST_CMC, 26)))          9.00 4.00    0.87   0.025 *
s(pmax(31, pmin(ClimSSS_HYCOM, 36.5)))     9.00 1.09    0.85   0.020 *
s(pmax(250, pmin(ClimPP_CAFE, 850)))       9.00 2.92    0.89   0.185
---
Signif. codes:  0 '***' 0.001 '**' 0.01 '*' 0.05 '.' 0.1 ' ' 1
```

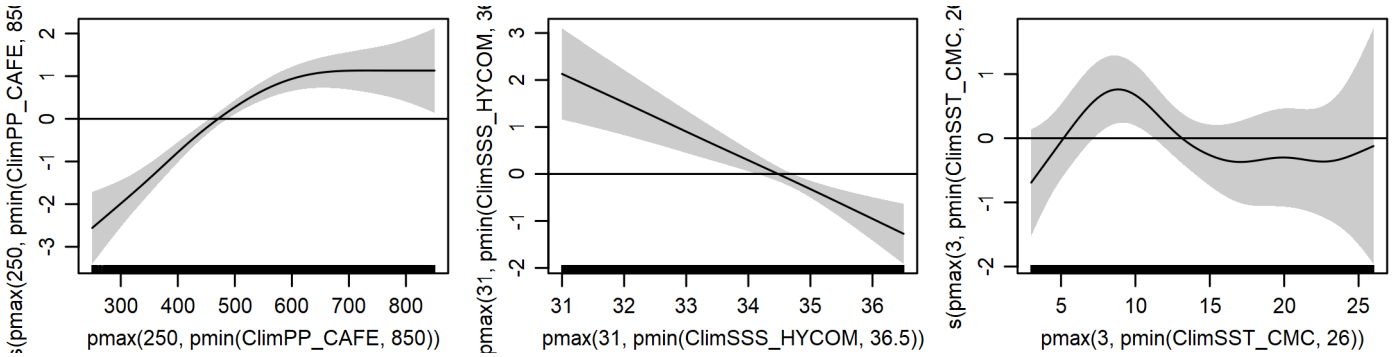

(a) Climatological net primary productivity (mg C m^{-2} day^{-1}) (CAFE model)

(b) Climatological sea surface salinity (PSU)

(c) Climatological sea surface temperature (°C)

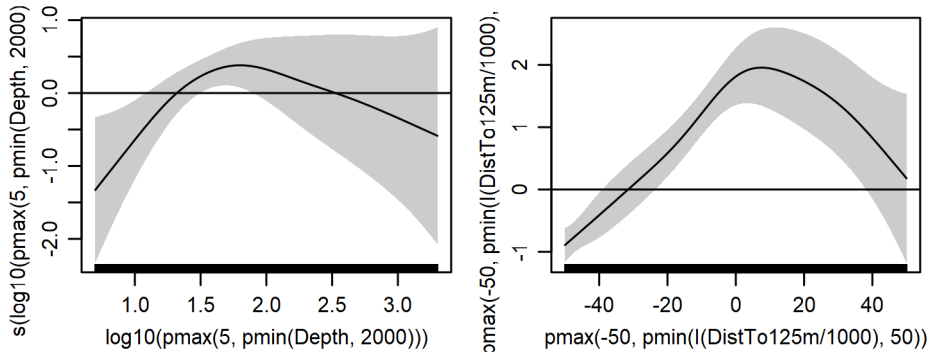

(d) Seafloor depth (m)

(e) Distance to 125m isobath (km)

Figure 72: Functional plots for the final model for the region South of Nova Scotia (Excluding LIS and FL-GA NARW EWS) for Winter. Transforms and other treatments are indicated in axis labels. *log10* indicates the covariate was $\log_{10}$ transformed. *pmax* and *pmin* indicate the covariate's minimum and maximum values, respectively, were Winsorized to the values shown. Winsorization was used to prevent runaway extrapolations during prediction when covariates exceeded sampled ranges, or for ecological reasons, depending on the covariate. */1000* indicates meters were transformed to kilometers for interpretation convenience.

Table 26: Covariates used in the final model for the region South of Nova Scotia (Excluding LIS and FL-GA NARW EWS) for Winter.

Covariate	Description
ClimPP_CAFE	Climatological monthly mean net primary productivity (mg C m^{-2} day^{-1}) from the Carbon, Absorption, and Fluorescence Euphotic-resolving (CAFE) model (Silsbe et al. (2016))
ClimSSS_HYCOM	Climatological monthly mean sea surface salinity (PSU) from the HYCOM GOFS 3.1 1/12° ocean model (Chassignet et al. (2009))
ClimSST_CMC	Climatological monthly mean sea surface temperature (°C) from GHRSST Level 4 CMC0.2deg and CMC0.1deg (Brasnett (2008); Canada Meteorological Center (2012); Meissner et al. (2016); Canada Meteorological Center (2016))
Depth	Depth (m) of the seafloor, from SRTM30_PLUS (Becker et al. (2009))
DistTo125m	Distance (km) to the 125m isobath, derived from SRTM30_PLUS (Becker et al. (2009))

4.1.1.2 Diagnostic Plots

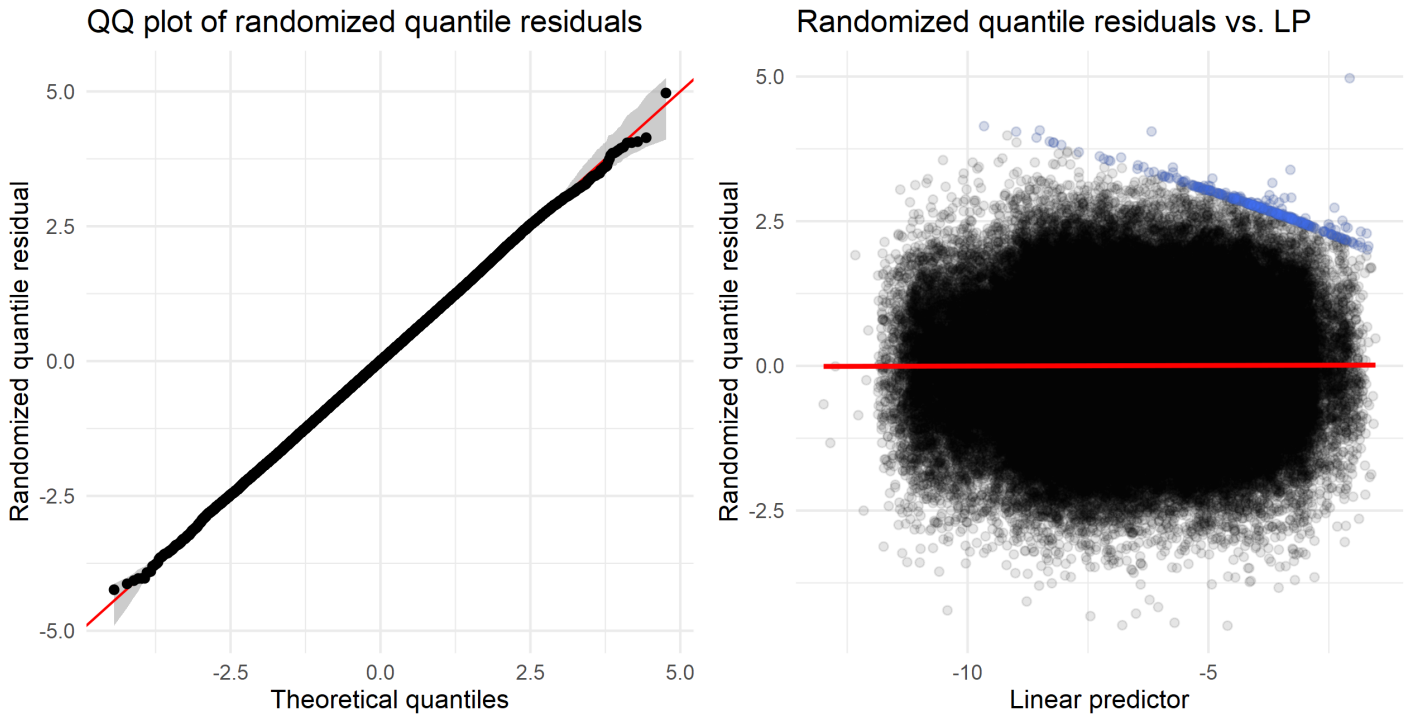

Figure 73: Residual plots for the final model for the region South of Nova Scotia (Excluding LIS and FL-GA NARW EWS) for Winter.

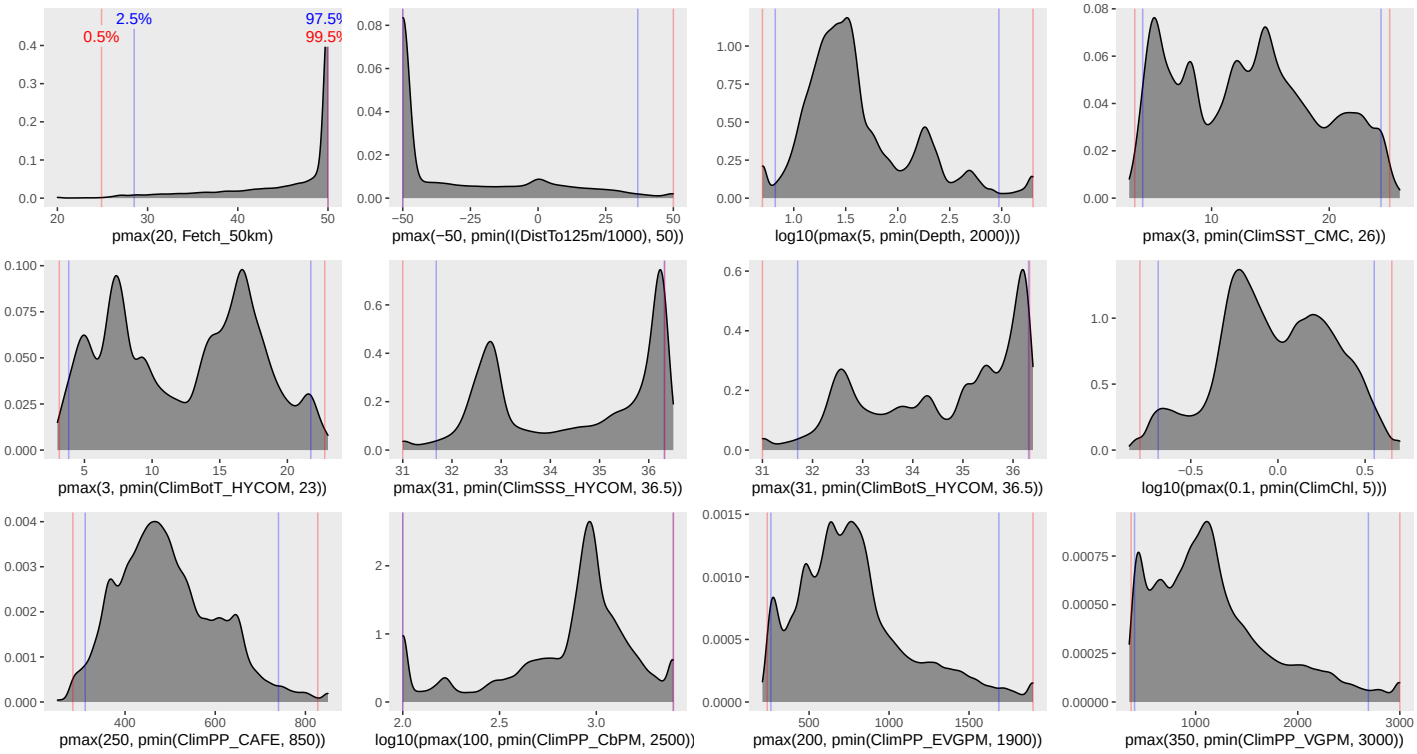

Figure 74: Density histograms showing the distributions of the covariates considered during the final model selection step. The final model may have included only a subset of the covariates shown here (see Figure 72), and additional covariates may have been considered in preceding selection steps. Red and blue lines enclose 99% and 95% of the distributions, respectively. Transforms and other treatments are indicated in axis labels. *log10* indicates the covariate was $\log_{10}$ transformed. *pmax* and *pmin* indicate the covariate's minimum and maximum values, respectively, were Winsorized to the values shown. Winsorization was used to prevent runaway extrapolations during prediction when covariates exceeded sampled ranges, or for ecological reasons, depending on the covariate. */1000* indicates meters were transformed to kilometers for interpretation convenience.

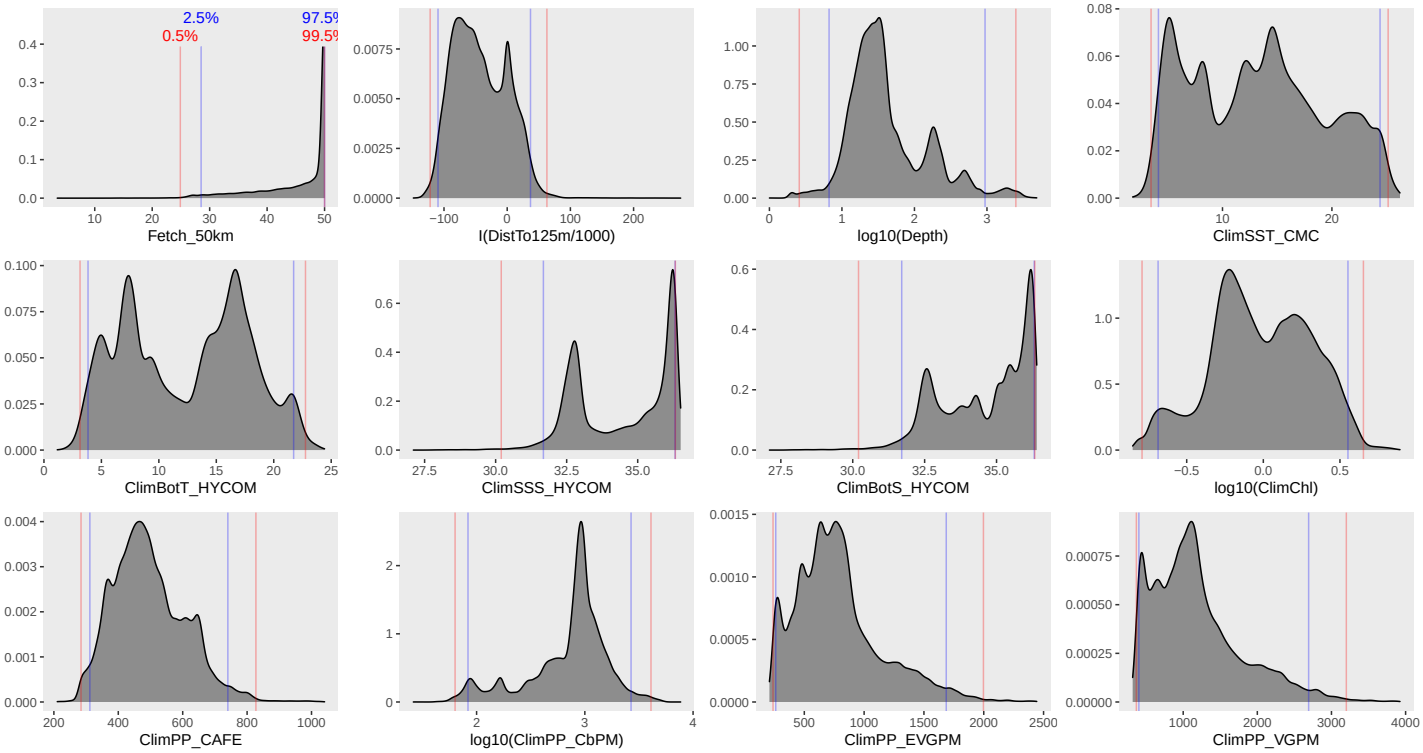

Figure 75: Density histograms shown in Figure 74 replotted without Winsorization, to show the full range of sampling represented by survey segments.

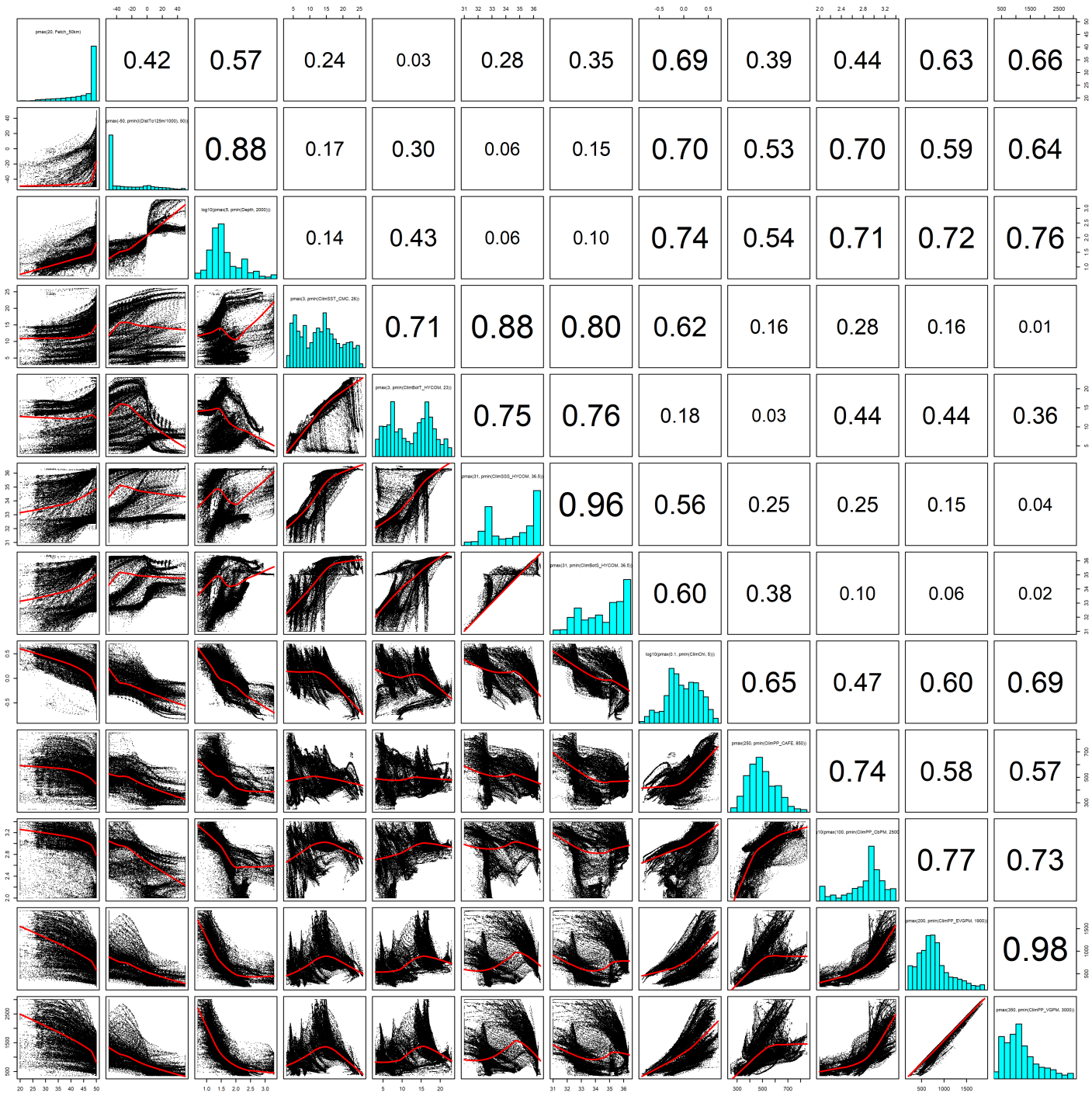

Figure 76: Scatterplot matrix of the covariates considered during the final model selection step. The final model may have included only a subset of the covariates shown here (see Figure 72), and additional covariates may have been considered in preceding selection steps. Covariates are transformed and Winsorized as shown in Figure 74. This plot is used to check simple correlations between covariates (via pairwise Pearson coefficients above the diagonal) and visually inspect for concurvity (via scatterplots and red lowess curves below the diagonal).

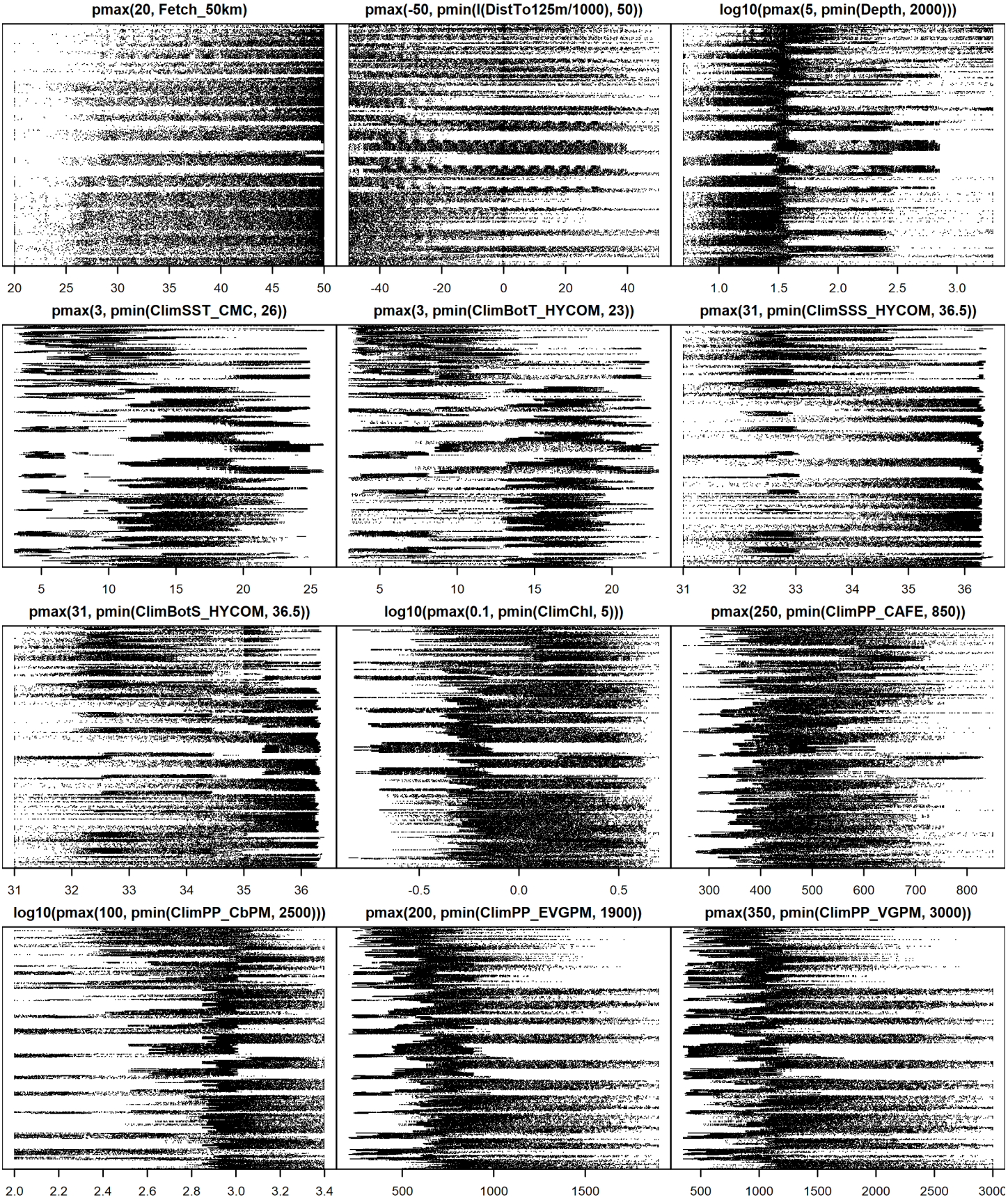

Figure 77: Dotplot of the covariates considered during the final model selection step. The final model may have included only a subset of the covariates shown here (see Figure 72), and additional covariates may have been considered in preceding selection steps. Covariates are transformed and Winsorized as shown in Figure 74. This plot is used to check for suspicious patterns and outliers in the data. Points are ordered vertically by segment ID, sequentially in time.

4.1.1.3 Extrapolation Diagnostics

4.1.1.3.1 Univariate Extrapolation

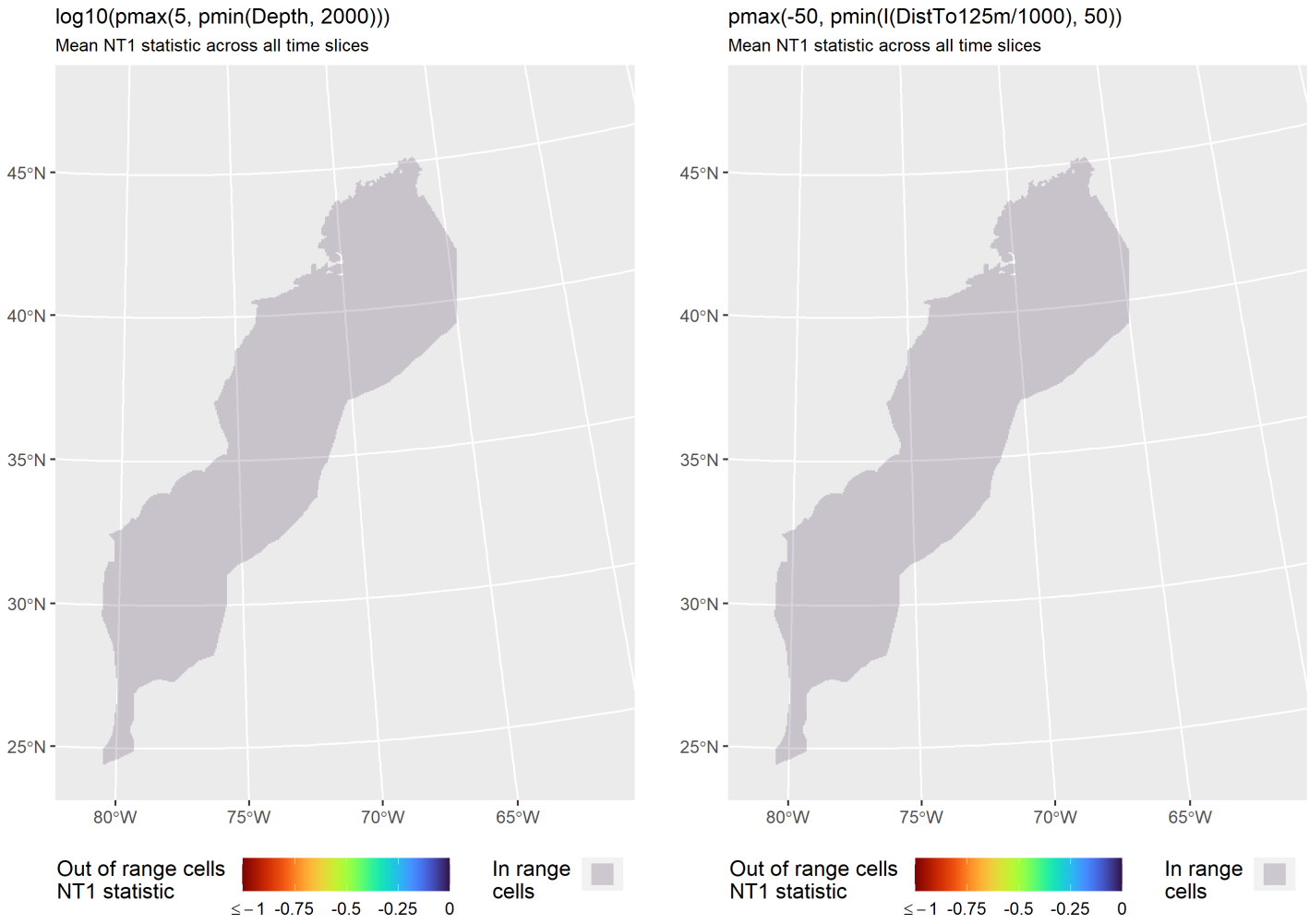

(a) Depth covariate

(b) DistTo125m covariate

Figure 78: NT1 statistic (Mesgaran et al. (2014)) for static covariates used in the model for the region South of Nova Scotia (Excluding LIS and FL-GA NARW EWS) for Winter. Areas outside the sampled range of a covariate appear in color, indicating univariate extrapolation of that covariate occurred there. Areas within the sampled range appear in gray, indicating it did not occur.

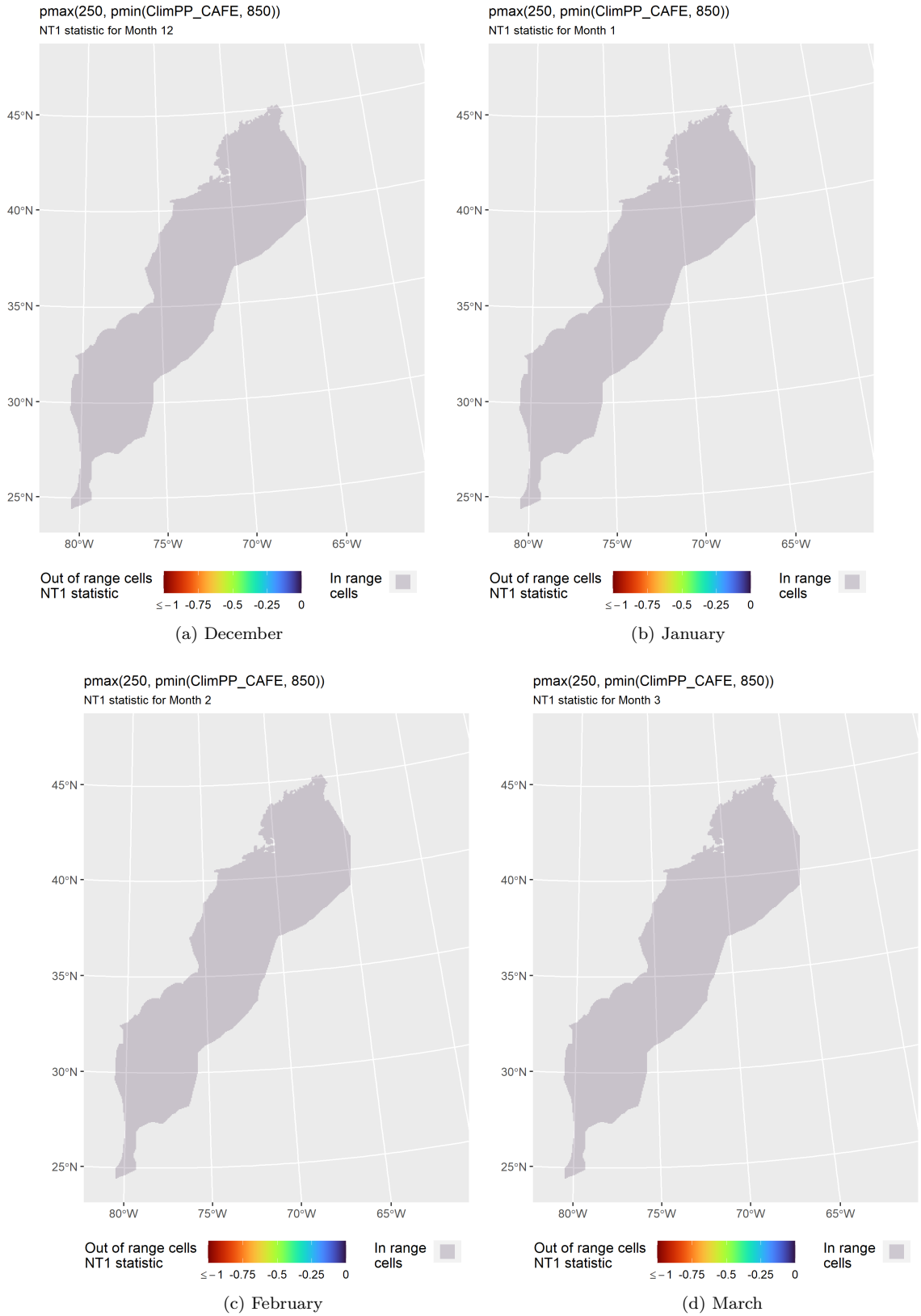

(a) December (b) January

(c) February (d) March

Figure 79: NT1 statistic (Mesgaran et al. (2014)) for the ClimPP_CAFE covariate in the model for the region South of Nova Scotia (Excluding LIS and FL-GA NARW EWS) for Winter. Areas outside the sampled range of a covariate appear in color, indicating univariate extrapolation of that covariate occurred there during the month. Areas within the sampled range appear in gray, indicating it did not occur.

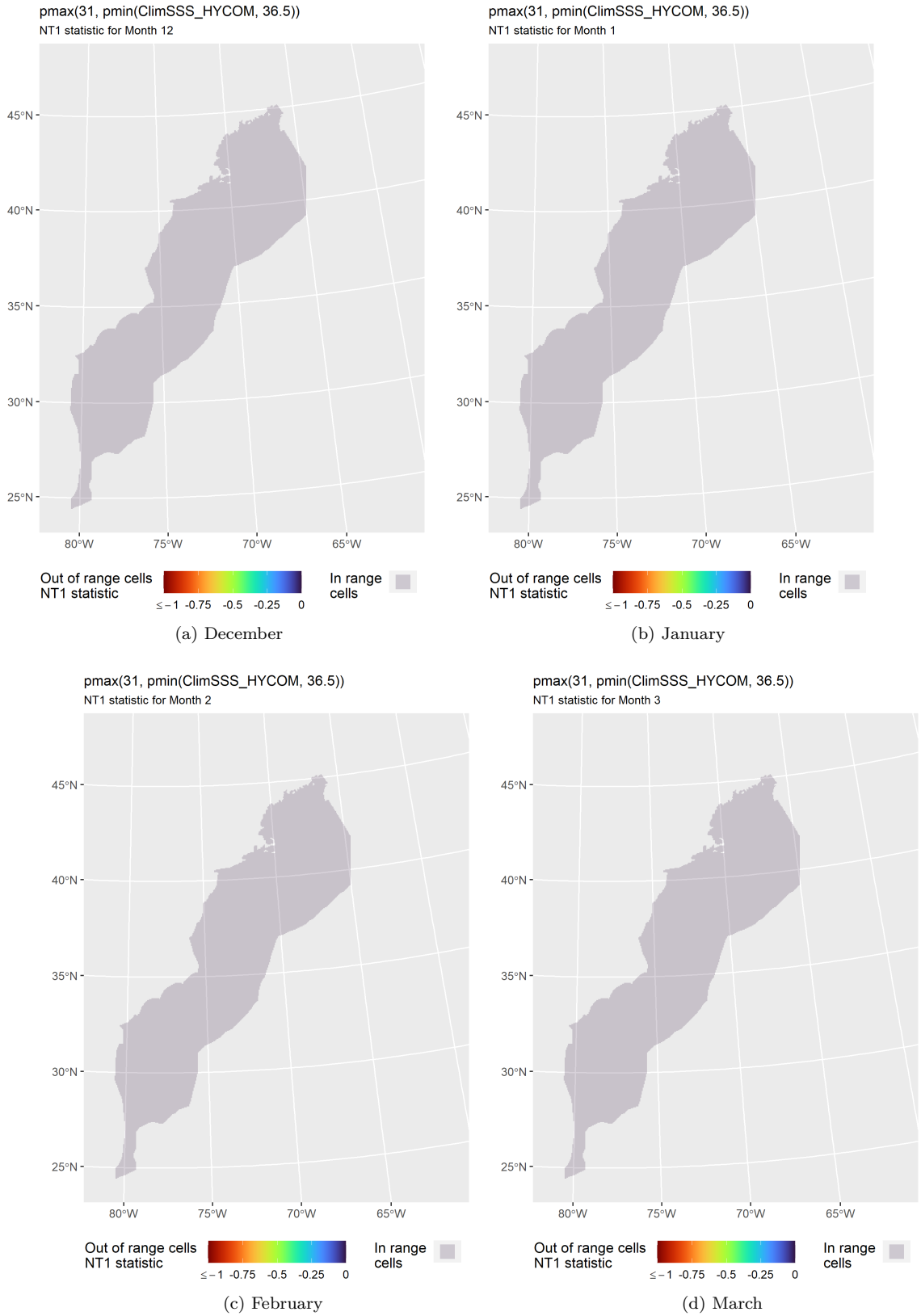

(a) December (b) January

(c) February (d) March

Figure 80: NT1 statistic (Mesgaran et al. (2014)) for the ClimSSS_HYCOM covariate in the model for the region South of Nova Scotia (Excluding LIS and FL-GA NARW EWS) for Winter. Areas outside the sampled range of a covariate appear in color, indicating univariate extrapolation of that covariate occurred there during the month. Areas within the sampled range appear in gray, indicating it did not occur.

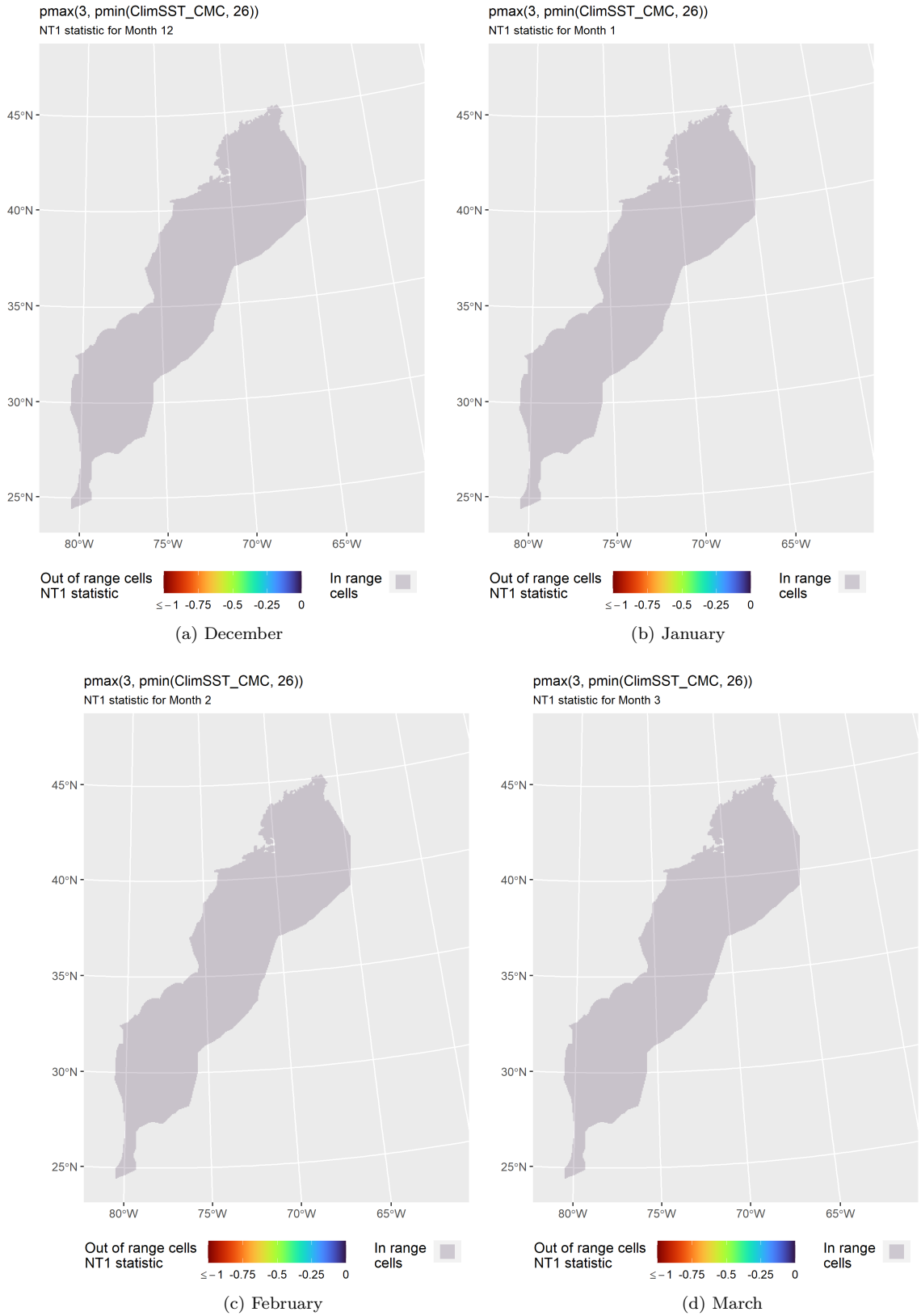

(a) December (b) January

(c) February (d) March

Figure 81: NT1 statistic (Mesgaran et al. (2014)) for the ClimSST_CMC covariate in the model for the region South of Nova Scotia (Excluding LIS and FL-GA NARW EWS) for Winter. Areas outside the sampled range of a covariate appear in color, indicating univariate extrapolation of that covariate occurred there during the month. Areas within the sampled range appear in gray, indicating it did not occur.

4.1.1.3.2 Multivariate Extrapolation

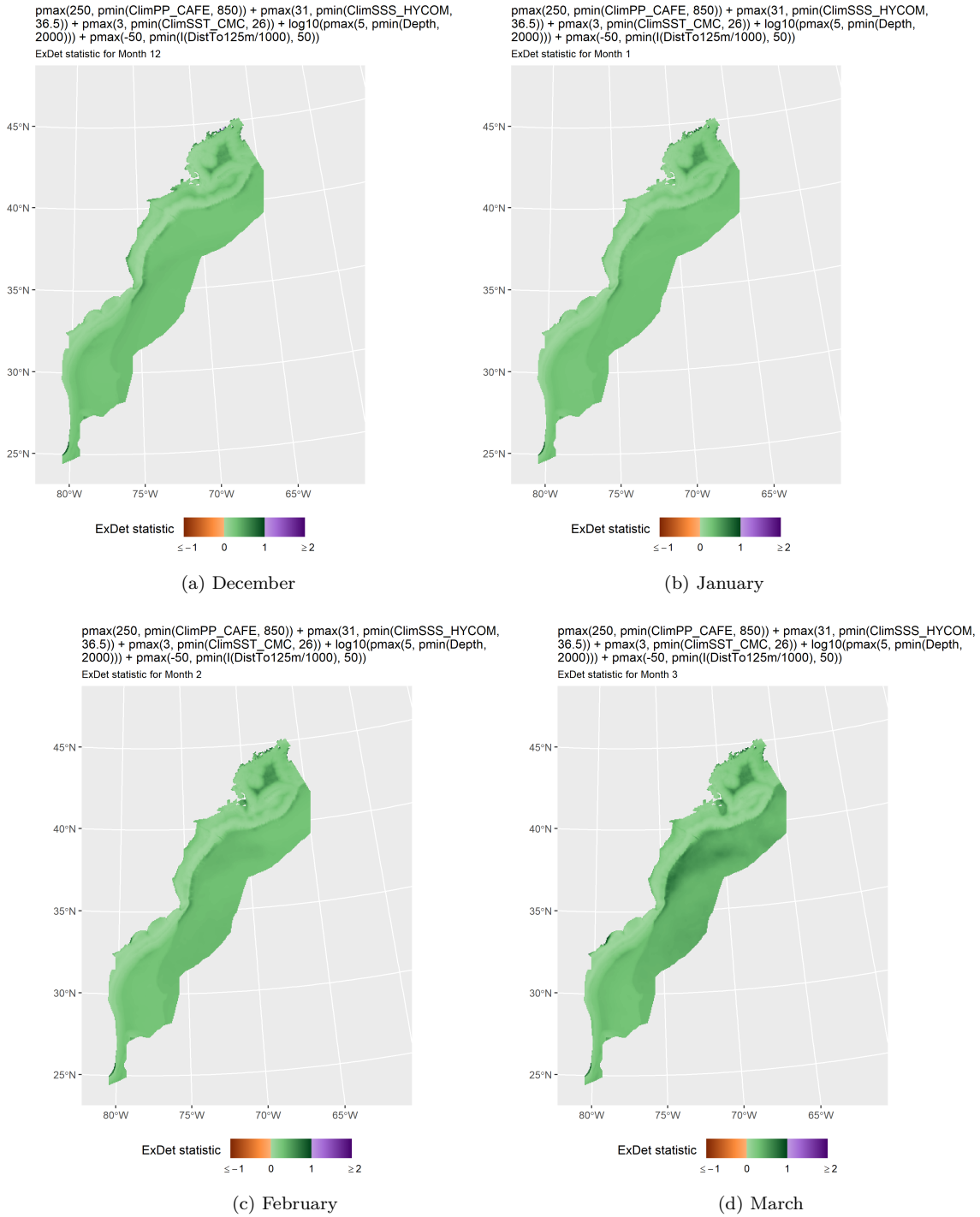

(a) December

(b) January

(c) February

(d) March

Figure 82: ExDet statistic (Mesgaran et al. (2014)) for all of the covariates used in the model for the region South of Nova Scotia (Excluding LIS and FL-GA NARW EWS) for Winter. Areas in orange (ExDet < 0) required univariate extrapolation of one or more covariates (see previous section). Areas in purple (ExDet > 1), did not require univariate extrapolation but did require multivariate extrapolation, by virtue of having novel combinations of covariates not represented in the survey data, according to the NT2 statistic (Mesgaran et al. (2014)). Areas in green ($0 \geq$ ExDet ≤ 1) did not require either type of extrapolation.

4.1.2 Florida-Georgia NARW EWS Area

The surveys incorporated into this region reported 102 sightings totalling 104 individual humpback whales (Figure 83). Although this count was less than 25% of that reported for the rest of the east coast, the effort conducted in this area was about 240% of that conducted over the rest of the coast, indicating that density should be much lower than for the rest of the coast.

Given the small size of this area and the small count of sightings relative to the quantity of effort, we fitted a relatively parsimoneous model of three candidate covariates; only two were retained (Figure 72). For the first candidate, we tested distance to shore and depth; both were dropped during model selection. For the second, we used a binary factor representing the "era" of either 2001-2009 or 2010-2020, based on the presence of a clear interannual pattern in which the first humpback sightings were not logged until the winter of 2008/09 and then several sightings occurred sporadically every year thereafter. We caution that it is unknown why humpbacks apparently began using this area at this time, but note that important shifts in the Gulf Stream occurred around 2009-2010 (Ezer 2019; Gonçalves Neto et al. 2021) which have been implicated in changes in cetacean distributions (Meyer-Gutbrod et al. 2021; Thorne et al. 2022).

For the third covariate, we tested a list of dynamic covariates in both contemporaneous and climatological formulations. In every model with a contemporaneous covariate, that covariate was dropped and distance to shore was retained instead. The resulting model, containing Era and distance to shore, was outranked by three models that included Era and one climatological covariate, when ranked by REML score (Wood 2011) or AIC. We selected the best scoring model with a climatological covariate, which was primary productivity estimated by the Vertically Generalized Production Model (VGPM) (Behrenfeld and Falkowski 1997). The functional relationship for this covariate (Figure 72) indicated increasing density with increasing primary productivity, corresponding to the inshore region where humpback sightings were concentrated. We do not assert that primary productivity itself explains humpbacks' presence here; this covariate is likely a proxy for some other habitat condition that makes the area attractive.

In any case, predicted density was quite low, averaging only one whale in the region across the four-month season for the modeled years (2001/02 - 2019/20) (Figure 84). This is consistent with the temporal pattern in the sightings, in which rarely more than one whale was sighted on a given day of surveying, and then days or weeks later another single animal was sighted, likely the same whale, in a similar location. The resulting density was so low that it did not exceed the darkest color on our density color scale except in one month, March (Figure 112).

4.1.2.1 Final Model

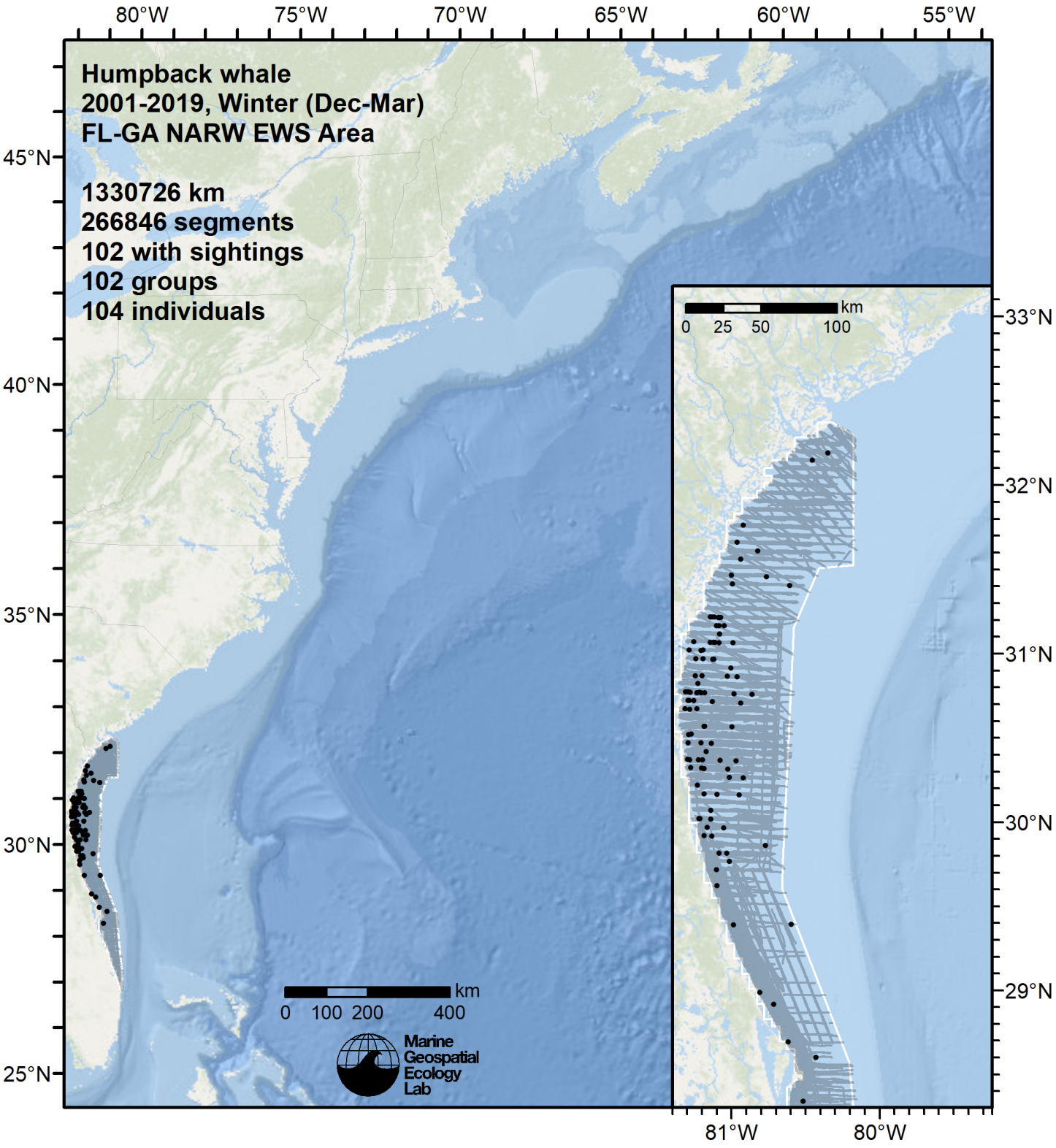

Figure 83: Survey segments used to fit the model for the region FL-GA NARW EWS Area for Winter. Black points indicate segments with observations.

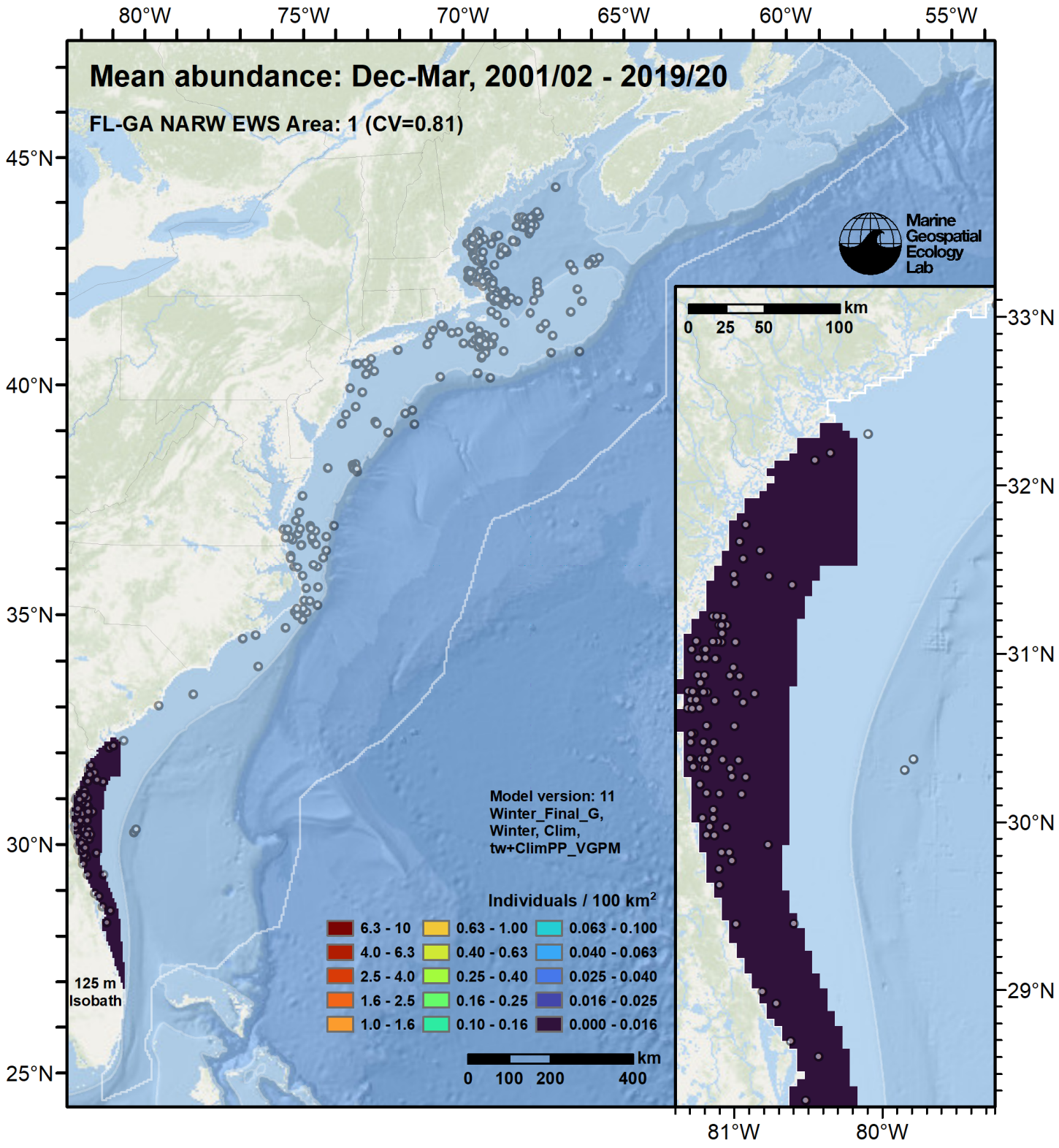

Figure 84: Humpback whale mean density for the indicated period, as predicted by the model for the region FL-GA NARW EWS Area for Winter. Open circles indicate segments with observations. Mean total abundance and its coefficient of variation (CV) are given in the subtitle. Variance was estimated with the analytic approach given by Miller et al. (2022), Appendix S1, and accounts both for uncertainty in model parameter estimates, the mean difference in density between the eras (via Era as a factor covariate), and for seasonal variability in dynamic covariates but not interannual variability in them, as these covariates were monthly climatological averages.

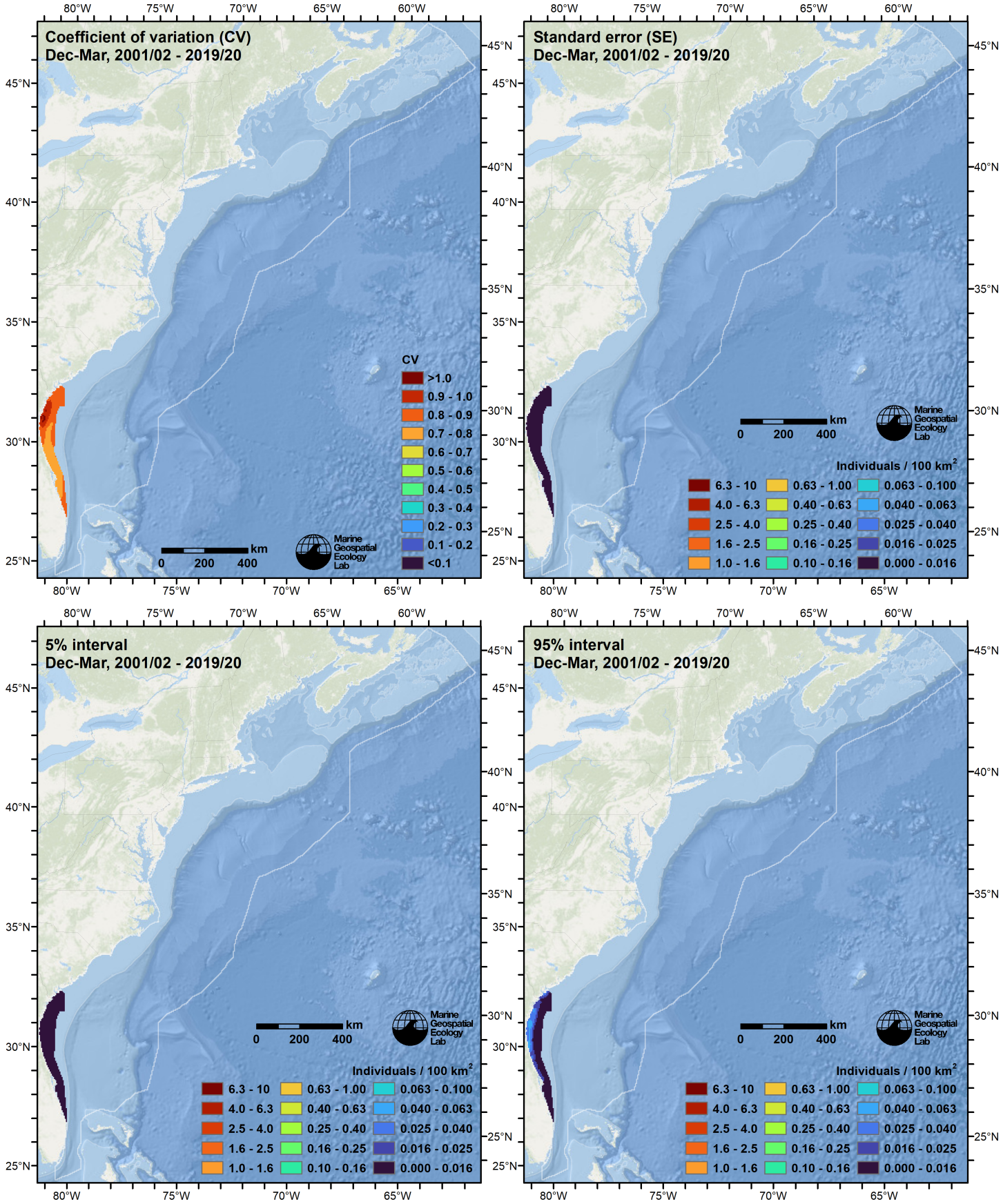

Figure 85: Uncertainty statistics for the humpback whale mean density surface (Figure 84) predicted by the model for the region FL-GA NARW EWS Area for Winter. Variance was estimated with the analytic approach given by Miller et al. (2022), Appendix S1, and accounts both for uncertainty in model parameter estimates, the mean difference in density between the eras (via Era as a factor covariate), and for seasonal variability in dynamic covariates but not interannual variability in them, as these covariates were monthly climatological averages.

Statistical output for this model:

```
Family: Tweedie(p=1.033)
Link function: log

Formula:
IndividualsCorrected ~ offset(log(SegmentArea)) + Era + s(pmax(1100,
    pmin(ClimPP_VGPM, 4200)), bs = "ts")

Parametric coefficients:
             Estimate Std. Error t value Pr(>|t|)
(Intercept)  -25.0958     0.2715  -92.44  < 2e-16 ***
Era2010-2020   1.9264     0.2871    6.71 1.95e-11 ***
---
Signif. codes:  0 ’***’ 0.001 ’**’ 0.01 ’*’ 0.05 ’.’ 0.1 ’ ’ 1

Approximate significance of smooth terms:
                                        edf Ref.df    F p-value
s(pmax(1100, pmin(ClimPP_VGPM, 4200))) 1.121      9 4.19  <2e-16 ***
---
Signif. codes:  0 ’***’ 0.001 ’**’ 0.01 ’*’ 0.05 ’.’ 0.1 ’ ’ 1

R-sq.(adj) =  0.000415   Deviance explained =    8%
-REML =  837.5  Scale est. = 3.2337    n = 256770

Method: REML   Optimizer: outer newton
full convergence after 17 iterations.
Gradient range [-7.53309e-05,9.209866e-11]
(score 837.5007 & scale 3.233703).
Hessian positive definite, eigenvalue range [0.548958,2845.32].
Model rank =  11 / 11

Basis dimension (k) checking results. Low p-value (k-index<1) may
indicate that k is too low, especially if edf is close to k’.

                                        k’  edf k-index p-value
s(pmax(1100, pmin(ClimPP_VGPM, 4200))) 9.00 1.12    0.13  <2e-16 ***
---
Signif. codes:  0 ’***’ 0.001 ’**’ 0.01 ’*’ 0.05 ’.’ 0.1 ’ ’ 1
```

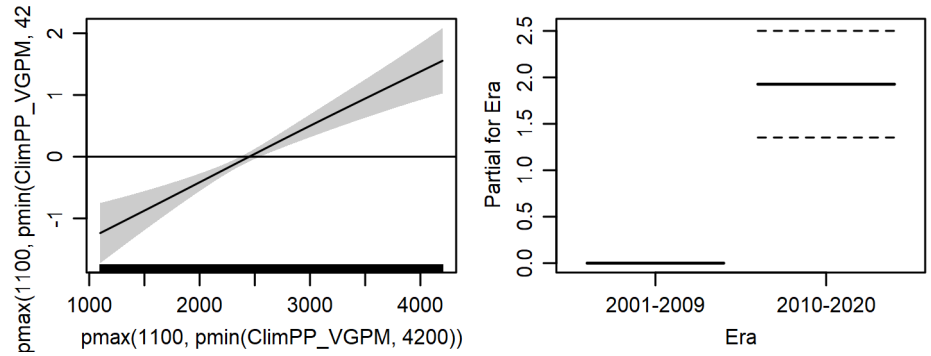

(a) Climatological net primary productivity (mg C m^{-2} day^{-1}) (VGPM)

(b) Era

Figure 86: Functional plots for the final model for the region FL-GA NARW EWS Area for Winter. Transforms and other treatments are indicated in axis labels. *log10* indicates the covariate was $\log_{10}$ transformed. *pmax* and *pmin* indicate the covariate's minimum and maximum values, respectively, were Winsorized to the values shown. Winsorization was used to prevent runaway extrapolations during prediction when covariates exceeded sampled ranges, or for ecological reasons, depending on the covariate. */1000* indicates meters were transformed to kilometers for interpretation convenience.

Table 27: Covariates used in the final model for the region FL-GA NARW EWS Area for Winter.

Covariate	Description
ClimPP_VGPM	Climatological monthly mean net primary productivity (mg C m^{-2} day^{-1}) from the Vertically Generalized Production Model (VGPM) (Behrenfeld and Falkowski (1997))

4.1.2.2 Diagnostic Plots

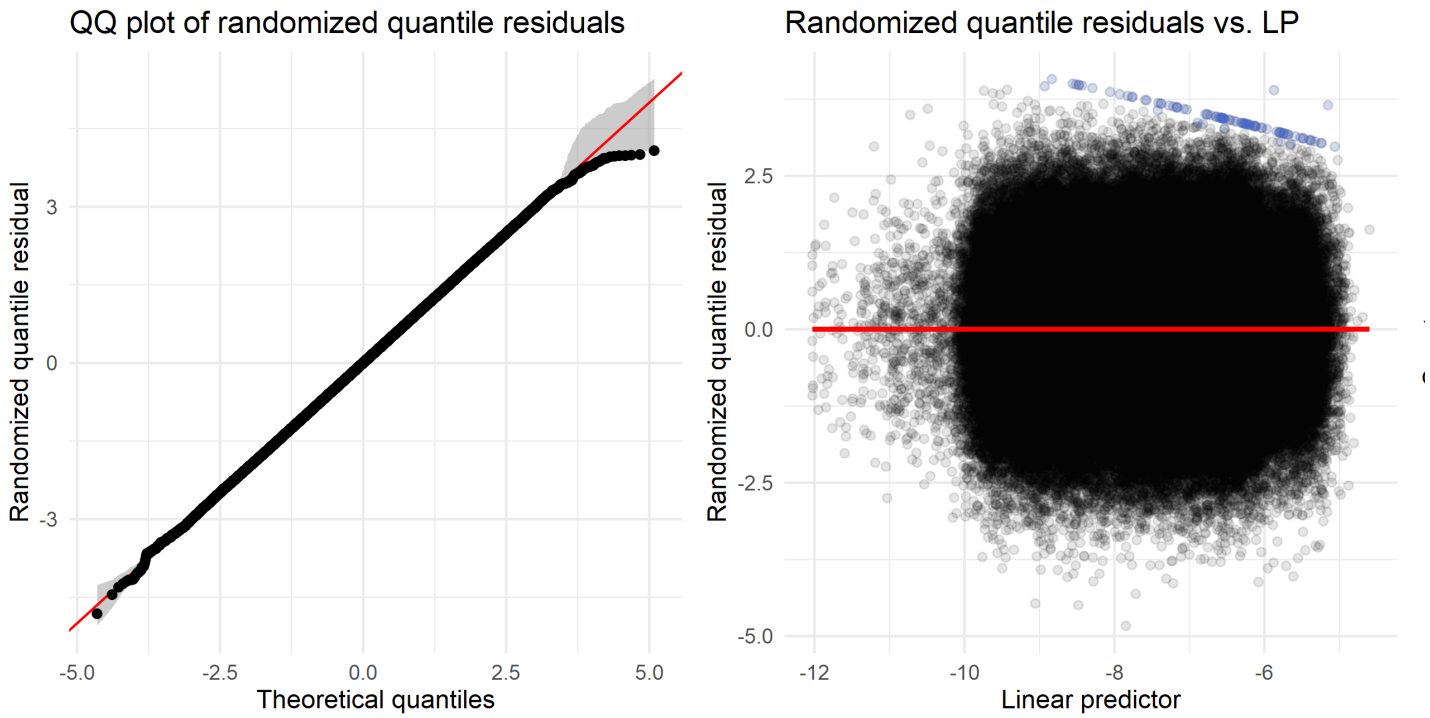

Figure 87: Residual plots for the final model for the region FL-GA NARW EWS Area for Winter.

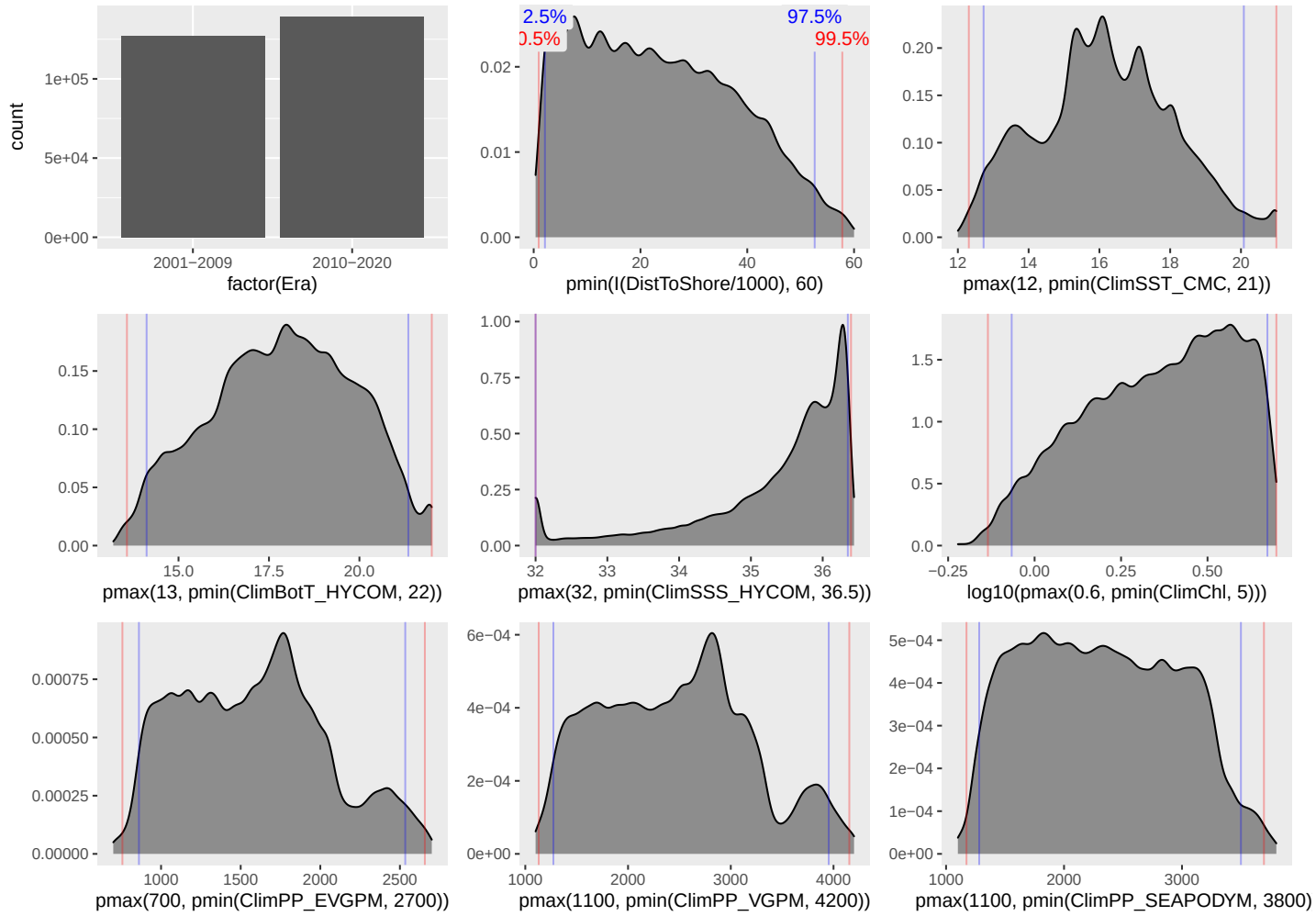

Figure 88: Density histograms showing the distributions of the covariates considered during the final model selection step. The final model may have included only a subset of the covariates shown here (see Figure 86), and additional covariates may have been considered in preceding selection steps. Red and blue lines enclose 99% and 95% of the distributions, respectively. Transforms and other treatments are indicated in axis labels. *log10* indicates the covariate was $\log_{10}$ transformed. *pmax* and *pmin* indicate the covariate's minimum and maximum values, respectively, were Winsorized to the values shown. Winsorization was used to prevent runaway extrapolations during prediction when covariates exceeded sampled ranges, or for ecological reasons, depending on the covariate. */1000* indicates meters were transformed to kilometers for interpretation convenience.

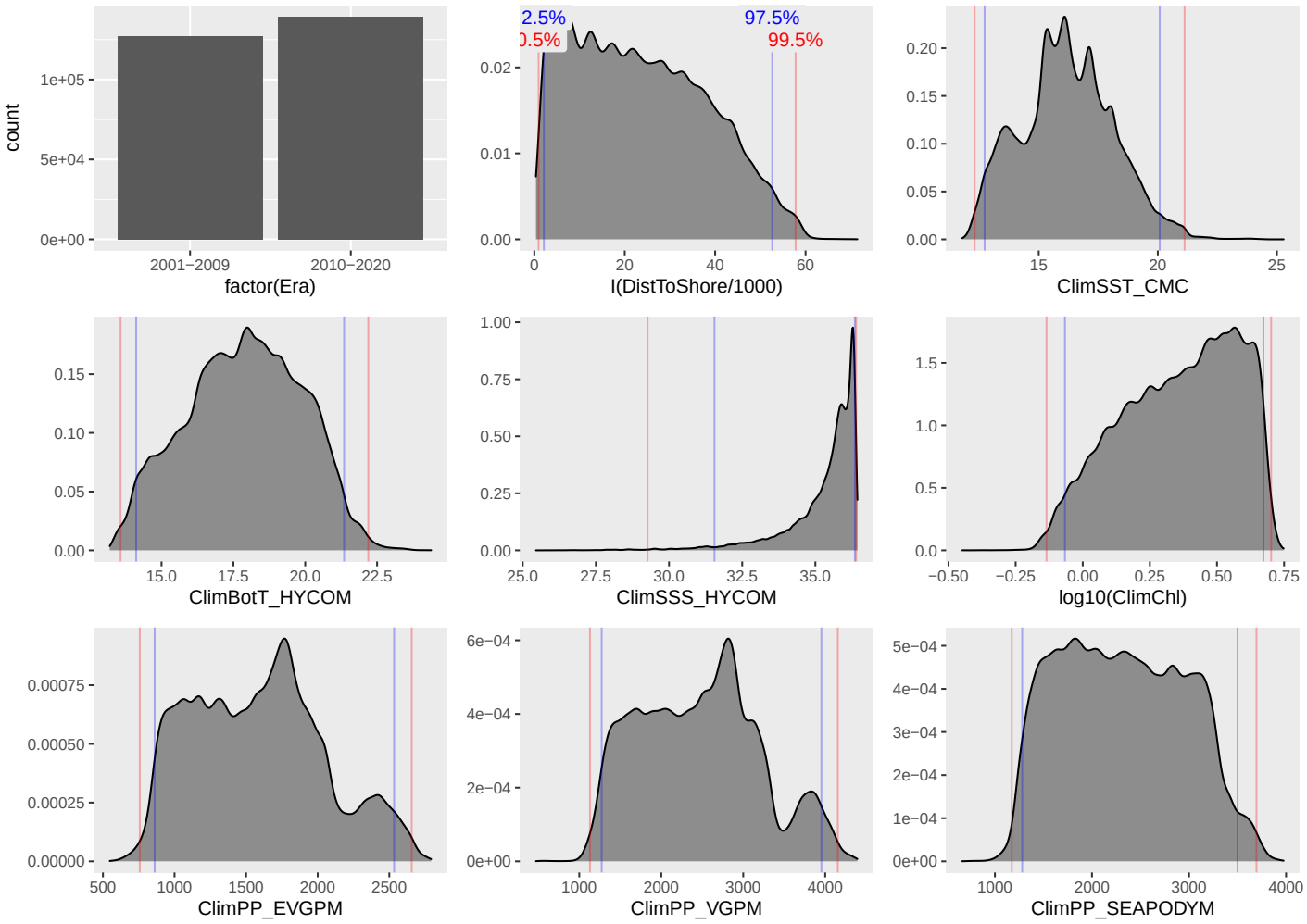

Figure 89: Density histograms shown in Figure 88 replotted without Winsorization, to show the full range of sampling represented by survey segments.

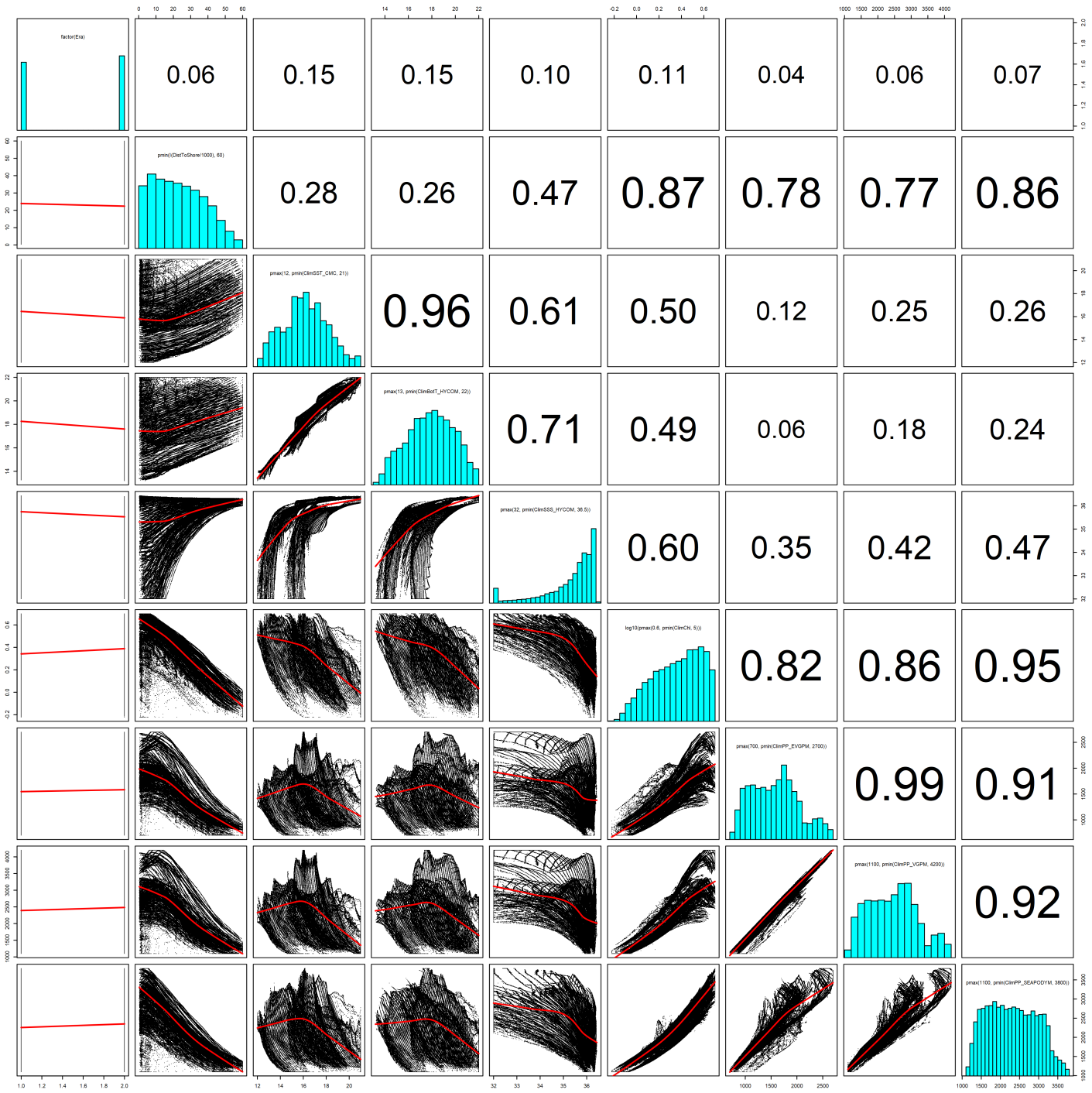

Figure 90: Scatterplot matrix of the covariates considered during the final model selection step. The final model may have included only a subset of the covariates shown here (see Figure 86), and additional covariates may have been considered in preceding selection steps. Covariates are transformed and Winsorized as shown in Figure 88. This plot is used to check simple correlations between covariates (via pairwise Pearson coefficients above the diagonal) and visually inspect for concurvity (via scatterplots and red lowess curves below the diagonal).

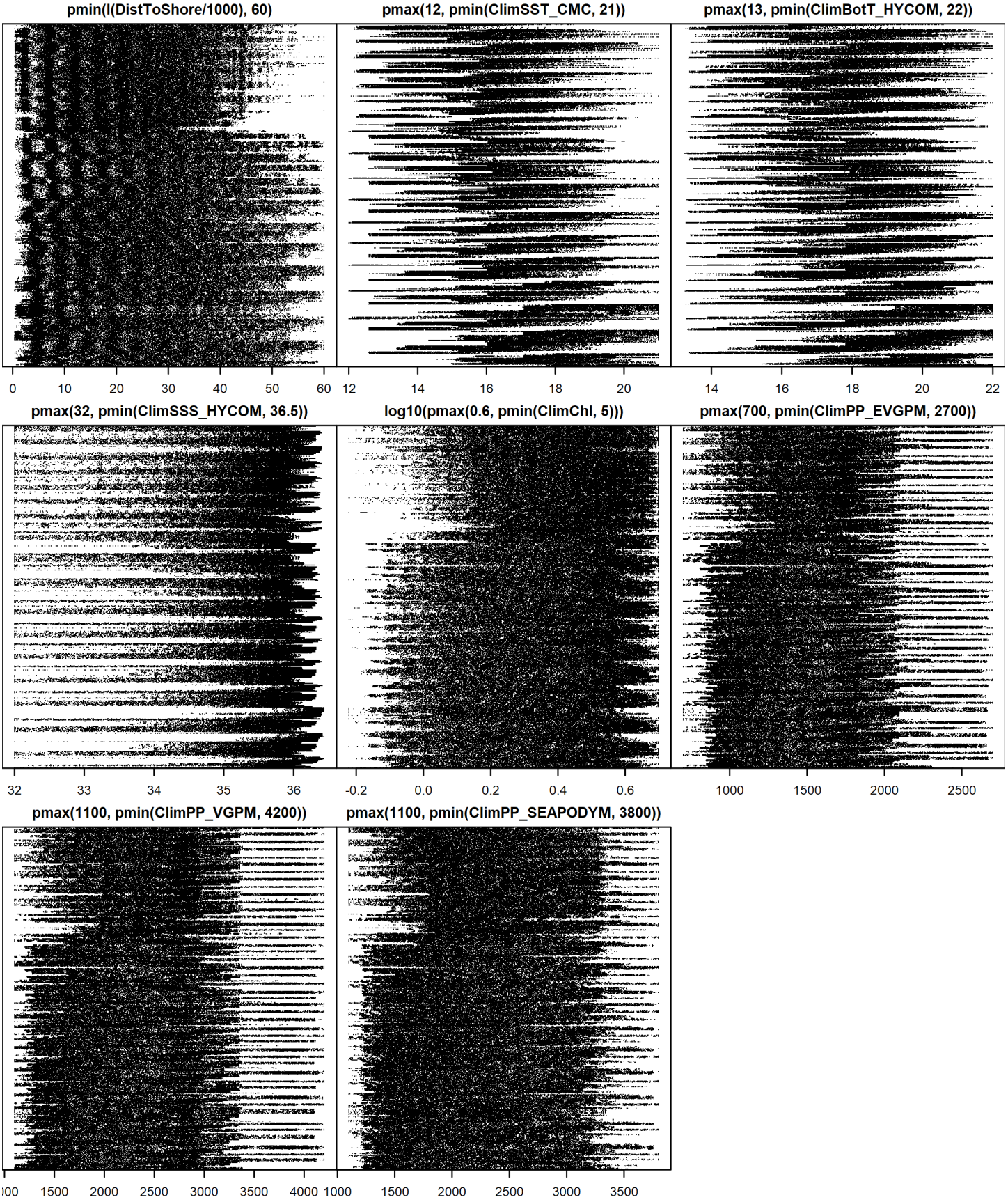

Figure 91: Dotplot of the covariates considered during the final model selection step. The final model may have included only a subset of the covariates shown here (see Figure 86), and additional covariates may have been considered in preceding selection steps. Covariates are transformed and Winsorized as shown in Figure 88. This plot is used to check for suspicious patterns and outliers in the data. Points are ordered vertically by segment ID, sequentially in time.

4.1.2.3 Extrapolation Diagnostics

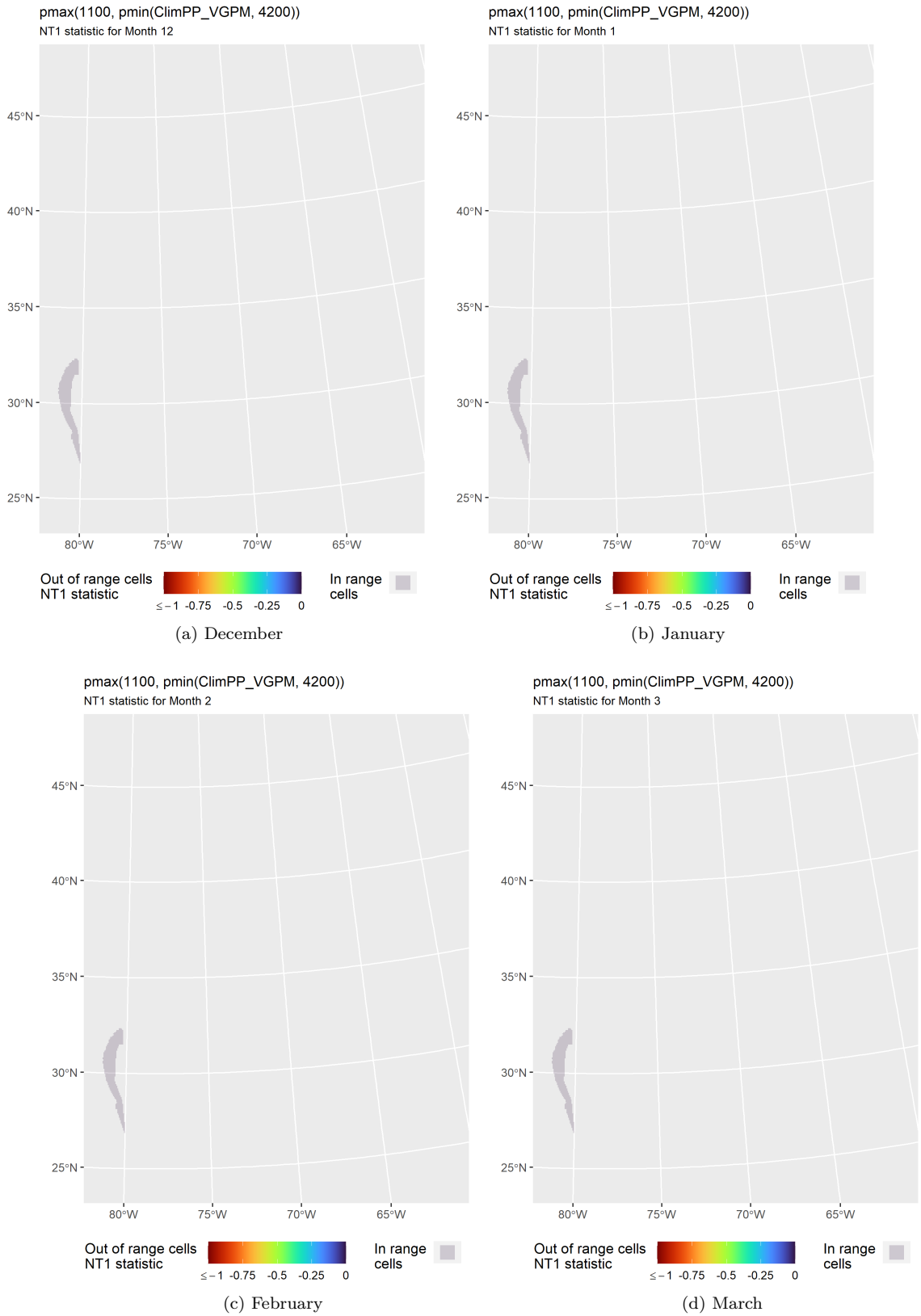

(a) December (b) January

(c) February (d) March

Figure 92: NT1 statistic ((ref:Mod2EXmesgaran2014)) for the ClimPP_VGPM covariate in the model for the region FL-GA NARW EWS Area for Winter. Areas outside the sampled range of a covariate appear in color, indicating univariate extrapolation of that covariate occurred there during the month. Areas within the sampled range appear in gray, indicating it did not occur.

4.2 Summer

For summer (April-November), we fitted a single model spanning the entire study area. The surveys incorporated into the model logged over 1 million linear km of effort and more than 3800 sightings (Figure 93). Most were scattered across the continental shelf, from North Carolina to the northernmost extent of surveying, including the upper Bay of Fundy and the northeastern Scotian Shelf. Surveying of the Scotian Shelf was restricted mainly to July-September. Passive acoustic monitoring indicated consistent presence in preceding and following months (Davis et al. 2020; Delarue et al. 2022), so we believe it is reasonable to predict our model over the Scotian Shelf during those months, but advise caution. We note that acoustic detections were relatively low during July-September compared to the preceding and following months, which suggests density could actually be higher during those months, but this difference could also be due to seasonal changes in vocalization behavior.

Similar to North Atlantic right whale, the Gulf of Maine humpback whale population size has been modeled from photographic identifications with a capture-mark-recapture (CMR) method (Robbins and Pace 2018). The most recently available iteration of this analysis, in the 2019 NOAA Stock Assessment Report, showed a steady rise in the population from 2001-2010 followed by flat and slightly negative period from 2011-2013, followed by a recovery in 2014-2016 (Hayes et al. 2020 humpback whale Figure 3). Given knowledge that the summer population had grown while appearing to maintain roughly the same spatial distribution, we included Year as a continuous (smoothed) covariate in the model to account for this growth, which we assumed would be poorly explained by contemporaneous oceanographic covariates on the feeding grounds. To try to constrain this covariate to the main trend in the population and maintain its interpretability, we limited it to basis functions with three degrees of freedom (`k=4`).

The model selection procedure yielded a large number of candidate models, most showing complex functional relationships, owing to the large number of segments and sightings used to fit the model, and that the model spanned several regional ecosystems where humpbacks were present (e.g. the Mid-Atlantic Bight, the New York Bight, the Gulf of Maine, and the Scotian Shelf). When ranked by REML score (Wood 2011), the highest ranked models with climatological covariates slightly outranked those with contemporaneous covariates and explained 0.5-0.8% more deviance. However, predictions from the best climatological-covariate models showed some extreme values along coastal Maine early in the season, where humpbacks were present according to acoustic monitoring but survey effort was sparse. The highest ranked contemporaneous model did not show this problem so we selected it as best.

The model was one of the most complex among all of those in our circa-2022 cetacean density models. In addition to the Year covariate, it retained three static covariates and four dynamic covariates (Table 28). All of the relationships fitted to covariates other than Year were complex, with least 5 effective degrees of freedom (Figure 96).

The relationship fitted for Year resembled the population trend estimated in the SAR's CMR model (Hayes et al. 2020 humpback whale Figure 3A), with a strong rise until about 2010, then a slight dip followed by a slight rise. The timing of the slight dip and rise was stretched out over the 2011-2020 period, rather than 2011-2016 as occurred in the SAR's CMR model. Nevertheless, we interpreted the relationship fitted to Year as conforming to the CMR model's trend well enough that it was probably doing the job we intended, which was to account for population change and allow the other covariates to account for spatial and seasonal changes in density.

The relationship fitted for depth was bimodal, with a higher peak at 50 m and a lower one 800 m (1.7 and 2.9 in $\log_{10}$ scale, respectively). This relationship was hard to interpret; possibly the first hump was used to boost density across the mid-shelf southeast of Nantucket Shoals, while the second was used to account for a few sightings that occurred along the continental slope. The relationship for distance to the 125 m isobath showed a strong peak right at the isobath, likely reflecting an affinity of the species for the steep edges of banks in the Gulf of Maine (Hazen et al. 2009) and possibly the Scotian Shelf also, as well as the continental shelf down the mid-Atlantic. The relationship for fetch was hump-shaped and peaked at 45 km, indicating higher density close to shore but not in highly enclosed areas, consistent with where sightings occurred around Cape Cod, the edge of the Gulf of Maine, and Nova Scotia.

Turning to dynamic covariates, the relationship fitted for SST showed a positive influence on density between 3-23 °C, one of the widest ranges for baleen whales that we modeled and reflecting the presence of humpbacks both in cold, northern waters and warm, mid-Atlantic waters throughout the season. The relationship for sea surface salinity showed a peak at slightly saltier than 32 PSU, and a strong decline in saltier waters, indicating an avoidance of waters offshore and the shelf south of Cape Hatteras. The decline toward fresher waters indicated reduced density in estuarine environments, such as Long Island Sound, where whales were sighted opportunistically in recent years but not reported on any line transect surveys. The relationship fitted for primary productivity estimated by the VGPM model was hump-shaped, with a negative influence at both low values, as occurs in oligotrophic waters offshore, and high values, as occurs in estuarine and inshore waters. Finally, the relationship fitted for distance to SST fronts was complex but generally indicated higher density closer to fronts.

4.2.1 Final Model

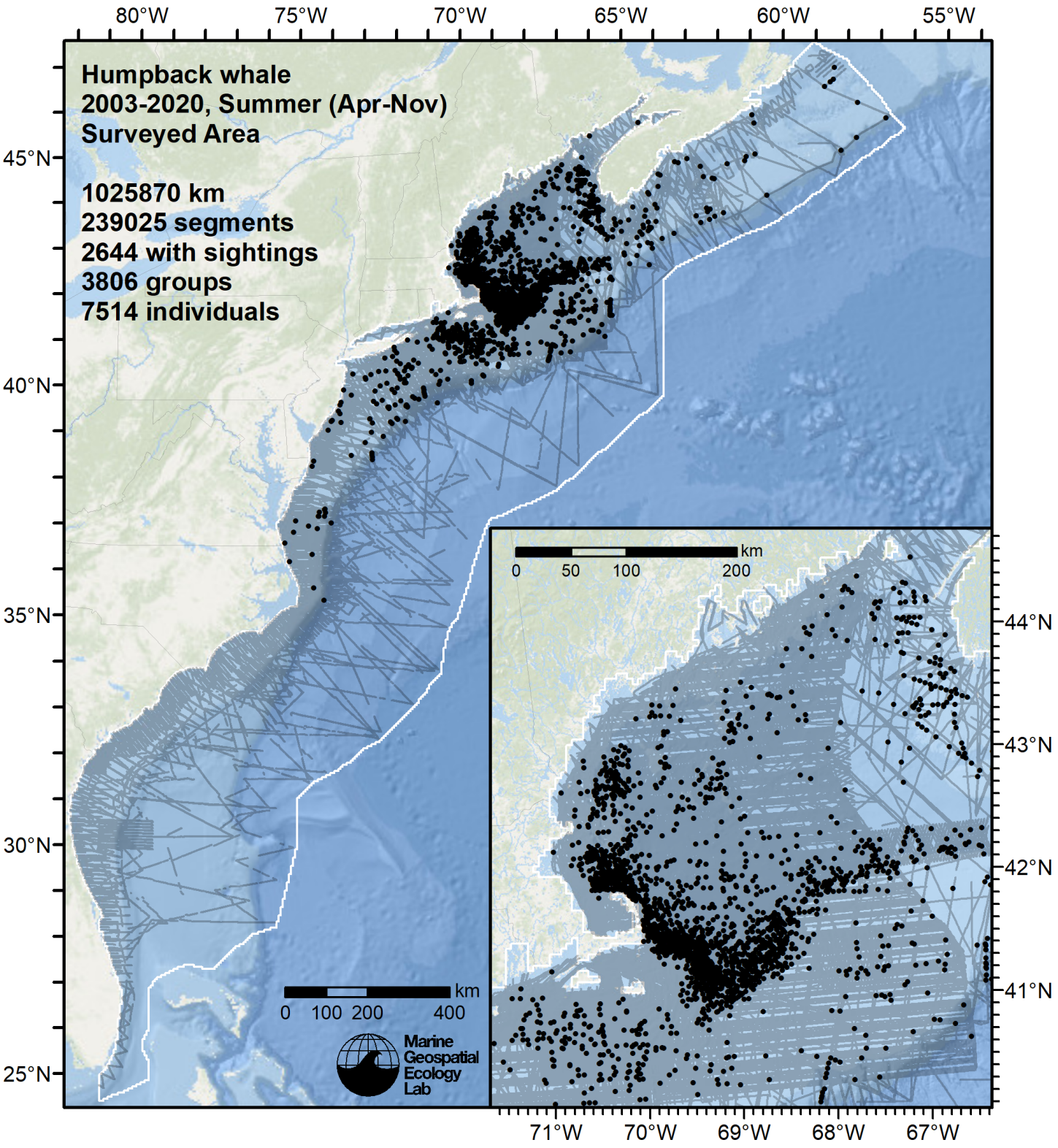

Figure 93: Survey segments used to fit the model for Summer. Black points indicate segments with observations.

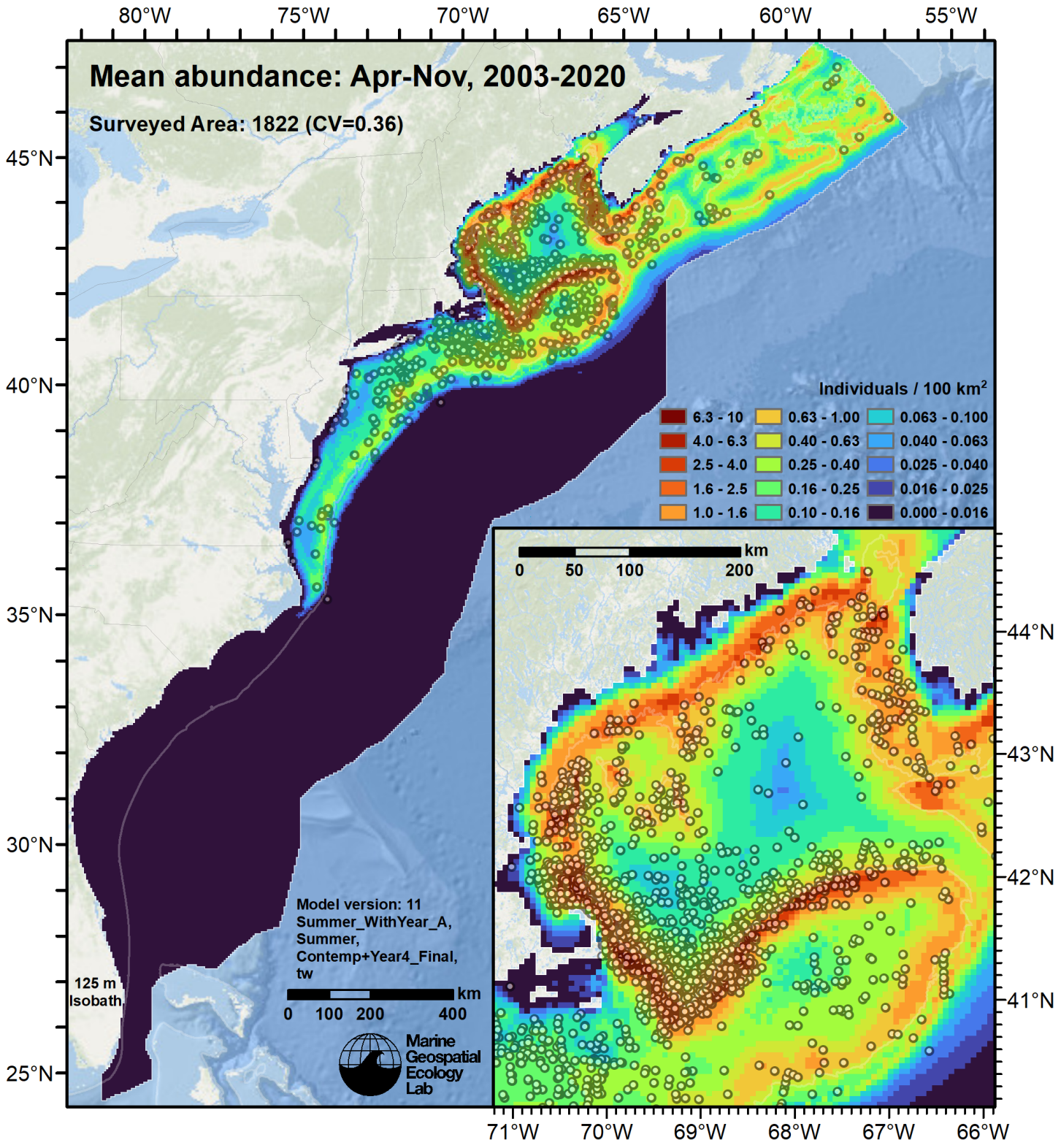

Figure 94: Humpback whale mean density for the indicated period, as predicted by the model for Summer. Open circles indicate segments with observations. Mean total abundance and its coefficient of variation (CV) are given in the subtitle. Variance was estimated with the analytic approach given by Miller et al. (2022), Appendix S1, and accounts both for uncertainty in model parameter estimates and for seasonal and interannual variability in dynamic covariates.

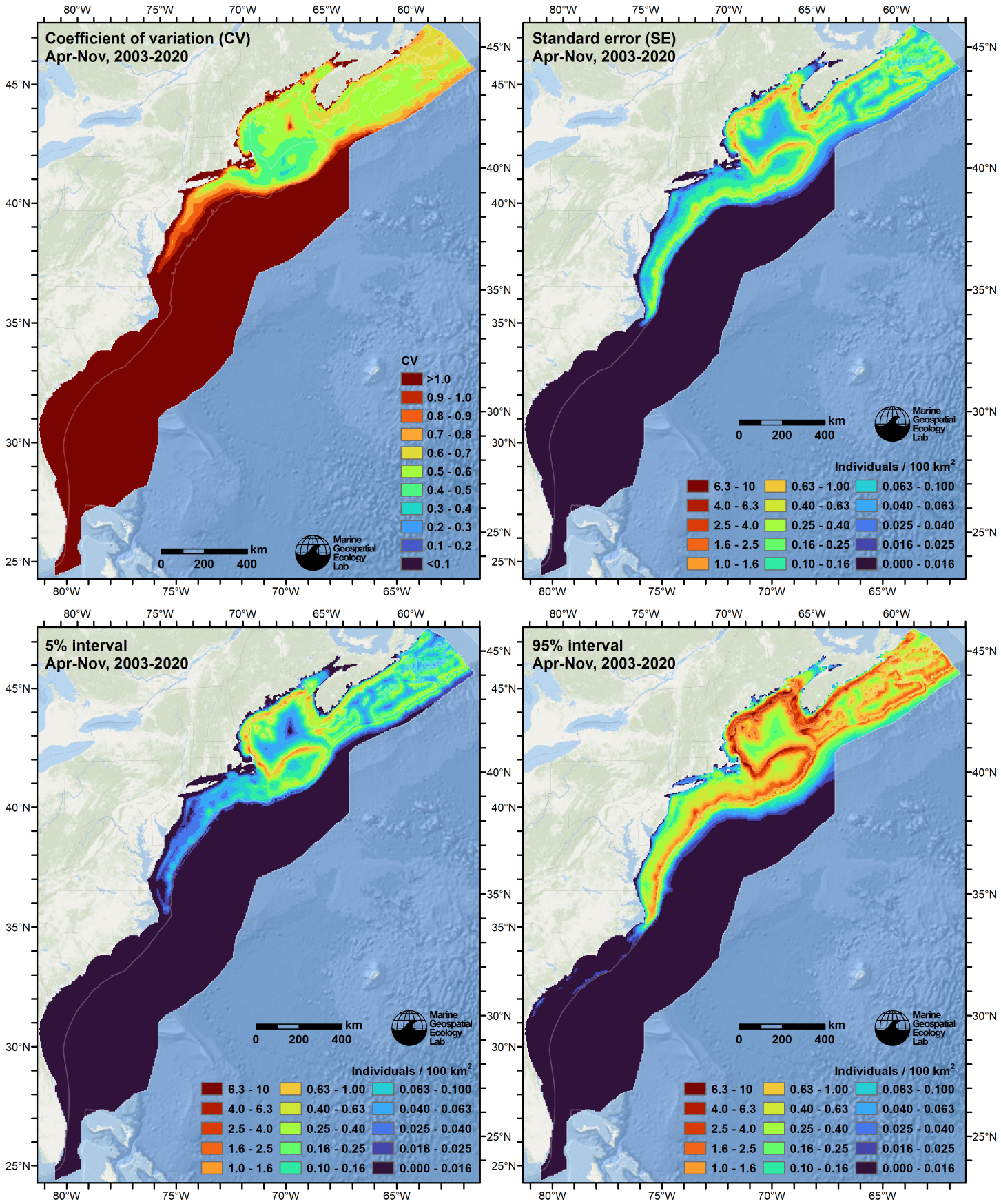

Figure 95: Uncertainty statistics for the humpback whale mean density surface (Figure 94) predicted by the model for Summer. Variance was estimated with the analytic approach given by Miller et al. (2022), Appendix S1, and accounts both for uncertainty in model parameter estimates and for seasonal and interannual variability in dynamic covariates.

Statistical output for this model:

```
Family: Tweedie(p=1.229)
Link function: log

Formula:
IndividualsCorrected ~ offset(log(SegmentArea)) + s(Year, bs = "ts",
    k = 4) + s(pmax(20, Fetch_50km), bs = "ts") + s(log10(pmax(3,
    pmin(Depth, 2000))), bs = "ts") + s(pmax(-125, pmin(I(DistTo125m/1000),
    100)), bs = "ts") + s(SST_CMC, bs = "ts") + s(pmax(31, pmin(SSS_HYCOM,
    36.5)), bs = "ts") + s(pmin(I(DistToFront105/1000), 75),
    bs = "ts") + s(pmax(300, pmin(PP_VGPM, 3700)), bs = "ts")

Parametric coefficients:
            Estimate Std. Error t value Pr(>|t|)
(Intercept) -22.7337     0.2284  -99.53   <2e-16 ***
---
Signif. codes:  0 '***' 0.001 '**' 0.01 '*' 0.05 '.' 0.1 ' ' 1

Approximate significance of smooth terms:
                                           edf Ref.df       F p-value
s(Year)                                  2.780      3  35.960  <2e-16 ***
s(pmax(20, Fetch_50km))                  5.578      9  15.413  <2e-16 ***
s(log10(pmax(3, pmin(Depth, 2000))))     7.670      9  22.546  <2e-16 ***
s(pmax(-125, pmin(I(DistTo125m/1000), 100))) 8.215      9 110.117  <2e-16 ***
s(SST_CMC)                               6.682      9  19.483  <2e-16 ***
s(pmax(31, pmin(SSS_HYCOM, 36.5)))       5.452      9  28.124  <2e-16 ***
s(pmin(I(DistToFront105/1000), 75))      5.262      9   5.728  <2e-16 ***
s(pmax(300, pmin(PP_VGPM, 3700)))        5.668      9  19.294  <2e-16 ***
---
Signif. codes:  0 '***' 0.001 '**' 0.01 '*' 0.05 '.' 0.1 ' ' 1

R-sq.(adj) =  0.0371   Deviance explained = 29.3%
-REML =  17825  Scale est. = 8.8073    n = 239025

Method: REML   Optimizer: outer newton
full convergence after 13 iterations.
Gradient range [-0.00116581,0.0006657252]
(score 17824.86 & scale 8.807338).
Hessian positive definite, eigenvalue range [1.102297,15013.07].
Model rank =  67 / 67

Basis dimension (k) checking results. Low p-value (k-index<1) may
indicate that k is too low, especially if edf is close to k'.

                                           k'  edf k-index p-value
s(Year)                                  3.00 2.78    0.86   0.040 *
s(pmax(20, Fetch_50km))                  9.00 5.58    0.89   0.620
s(log10(pmax(3, pmin(Depth, 2000))))     9.00 7.67    0.86   0.045 *
s(pmax(-125, pmin(I(DistTo125m/1000), 100))) 9.00 8.22    0.88   0.525
s(SST_CMC)                               9.00 6.68    0.83   0.005 **
s(pmax(31, pmin(SSS_HYCOM, 36.5)))       9.00 5.45    0.80  <2e-16 ***
s(pmin(I(DistToFront105/1000), 75))      9.00 5.26    0.87   0.160
s(pmax(300, pmin(PP_VGPM, 3700)))        9.00 5.67    0.85   0.030 *
---
Signif. codes:  0 '***' 0.001 '**' 0.01 '*' 0.05 '.' 0.1 ' ' 1
```

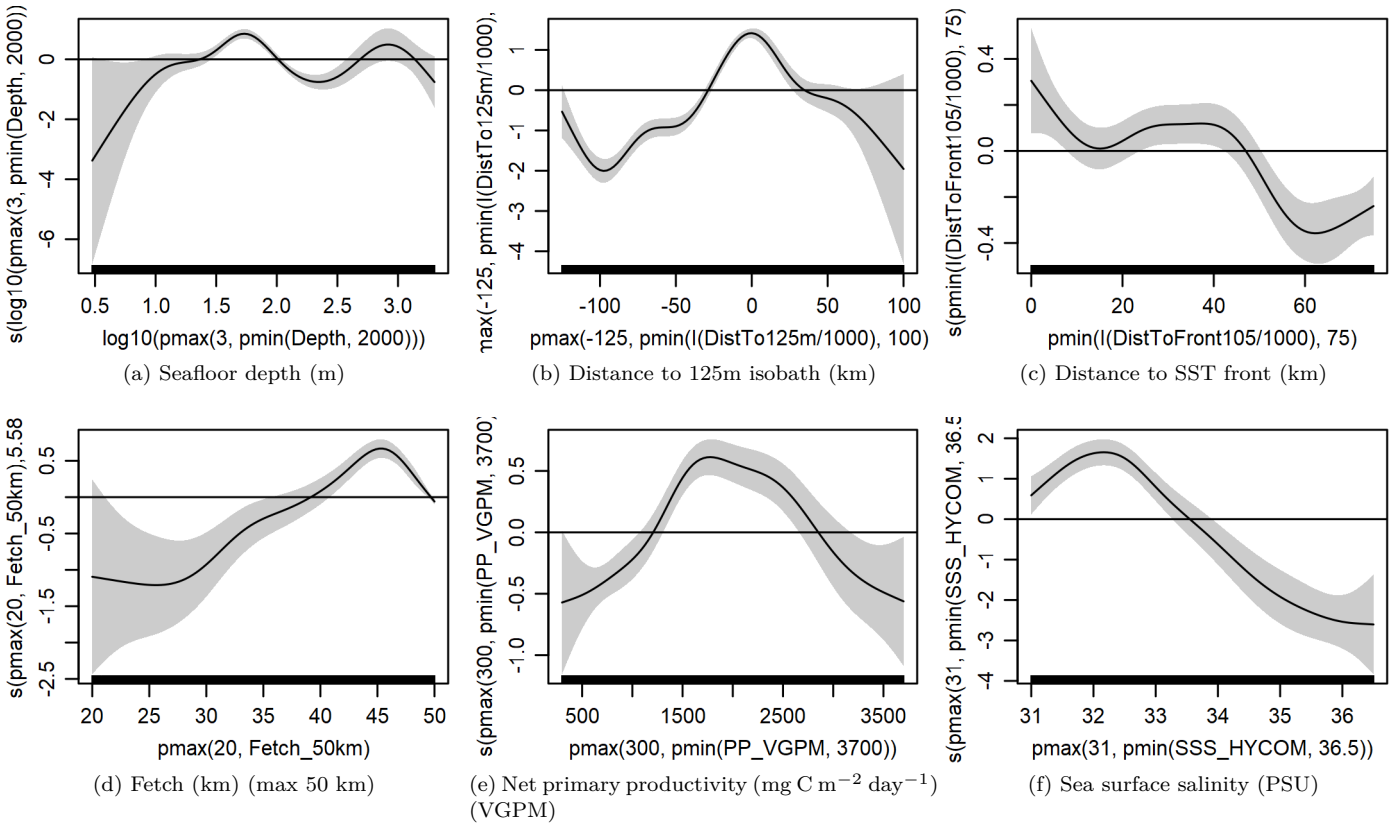

(a) Seafloor depth (m)

(b) Distance to 125m isobath (km)

(c) Distance to SST front (km)

(d) Fetch (km) (max 50 km)

(e) Net primary productivity (mg C m^{-2} day^{-1}) (VGPM)

(f) Sea surface salinity (PSU)

(g) Sea surface temperature (°C)

(h) Year

Figure 96: Functional plots for the final model for Summer. Transforms and other treatments are indicated in axis labels. *log10* indicates the covariate was $\log_{10}$ transformed. *pmax* and *pmin* indicate the covariate's minimum and maximum values, respectively, were Winsorized to the values shown. Winsorization was used to prevent runaway extrapolations during prediction when covariates exceeded sampled ranges, or for ecological reasons, depending on the covariate. */1000* indicates meters were transformed to kilometers for interpretation convenience.

Table 28: Covariates used in the final model for Summer.

Covariate	Description
Depth	Depth (m) of the seafloor, from SRTM30_PLUS (Becker et al. (2009))
DistTo125m	Distance (km) to the 125m isobath, derived from SRTM30_PLUS (Becker et al. (2009))
DistToFront105	Monthly mean distance (km) to the closest sea surface temperature front detected in daily GHRSST Level 4 CMC0.2deg and CMC0.1deg images (Brasnett (2008); Canada Meteorological Center (2012); Meissner et al. (2016); Canada Meteorological Center (2016)) with MGET's implementation of the Canny edge detector (Roberts et al. (2010); Canny (1986))

Table 28: Covariates used in the final model for Summer. *(continued)*

Covariate	Description
Fetch_50km	Fetch (km): mean distance to shore averaged over 16 radial directions, limited to a maximum of 50 km
PP_VGPM	Monthly mean net primary productivity (mg C m^{-2} day^{-1}) from the Vertically Generalized Production Model (VGPM) (Behrenfeld and Falkowski (1997))
SSS_HYCOM	Monthly mean sea surface salinity (PSU) from the HYCOM GOFS 3.1 1/12° ocean model (Chassignet et al. (2009))
SST_CMC	Monthly mean sea surface temperature (°C) from GHRSST Level 4 CMC0.2deg and CMC0.1deg (Brasnett (2008); Canada Meteorological Center (2012); Meissner et al. (2016); Canada Meteorological Center (2016))

4.2.2 Diagnostic Plots

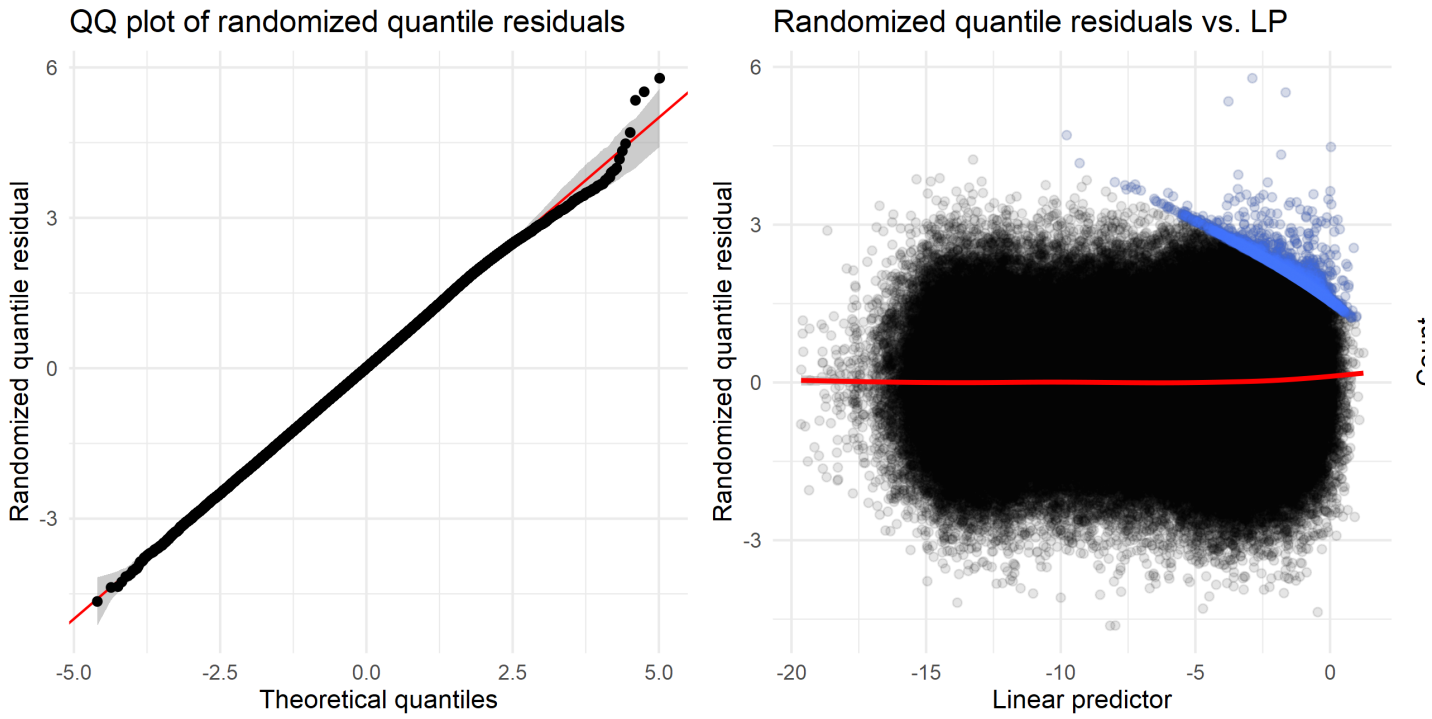

Figure 97: Residual plots for the final model for Summer.

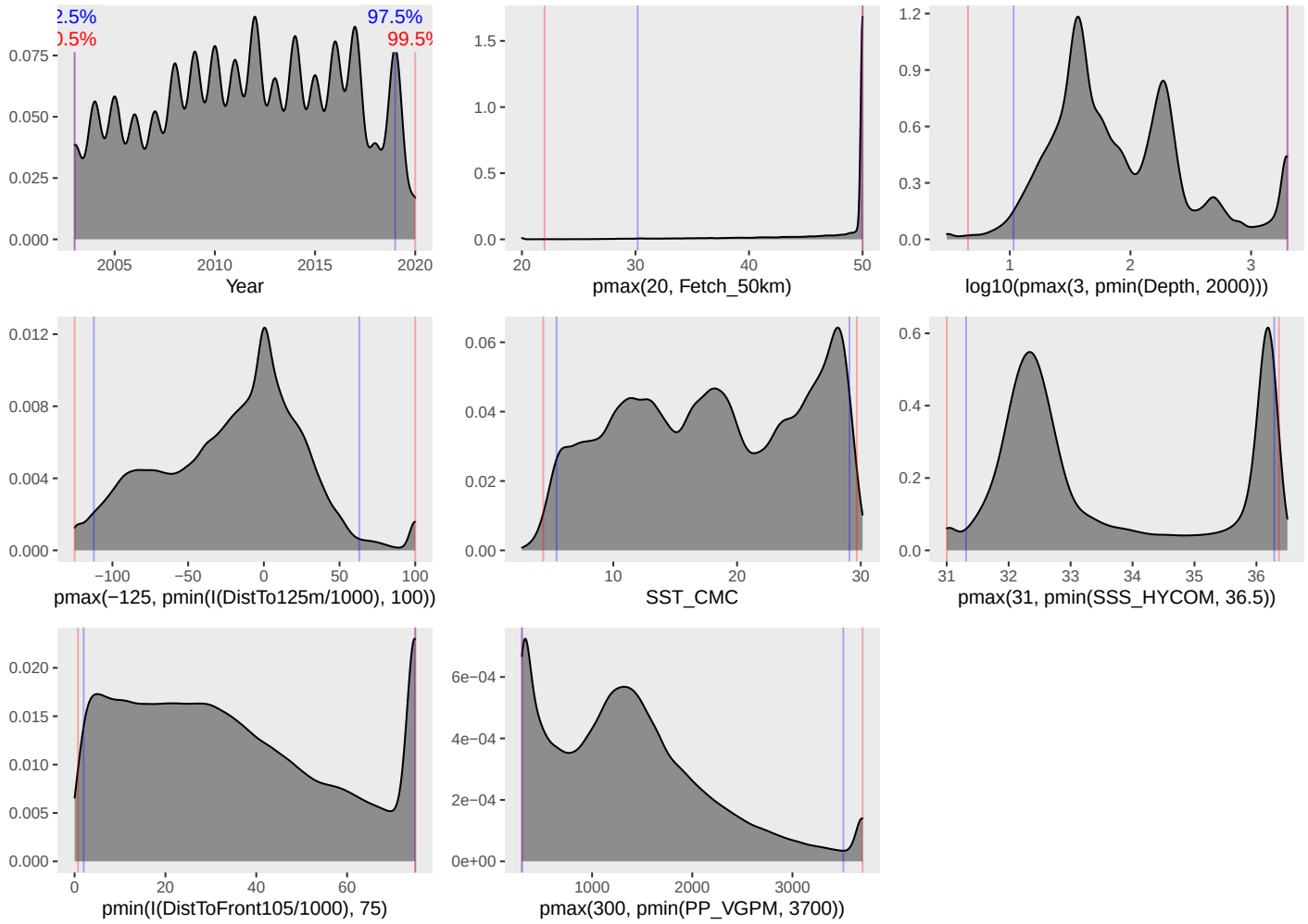

Figure 98: Density histograms showing the distributions of the covariates considered during the final model selection step. The final model may have included only a subset of the covariates shown here (see Figure 96), and additional covariates may have been considered in preceding selection steps. Red and blue lines enclose 99% and 95% of the distributions, respectively. Transforms and other treatments are indicated in axis labels. *log10* indicates the covariate was $\log_{10}$ transformed. *pmax* and *pmin* indicate the covariate's minimum and maximum values, respectively, were Winsorized to the values shown. Winsorization was used to prevent runaway extrapolations during prediction when covariates exceeded sampled ranges, or for ecological reasons, depending on the covariate. */1000* indicates meters were transformed to kilometers for interpretation convenience.

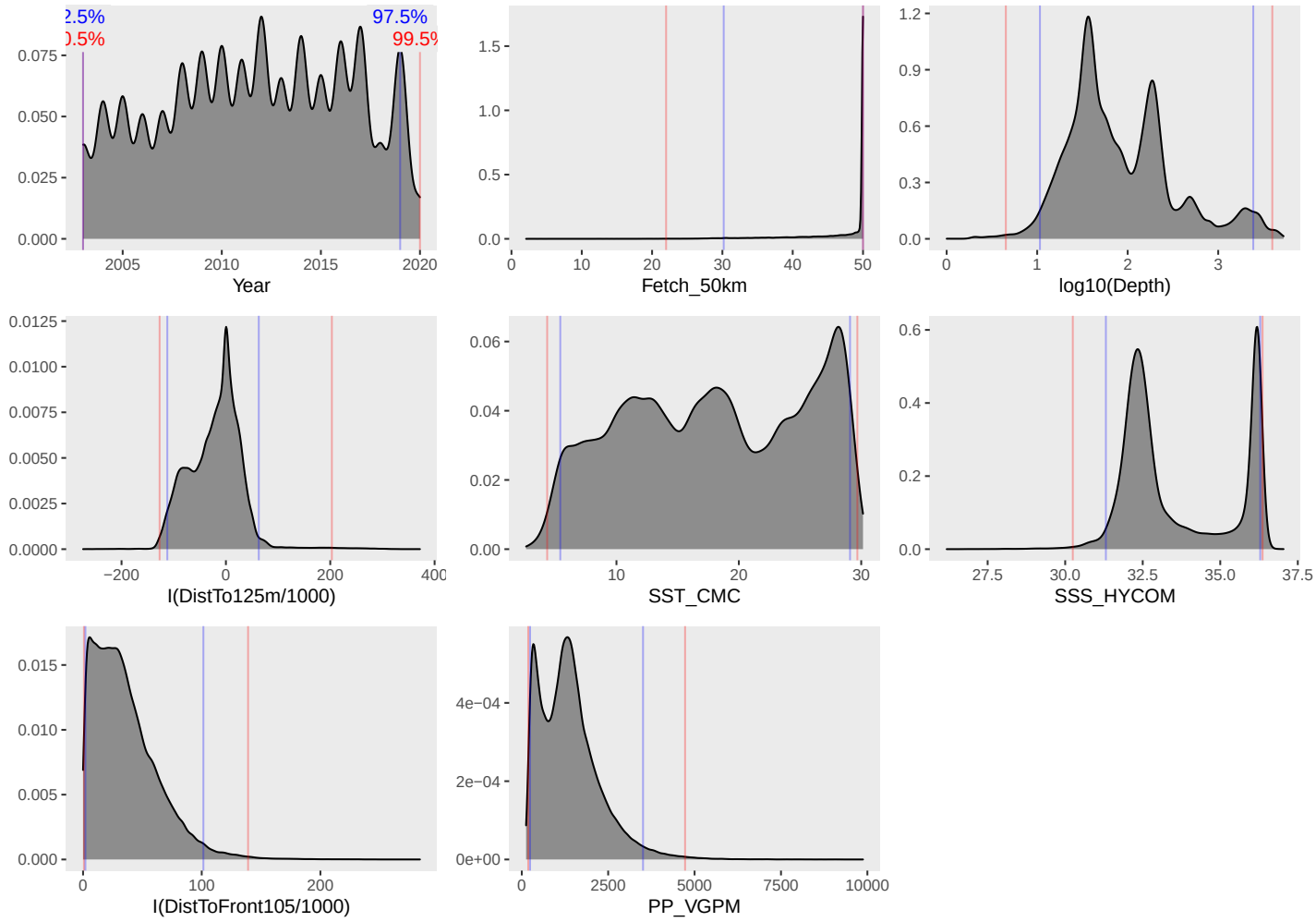

Figure 99: Density histograms shown in Figure 98 replotted without Winsorization, to show the full range of sampling represented by survey segments.

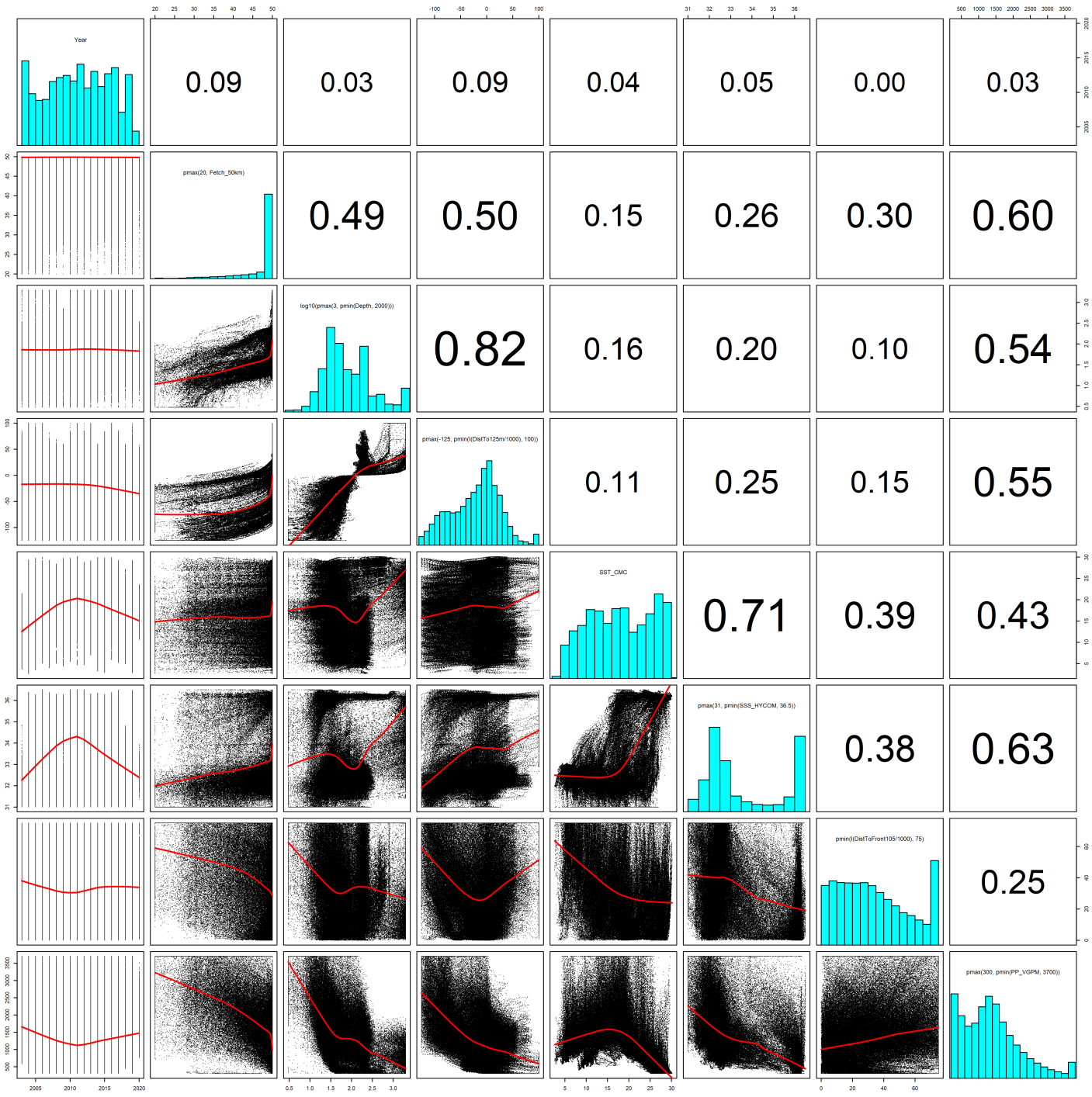

Figure 100: Scatterplot matrix of the covariates considered during the final model selection step. The final model may have included only a subset of the covariates shown here (see Figure 96), and additional covariates may have been considered in preceding selection steps. Covariates are transformed and Winsorized as shown in Figure 98. This plot is used to check simple correlations between covariates (via pairwise Pearson coefficients above the diagonal) and visually inspect for concurvity (via scatterplots and red lowess curves below the diagonal).

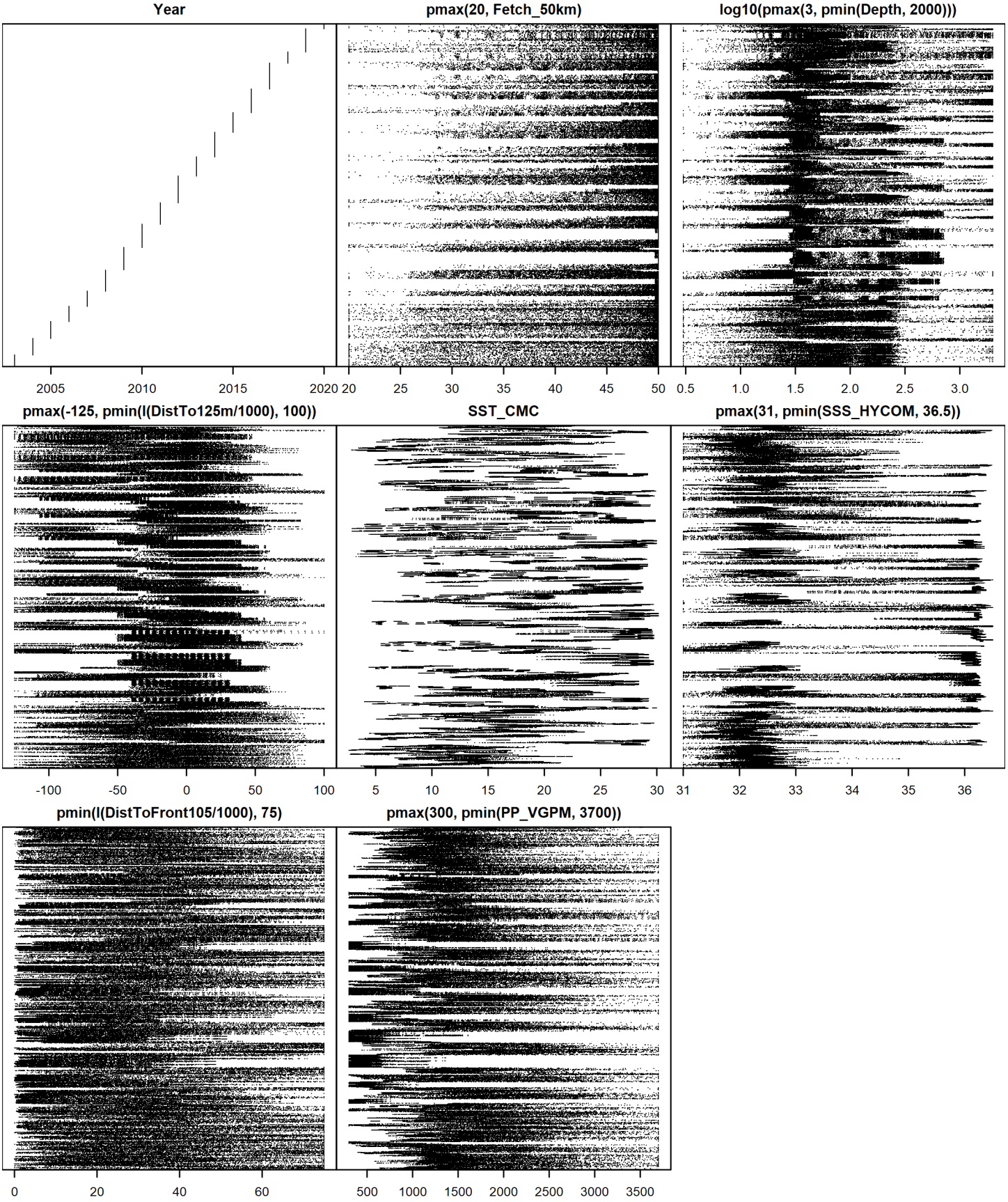

Figure 101: Dotplot of the covariates considered during the final model selection step. The final model may have included only a subset of the covariates shown here (see Figure 96), and additional covariates may have been considered in preceding selection steps. Covariates are transformed and Winsorized as shown in Figure 98. This plot is used to check for suspicious patterns and outliers in the data. Points are ordered vertically by segment ID, sequentially in time.

4.2.3 Extrapolation Diagnostics

4.2.3.1 Univariate Extrapolation

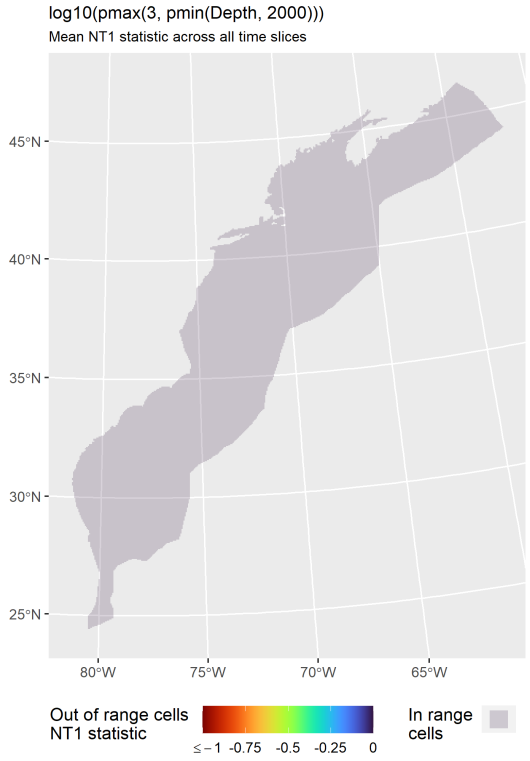

(a) Depth covariate

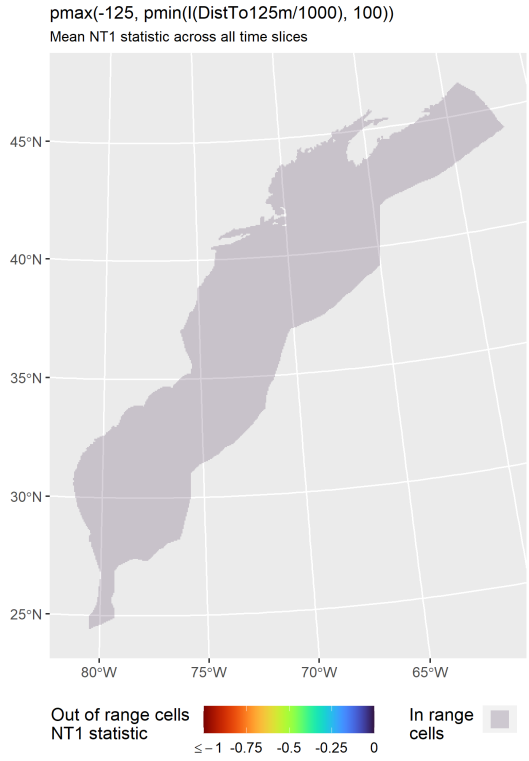

(b) DistTo125m covariate

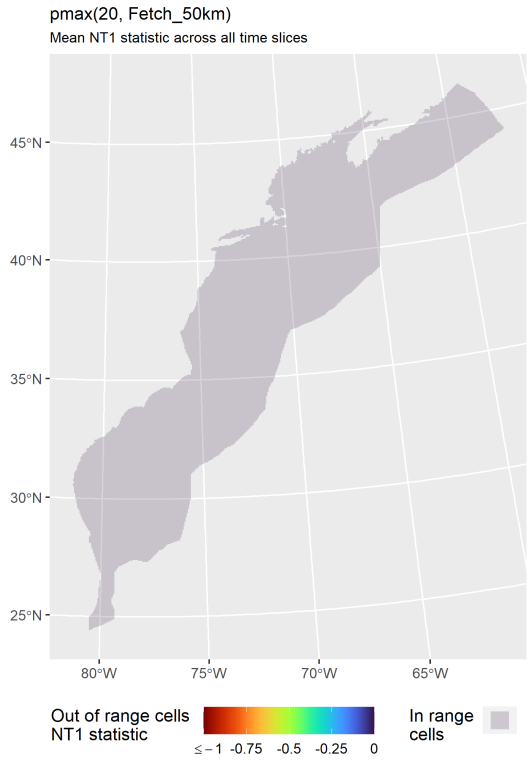

(c) Fetch_50km covariate

Figure 102: NT1 statistic (Mesgaran et al. (2014)) for static covariates used in the model for Summer. Areas outside the sampled range of a covariate appear in color, indicating univariate extrapolation of that covariate occurred there. Areas within the sampled range appear in gray, indicating it did not occur.

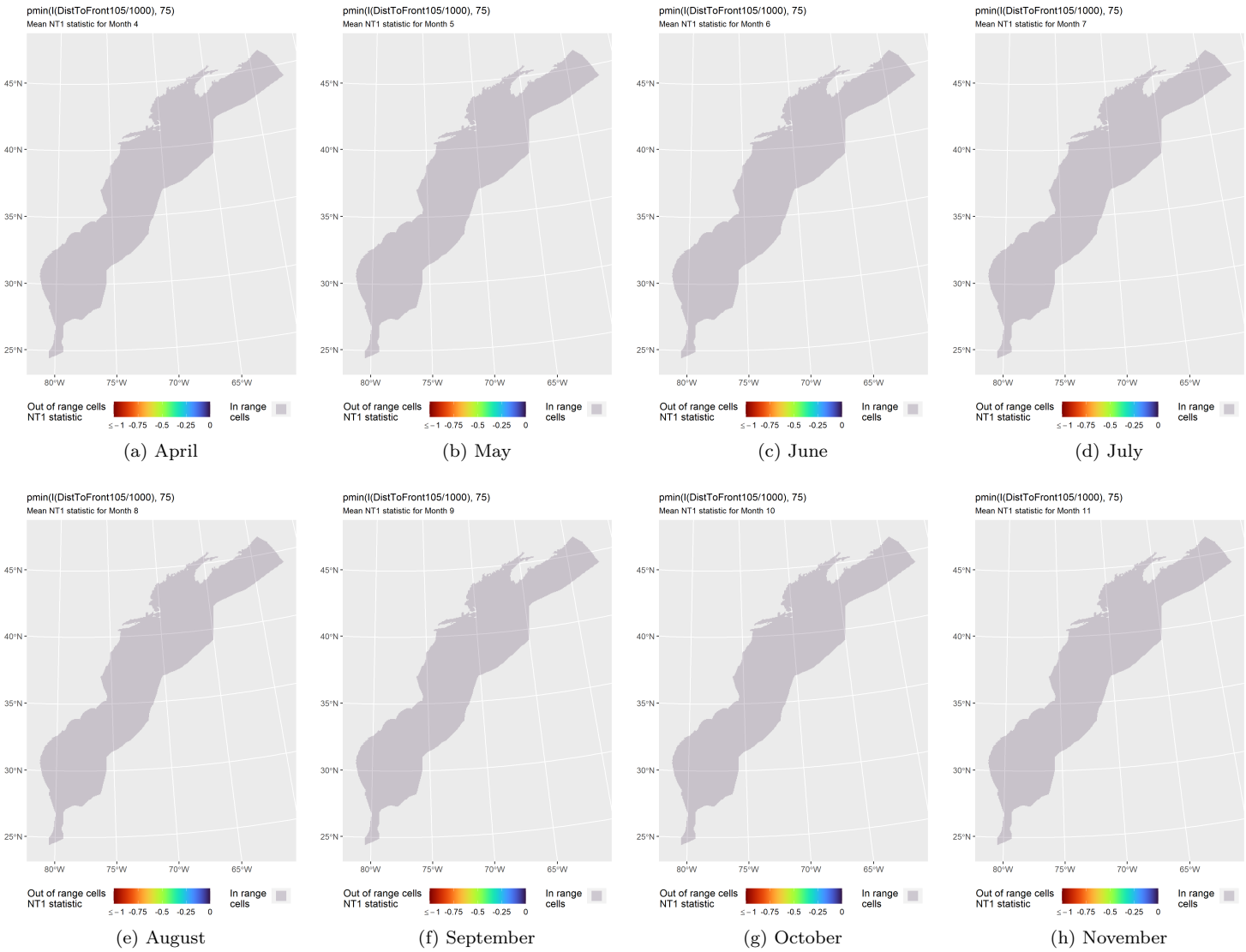

(a) April (b) May (c) June (d) July

(e) August (f) September (g) October (h) November

Figure 103: NT1 statistic (Mesgaran et al. (2014)) for the DistToFront105 covariate in the model for Summer. Areas outside the sampled range of a covariate appear in color, indicating univariate extrapolation of that covariate occurred there during the month. Areas within the sampled range appear in gray, indicating it did not occur.

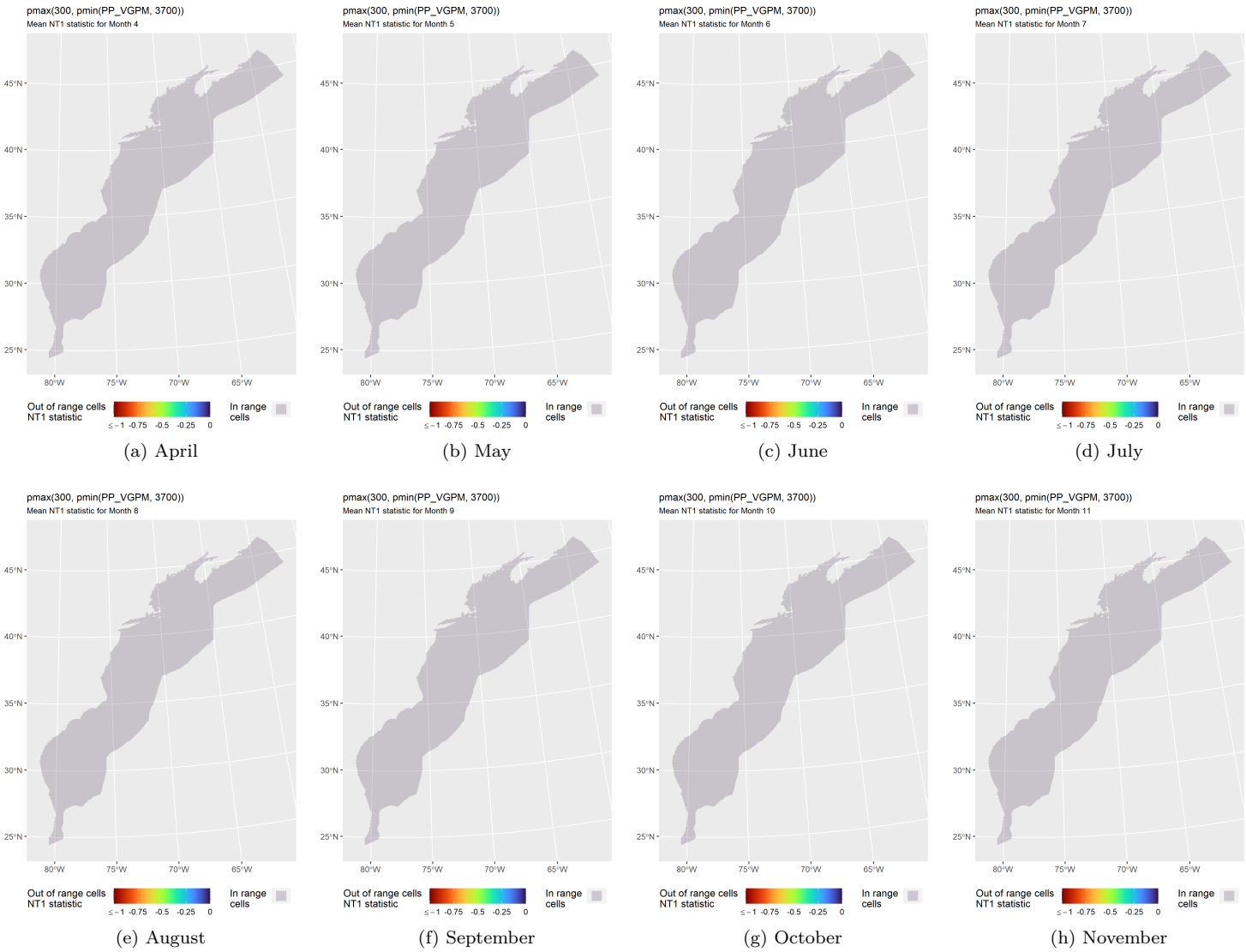

(a) April (b) May (c) June (d) July

(e) August (f) September (g) October (h) November

Figure 104: NT1 statistic (Mesgaran et al. (2014)) for the PP_VGPM covariate in the model for Summer. Areas outside the sampled range of a covariate appear in color, indicating univariate extrapolation of that covariate occurred there during the month. Areas within the sampled range appear in gray, indicating it did not occur.

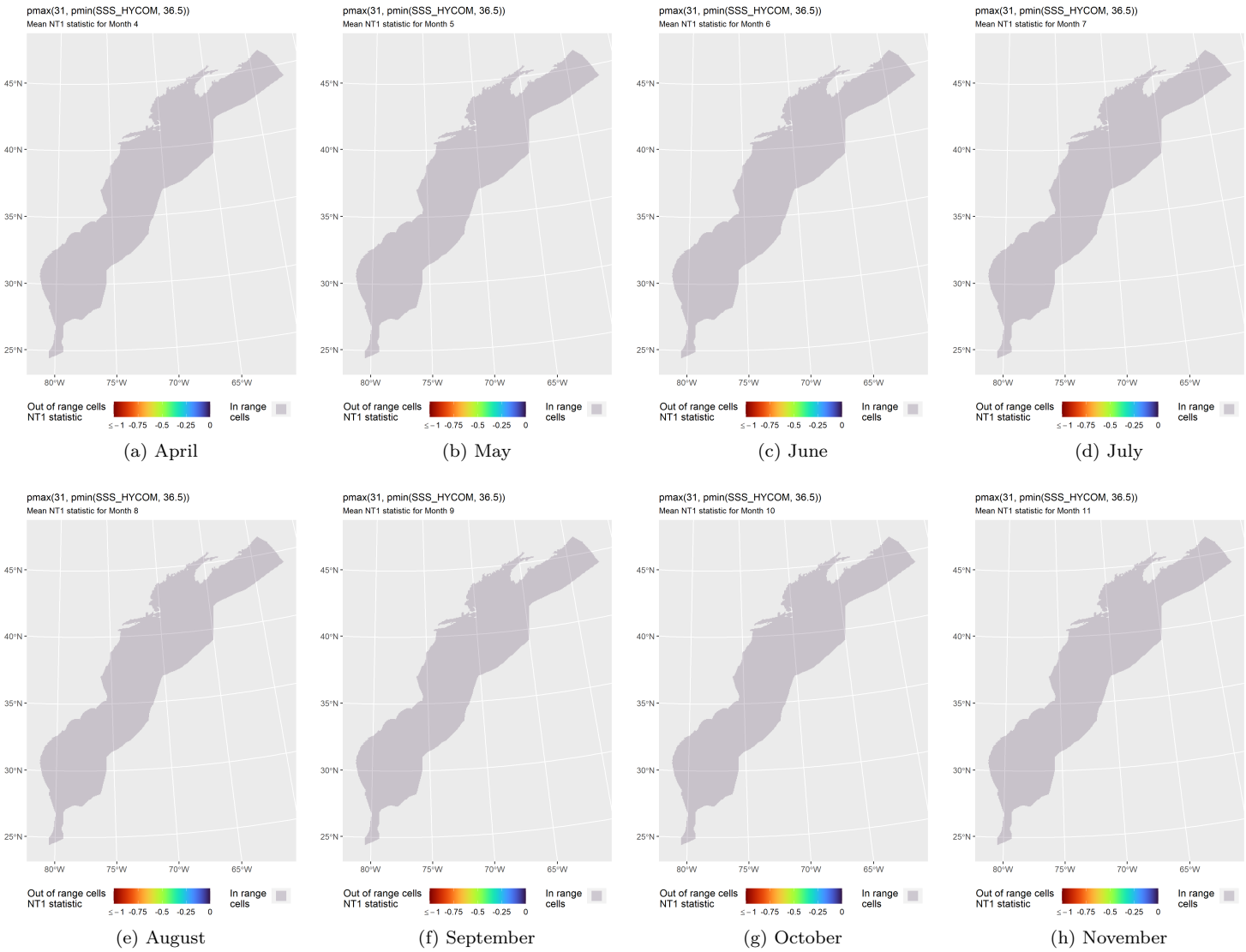

(a) April (b) May (c) June (d) July

(e) August (f) September (g) October (h) November

Figure 105: NT1 statistic (Mesgaran et al. (2014)) for the SSS_HYCOM covariate in the model for Summer. Areas outside the sampled range of a covariate appear in color, indicating univariate extrapolation of that covariate occurred there during the month. Areas within the sampled range appear in gray, indicating it did not occur.

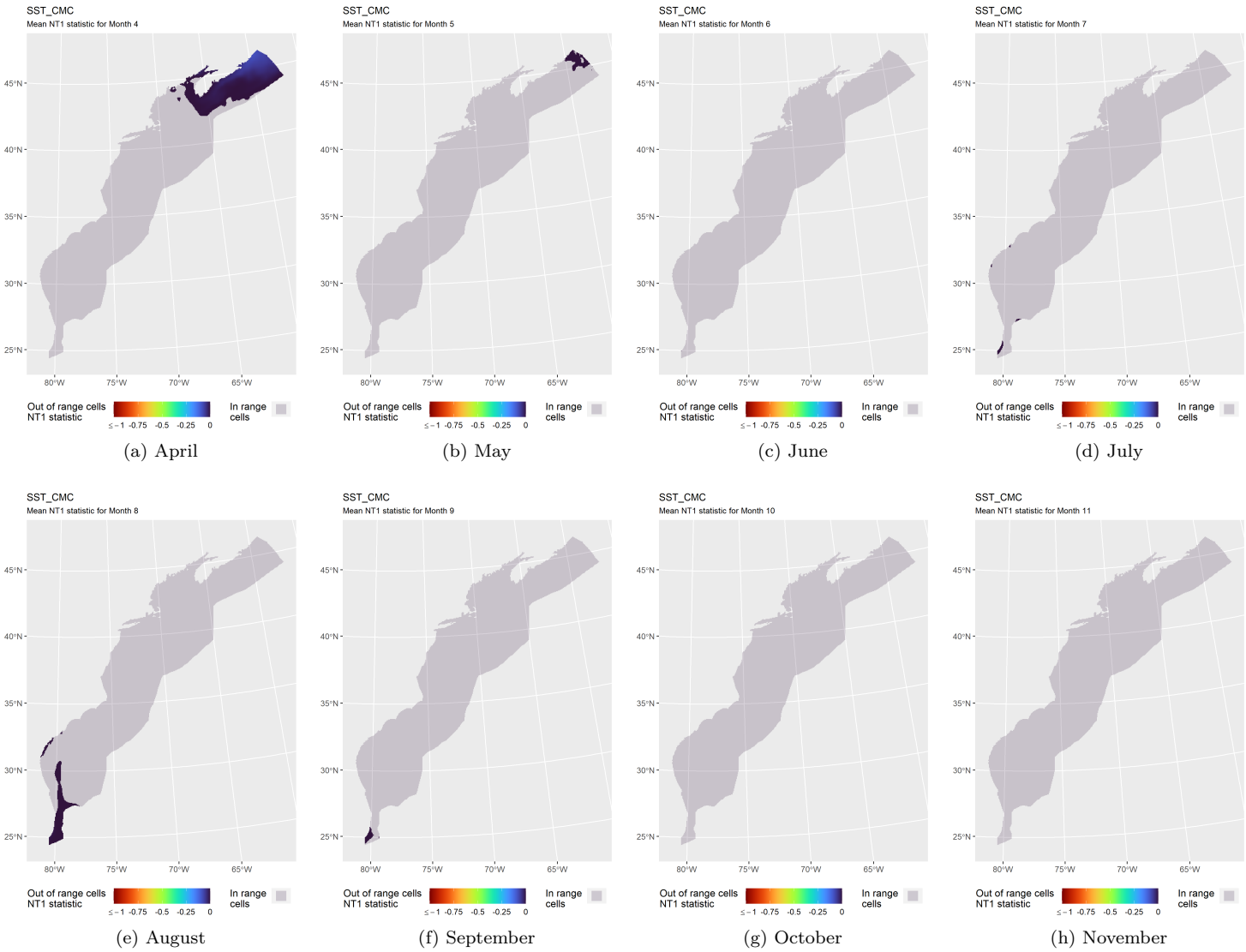

(a) April (b) May (c) June (d) July

(e) August (f) September (g) October (h) November

Figure 106: NT1 statistic (Mesgaran et al. (2014)) for the SST_CMC covariate in the model for Summer. Areas outside the sampled range of a covariate appear in color, indicating univariate extrapolation of that covariate occurred there during the month. Areas within the sampled range appear in gray, indicating it did not occur.

4.2.3.2 Multivariate Extrapolation

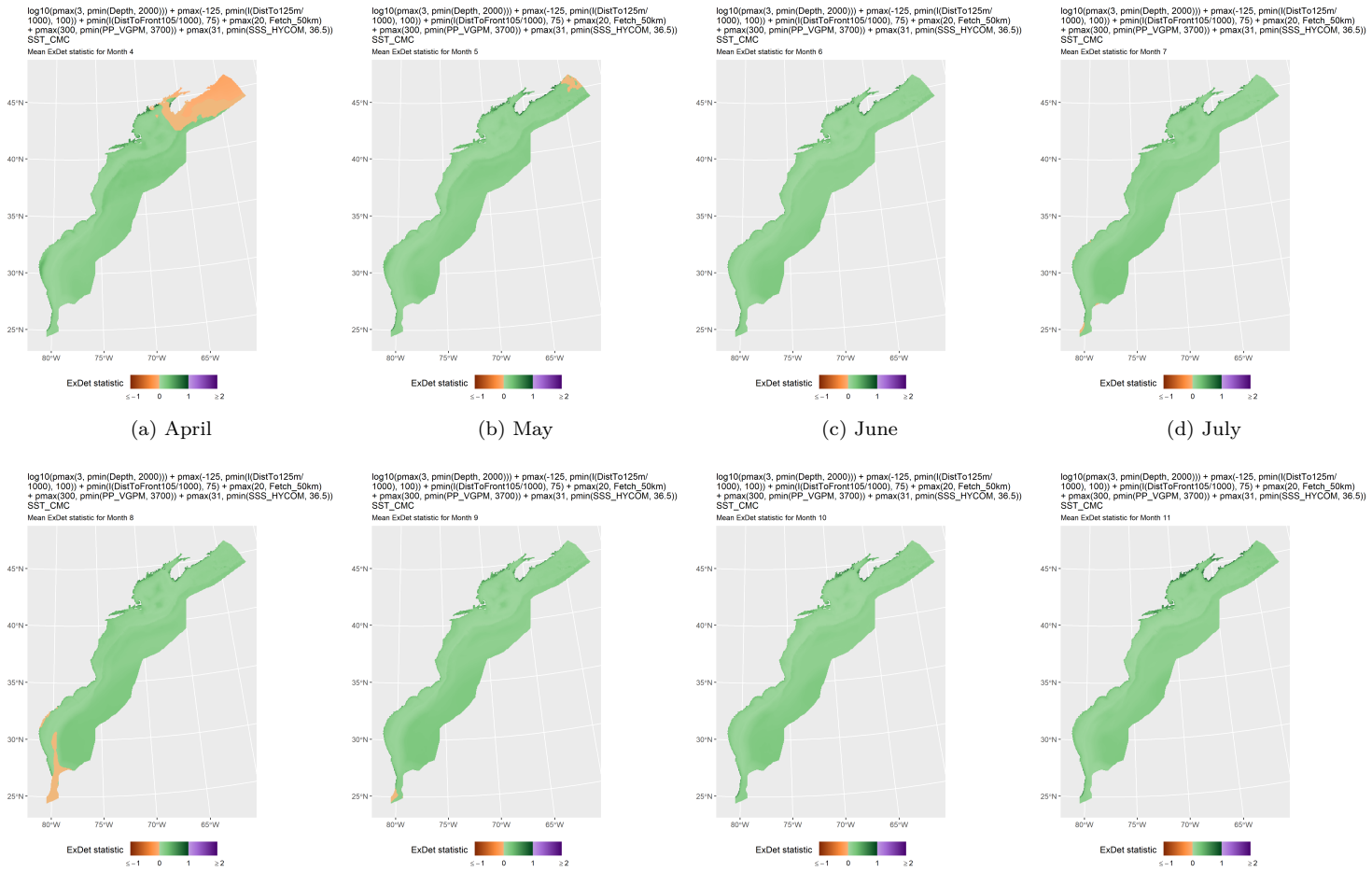

(a) April (b) May (c) June (d) July

(e) August (f) September (g) October (h) November

Figure 107: ExDet statistic (Mesgaran et al. (2014)) for all of the covariates used in the model for Summer. Areas in orange (ExDet < 0) required univariate extrapolation of one or more covariates (see previous section). Areas in purple (ExDet > 1), did not require univariate extrapolation but did require multivariate extrapolation, by virtue of having novel combinations of covariates not represented in the survey data, according to the NT2 statistic (Mesgaran et al. (2014)). Areas in green ($0 \geq$ ExDet ≤ 1) did not require either type of extrapolation.

5 Predictions

Based on our evaluation of this model in the context of what is known of this species (see Section 6), we summarized its predictions for the period December 2009 - November 2020 into monthly climatological density and uncertainty surfaces, shown in the maps below.

5.1 Summarized Predictions

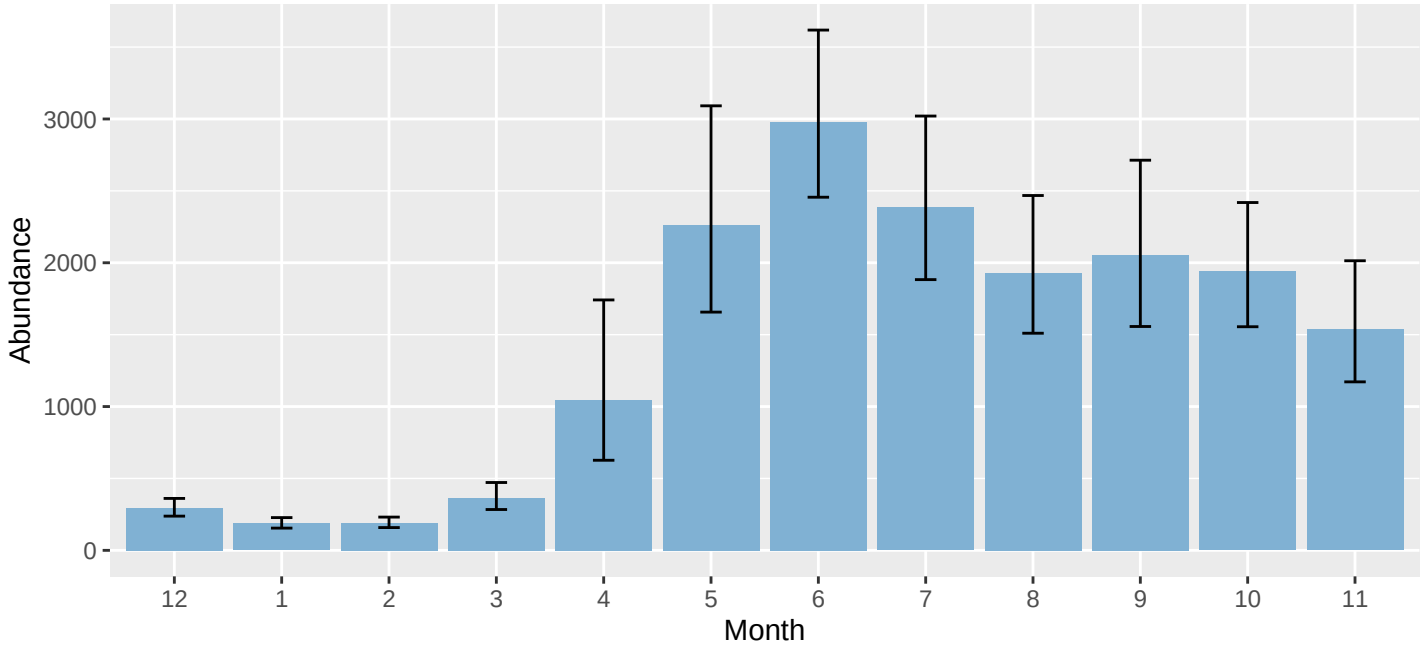

Figure 108: Mean monthly abundance for the prediction area for December 2009 - November 2020. Note that the prediction area was not the same for all months (see Table 29 below and maps following). Error bars are a 95% interval, made with a log-normal approximation using the prediction's CV. The CV was estimated with the analytic approach given by Miller et al. (2022), Appendix S1, and accounts both for uncertainty in model parameter estimates and for temporal variability in dynamic covariates.

Table 29: Mean monthly abundance and density for the prediction area for December 2009 - November 2020. CV and intervals estimated as described for the previous figure.

Month	Abundance	CV	95% Interval	Area (km^2)	Density (individuals / 100 km^2)
12	293	0.107	238 - 361	1,088,850	0.027
1	188	0.099	155 - 228	1,088,850	0.017
2	191	0.097	158 - 231	1,088,850	0.018
3	366	0.130	284 - 472	1,088,850	0.034
4	1,045	0.265	627 - 1,741	1,272,925	0.082
5	2,263	0.160	1,657 - 3,091	1,272,925	0.178
6	2,981	0.099	2,456 - 3,618	1,272,925	0.234
7	2,385	0.121	1,883 - 3,020	1,272,925	0.187
8	1,930	0.126	1,510 - 2,468	1,272,925	0.152
9	2,055	0.142	1,557 - 2,713	1,272,925	0.161
10	1,940	0.113	1,555 - 2,419	1,272,925	0.152
11	1,536	0.139	1,172 - 2,014	1,272,925	0.121

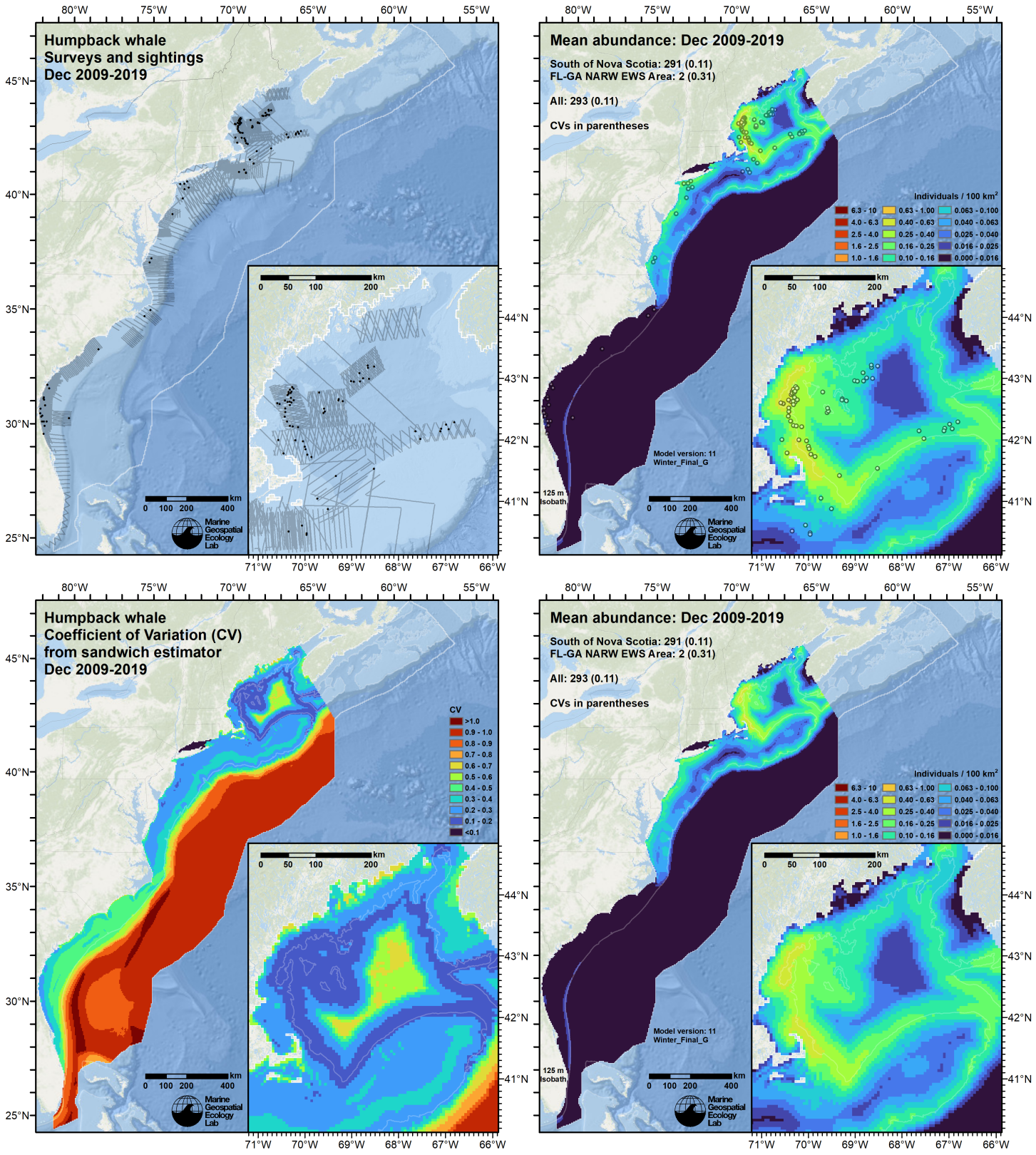

Figure 109: Survey effort and observations (top left), predicted density with observations (top right), predicted density without observations (bottom right), and coefficient of variation of predicted density (bottom left), for the month of December for the given era. Variance was estimated with the analytic approach given by Miller et al. (2022), Appendix S1, and accounts both for uncertainty in model parameter estimates and for temporal variability in dynamic covariates.

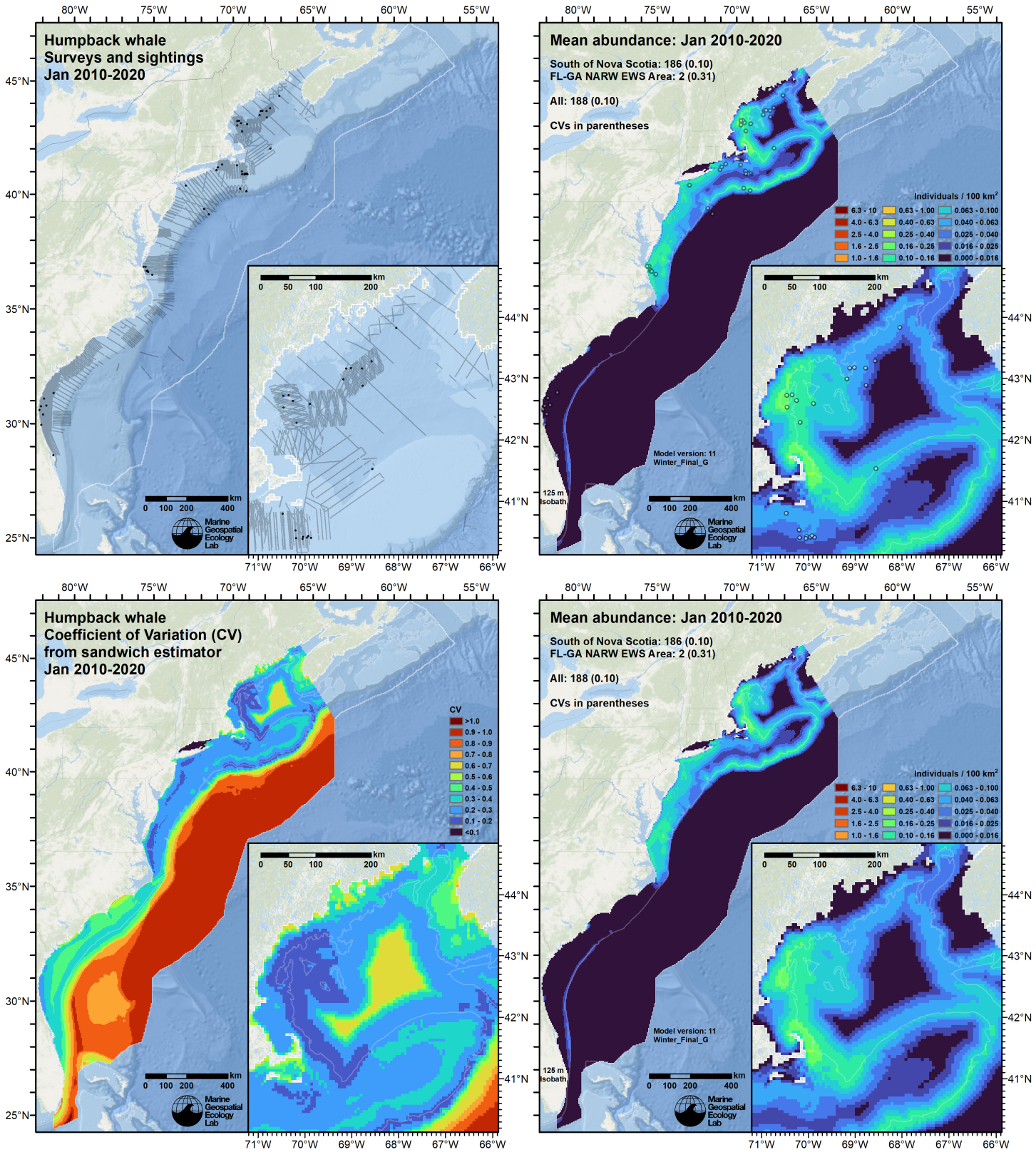

Figure 110: Survey effort and observations (top left), predicted density with observations (top right), predicted density without observations (bottom right), and coefficient of variation of predicted density (bottom left), for the month of January for the given era. Variance was estimated with the analytic approach given by Miller et al. (2022), Appendix S1, and accounts both for uncertainty in model parameter estimates and for temporal variability in dynamic covariates.

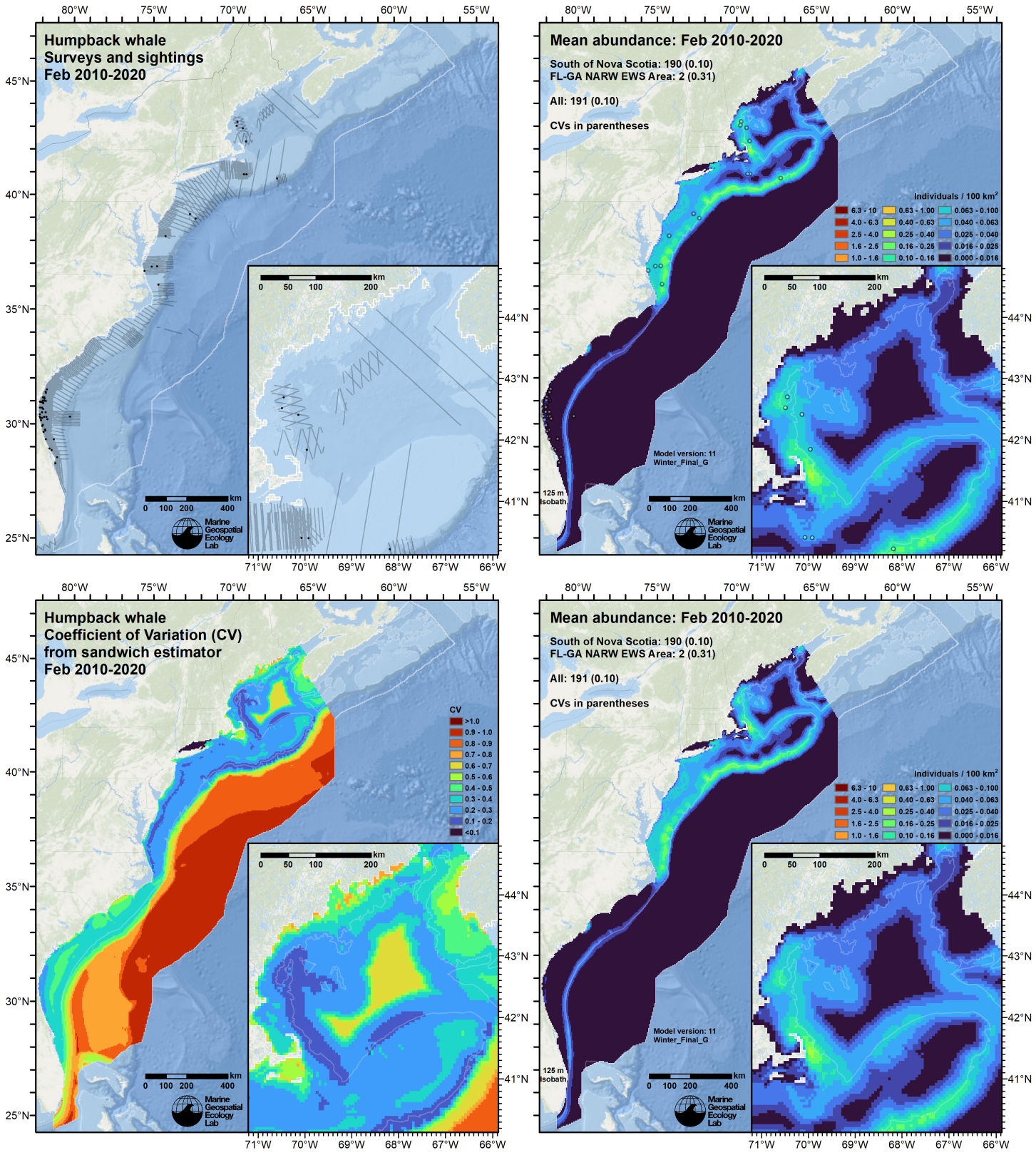

Figure 111: Survey effort and observations (top left), predicted density with observations (top right), predicted density without observations (bottom right), and coefficient of variation of predicted density (bottom left), for the month of February for the given era. Variance was estimated with the analytic approach given by Miller et al. (2022), Appendix S1, and accounts both for uncertainty in model parameter estimates and for temporal variability in dynamic covariates.

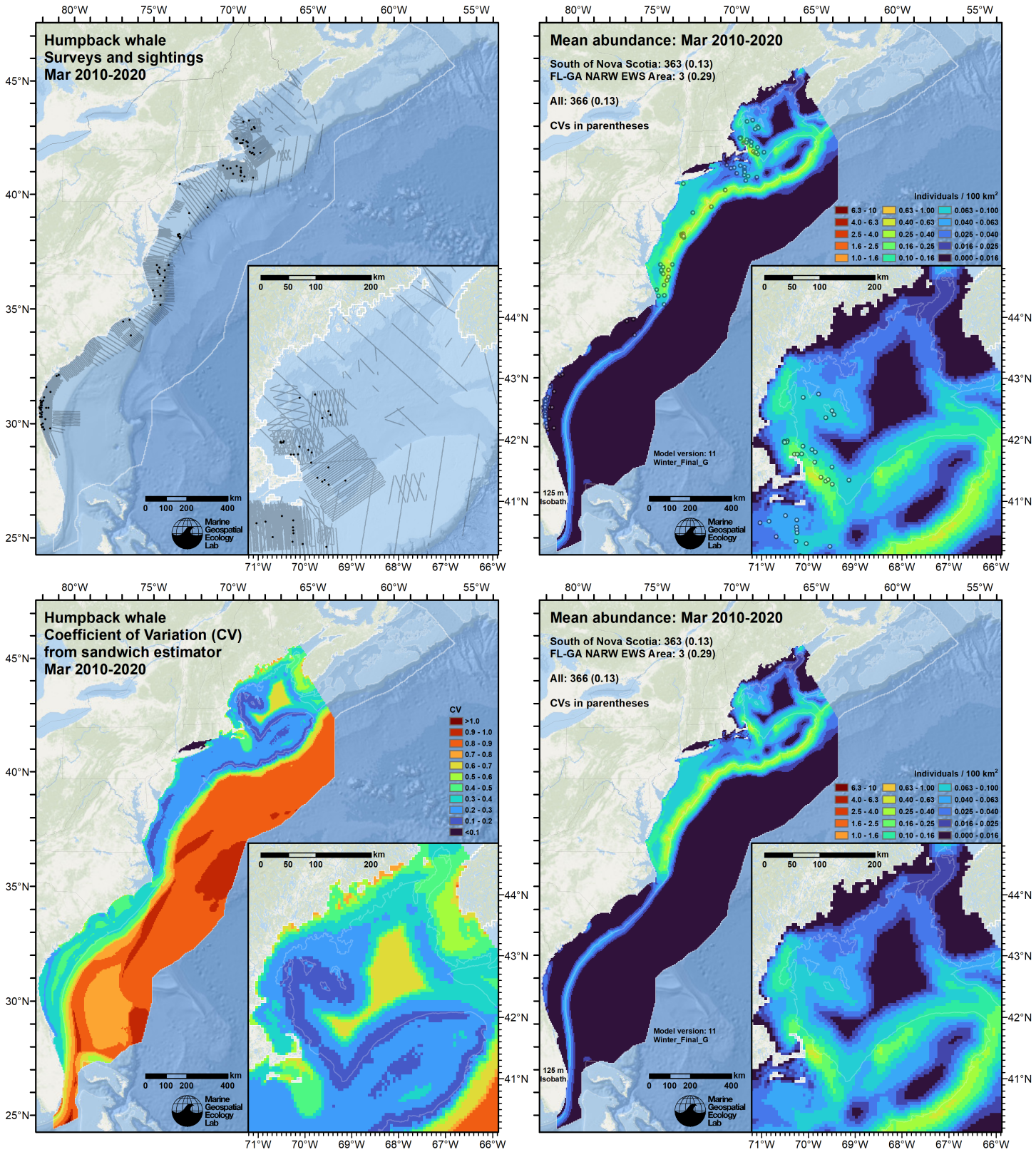

Figure 112: Survey effort and observations (top left), predicted density with observations (top right), predicted density without observations (bottom right), and coefficient of variation of predicted density (bottom left), for the month of March for the given era. Variance was estimated with the analytic approach given by Miller et al. (2022), Appendix S1, and accounts both for uncertainty in model parameter estimates and for temporal variability in dynamic covariates.

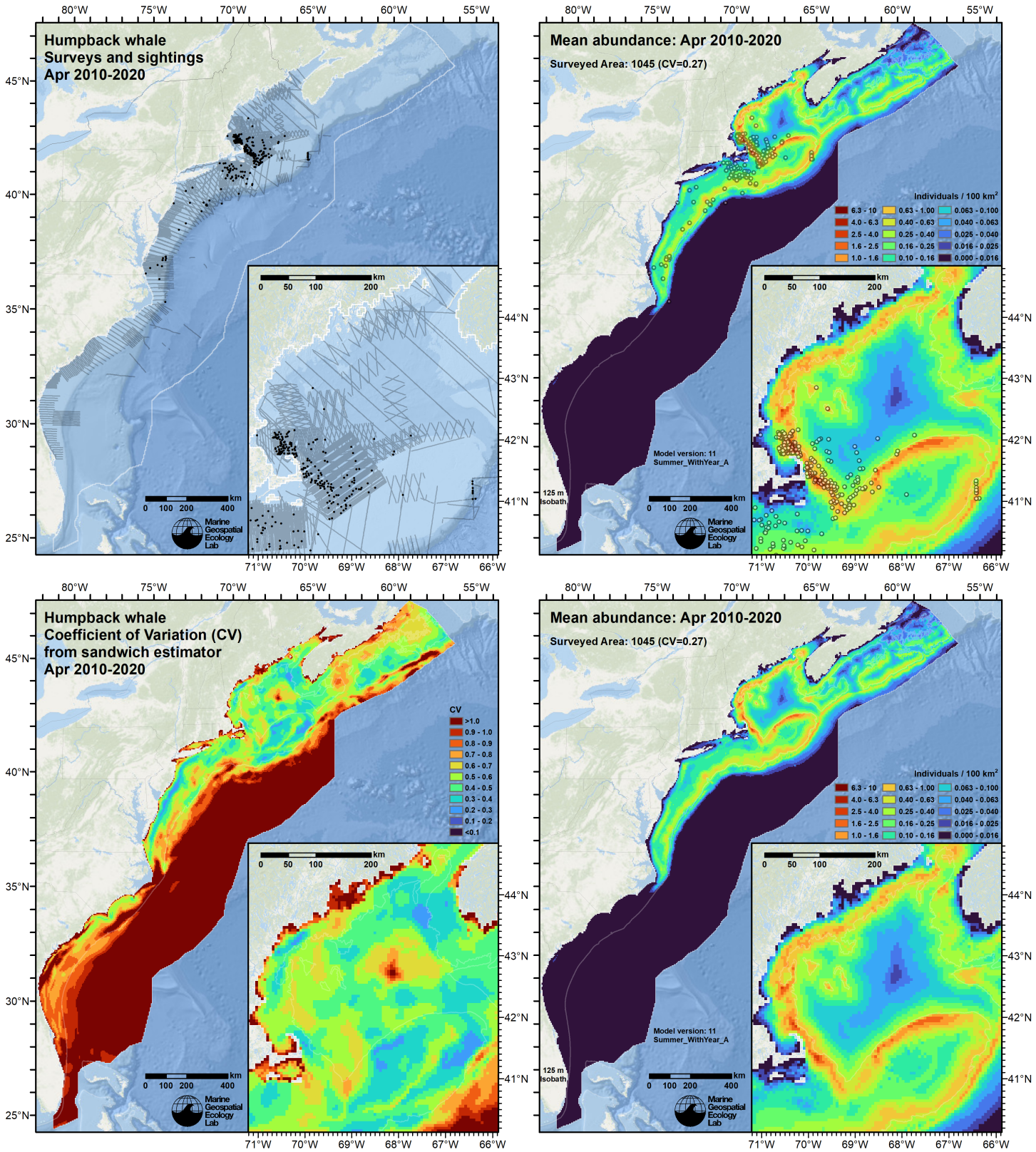

Figure 113: Survey effort and observations (top left), predicted density with observations (top right), predicted density without observations (bottom right), and coefficient of variation of predicted density (bottom left), for the month of April for the given era. Variance was estimated with the analytic approach given by Miller et al. (2022), Appendix S1, and accounts both for uncertainty in model parameter estimates and for temporal variability in dynamic covariates.

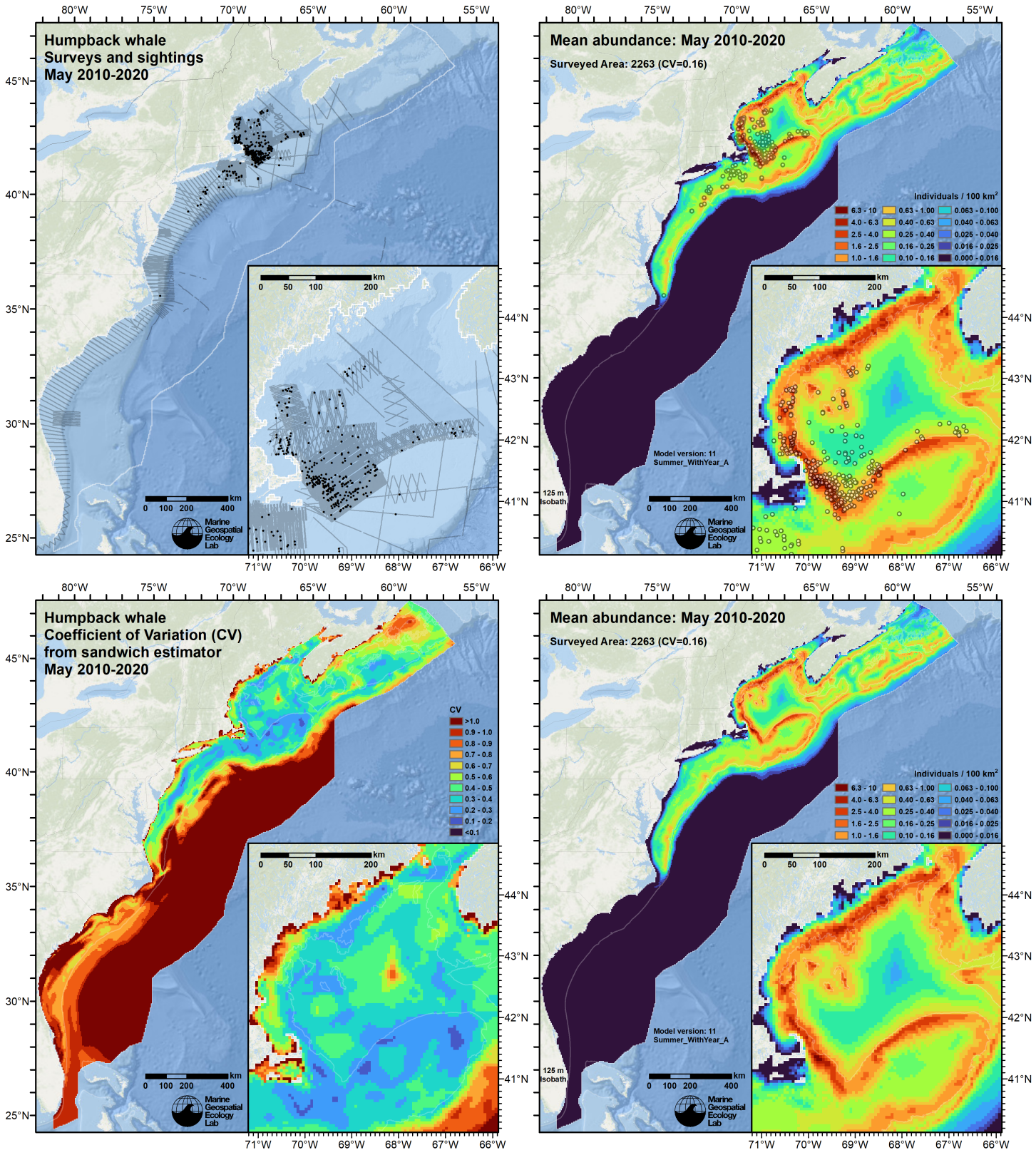

Figure 114: Survey effort and observations (top left), predicted density with observations (top right), predicted density without observations (bottom right), and coefficient of variation of predicted density (bottom left), for the month of May for the given era. Variance was estimated with the analytic approach given by Miller et al. (2022), Appendix S1, and accounts both for uncertainty in model parameter estimates and for temporal variability in dynamic covariates.

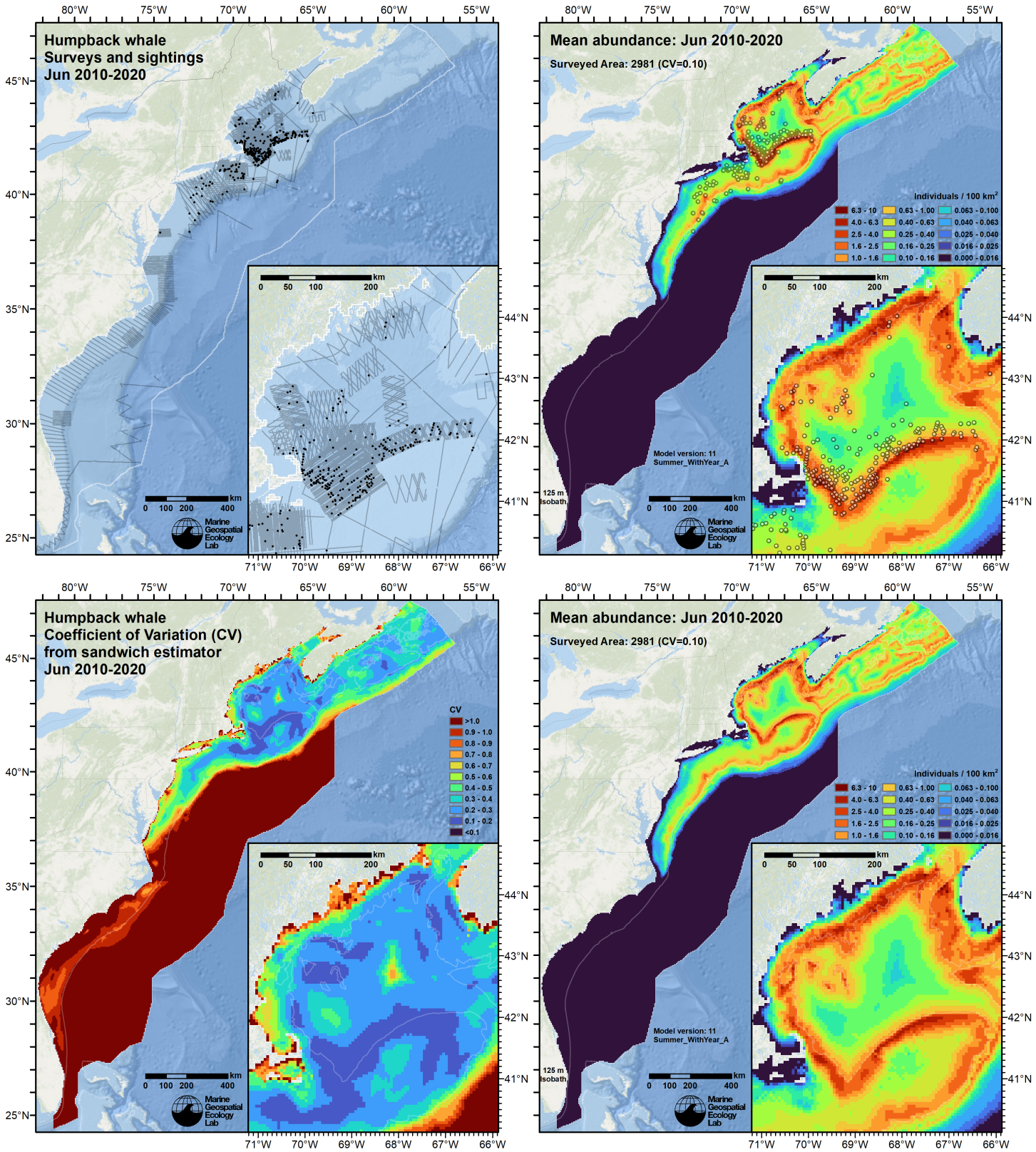

Figure 115: Survey effort and observations (top left), predicted density with observations (top right), predicted density without observations (bottom right), and coefficient of variation of predicted density (bottom left), for the month of June for the given era. Variance was estimated with the analytic approach given by Miller et al. (2022), Appendix S1, and accounts both for uncertainty in model parameter estimates and for temporal variability in dynamic covariates.

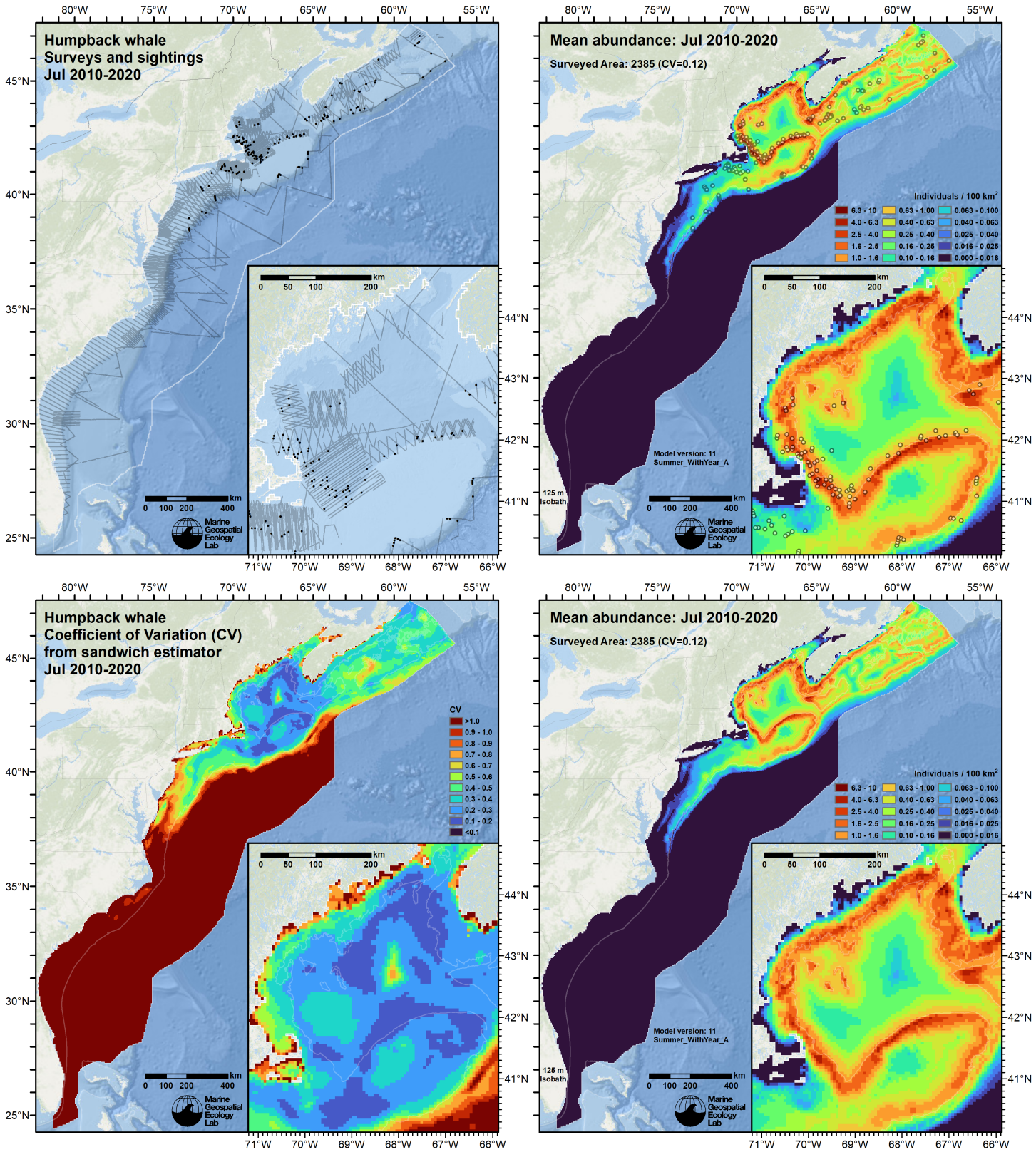

Figure 116: Survey effort and observations (top left), predicted density with observations (top right), predicted density without observations (bottom right), and coefficient of variation of predicted density (bottom left), for the month of July for the given era. Variance was estimated with the analytic approach given by Miller et al. (2022), Appendix S1, and accounts both for uncertainty in model parameter estimates and for temporal variability in dynamic covariates.

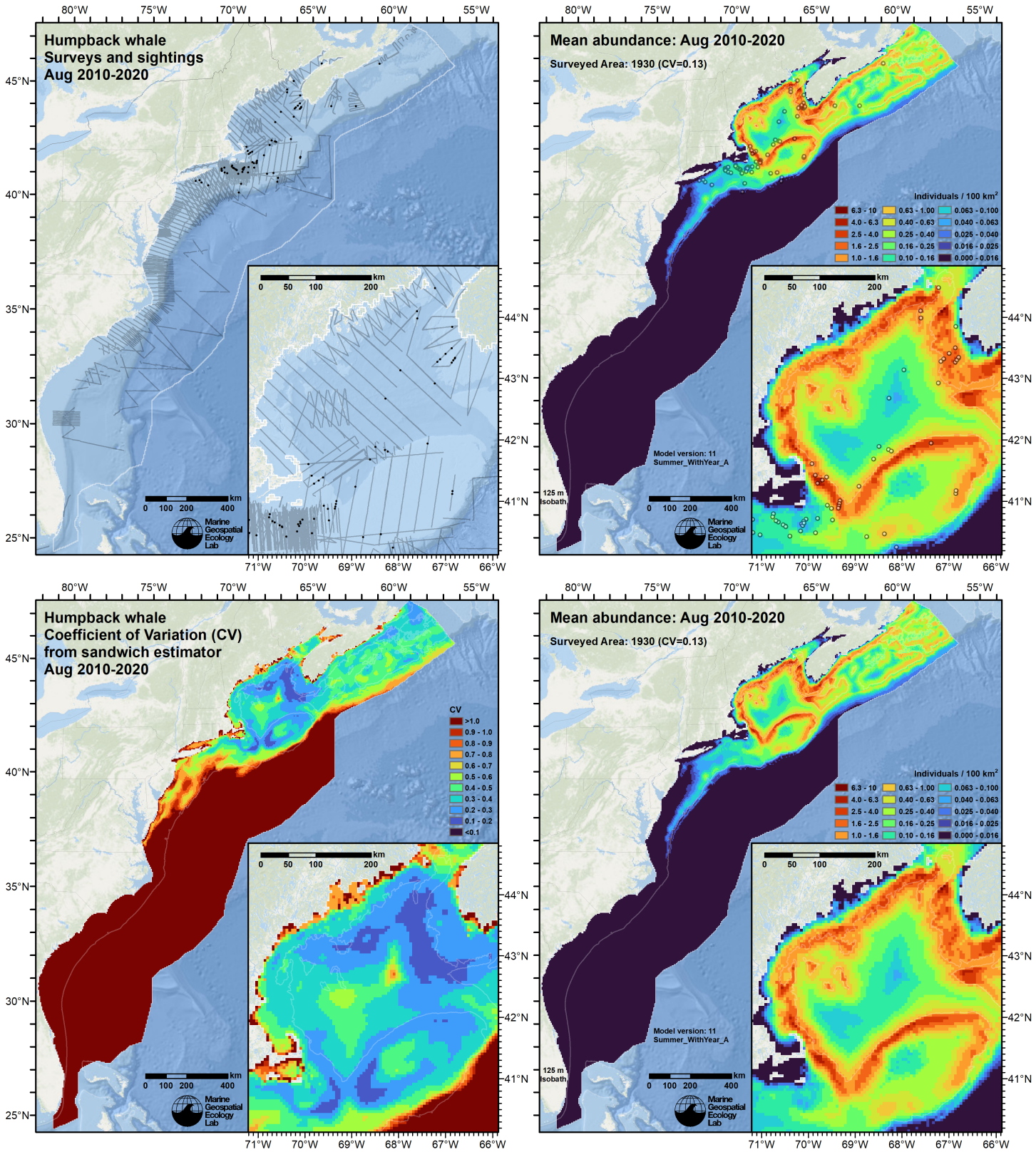

Figure 117: Survey effort and observations (top left), predicted density with observations (top right), predicted density without observations (bottom right), and coefficient of variation of predicted density (bottom left), for the month of August for the given era. Variance was estimated with the analytic approach given by Miller et al. (2022), Appendix S1, and accounts both for uncertainty in model parameter estimates and for temporal variability in dynamic covariates.

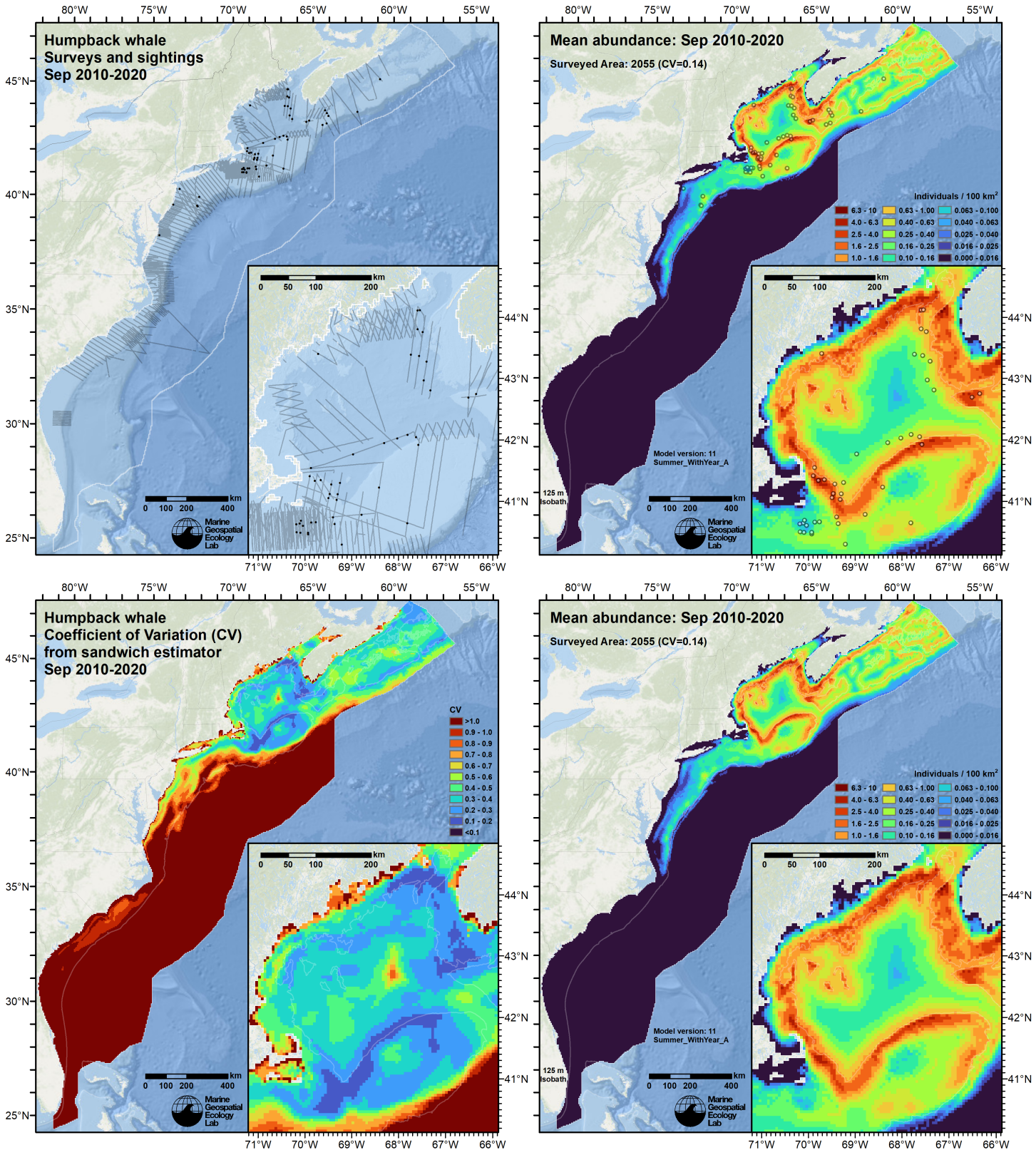

Figure 118: Survey effort and observations (top left), predicted density with observations (top right), predicted density without observations (bottom right), and coefficient of variation of predicted density (bottom left), for the month of September for the given era. Variance was estimated with the analytic approach given by Miller et al. (2022), Appendix S1, and accounts both for uncertainty in model parameter estimates and for temporal variability in dynamic covariates.

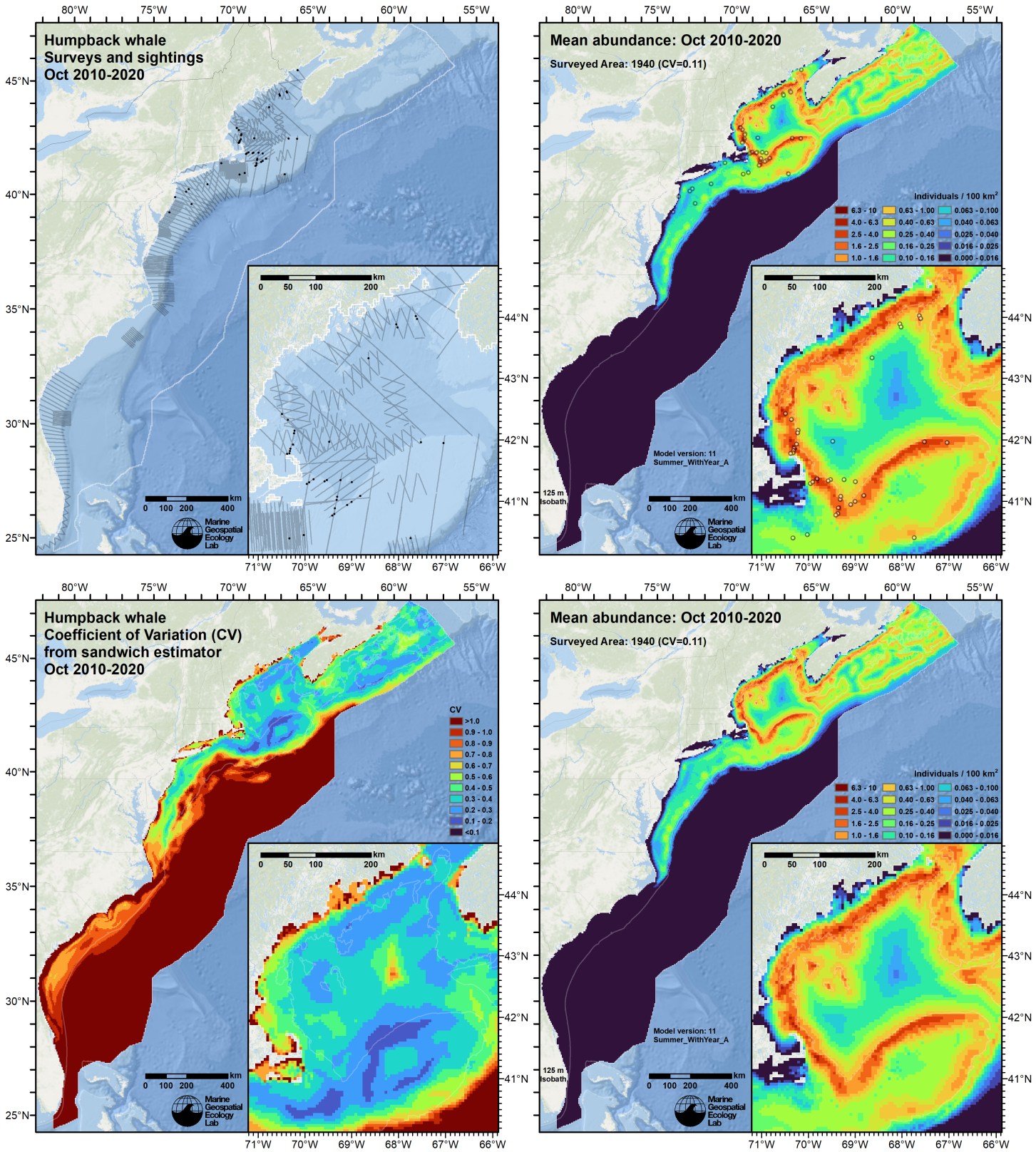

Figure 119: Survey effort and observations (top left), predicted density with observations (top right), predicted density without observations (bottom right), and coefficient of variation of predicted density (bottom left), for the month of October for the given era. Variance was estimated with the analytic approach given by Miller et al. (2022), Appendix S1, and accounts both for uncertainty in model parameter estimates and for temporal variability in dynamic covariates.

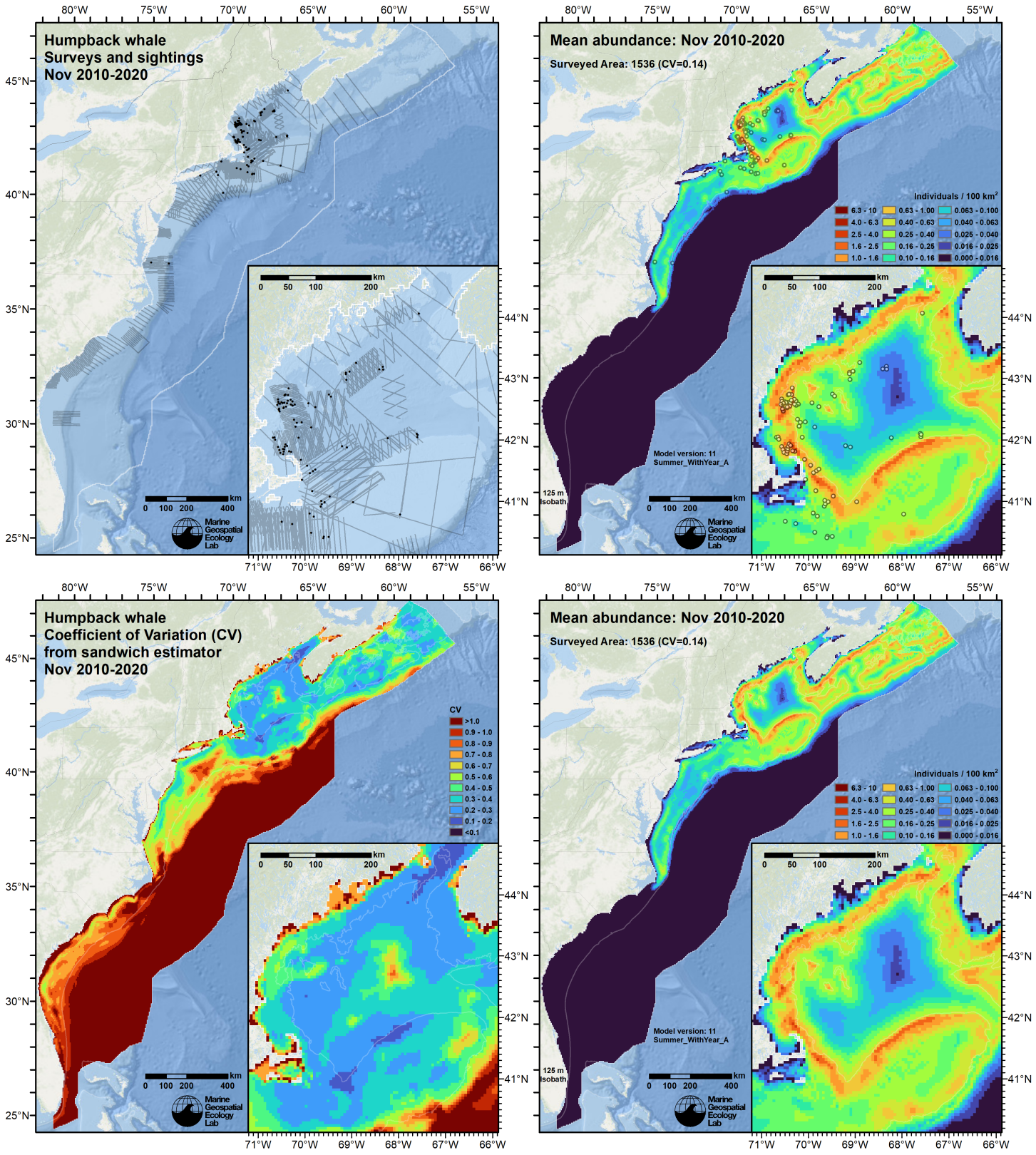

Figure 120: Survey effort and observations (top left), predicted density with observations (top right), predicted density without observations (bottom right), and coefficient of variation of predicted density (bottom left), for the month of November for the given era. Variance was estimated with the analytic approach given by Miller et al. (2022), Appendix S1, and accounts both for uncertainty in model parameter estimates and for temporal variability in dynamic covariates.

5.2 Abundance Comparisons

5.2.1 NOAA Stock Assessment Reports

Table 30: Comparison of the most recent abundance estimates from the 2019 NOAA Stock Assessment Report (SAR) (Hayes et al. (2020)), to estimates extracted from the multi-year mean density surfaces we provide to model users (Section 5.1). The SAR presented two estimates for the most recent year it listed (2016): one from line transect surveys, and the other from a capture-mark-recapture (CMR) model made from sightings of photographically-identified humpbacks. Figure 121 shows the zones used to extract abundances from the density model's predictions for comparison to the line transect estimates. Figure 122 shows the SAR's CMR Sampling Stratum overlaid on the density model's mean predictions for June, July, and August, and the extracted abundances.

2019 Stock Assessment Report			Density Model		
Month/Year	Area	N_{est}	Period	Zone	Abundance
Jun-Sep 2016	Central Virginia to lower BoF[a]	2,368	Jun-Sep 2010-2020	NEFSC	1,035
Jun-Aug 2016	Florida to Central Virginia[b]		Jun-Aug 2010-2020	SEFSC	35
Aug-Sep 2016	Bay of Fundy to Halifax[c]	742	Aug-Sep 2010-2020	BoF to Halifax	690
Jun-Sep 2016	Total	3,110	Jun-Sep 2010-2020	Total	1,760
Mid-summer 2016	CMR Sampling Stratum	1,396	Jun-Jul 2010-2020	CMR Stratum	919
			Jun-Jul 2010-2020	+25 km buffer	1,060

[a] Estimate originally from Palka (2020). This total combined estimates for Palka's continental shelf stratum (called 'Gulf of Maine' by Palka) of 1,372 and shelf-break stratum (called 'Shelf' by Palka) of 996.

[b] The SAR did not list this region, but the 2016 SEFSC survey that covered it, documented by Garrison (2020), did not report any humpback sightings.

[c] The SAR reported this as a 'rough number to add to the estimate from U.S. waters', which it derived from the Canada DFO 2016 NAISS survey documented by Lawson and Gosselin (2018).

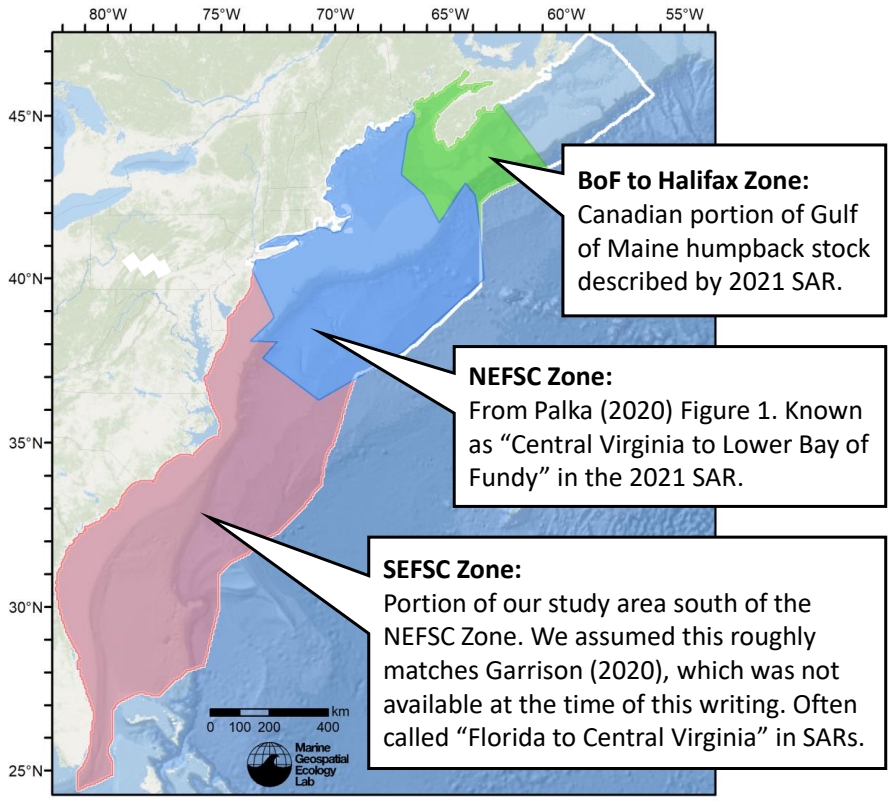

Figure 121: Zones for which we extracted abundance estimates from the density model for comparison to estimates derived from 2016 line transect surveys, as reported by the 2019 SAR (Hayes et al. 2020).

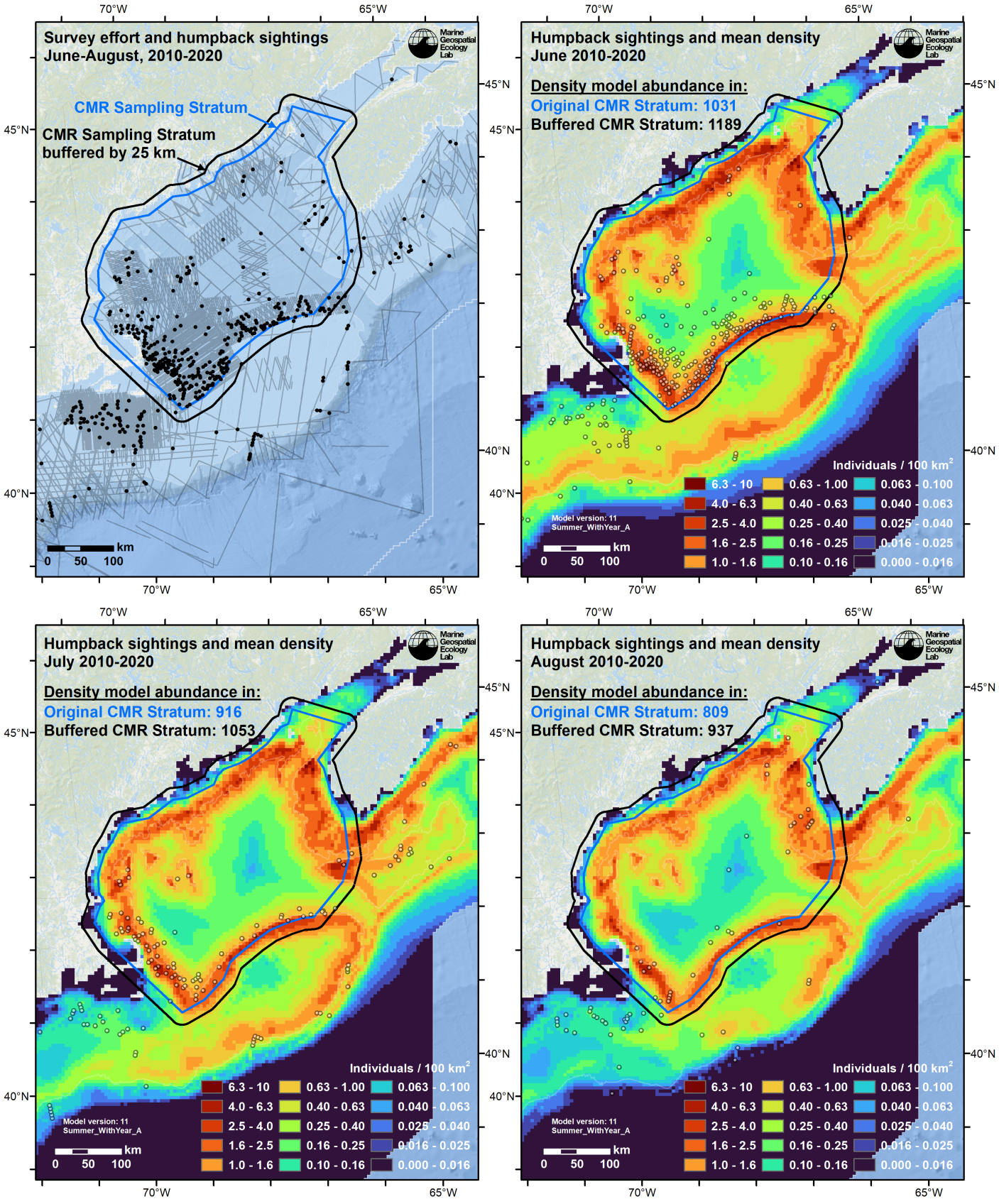

Figure 122: Humpback CMR Sampling Stratum (blue polygon) from the 2019 SAR (Hayes et al. 2020) overlaid on this model's survey effort transects and sightings for June-August of 2010-2020 (upper left), and on mean density maps for the same years for the months of June (upper right), July (lower left), and August (lower right). Black polygon represents a 25 km buffer, to more fully capture density predicted by the model around the edge of the CMR Sampling Stratum. Blue and black text gives total abundance from the density model within the blue and black polygons.

5.2.2 Previous Density Model

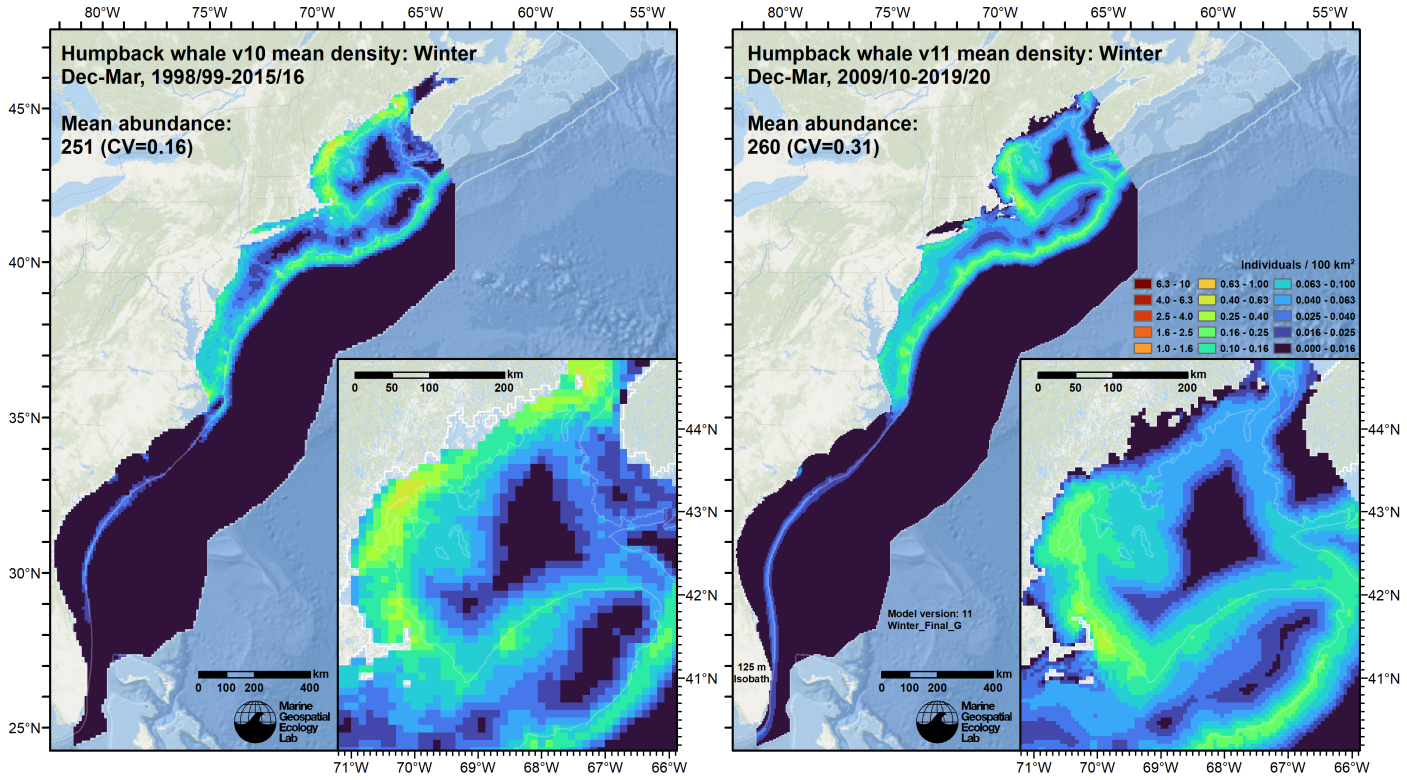

Figure 123: Comparison of the mean density predictions from the previous model (left) released by Roberts et al. (2017) to those from this model (right) for the Winter season.

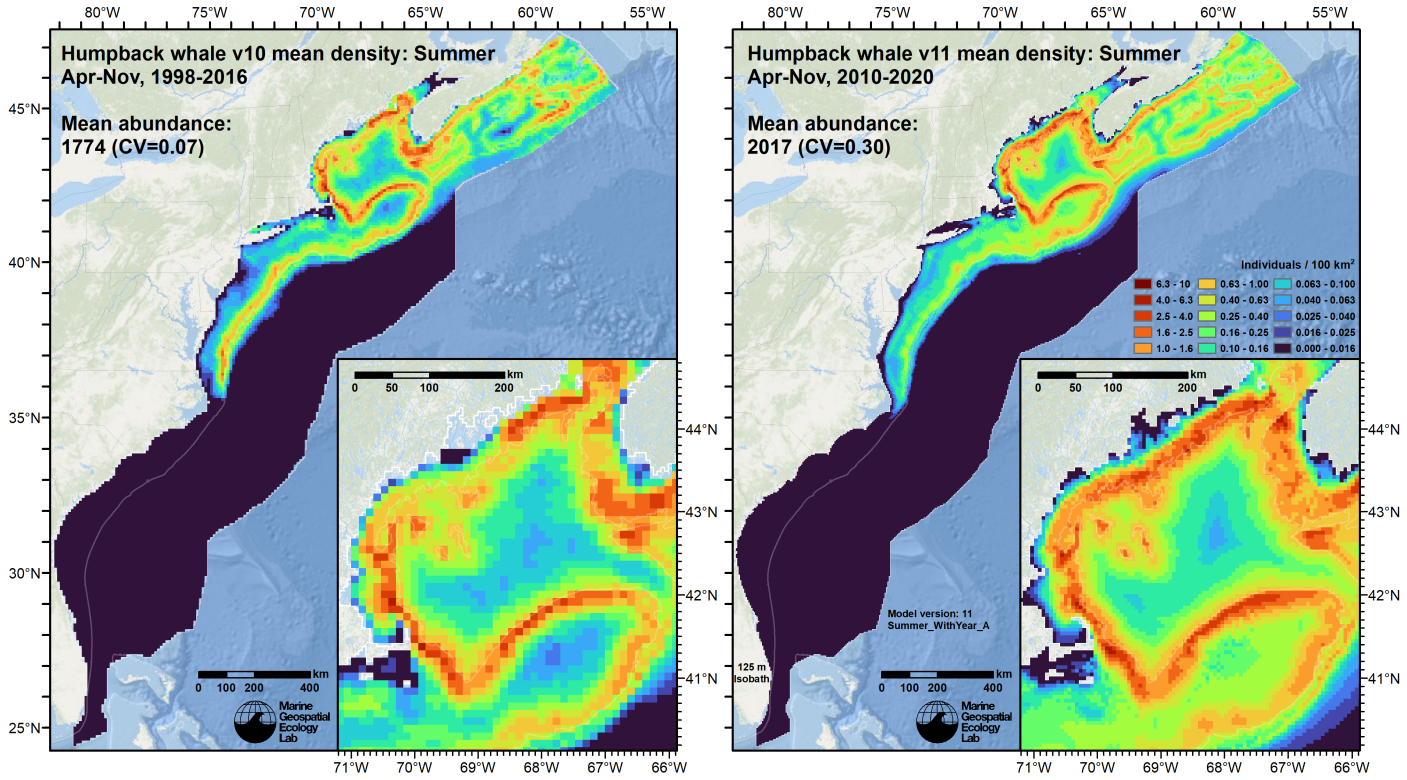

Figure 124: Comparison of the mean density predictions from the previous model (left) released by Roberts et al. (2017) to those from this model (right) for the Summer season.

5.3 Comparison to Passive Acoustic Monitoring

To facilitate qualitative comparison of passive acoustic monitoring (PAM) detections to visual sightings and density predictions, we overlaid PAM results from Davis et al. (2020) on maps of visual segments and sightings and of density predictions. In each figure below, red circles and white dots represent PAM stations. White dots indicate that at that station, there were no days in which Davis et al. determined the species was acoustically present. Red circles indicate that the species was acoustically present, with the size of the circle indicating the percentage of days of the month it was present. The maps underlying the acoustic data are the effort segments and sightings (left side) used to fit the model, and the mean density prediction (right side), for the given month.

Note that each PAM station was usually only deployed for one of the years in the range listed. If a deployment was repeated in a subsequent year, it was treated as a separate station and allocated its own symbol. At such locations, the map may contain several different symbols, such as a white dot inside a red circle, or several red circles of different sizes, indicating interannual variability in acoustic presence at that location. Because both visual and acoustic surveys were very patchy across time, with multi-year coverage only occurring in a small number of specific areas, we urge caution in drawing firm conclusions about the species' distribution from the points and circles without considering the degree of interannual replication in coverage.

We gratefully acknowledge G. Davis and coauthors for making these data available for this comparison.

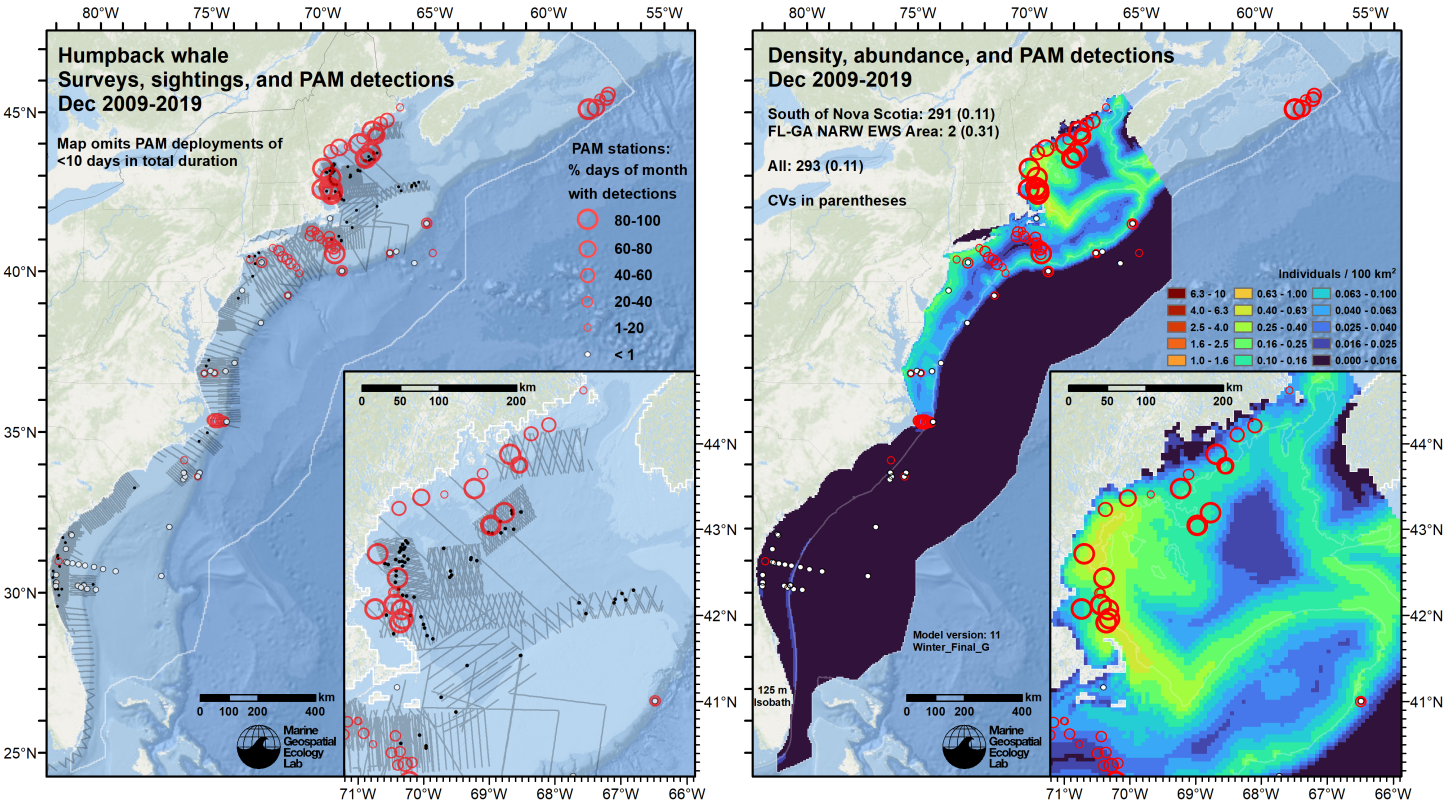

Figure 125: Passive acoustic monitoring stations (red circles and white dots) symbolized by detection rate, overlaid on visual segments and sightings (left) and predicted density (right), for the month of December for the given era.

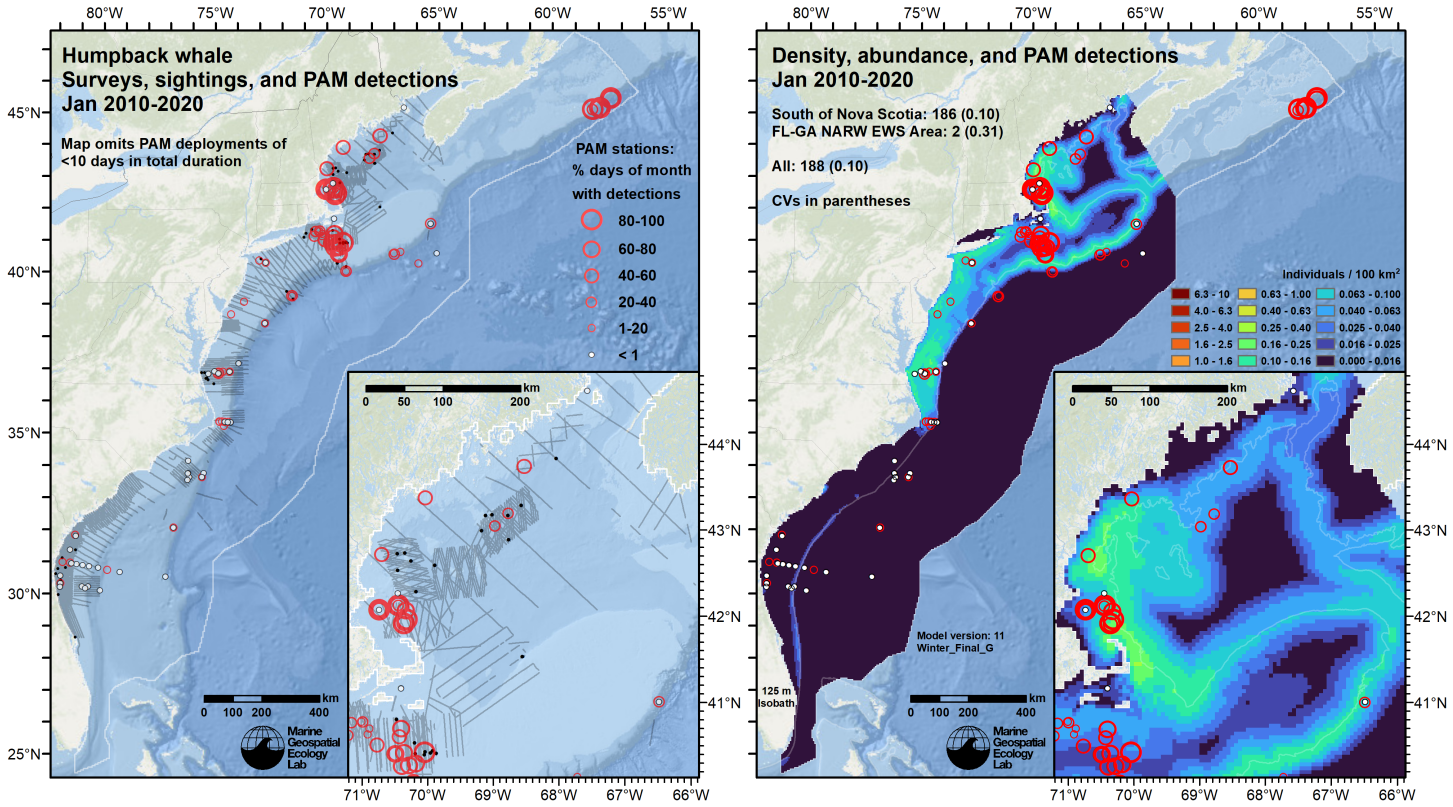

Figure 126: Passive acoustic monitoring stations (red circles and white dots) symbolized by detection rate, overlaid on visual segments and sightings (left) and predicted density (right), for the month of January for the given era.

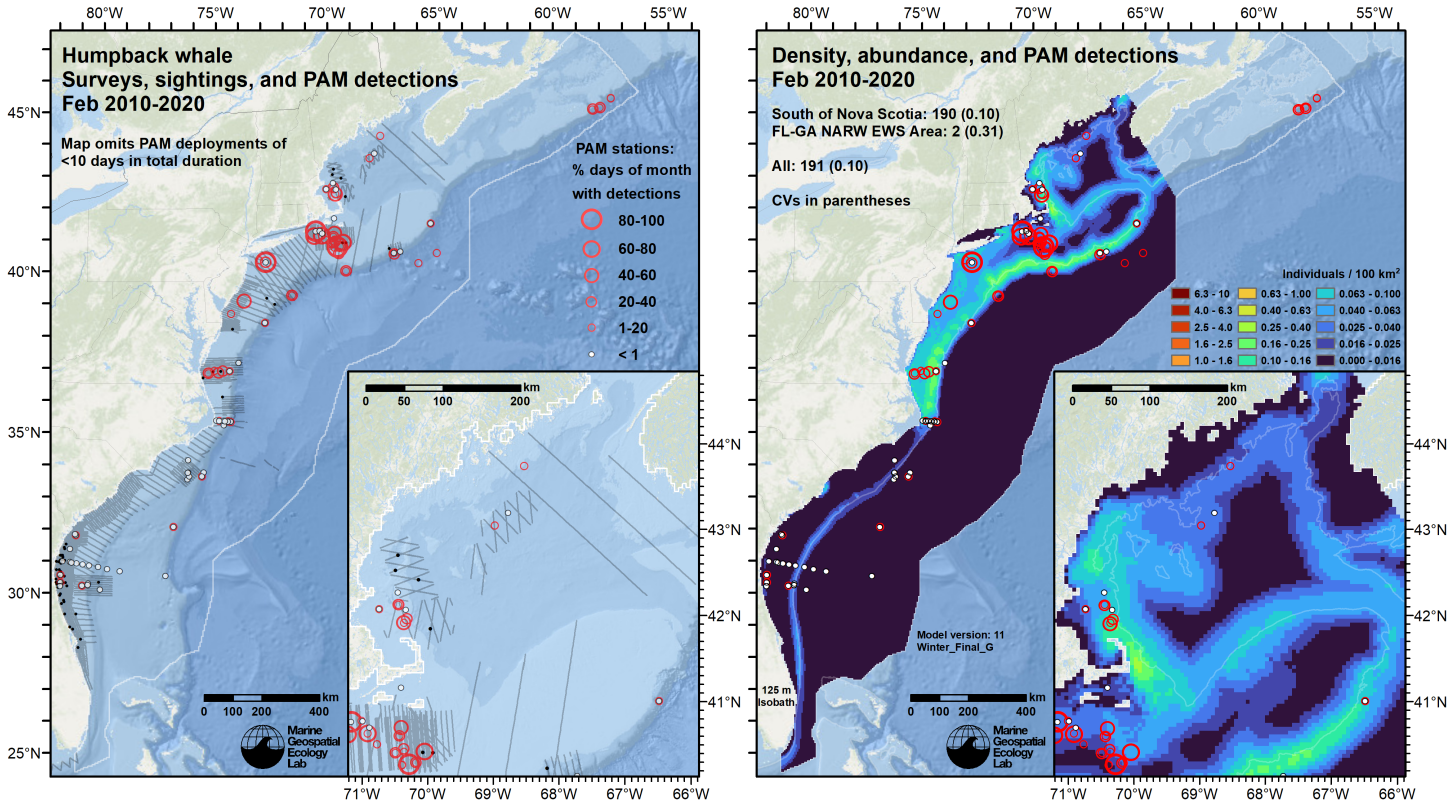

Figure 127: Passive acoustic monitoring stations (red circles and white dots) symbolized by detection rate, overlaid on visual segments and sightings (left) and predicted density (right), for the month of February for the given era.

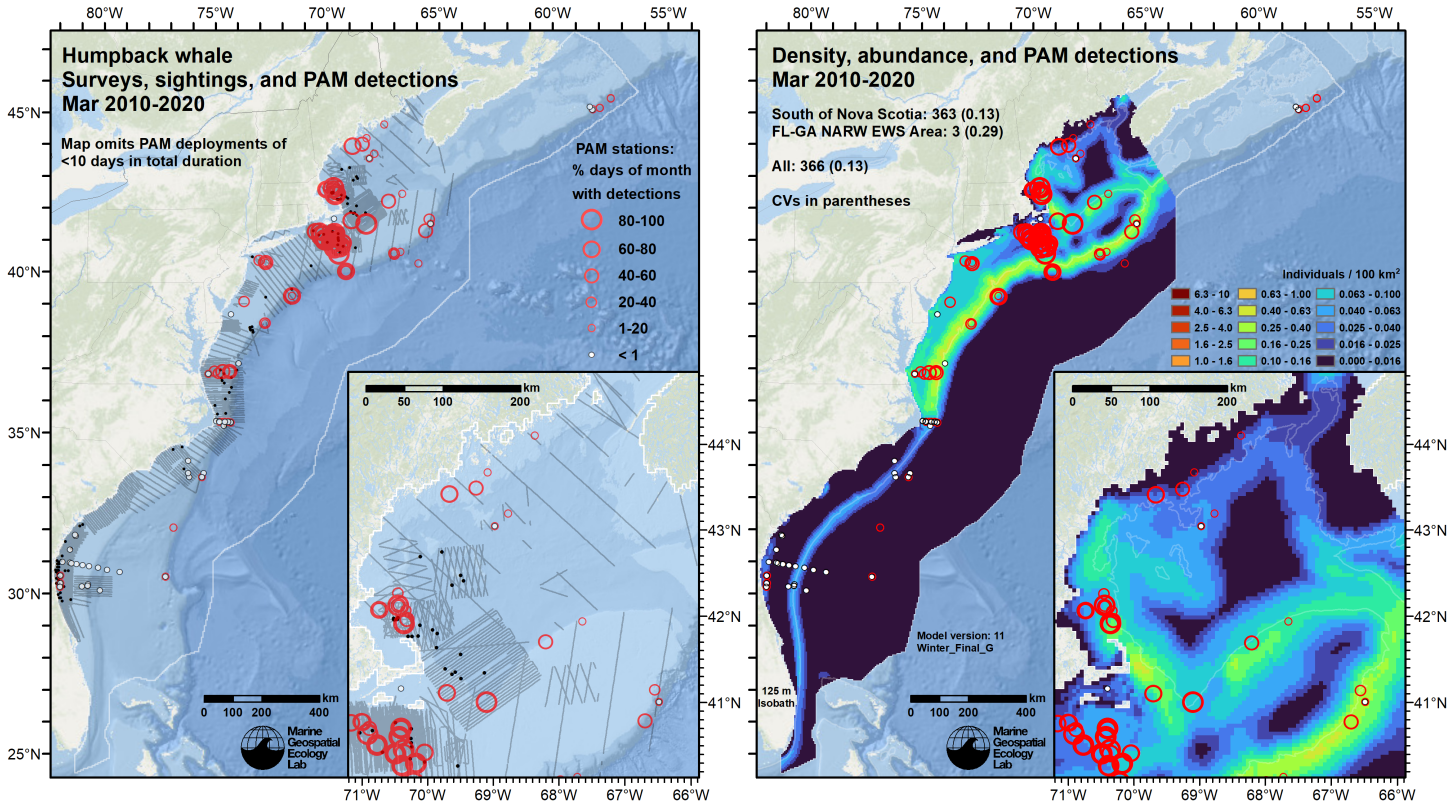

Figure 128: Passive acoustic monitoring stations (red circles and white dots) symbolized by detection rate, overlaid on visual segments and sightings (left) and predicted density (right), for the month of March for the given era.

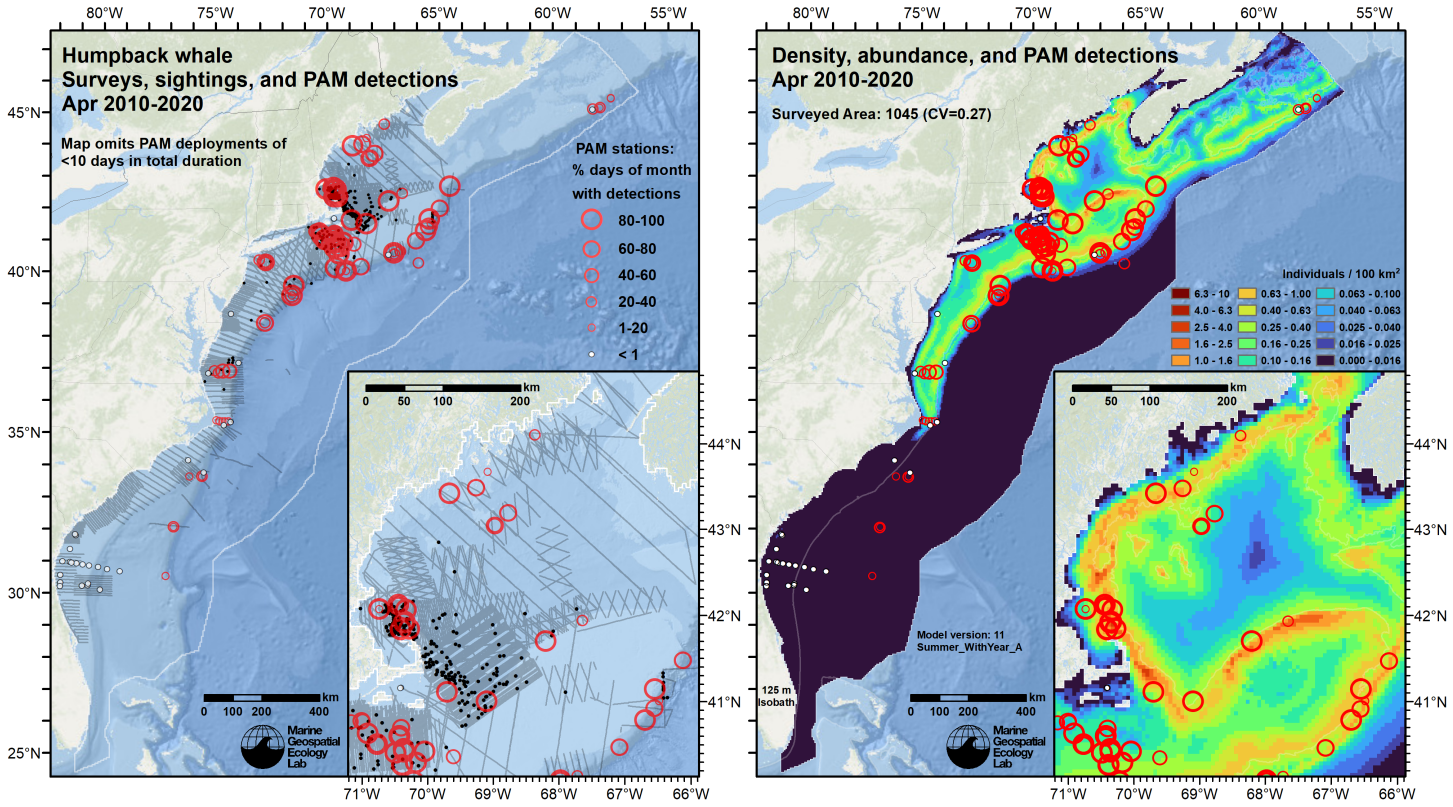

Figure 129: Passive acoustic monitoring stations (red circles and white dots) symbolized by detection rate, overlaid on visual segments and sightings (left) and predicted density (right), for the month of April for the given era.

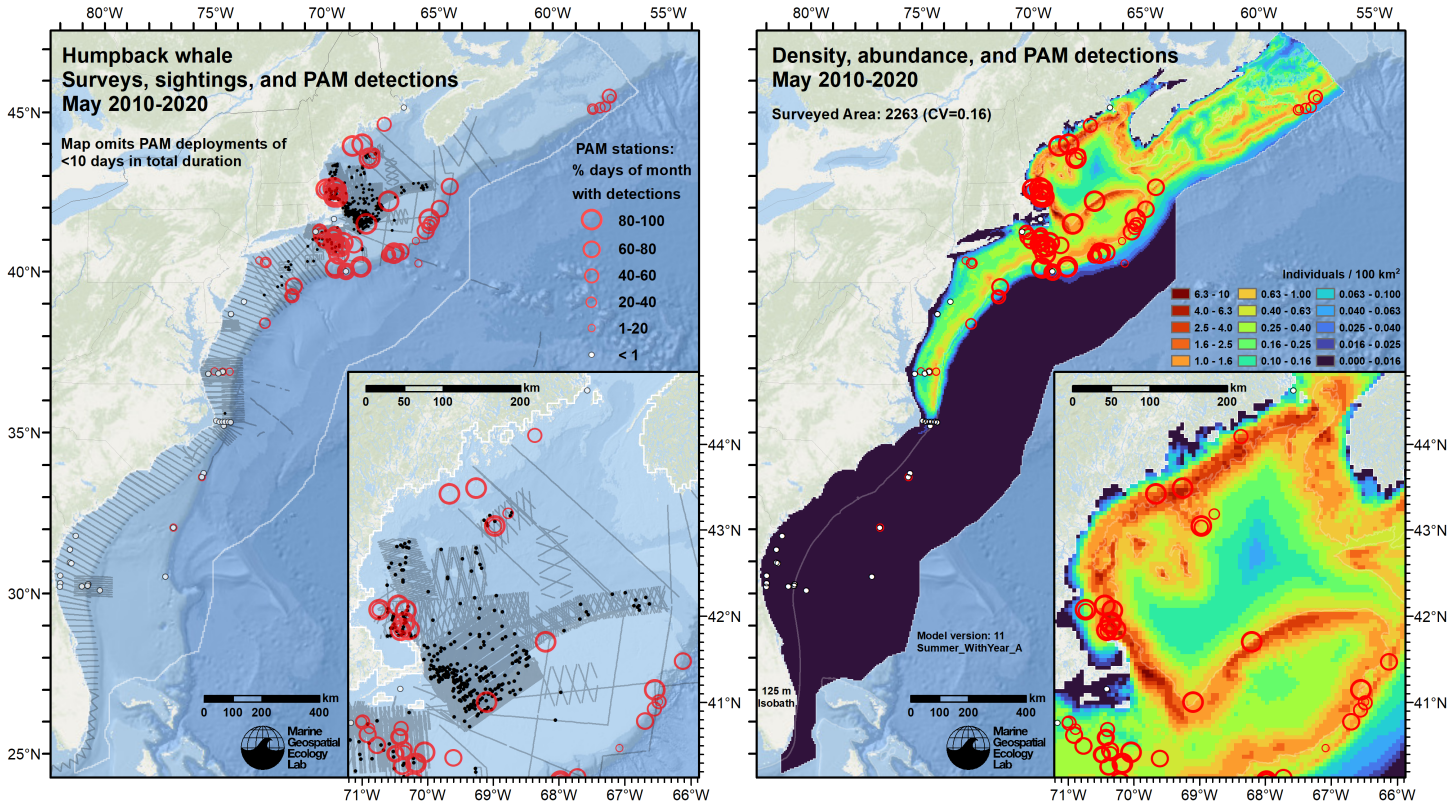

Figure 130: Passive acoustic monitoring stations (red circles and white dots) symbolized by detection rate, overlaid on visual segments and sightings (left) and predicted density (right), for the month of May for the given era.

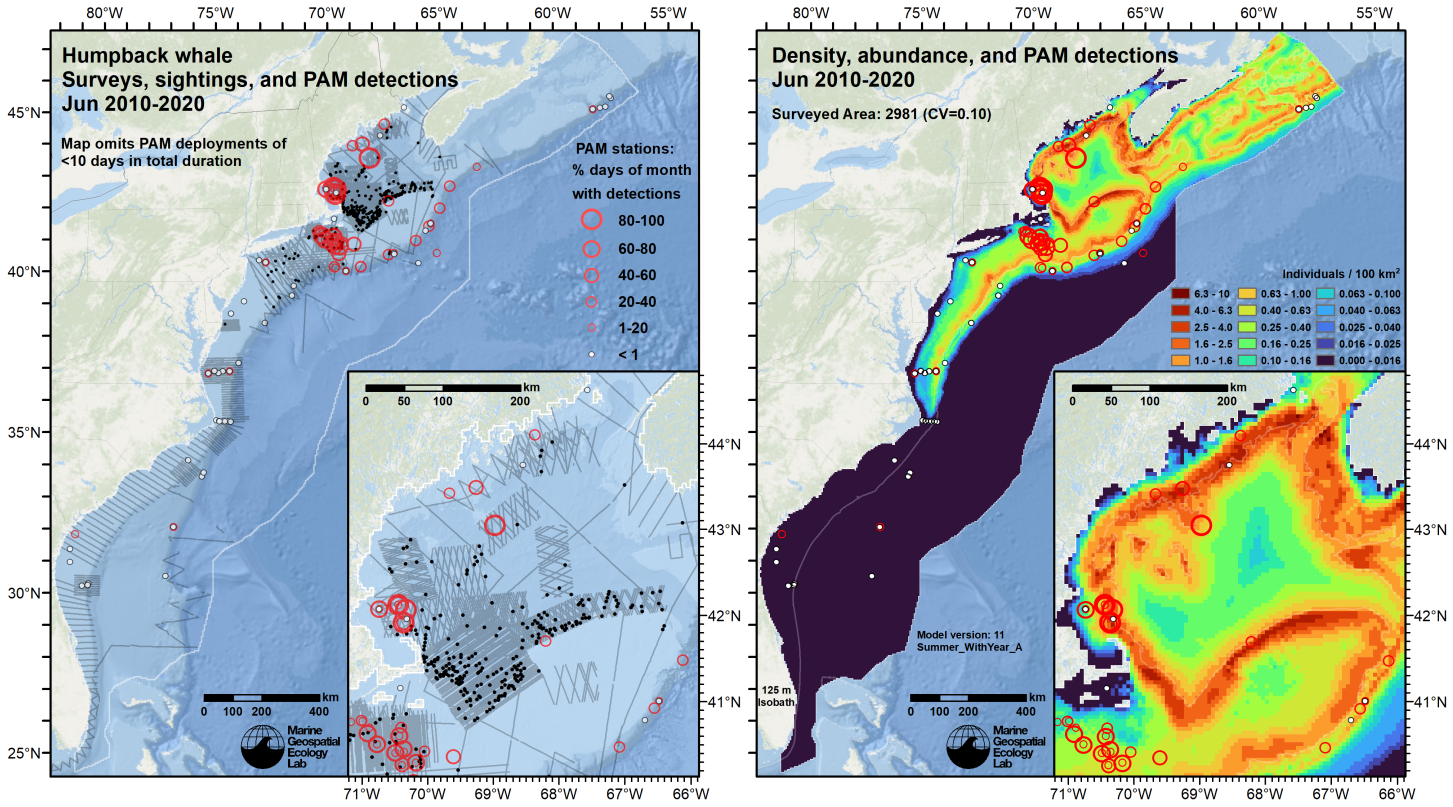

Figure 131: Passive acoustic monitoring stations (red circles and white dots) symbolized by detection rate, overlaid on visual segments and sightings (left) and predicted density (right), for the month of June for the given era.

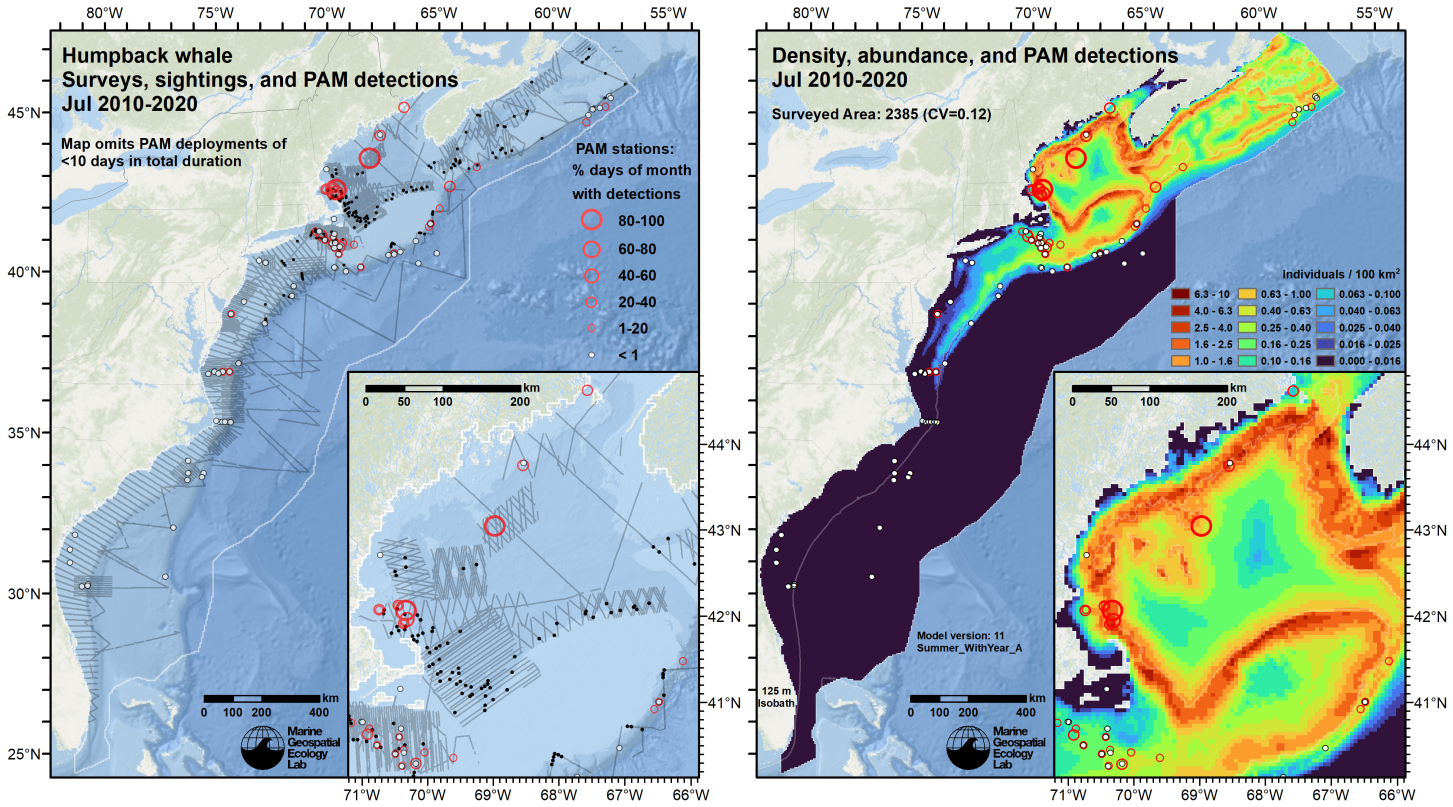

Figure 132: Passive acoustic monitoring stations (red circles and white dots) symbolized by detection rate, overlaid on visual segments and sightings (left) and predicted density (right), for the month of July for the given era.

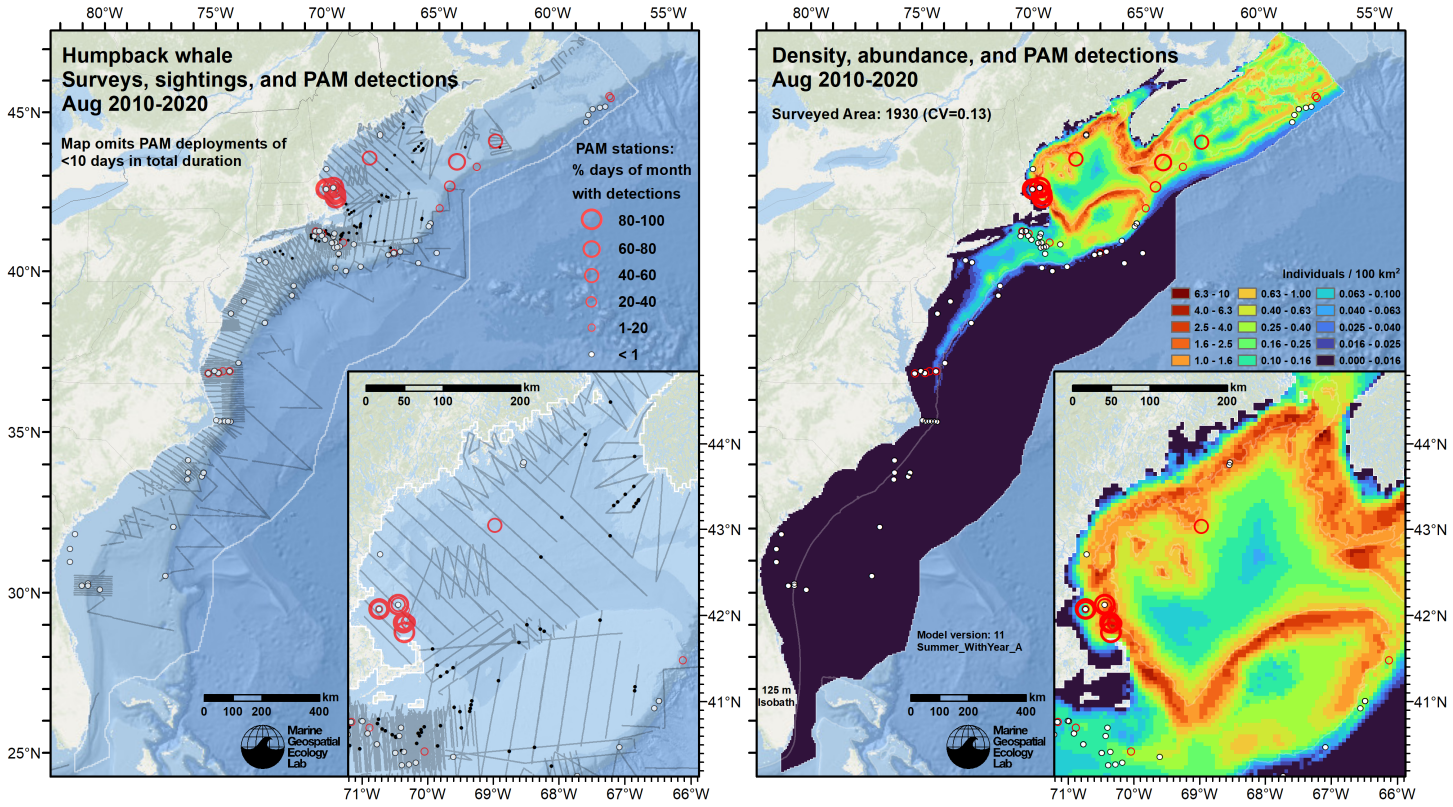

Figure 133: Passive acoustic monitoring stations (red circles and white dots) symbolized by detection rate, overlaid on visual segments and sightings (left) and predicted density (right), for the month of August for the given era.

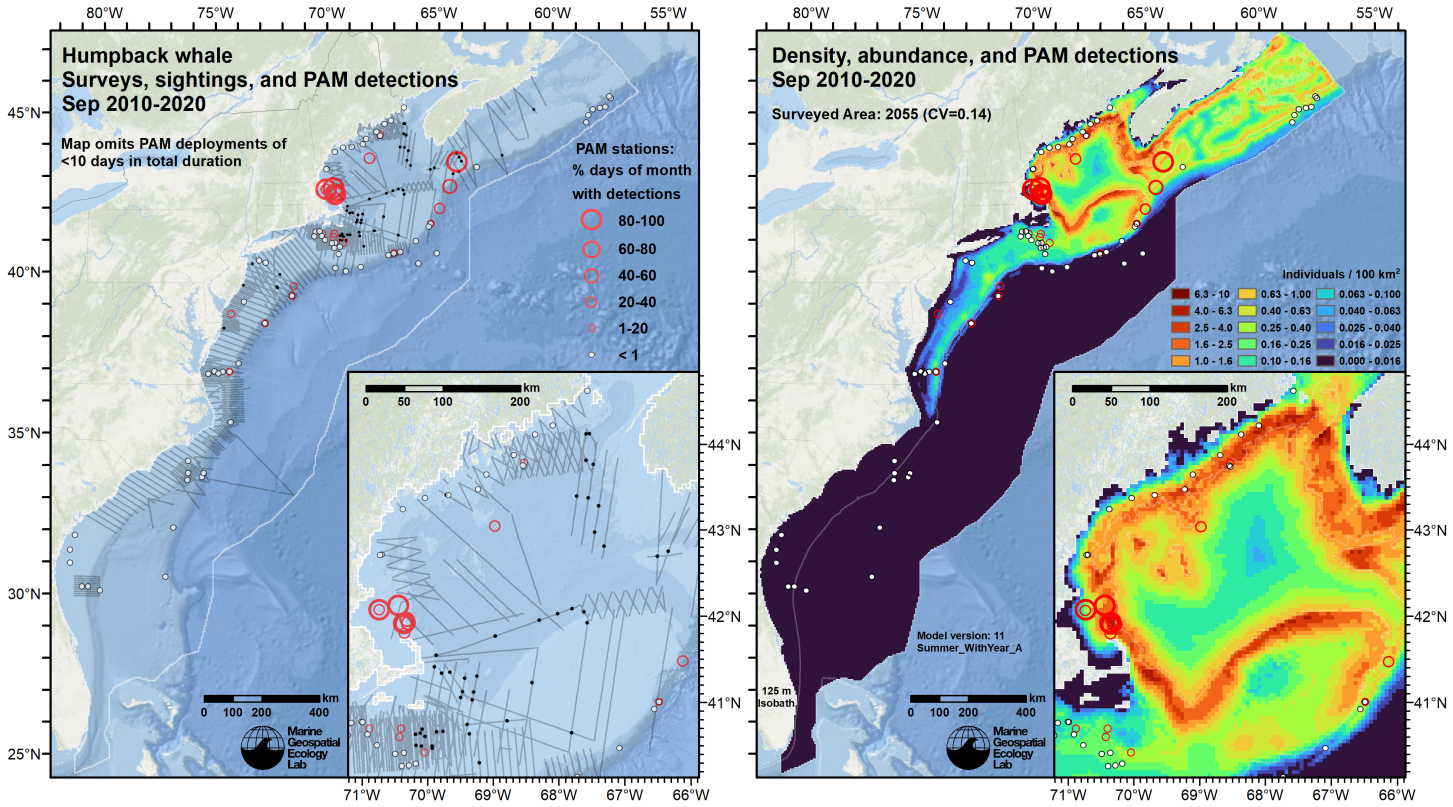

Figure 134: Passive acoustic monitoring stations (red circles and white dots) symbolized by detection rate, overlaid on visual segments and sightings (left) and predicted density (right), for the month of September for the given era.

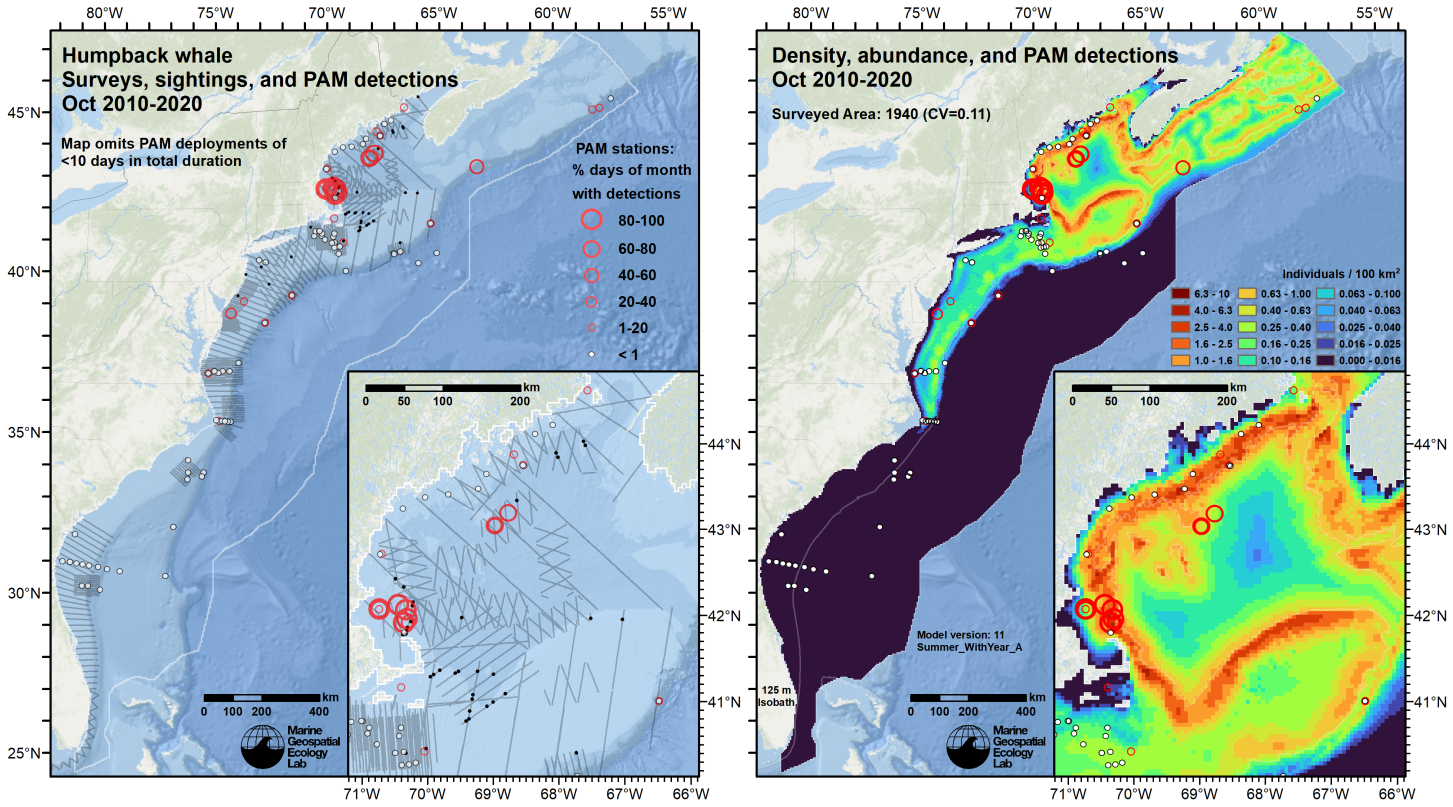

Figure 135: Passive acoustic monitoring stations (red circles and white dots) symbolized by detection rate, overlaid on visual segments and sightings (left) and predicted density (right), for the month of October for the given era.

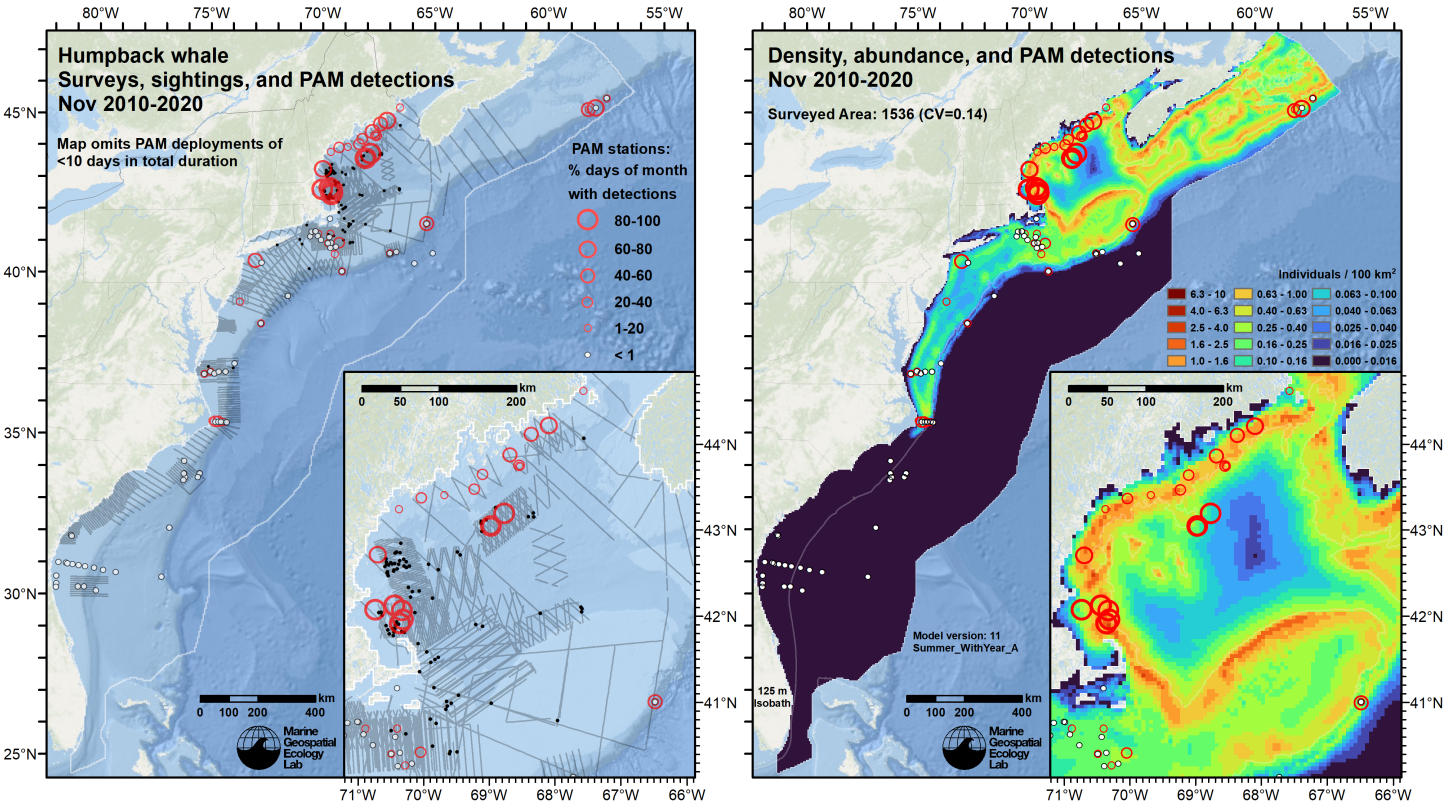

Figure 136: Passive acoustic monitoring stations (red circles and white dots) symbolized by detection rate, overlaid on visual segments and sightings (left) and predicted density (right), for the month of November for the given era.

6 Discussion

In our study area, like North Atlantic right whale, the humpback whale population appears to have undergone noteworthy changes over the past two decades. Particularly important events seemed to have occurred around 2009-2010, when the summer population stopped growing and declined for several years (Hayes et al. 2020 humpback whale Figure 3A), while at the same time humpbacks began appearing close to the Florida and Georgia coast in winter, and important shifts in the Gulf Stream occurred (Ezer 2019; Gonçalves Neto et al. 2021) that were subsequently implicated in changes to the distributions of other cetacean species (Meyer-Gutbrod et al. 2021; Thorne et al. 2022).

To account for the trend in the summer population, we included Year as a smoothed covariate in our summer model. The fitted relationship resembled the trend estimated from an independent photographic capture-mark-recapture (CMR) model (see Section 4.2). Given the agreement between these results and the possibility that a regime shift occurred around 2009-2010, we built summaries of density for three periods: "2003-2008", spanning December 2002 - November 2009; "2003-2019", spanning December 2002 - November 2020; and "2009-2019", spanning December 2009 - November 2020. There are 12 monthly summaries for each period. For species management purposes, such as for the estimation of incidental takes for permits under the U.S. Marine Mammal Protection Act, we recommend latest period be used (2009-2019). The summaries presented in Section 5 are for this period. However, interested parties should always consult with the authoritative agency (e.g. NOAA Office of Protected Resources) when developing permit applications.

NOAA's best estimate for the summer Gulf of Maine population, 1,346 whales, was taken from the CMR model's estimate for mid-summer 2016. Total abundance estimated by our model for the June-August 2009-2019 summary period was 919 whales for the CMR's Sampling Stratum polygon (Table 30), about 32% lower than the CMR estimate. The CMR's polygon, as shown in NOAA's map, did not extend all the way to the coastline, nor did it enclose the band of high density predicted by our model to extend around the northern edge of Georges Bank (Figure 122). If these areas are included by buffering the CMR polygon by 25 km, the total abundance estimated by our model was 1,060, about 22% lower. NOAA's Stock Assessment Report also included abundances estimated by 2016 line transect surveys of U.S. waters and of the Canadian Bay of Fundy and Scotian Shelf. These estimates were 2,368 and 742 whales, respectively. For the same regions, our model estimated 1,070 and 690 whales, about 55% and 7% lower, respectively.

Given the substantially lower abundance estimates obtained from our model, we caution that our model may underestimate density, particularly in the Gulf of Maine, where the difference was largest. We can offer several possible explanations for the

difference. One possibility simply concerns seasonal timing. Our model estimated a peak abundance in June of 2,981 whales in the study area (Figure 108; Table 29), which compares much more closely to NOAA's total abundance estimate from 2016 line transect surveys of 3,110 (Table 30). It greatly exceeds a hybrid estimate comprised of NOAA's CMR estimate for the Gulf of Maine of 1,396 and the Canadian 2016 line transect survey's estimate of 742, totaling 2138. Thus, it may be that our model overestimated abundance in June or underestimated it in later months, or both, or that the differences between our model and the other models comes down to the months and regions used to make summary comparisons.

Another possibility is that our model underestimated perception or availability bias for large groups of humpbacks observed on aerial surveys. For perception bias, we used estimates from Palka et al. (2021) for sightings of 1-2 whales; this seemed appropriate as over 95% of their sightings were of 1 or 2 whales (their remaining sightings were of 3 to 6 whales). We assumed that groups of three or more whales available at the surface would never be missed, based on discussions with observers. Supporting this were other published estimates or assumptions of negligible perception bias for humpback whales, e.g. estimates of $g_{0P} = 0.98$ in Greenland (Heide-Jørgensen et al. 2012; Hansen et al. 2019), or an assumption of $g_{0P} = 1$ in California (Carretta et al. 2000), regardless of group size. However, it is possible that our assumption of $g_{0P} = 1$ for groups of 3 or more whales was not realistic, in which case our density estimate was biased low.

For availability bias, for sightings of more than one animal, we followed Palka et al. (2021) and McLellan et al. (2018) and corrected the single-animal estimate with an estimator that assumed that animals in the group dove asynchronously, which quickly boosted the availability bias correction factor to 1 as group size increased. For example, for the NOAA AMAPPS aerial surveys, our correction factor for a single humpback was 0.524; for two: 0.777; for three: 0.892; for six: 0.988. However, humpback groups are known to employ bubble net feeding and other strategies for which diving behavior may be highly synchronized among whales in the group (Hain et al. 1982; Wiley et al. 2011; Lomac-MacNair et al. 2022; Mastick et al. 2022). It is not clear what effect these behaviors might have on availability bias, and an assumption of complete synchronicity may not be appropriate. For example, during bubble net feeding, some evidence of the submerged whales may be visible at the surface (e.g. bubbles) and recognized by observers. Nevertheless, we caution that our assumption of completely asynchronous behavior may push our availability bias correction too far toward 1, which would also bias density low.

We anticipate this potential problem mainly exists north of Cape Hatteras. Farther south, 98% of the sightings were of a single whale and the remainder were of two whales. These include the more than 100 sightings reported in the core right whale calving ground of coastal Florida and Georgia. Although this was a substantial number of sightings in absolute terms, it was small compared to the very large amount of effort that occurred there, which targeted right whales but also recorded other large whales. We believe the low density estimated there is reasonable, and was not affected by the bias correction questions raised above.

Compared to our prior density model, the new model for winter (December-March) estimated a similar total abundance and distribution of density (Figure 123). Lower density was predicted along coastal Maine, an area where no sightings were reported, but effort was low and largely dated back to the 2000s, and model uncertainty was high (Figure 71). Between Cape Hatteras and Cape Cod, the new model spread density more evenly across the shelf, better agreeing with passive acoustic monitoring, which appeared to show humpbacks spread across the shelf (Figures 125-128). The new model continued to predict some density very close to shore; these predictions reflect the occurrence of sightings close to shore that were used in our model, and are also supported by sightings and tagging data not able to be used in our model, in areas such as Chesapeake Bay (Aschettino et al. 2020) and off New York City (Chou et al. 2022). For the new model, in Long Island Sound, where no sightings had been reported by surveys in our model or been archived in the OBIS-SEAMAP repository (Halpin et al. 2009), we assumed the species was absent during these months.

The new model for summer (April-November) predicted about 14% higher abundance in a roughly similar distribution, with some important differences (Figure 124). Density was higher throughout the Gulf of Maine and lower down the mid-Atlantic shelf break south of Georges Bank. Density was higher across the inner shelf but remained low in the most inshore areas. We caution that substantial sightings have been reported in certain inshore areas from sources not utilizable in our model, particularly in New York, where such sightings have been increasing in recent years (King et al. 2021; Chou et al. 2022). Lower but non-zero density was predicted in Long Island Sound, where humpbacks have been sighted opportunistically in recent years but, like in winter, no sightings were reported by surveys in our model or to OBIS-SEAMAP.

Finally, we note that the prior summer model's CV of mean abundance (0.07) was substantially lower than that (0.30) of the new summer model. The CV of the prior model was unrealistically low because that model only accounted for uncertainty in model parameter estimates, while the new model also accounted for seasonal and interannual variability in predictions. The prior winter model's CV of mean abundance (0.16) was also lower than that (0.31) of the new winter model. While both winter models utilized climatological covariates, and therefore did not account for interannual variability, the new model's statistical approach to uncertainty estimation did better account for seasonal variability.

References

Aschettino JM, Engelhaupt DT, Engelhaupt AG, DiMatteo A, Pusser T, Richlen MF, Bell JT (2020) Satellite Telemetry Reveals Spatial Overlap Between Vessel High-Traffic Areas and Humpback Whales (Megaptera novaeangliae) Near the Mouth of the Chesapeake Bay. Front Mar Sci 7:121. doi: 10.3389/fmars.2020.00121

Barco SG (2002) Population identity of humpback whales (Megaptera novaeangliae) in the waters of the US mid-Atlantic states. J Cetacean Res Manage 4:135–141.

Barco SG, Burt L, DePerte A, Digiovanni R Jr. (2015) Marine Mammal and Sea Turtle Sightings in the Vicinity of the Maryland Wind Energy Area July 2013-June 2015, VAQF Scientific Report #2015-06. Virginia Aquarium & Marine Science Center Foundation, Virginia Beach, VA

Becker JJ, Sandwell DT, Smith WHF, Braud J, Binder B, Depner J, Fabre D, Factor J, Ingalls S, Kim S-H, Ladner R, Marks K, Nelson S, Pharaoh A, Trimmer R, Von Rosenberg J, Wallace G, Weatherall P (2009) Global Bathymetry and Elevation Data at 30 Arc Seconds Resolution: SRTM30_PLUS. Marine Geodesy 32:355–371. doi: 10.1080/01490410903297766

Behrenfeld MJ, Falkowski PG (1997) Photosynthetic rates derived from satellite-based chlorophyll concentration. Limnology and oceanography 42:1–20. doi: 10.4319/lo.1997.42.1.0001

Brasnett B (2008) The impact of satellite retrievals in a global sea-surface-temperature analysis. Quarterly Journal of the Royal Meteorological Society 134:1745–1760. doi: 10.1002/qj.319

Brown DM, Robbins J, Sieswerda PL, Ackerman C, Aschettino JM, Barco S, Boye T, DiGiovanni RA, Durham K, Engelhaupt A, Hill A, Howes L, Johnson KF, Jones L, King CD, Kopelman AH, Laurino M, Lonergan S, Mallette SD, Pepe M, Ramp C, Rayfield K, Rekdahl M, Rosenbaum HC, Schoelkopf R, Schulte D, Sears R, Stepanuk JEF, Tackaberry JE, Weinrich M, Parsons ECM, Wiedenmann J (2022) Site fidelity, population identity and demographic characteristics of humpback whales in the New York Bight apex. J Mar Biol Ass 102:157–165. doi: 10.1017/S0025315422000388

Buckland ST, Anderson DR, Burnham KP, Laake JL, Borchers DL, Thomas L (2001) Introduction to Distance Sampling: Estimating Abundance of Biological Populations. Oxford University Press, Oxford, UK

Burt ML, Borchers DL, Jenkins KJ, Marques TA (2014) Using mark-recapture distance sampling methods on line transect surveys. Methods in Ecology and Evolution 5:1180–1191. doi: 10.1111/2041-210X.12294

Canada Meteorological Center (2012) GHRSST Level 4 CMC0.2deg Global Foundation Sea Surface Temperature Analysis Version 2.0. PODAAC, CA, USA. doi: 10.5067/GHCMC-4FM02

Canada Meteorological Center (2016) GHRSST Level 4 CMC0.1deg Global Foundation Sea Surface Temperature Analysis Version 3.0. PODAAC, CA, USA. doi: 10.5067/GHCMC-4FM03

Cañadas A, Roberts JJ, Yack TM, Halpin PN (2021) Development of Exploratory Marine Species Density Models in the NAVEUR/C6F Study Area. Report prepared for Naval Facilities Engineering Command, Atlantic under Contract No. N62470-15-D-8006, Task Order 18F4048. Duke University Marine Geospatial Ecology Lab, Durham, NC

Canny JF (1986) A computational approach to edge detection. IEEE Transactions on Pattern Analysis and Machine Intelligence 8:679–698. doi: 10.1016/B978-0-08-051581-6.50024-6

Carretta JV, Lowry MS, Stinchcomb CE, Lynn MS, E. CR (2000) Distribution and abundance of marine mammals at San Clemente Island and surrounding offshore waters: Results from aerial and ground surveys in 1998 and 1999. NOAA Administrative Report LJ-00-02. NOAA National Marine Fisheries Service, Southwest Fisheries Center, La Jolla, CA

Chassignet E, Hurlburt H, Metzger EJ, Smedstad O, Cummings J, Halliwell G, Bleck R, Baraille R, Wallcraft A, Lozano C, Tolman H, Srinivasan A, Hankin S, Cornillon P, Weisberg R, Barth A, He R, Werner F, Wilkin J (2009) US GODAE: Global Ocean Prediction with the HYbrid Coordinate Ocean Model (HYCOM). Oceanog 22:64–75. doi: 10.5670/oceanog.2009.39

Chou E, Rekdahl ML, Kopelman AH, Brown DM, Sieswerda PL, DiGiovanni RA, Rosenbaum HC (2022) Occurrence of baleen whales in the New York Bight, 1998–2017: Insights from opportunistic data. J Mar Biol Ass 102:438–444. doi: 10.1017/S0025315422000716

Clapham P, Barlow J, Bessinger M, Cole T, Mattila D, Pace R, Pallka D, Robbins J, Seton R (2003) Abundance and demographic parameters of humpback whales from the Gulf of Maine, and stock definition relative to the Scotian Shelf. Journal of Cetacean Research and Management 5:13–22.

Cole T, Gerrior P, Merrick RL (2007) Methodologies of the NOAA National Marine Fisheries Service Aerial Survey Program for Right Whales (Eubalaena glacialis) in the Northeast U.S., 1998-2006. U.S. Department of Commerce, Woods Hole, MA

Cotter MP (2019) Aerial Surveys for Protected Marine Species in the Norfolk Canyon Region: 2018–2019 Final Report. HDR, Inc., Virginia Beach, VA

Davis GE, Baumgartner MF, Corkeron PJ, Bell J, Berchok C, Bonnell JM, Bort Thornton J, Brault S, Buchanan GA, Cholewiak DM, Clark CW, Delarue J, Hatch LT, Klinck H, Kraus SD, Martin B, Mellinger DK, Moors-Murphy H, Nieukirk S, Nowacek DP, Parks SE, Parry D, Pegg N, Read AJ, Rice AN, Risch D, Scott A, Soldevilla MS, Stafford KM, Stanistreet JE, Summers E, Todd S, Van Parijs SM (2020) Exploring movement patterns and changing distributions of baleen whales in the western North Atlantic using a decade of passive acoustic data. Glob Change Biol gcb.15191. doi: 10.1111/gcb.15191

Delarue JJ-Y, Moors-Murphy H, Kowarski KA, Davis GE, Urazghildiiev IR, Martin SB (2022) Acoustic occurrence of baleen whales, particularly blue, fin, and humpback whales, off eastern Canada, 2015-2017. Endang Species Res 47:265–289. doi: 10.3354/esr01176

Ezer T (2019) Regional Differences in Sea Level Rise Between the Mid-Atlantic Bight and the South Atlantic Bight: Is the Gulf Stream to Blame? Earth's Future 7:771–783. doi: 10.1029/2019EF001174

Foley HJ, Paxton CGM, McAlarney RJ, Pabst DA, Read AJ (2019) Occurrence, Distribution, and Density of Protected Species in the Jacksonville, Florida, Atlantic Fleet Training and Testing (AFTT) Study Area. Duke University Marine Lab, Beaufort, NC

Garrison LP (2020) Abundance of cetaceans along the southeast U.S. East coast from a summer 2016 vessel survey. PRD Contribution # PRD-2020-04. NOAA National Marine Fisheries Service, Southeast Fisheries Science Center, Miami, FL

Garrison LP, Martinez A, Maze-Foley K (2010) Habitat and abundance of cetaceans in Atlantic Ocean continental slope waters off the eastern USA. Journal of Cetacean Research and Management 11:267–277.

Geo-Marine, Inc. (2010) New Jersey Department of Environmental Protection Baseline Studies Final Report Volume III: Marine Mammal and Sea Turtle Studies. Geo-Marine, Inc., Plano, TX

Gonçalves Neto A, Langan JA, Palter JB (2021) Changes in the Gulf Stream preceded rapid warming of the Northwest Atlantic Shelf. Commun Earth Environ 2:74. doi: 10.1038/s43247-021-00143-5

Gowan TA, Ortega-Ortiz JG (2014) Wintering Habitat Model for the North Atlantic Right Whale (Eubalaena glacialis) in the Southeastern United States. PLoS ONE 9:e95126. doi: 10.1371/journal.pone.0095126

Hain JHW, Carter GR, Kraus SD, Mayo CA, Winn HE (1982) Feeding behavior of the humpback whale, Megaptera novaeangliae, in the western North Atlantic. Fishery Bulletin 80:259–268.

Halpin P, Read A, Fujioka E, Best B, Donnelly B, Hazen L, Kot C, Urian K, LaBrecque E, Dimatteo A, Cleary J, Good C, Crowder L, Hyrenbach KD (2009) OBIS-SEAMAP: The World Data Center for Marine Mammal, Sea Bird, and Sea Turtle Distributions. Oceanography 22:104–115. doi: 10.5670/oceanog.2009.42

Hansen RG, Boye TK, Larsen RS, Nielsen NH, Tervo O, Nielsen RD, Rasmussen MH, Sinding MHS, Heide-Jørgensen MP (2019) Abundance of whales in West and East Greenland in summer 2015. NAMMCO Scientific Publications. doi: 10.7557/3.4689

Hayes SA, Josephson E, Maze-Foley K, Rosel PE, Byrd B, Chavez-Rosales S, Cole TV, Garrison LP, Hatch J, Henry A, Horstman SC, Litz J, Lyssikatos MC, Mullin KD, Orphanides C, Pace RM, Palka DL, Powell J, Wenzel FW (2020) US Atlantic and Gulf of Mexico Marine Mammal Stock Assessments - 2019. NOAA National Marine Fisheries Service, Northeast Fisheries Science Center, Woods Hole, MA

Hazen E, Friedlaender A, Thompson M, Ware C, Weinrich M, Halpin P, Wiley D (2009) Fine-scale prey aggregations and foraging ecology of humpback whales Megaptera novaeangliae. Mar Ecol Prog Ser 395:75–89. doi: 10.3354/meps08108

Heide-Jørgensen MP, Laidre KL, Hansen RG, Burt ML, Simon M, Borchers DL, Hansen J, Harding K, Rasmussen M, Dietz R, Teilman J (2012) Rate of increase and current abundance of humpback whales in West Greenland. Journal of Cetacean Research and Management 12:1–12.

Katona SK, Beard JA (1990) Population size, migrations and feeding aggregations of the humpback whale (Megaptera novaeangliae) in the western North Atlantic Ocean. Rep int Whal Commn 295–305.

Kennedy AS, Zerbini AN, Vásquez OV, Gandilhon N, Clapham PJ, Adam O (2014) Local and migratory movements of humpback whales (*Megaptera Novaeangliae*) satellite-tracked in the North Atlantic Ocean. Canadian Journal of Zoology 92:9–18. doi: 10.1139/cjz-2013-0161

King CD, Chou E, Rekdahl ML, Trabue SG, Rosenbaum HC (2021) Baleen whale distribution, behaviour and overlap with anthropogenic activity in coastal regions of the New York Bight. Marine Biology Research 17:380–400. doi: 10.1080/17451000.2021.1967993

Kowarski KA, Martin SB, Maxner EE, Lawrence CB, Delarue JJ-Y, Miksis-Olds JL (2022) Cetacean acoustic occurrence on the US Atlantic Outer Continental Shelf from 2017 to 2020. Marine Mammal Science mms.12962. doi: 10.1111/mms.12962

Laake JL, Calambokidis J, Osmek SD, Rugh DJ (1997) Probability of Detecting Harbor Porpoise From Aerial Surveys: Estimating g(0). Journal of Wildlife Management 61:63–75. doi: 10.2307/3802415

Lawson JW, Gosselin J-F (2018) Estimates of cetacean abundance from the 2016 NAISS aerial surveys of eastern Canadian waters, with a comparison to estimates from the 2007 TNASS. NAMMCO SC/25/AE/09. In: Proceedings of the NAMMCO 25th Scientific Committee (SC). North Atlantic Marine Mammal Commission, Bergen-Tromsø, Norway,

Leiter S, Stone K, Thompson J, Accardo C, Wikgren B, Zani M, Cole T, Kenney R, Mayo C, Kraus S (2017) North Atlantic right whale Eubalaena glacialis occurrence in offshore wind energy areas near Massachusetts and Rhode Island, USA. Endang Species Res 34:45–59. doi: 10.3354/esr00827

Lomac-MacNair KS, Zoidis AM, Ireland DS, Rickard ME, McKown KA (2022) Fin, Humpback, and Minke Whale Foraging Events in the New York Bight as Observed from Aerial Surveys, 2017-2020. Aquat Mamm 48:142–158. doi: 10.1578/AM.48.2.2022.142

Mallette SD, Lockhart GG, McAlarney RJ, Cummings EW, McLellan WA, Pabst DA, Barco SG (2014) Documenting Whale Migration off Virginia's Coast for Use in Marine Spatial Planning: Aerial and Vessel Surveys in the Proximity of the Virginia Wind Energy Area (VA WEA), VAQF Scientific Report 2014-08. Virginia Aquarium & Marine Science Center Foundation, Virginia Beach, VA

Mallette SD, Lockhart GG, McAlarney RJ, Cummings EW, McLellan WA, Pabst DA, Barco SG (2015) Documenting Whale Migration off Virginia's Coast for Use in Marine Spatial Planning: Aerial Surveys in the Proximity of the Virginia Wind Energy Area (VA WEA) Survey/Reporting Period: May 2014 - December 2014, VAQF Scientific Report 2015-02. Virginia Aquarium & Marine Science Center Foundation, Virginia Beach, VA

Mallette SD, McAlarney RJ, Lockhart GG, Cummings EW, Pabst DA, McLellan WA, Barco SG (2017) Aerial Survey Baseline Monitoring in the Continental Shelf Region of the VACAPES OPAREA: 2016 Annual Progress Report. Virginia Aquarium & Marine Science Center Foundation, Virginia Beach, VA

Marsh H, Sinclair DF (1989) Correcting for Visibility Bias in Strip Transect Aerial Surveys of Aquatic Fauna. The Journal of Wildlife Management 53:1017. doi: 10.2307/3809604

Mastick NC, Wiley D, Cade DE, Ware C, Parks SE, Friedlaender AS (2022) The effect of group size on individual behavior of bubble-net feeding humpback whales in the southern Gulf of Maine. Marine Mammal Science 38:959–974. doi: 10.1111/mms.12905

Mattila DK, Clapham PJ (1989) Humpback whales, Megaptera novaeangliae, and other cetaceans on Virgin Bank and in the northern Leeward Islands, 1985 and 1986. Canadian Journal of Zoology 67:2201–2211.

Mattila DK, Clapham PJ, Katona SK, Stone GS (1989) Population composition of humpback whales, Megaptera novaeangliae, on Silver Bank, 1984. Can J Zool 67:281–285. doi: 10.1139/z89-041

Mattila DK, Clapham PJ, Vásquez O, Bowman RS (1994) Occurrence, population composition, and habitat use of humpback whales in Samana Bay, Dominican Republic. Canadian Journal of Zoology 72:1898–1907.

McAlarney R, Cummings E, McLellan W, Pabst A (2018) Aerial Surveys for Protected Marine Species in the Norfolk Canyon Region: 2017 Annual Progress Report. University of North Carolina Wilmington, Wilmington, NC

McLellan WA, McAlarney RJ, Cummings EW, Read AJ, Paxton CGM, Bell JT, Pabst DA (2018) Distribution and abundance of beaked whales (Family Ziphiidae) Off Cape Hatteras, North Carolina, U.S.A. Marine Mammal Science. doi: 10.1111/mms.12500

Meissner T, Wentz FJ, Scott J, Vazquez-Cuervo J (2016) Sensitivity of Ocean Surface Salinity Measurements From Spaceborne L-Band Radiometers to Ancillary Sea Surface Temperature. IEEE Trans Geosci Remote Sensing 54:7105–7111. doi: 10.1109/TGRS.2016.2596100

Mesgaran MB, Cousens RD, Webber BL (2014) Here be dragons: A tool for quantifying novelty due to covariate range and correlation change when projecting species distribution models. Diversity Distrib 20:1147–1159. doi: 10.1111/ddi.12209

Meyer-Gutbrod E, Greene C, Davies K, Johns D (2021) Ocean Regime Shift is Driving Collapse of the North Atlantic Right Whale Population. Oceanog 34:22–31. doi: 10.5670/oceanog.2021.308

Miller DL, Becker EA, Forney KA, Roberts JJ, Cañadas A, Schick RS (2022) Estimating uncertainty in density surface models. PeerJ 10:e13950. doi: 10.7717/peerj.13950

Mullin KD, Fulling GL (2003) Abundance of cetaceans in the southern U.S. North Atlantic Ocean during summer 1998. Fishery Bulletin 101:603–613.

O'Brien O, Pendleton DE, Ganley LC, McKenna KR, Kenney RD, Quintana-Rizzo E, Mayo CA, Kraus SD, Redfern JV (2022) Repatriation of a historical North Atlantic right whale habitat during an era of rapid climate change. Sci Rep 12:12407. doi: 10.1038/s41598-022-16200-8

Palka D (2020) Cetacean Abundance in the US Northwestern Atlantic Ocean Summer 2016. Northeast Fish Sci Cent Ref Doc. 20-05. NOAA National Marine Fisheries Service, Northeast Fisheries Science Center, Woods Hole, MA

Palka D, Aichinger Dias L, Broughton E, Chavez-Rosales S, Cholewiak D, Davis G, DeAngelis A, Garrison L, Haas H, Hatch J, Hyde K, Jech M, Josephson E, Mueller-Brennan L, Orphanides C, Pegg N, Sasso C, Sigourney D, Soldevilla M, Walsh H (2021) Atlantic Marine Assessment Program for Protected Species: FY15 – FY19 (OCS Study BOEM 2021-051). U.S. Deptartment of the Interior, Bureau of Ocean Energy Management, Washington, DC

Palka DL (2006) Summer abundance estimates of cetaceans in US North Atlantic navy operating areas (NEFSC Reference Document 06-03). U.S. Department of Commerce, Northeast Fisheries Science Center, Woods Hole, MA

Palka DL, Chavez-Rosales S, Josephson E, Cholewiak D, Haas HL, Garrison L, Jones M, Sigourney D, Waring G, Jech M, Broughton E, Soldevilla M, Davis G, DeAngelis A, Sasso CR, Winton MV, Smolowitz RJ, Fay G, LaBrecque E, Leiness JB, Dettloff K, Warden M, Murray K, Orphanides C (2017) Atlantic Marine Assessment Program for Protected Species: 2010-2014 (OCS Study BOEM 2017-071). U.S. Deptartment of the Interior, Bureau of Ocean Energy Management, Washington, DC

Pendleton DE, Tingley MW, Ganley LC, Friedland KD, Mayo C, Brown MW, McKenna BE, Jordaan A, Staudinger MD (2022) Decadal-scale phenology and seasonal climate drivers of migratory baleen whales in a rapidly warming marine ecosystem. Global Change Biology 28:4989–5005. doi: 10.1111/gcb.16225

Quintana-Rizzo E, Leiter S, Cole T, Hagbloom M, Knowlton A, Nagelkirk P, O'Brien O, Khan C, Henry A, Duley P, Crowe L, Mayo C, Kraus S (2021) Residency, demographics, and movement patterns of North Atlantic right whales Eubalaena glacialis in an offshore wind energy development area in southern New England, USA. Endang Species Res 45:251–268. doi: 10.3354/esr01137

Ramp C, Delarue J, Palsbøll PJ, Sears R, Hammond PS (2015) Adapting to a Warmer Ocean—Seasonal Shift of Baleen Whale Movements over Three Decades. PLoS ONE 10:e0121374. doi: 10.1371/journal.pone.0121374

Read AJ, Barco S, Bell J, Borchers DL, Burt ML, Cummings EW, Dunn J, Fougeres EM, Hazen L, Hodge LEW, Laura A-M, McAlarney RJ, Peter N, Pabst DA, Paxton CGM, Schneider SZ, Urian KW, Waples DM, McLellan WA (2014) Occurrence, distribution and abundance of cetaceans in Onslow Bay, North Carolina, USA. Journal of Cetacean Research and Management 14:23–35.

Redfern JV, Kryc KA, Weiss L, Hodge BC, O'Brien O, Kraus SD, Quintana-Rizzo E, Auster PJ (2021) Opening a Marine Monument to Commercial Fishing Compromises Species Protections. Front Mar Sci 8:645314. doi: 10.3389/fmars.2021.645314

Robbins J (2007) Structure and dynamics of the Gulf of Maine humpback whale population. University of St. Andrews

Robbins J, Pace RM (2018) Trends in Abundance of North Atlantic Humpback Whales in the Gulf of Maine. NOAA/National Marine Fisheries Service, Northeast Fisheries Science Center, Woods Hole, MA

Roberts JJ, Best BD, Dunn DC, Treml EA, Halpin PN (2010) Marine Geospatial Ecology Tools: An integrated framework for ecological geoprocessing with ArcGIS, Python, R, MATLAB, and C++. Environmental Modelling & Software 25:1197–1207. doi: 10.1016/j.envsoft.2010.03.029

Roberts JJ, Best BD, Mannocci L, Fujioka E, Halpin PN, Palka DL, Garrison LP, Mullin KD, Cole TVN, Khan CB, McLellan WA, Pabst DA, Lockhart GG (2016) Habitat-based cetacean density models for the U.S. Atlantic and Gulf of Mexico. Scientific Reports 6:22615. doi: 10.1038/srep22615

Roberts JJ, Mannocci L, Halpin PN (2017) Final Project Report: Marine Species Density Data Gap Assessments and Update for the AFTT Study Area, 2016-2017 (Opt. Year 1), Document Version 1.4. Duke University Marine Geospatial Ecology Lab, Durham, NC

Roberts JJ, Yack TM, Halpin PN (2023) Marine mammal density models for the U.S. Navy Atlantic Fleet Training and Testing (AFTT) study area for the Phase IV Navy Marine Species Density Database (NMSDD), Document Version 1.3. Duke University Marine Geospatial Ecology Lab, Durham, NC

Robertson FC, Koski WR, Brandon JR, Thomas TA, Trites AW (2015) Correction factors account for the availability of bowhead whales exposed to seismic operations in the Beaufort Sea. Journal of Cetacean Research and Management 15:35–44.

Ryan C, Boisseau O, Cucknell A, Romagosa M, Moscrop A, McLanaghan R (2013) Final report for trans-Atlantic research passages between the UK and USA via the Azores and Iceland, conducted from R/V Song of the Whale 26 March to 28 September 2012. Marine Conservation Research International, Essex, UK

Silsbe GM, Behrenfeld MJ, Halsey KH, Milligan AJ, Westberry TK (2016) The CAFE model: A net production model for global ocean phytoplankton. Global Biogeochemical Cycles 30:1756–1777. doi: 10.1002/2016GB005521

Smith TD, Allen J, Clapham PJ, Hammond PS, Katona S, Larsen F, Lien J, Mattila D, Palsbøll PJ, Sigurjónsson J, Stevick PT, ØIen N (1999) An Ocean-Basin-Wide Mark-Recapture Study of the North Atlantic Humpback Whale (megaptera Novaeangliae). Marine Mammal Science 15:1–32. doi: 10.1111/j.1748-7692.1999.tb00779.x

Stone GS, Katona SK, Tucker EB (1987) History, migration and present status of humpback whales Megaptera novaeangliae at Bermuda. Biological Conservation 42:133–145. doi: 10.1016/0006-3207(87)90019-X

Stone KM, Leiter SM, Kenney RD, Wikgren BC, Thompson JL, Taylor JKD, Kraus SD (2017) Distribution and abundance of cetaceans in a wind energy development area offshore of Massachusetts and Rhode Island. J Coast Conserv 21:527–543. doi: 10.1007/s11852-017-0526-4

Swingle WM, Barco SG, Pitchford TD, Mclellan WA, Pabst D (1993) Appearance of juvenile humpback whales feeding in the nearshore waters of Virginia. Marine Mammal Science 9:309–315.

Thorne LH, Heywood EI, Hirtle NO (2022) Rapid restructuring of the odontocete community in an ocean warming hotspot. Global Change Biology gcb.16382. doi: 10.1111/gcb.16382

Torres LG, Mclellan WA, Meagher E, Pabst DA (2005) Seasonal distribution and relative abundance of bottlenose dolphins, Tursiops truncatus, along the US mid-Atlantic coast. Journal of Cetacean Research and Management 7:153.

Weiss S, Frasier K, Trickey J, Baumann-Pickering S, Hildebrand J, Van Parijs S, Cholewiak D (2020) Analysis of Acoustic Occurrence and Ecology of North Atlantic Shelf Break Species and Effects of Anthropogenic Noise Impacts: FY 2019 Progress Report.

Whitt AD, Powell JA, Richardson AG, Bosyk JR (2015) Abundance and distribution of marine mammals in nearshore waters off New Jersey, USA. Journal of Cetacean Research and Management 15:45–59.

Wiley D, Ware C, Bocconcelli A, Cholewiak D, Friedlaender A, Thompson M, Weinrich M (2011) Underwater components of humpback whale bubble-net feeding behaviour. Behav 148:575–602. doi: 10.1163/000579511X570893

Wiley DN, Asmutis RA, Pichford TD, Gannon DP (1995) Stranding and mortality of humpback whales, Megaptera novaeangliae, in the mid-Atlantic and southeast United States, 1985-1992. Fishery Bulletin 93:196–205.

Winn HE, Edel RK, Taruski AG (1975) Population estimate of the humpback whale (Megaptera novaeangliae) in the West Indies by visual and acoustic techniques. Journal of the Fisheries Board of Canada 32:499–506.

Wood SN (2011) Fast stable restricted maximum likelihood and marginal likelihood estimation of semiparametric generalized linear models. Journal of the Royal Statistical Society: Series B (Statistical Methodology) 73:3–36. doi: 10.1111/j.1467-9868.2010.00749.x

Zoidis AM, Lomac-MacNair KS, Ireland DS, Rickard ME, McKown KA, Schlesinger MD (2021) Distribution and density of six large whale species in the New York Bight from monthly aerial surveys 2017 to 2020. Continental Shelf Research 230:104572. doi: 10.1016/j.csr.2021.104572